University of Arkansas, Fayetteville
ScholarWorks@UARK

Theses and Dissertations

8-2014

Atomistic Simulation and Virtual Diffraction Characterization of Alumina Interfaces: Evaluating Structure and Stability for Predictive Physical Vapor Deposition Models

Shawn Patrick Coleman
University of Arkansas, Fayetteville

Follow this and additional works at: http://scholarworks.uark.edu/etd

 Part of the Applied Mechanics Commons, Metallurgy Commons, and the Nanoscience and Nanotechnology Commons

Recommended Citation
Coleman, Shawn Patrick, "Atomistic Simulation and Virtual Diffraction Characterization of Alumina Interfaces: Evaluating Structure and Stability for Predictive Physical Vapor Deposition Models" (2014). *Theses and Dissertations*. 2185.
http://scholarworks.uark.edu/etd/2185

This Dissertation is brought to you for free and open access by ScholarWorks@UARK. It has been accepted for inclusion in Theses and Dissertations by an authorized administrator of ScholarWorks@UARK. For more information, please contact scholar@uark.edu, ccmiddle@uark.edu.

Atomistic Simulation and Virtual Diffraction Characterization of Alumina Interfaces: Evaluating Structure and Stability for Predictive Physical Vapor Deposition Models

Atomistic Simulation and Virtual Diffraction Characterization of Alumina Interfaces: Evaluating Structure and Stability for Predictive Physical Vapor Deposition Models

A dissertation submitted in partial fulfillment
of the requirements for the degree of
Doctor of Philosophy in Mechanical Engineering

by

Shawn Coleman
University of Notre Dame
Bachelor of Science in Chemical Engineering, 2010

August 2014
University of Arkansas

This dissertation is approved for recommendation to the Graduate Council.

_____
Dr. Douglas E. Spearot
Dissertation Director

_____
Dr. Shui-Qing Yu
Committee Member

_____
Dr. Po-Hao Huang
Committee Member

_____
Dr. Paul Millett
Committee Member

_____
Dr. Uchechukwu Wejinya
Committee Member

ABSTRACT

The objectives of this work are to investigate the structure and energetic stability of different alumina (Al_2O_3) phases using atomistic simulation and virtual diffraction characterization. To meet these objectives, this research performs molecular statics and molecular dynamics simulations employing the reactive force-field (ReaxFF) potential to model bulk, interface, and surface structures in the θ-, γ-, κ-, and α-Al_2O_3 system. Simulations throughout this study are characterized using a new virtual diffraction algorithm, developed and implemented for this work, that creates both selected area electron diffraction (SAED) and x-ray diffraction (XRD) line profiles without assuming prior knowledge of the crystal system. First, the transferability of the ReaxFF potential is evaluated by modelling different alumina bulk systems. ReaxFF is shown to correctly predict the energetic stability of α-Al_2O_3 among the crystalline alumina phases, but incorrectly predicts an even lower energy amorphous phase. Virtual XRD patterns uniquely identify each phase and validate the minimum energy bulk structures through experimental comparison. Second, stable and metastable alumina surfaces are studied at 0, 300, 500, and 700 K. ReaxFF predicts minimum energy surface structures and energies in good agreement with prior studies at 0 K; however, select surface models at 500 and 700 K undergo significant reconstructions caused by the unnatural bias for a lower-energy amorphous phase. Virtual SAED analysis performed on alumina surfaces allow advanced characterization and direct experimental validation of select models. Third, ReaxFF is used to model homophase and heterophase alumina interfaces at 0 K. Predicted minimum energy structures of α-Al_2O_3 interfaces show good agreement with prior works, which provides the foundation for the first atomistic study of metastable alumina grain boundaries and heterophase alumina interfaces. Virtual SAED patterns characterize select alumina interfaces and help guide the construction of

low-energy heterophase alumina interfaces by providing insight into crystallographic compatibilities. Combined, the energetic data extracted from bulk, surface, and interface simulations as well as insights gained through virtual diffraction will aid the development of mesoscale predictive models of polycrystalline alumina formation during physical vapor deposition.

ACKNOWLEDGEMENTS

There are many people to thank and acknowledge for their guidance and support during my graduate studies. First and foremost, I would like to extend my gratitude to my academic and research advisor, Dr. Douglas E. Spearot. The direction and financial support for the enclosed research was provided by Dr. Spearot's National Science Foundation (NSF) Faculty Early Career Development Grant (#0954505) titled: CAREER: Computational Modeling of Microstructure Evolution during Vapor Deposition. I would like to thank Dr. Spearot for all the time, helpful advice, and encouragements he has provided me throughout my graduate studies. I would also like to thank all my colleagues in Dr. Spearot's research group: James Stewart, Khanh Dang, Mehrdad Sichani, and Wesley Barrows for their always fruitful and entertaining discussions. As well, I would like to thank Dr. Laurent Capolungo at the Georgia Institute of Technology for his collaboration on our seminal virtual diffraction publication.

During my graduate studies, I had the opportunity to conduct two internships at Sandia National Laboratories (SNL) in Albuqurue, NM. These internships were conducted under the direction of Dr. Stephen Foiles and Dr. Christopher Weinberger whom I would like to thank for their guidance, support, and helpful advice. I would also like to thank Dr. Garritt Tucker and Dr. Eric Homer whom I met as an intern during their postdoctoral appointments at SNL for their helpful encouragements and collaborations. In addition, I would like to thank Dr. Aidan Thompson and Dr. Steve Plimpton from SNL for their extensive work developing and maintaining the LAMMPS molecular dynamics simulator used throughout my research.

Simulations in this work were performed on resources supported in part by the NSF under grants #0963249, #0959124, #0918970, managed by the Arkansas High Performance Computing Center (AHPCC) as well as resources provided by the Extreme Science and Engineering

Discovery Environment (XSEDE), which is supported by NSF grant #ACI-1053575. I would like to thank all the support staff at AHPCC whom have impacted my computing experience, including: Mr. Jeff Pummill, Dr. David Chaffin, Dr. Pawel Wolinski, and Dr. Rick McMullen. In addition, I would like to thank the members of the XSEDE extended collaborative support services team assigned to this project whom provided assistance optimizing the visual code and enabled high-throughput studies. They include: Dr. Mark Vanmoer, Dr. Sudhakar Pamidighantam, Dr. Yang Wang, Dr. Lars Koesterke, Dr. Luis Cueva-Parra, and Ms. Paula Bermudez.

Lastly, I would like to thank my family and friends who have walked with me throughout this journey. Their unconditional support and guidance have allowed me to become the person I am today – Thank you.

DEDICATION

Mathew Stewart Nye

&

Leigh Whitney Nye

TABLE OF CONTENTS

LIST OF TABLES

LIST OF FIGURES

LIST OF ABBREVIATIONS AND VARIABLES

Applications

PVD	Physical vapor deposition
SZD	Structural zone diagram

Crystallography and Grain Boundaries

XRD	X-ray diffraction (pattern)
SAD	Selected area diffraction (pattern)
SAED	Selected area electron diffraction (SAED)
FCC	Face-centered cubic crystal
BCC	Body-centered cubic crystal
HCP	Hexagonal closed-packed crystal
GB	Grain boundary
STGB	Symmetric tilt grain boundary
CSL	Coincident site lattice
Σ	Reciprocal density of coincident lattice sites between crystal regions

Atomistic Simulations

MD	Molecular dynamics
MS	Molecular statics
NVE	Microcanonical ensemble – number of atoms, volume and total energy constant
NVT	Canonical ensemble – number of atoms, volume and temperature constant
NEB	Nudged elastic band
ReaxFF	Reactive Force-Field
LAMMPS	Large-scale Atomic/Molecular Massively Parallel Simulator
EAM	Embedded-atom method
N	Number of atoms
V	System volume
T	System temperature
$\mathbf{F}_i$	Force acting on atom i
$\mathbf{U}_i$	Interatomic potential function evaluated at atom i
∇	Spatial gradient operator
$\mathbf{r}_i$	Initial position of atom i
$\dot{\mathbf{r}}_i$	Velocity of atom i
$\ddot{\mathbf{r}}_i$	Acceleration of atom i
m_i	Atomic mass of atom i

k_B	Boltzmann constant.
t	Time at step
Δt	Duration of a timestep
ζ	Frictional term added for Nosé-Hoover style thermostats
v_T	Thermostat rate added for Nosé-Hoover style thermostats
T_0	Temperature of external thermal reservoir for Nosé-Hoover style thermostats
$\mathbf{r}_\mathrm{N}$	All atom positions
$\mathbf{U}_i(\mathbf{r}_\mathrm{N})$	Potential energy of the system evaluated with all atoms
k	Arbitrary state of the system during molecular statics
$\alpha^{(k)}$	Magnitude of the step used during molecular statics
$\mathbf{d}^{(k)}$	Search direction used during molecular statics
$\beta^{(k)}$	Update parameter used during molecular statics
r_{ij}	Interatomic distance between atoms i and j
RDF	Radial distribution function
CNA	Common neighbor-analysis
HF	Hartree-Fock
DFT	Density functional theory
LDA	Local density approximation
GGA	Generalized gradient approximations

Interatomic Potentials

E_Pair	Potential energy contribution due to pair-wise interactions
A	Magnitude of repulsive interaction in Buckingham potential
ρ	Radius of repulsive interaction in Buckingham potential
C	Optimization parameter for attractive interaction in Buckingham potential
E_Coulomb	Potential energy contribution due to Coulombic forces (electrostatic interactions)
q_i	Electrostatic charge associated with atom i
C	Energy-conversion and magnitude constant for Coulombic interactions
ε	Dielectric constant
γ_{ij}	Overlap parameter that adjusts for shielding effects
E_Bond	Potential energy contribution due to bonds (ReaxFF)
BO'_{ij}	Continuous bond order parameter
BO_{ij}	Corrected bond order parameter

σ	Single bond
π	Double bond
$\pi\pi$	Triple bond
$p_{\mathrm{bo},n}$	Bond order parameters
D_e	Bond energy parameter
p_{be}	Bond energy parameter
Δ'_i	Corrected difference between the bond order and the expected from its valency
Val_i	Valency of atom i
$\Delta'_{\mathrm{lp},i}$	Difference between the number of lone pair electrons and expected value
$n_{\mathrm{lp},i}$,	Number of lone pair electrons around atom i
Δ^e_i	Difference between the number of valence electrons in the outer shell and the sum of the bond orders
λ_n	General parameters for ReaxFF (n=1-33)
E_{vdWaals}	Potential energy contribution due to van der Waals interactions (ReaxFF)
D_{ij}	ReaxFF parameter describing the magnitude of the van der Waals energy
α_{ij}	ReaxFF parameter describes the width of the minima well
r_{vdW}	ReaxFF parameter describing the ideal interatomic distance for the interaction
λ_W	ReaxFF parameter optimizing shielding interactions

Virtual Diffraction

relp	Reciprocal lattice point
relrod	Reciprocal lattice rod
$I_e(\mathbf{K})$	Electron diffraction intensity
$I_x(\mathbf{K})$	X-ray diffraction intensity
$\mathrm{F}(\mathbf{K})$	Structure factor
$\mathrm{F}^*(\mathbf{K})$	Complex conjugate of structure factor
$\mathrm{Lp}(\theta)$	Lorentz-polarization factor
f_j	Atomic scattering factor
θ	Diffraction (scattering) angle
λ	Wavelength of monochromatic radiation
d_{hkl}	Interplanar distance
$\mathbf{K}$	Reciprocal lattice vector

$\mathbf{k_D}$	Diffracted wave vector
$\mathbf{k_I}$	Incident wave vector
k	A spherically averaged position in reciprocal space
$\mathbf{B}_n$	Reciprocal lattice axis
$\mathbf{A}_n$	Real space lattice axis
c_n	Resolution parameter for virtual diffraction
$\mathbf{a}_i$	Length of a unit cell lattice in direction i
N_i	Number of units cells in direction i

Computer Science

MPI	Message passing interface
OpenMP	Open multi-processing
FFT	Fast Fourier transform
MIC	Many integrated core
VSMP	Virtual symmetric multiprocessing
HPC	High performance computing
AHPCC	Arkansas High Performance Computing Center
TACC	Texas Advanced Computing Center
SDSC	San Diego Supercomputing Center
NCSA	National Center for Supercomputing Applications
XSEDE	Extreme Science and Engineering Discovery Environment
ECSS	Extended Collaborative Support Services

LIST OF PAPERS

Chapter 3 Coleman, S.P., Spearot, D.E., and Foiles, S.M. (2014) Mechanism of grain boundary motion induced by artificial driving force molecular dynamics, Computational Materials Science, **86** 38-42.

Chapter 4 Coleman, S.P., Spearot, D.E., Capolungo, L. (2013) Virtual diffraction analysis of Ni [010] symmetric tilt grain boundaries, Modelling and Simulation in Materials Science and Engineering, **21** 055020.

Chapter 5 Coleman, S.P., Sichani, M.M., Spearot, D.E. (2014) A computational algorithm to produce virtual x-ray and electron diffraction patterns from atomistic simulations, JOM, **66** (3), 408-416.

Chapter 6 Coleman, S.P., Pamidighantam, S. Van Moer, M., Wang, Y., Koesterke, L. Spearot D.E (2014) Performance improvement and workflow development of virtual diffraction calculations, XSEDE14, *In Press.*

Chapter 7 Coleman, S.P. and Spearot, D.E. (2014) Atomistic simulation and virtual diffraction characterization of stable and metastable alumina surfaces, Acta Materialia, *Submitted*.

Chapter 8 Coleman, S.P. and Spearot, D.E. (2014) Atomistic simulation and virtual diffraction characterization of homophase and heterophase Al_2O_3 interfaces, Acta Materialia, *Submitted*.

Chapter 1: Introduction

1.1 Motivation

The motivation for this research is a desire to advance the understanding of microstructure formation and evolution during physical vapor deposition of polymorphic thin films. Despite vast experimentation and industrial use (cf. [1,2]), no quantitative, predictive model for microstructure formation and evolution has been established for the vapor deposition process of polycrystalline materials. This research uses atomistic simulations to elucidate important energetic and structural information pertaining to the surfaces and interfaces that influence phase nucleation and growth during physical vapor deposition. In addition, preliminary simulated ion bombardment on select alumina models are performed to understand the nanoscale mechanisms leading to phase nucleation and transformation. The data gathered from these atomistic simulations lay the framework for advanced phase-field simulations to provide a detailed understanding of the role of process conditions on microstructure morphology at the mesoscale.

Alumina is an ideal material system for this research due to its well-known polymorphism and vast industrial use in vapor-deposited coatings [3–6]. Vapor-deposited alumina thin films are used in electronic devices, optics, and as durable coatings in the cutting tool industry [7,8]. While these industries have different needs for alumina, the process by which the thin films are created is similar and the impact of microstructure on material properties is common to all applications.

Atomistic simulations provide an established route to compute the crucial energetic and structural data needed to create mesoscale predictive models of physical vapor deposition of polycrystalline alumina. Atomistic simulations provide the flexibility and control needed to systematically create, test, and characterize a variety of alumina interface and surface structures

that could only be achievable through a much larger experimental study. However, the complex structures of the various alumina phases pose a unique challenge for atomistic simulation characterization. The traditional atomistic simulation characterization methods that work well with cubic based structures (such as radial distribution functions [9], centrosymmetry [10], common neighbor-analysis [11], etc.) do not clearly identify the subtle structure differences among the various alumina phases. This motivated the development and implementation of a characterization technique for atomistic simulations based on the phenomena of x-ray and electron diffraction.

1.2 Alumina

Alumina is an abundant ceramic material that exhibits extraordinary structural flexibility [3–6]. The different Al_2O_3 phases are characterized by a range of unique physical properties which make them useful in a variety of coating applications [7,8]. These properties stem from only subtle differences within the crystal structure of its phases. In general, the alumina phases are composed of a close-packed oxygen sublattice surrounded by aluminum interstitials partially filling the octahedral and tetrahedral sites to maintain stoichiometry [12], shown in Figure 1.1. The type of close-packed arrangement of the oxygen sublattice and the degree of symmetry of the aluminum interstitials within each alumina unit cell determines the phase and properties of the material.

The structure of alumina phases has been studied extensively in the literature using both simulation and experimental approaches (cf. [13–23]). These studies show that both the κ- and α-Al_2O_3 crystal structures contain a face-centered-cubic (FCC) oxygen sublattice, whereas θ- and γ-Al_2O_3 oxygen atoms form a the hexagonal closed pack (HCP) arrangement [17]. Aluminum atoms partially fill 2/3 of the oxygen interstitial sites with varying degrees of symmetry. The α-

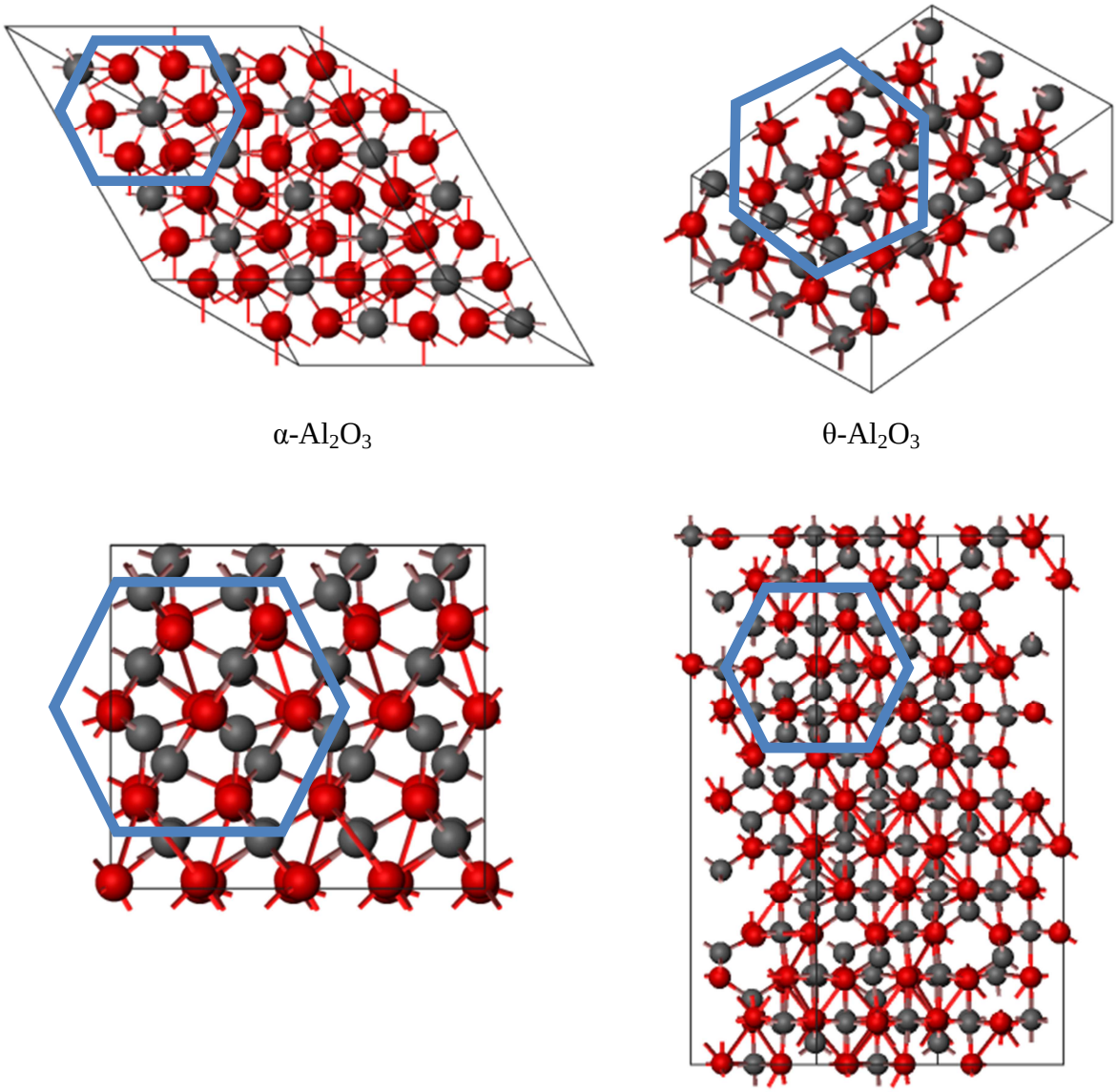

Figure 1.1: Crystal structures of α-Al_2O_3, γ-Al_2O_3, κ-Al_2O_3, and θ-Al_2O_3 show the disorder in the aluminum (gray) sub-lattice in the transition phases. The oxygen (red) lattice remains nearly close-packed in all structures.

Al_2O_3 phase, corundum, is the only thermodynamically stable alumina phase. The α-Al_2O_3 crystal is formed from a five atom tetragonal unit cell that contains the most symmetric ordering of the aluminum interstitials which are present only in octahedral sites [3]. The symmetry of the aluminum interstitials increases the density of α-Al_2O_3 and promotes directionality of the ionic

bonds between the atoms.

The metastable alumina phases have decreasing symmetry among the aluminum interstitials, which decreases their density and weakens bond strength by reducing bond directionality. The κ-Al_2O_3 metastable phase consists of an eight molecular unit (40 atom) orthogonal unit cell. In κ-Al_2O_3, the aluminum interstitials favor the octahedral sites as shown in a first-principles study by Yourdshahyan et al. [13–15]. The θ-Al_2O_3 phase has a ten atom unit cell with monoclinic symmetry as determined by Zhou et al. [22] and Borosy et al. [23] using experimental and simulation studies, respectively. Using a first-principles study, Borosy et al. showed that the aluminum atoms in θ-Al_2O_3 are evenly distributed in both the octahedral and tetrahedral sites [23]. The γ-Al_2O_3 phase is the least symmetric metastable phase examined in this research. It's structure was studied in detail by Paglia et al. using both experimental and simulation approaches [20,21]. In their work, Paglia et al. showed that γ-Al_2O_3 forms both cubic and slightly tetragonal-distorted spinel-like structures with aluminum interstitials located in 60-75% of oxygen octahedral sites of a 160-atom unit cell.

Due to subtle structural differences among the phases as well as the large unit cells for some of the metastable phases, identification and characterization of alumina based solely on local atomic positions is difficult. However, experimental characterization techniques such as x-ray diffraction (XRD) and selected area electron diffraction (SAED) have proven successful in distinguishing between alumina phases [24–28].

Alumina surfaces, in particular those formed by the κ- and α-Al_2O_3 phases, are widely used as protective coatings due to their wear resistance, chemical inertness, resistance to thermal shock, and high hardness [29,30]. However, the alumina material system is known to have several other metastable states whose properties are less ideal for these purposes that can readily

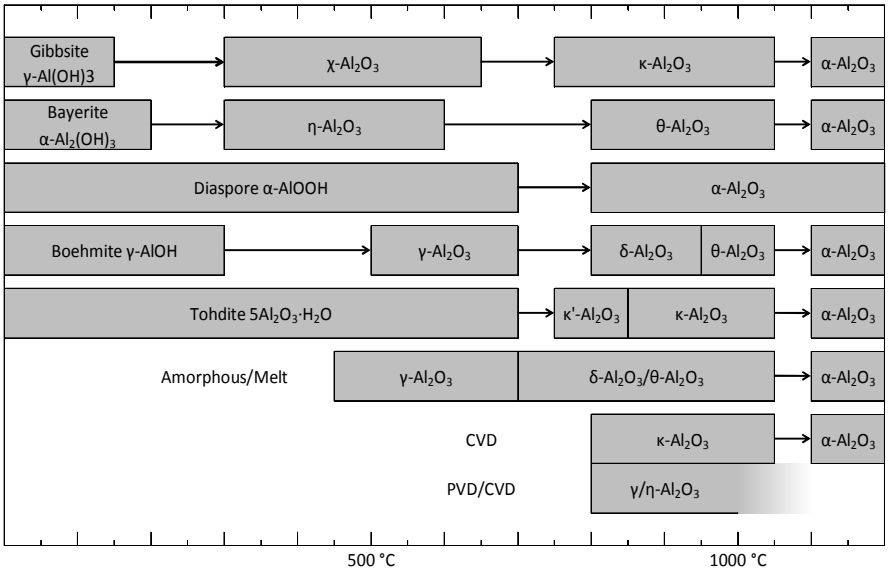

Figure 1.2: Transition sequence for alumina for different precursor materials and processing conditions [32].

form during deposition depending on the processing conditions [31]. For example, the less symmetric θ- and γ-Al_2O_3 metastable phases form readily at lower processing temperatures, approximately 704 K (30% of the melting temperature) [31]. These metastable phases are characterized by having lower surface energies and therefore exhibit higher surface areas, which would be more appropriate for catalytic supports.

The alumina material system experiences a complex phase transition series that is dependent on the material precursors and processing conditions [32–34]. Schematics of the phase transition series, such as the one in Figure 1.2 modeled after the results of Levin et al. [32], can be used as guides in determining the necessary processing conditions required for phase transformation. However, these schematics alone cannot accurately predict the criteria for phase transformation during physical vapor deposition. Instead, researchers must continually characterize alumina surfaces to determine the state of transformation under their particular processes.

1.3 Physical Vapor Deposition

Physical vapor deposition (PVD) is a process by which atoms condense from the vapor phase to form a solid thin film or coating on a substrate [35]. For example, in sputtering, atoms are removed from a target by high-energy ion bombardment. The removed atoms are ejected into the deposition chamber and upon reaching the substrate they condense to reform a solid material, resulting in energy reduction through bond formation. Deposition may be performed in either inert (Ar) or active atmospheres, i.e., prior to condensation atoms in the vapor phase may chemically react with gaseous species in the chamber to form compounds (e.g., Al_2O_3 [36,37]).

The microstructure of the solid deposit is largely determined by deposition conditions and the materials employed. For example, at low substrate temperatures or high deposition rates the adatoms that accumulate on the substrate surface may not have sufficient mobility to migrate to lower energy configurations prior to being covered up by the next deposited layer. Schematic maps, known as structure zone diagrams (SZDs) [38], have been proposed to correlate coating

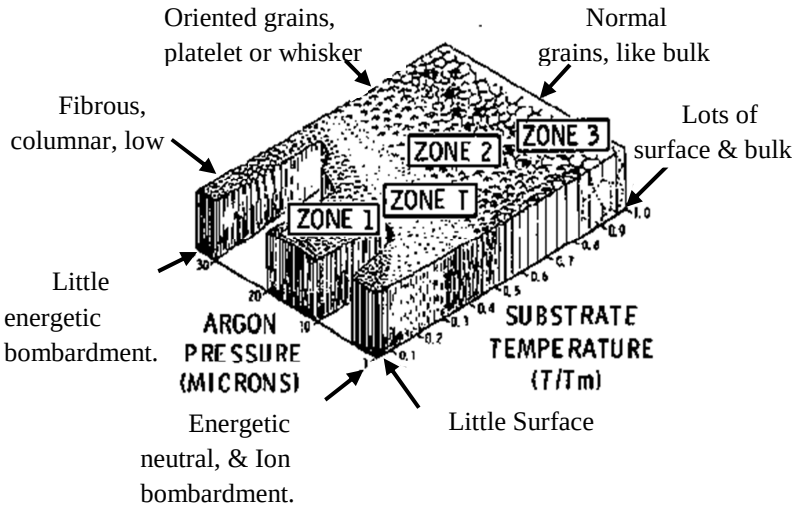

Figure 1.3: Example SZD showing the influence of deposition variables on thin film microstructure based on phenomenological observations [39].

morphology with deposition temperature and pressure, as shown in Figure 1.3 from Thornton [39]. The mechanical, electrical, and optical properties of the coating will change (often dramatically) within the deposition space in Figure 1.3. For evaporated or sputtered films, process zones are identified (1, 2, 3, and T in Figure 1.3) which differ by level of porosity and grain morphology.

While experimental observations of the type that lead to the SZD shown in Figure 1.3 are of tremendous importance, SZDs are heavily phenomenological and are only predictive if deposition is performed within the same process space. Consequently, different SZDs have been proposed in the literature for different PVD techniques, including sputtering [39], metal evaporation [40,41], RF sputtering [42], and magnetron sputtering [43,44]. Furthermore, SZDs do not account for the individual nanoscale mechanisms associated with microstructure formation and evolution (only processing conditions). Therefore, extensive experimentation would be required to extend SZDs to polymorphic thin films. Despite vast experimentation and industrial use, a quantitative model for microstructure formation and evolution during vapor deposition of polymorphic thin films has not been established.

1.4 Objectives

There are three main objectives of this work: (1) to develop and implement a virtual diffraction algorithm that generates x-ray and electron diffraction patterns directly form atomistic simulation data without *a priori* knowledge of the simulated crystal structure, (2) to utilize molecular statistics and molecular dynamics simulations to evaluate the energetic stability of different bulk alumina models as well as characterize metastable and stable alumina surfaces, and (3) to utilize molecular statistics and virtual diffraction to characterize homophase and heterophase alumina interfaces. Combined, the objectives of this work lay the framework for a

larger research study with the overarching goal to elucidate the fundamental nanoscale mechanisms that drive microstructure formation and evolution during PVD of polymorphic thin films.

1.5 Dissertation Structure

Because a portion of this research has been published previously in scholarly journals, this dissertation is structured in the "Published Papers" format in line with the University of Arkansas-Fayetteville Graduate School where published works are presented in their entirety as unique chapters to the dissertation. Before presenting published works, Chapter 2 provides a thorough background on the methods of atomistic simulations used throughout this research as well as outlines the traditional characterization methods commonly used in atomistic simulations. Chapter 2 also includes documentation outlining the search for an appropriate modeling method (i.e., interatomic potential) to describe the complex interatomic interactions within Al_2O_3.

Chapter 3 contains work conducted in collaboration with Dr. Stephen Foiles at Sandia National Laboratories that investigates grain boundary structures and mobility in nickel [45]. This work is included to highlight the capability of atomistic simulations to study interface structures and dynamics. Specifically, this work emphasizes the construction of grain boundary interfaces, techniques for analyzing grain boundary motion, and the capabilities of traditional atomistic methods to characterize face-centered cubic materials.

The development and implementation of a novel computational algorithm that produces virtual diffraction patterns are discussed in Chapters 4-6. Specifically, Chapter 4 includes a detailed description of the virtual diffraction algorithm along with a thorough case study examining select symmetric tilt grain boundaries in nickel, which was done in collaboration with Dr. Laurent Capolungo from the Georgia Institute of Technology [46]. Chapter 5 includes an

additional description of the virtual diffraction algorithm as well as results highlighting its capability and versatility through findings from atomistic simulations of select symmetric tilt nickel grain boundaries, nanocrystalline copper models, and a heterogeneous interface formed between α-Al_2O_3 (0001) and γ-Al_2O_3 (111) [47]. Note, analysis of copper nanocrystalline samples found in Chapter 5 are performed by fellow doctoral student Mehrdad M. Sichani. Chapter 6 highlights the implementation and optimization of the virtual diffraction algorithm into the LAMMPS molecular dynamics simulator [48] as well as the creation of an automated workflow that facilitates high throughput computation and visualization. Work presented in Chapter 6 is done in collaboration with Extended Collaborative Support Services (ECSS) provided though the Extreme Science and Engineering Discovery Environment (XSEDE). Specifically, the optimization of the virtual diffraction code for multilevel parallelism and offloading to heterogeneous computing architecture discussed in Chapter 6 are done in collaboration with Dr. Yang Wang and Dr. Lars Koesterke. Workflow development and integrated visualization discussed in Chapter 6 are done in collaboration with and Dr. Sudhakar Pamidighantam and Dr. Mark Vanmoer, respectively.

Chapter 7 discusses atomistic simulations of bulk alumina and alumina surfaces structures modeled using the reactive force-field (ReaxFF) interatomic potential [49,50] at 0, 300, 500, and 700 K [51]. Here, virtual x-ray diffraction patterns uniquely identify each phase and validate minimum energy bulk structures through experimental comparison. In addition, virtual selected area electron diffraction patterns identify significant structural reconstructions affecting select alumina surface models at 500 and 700 K. Energetic data computed from these simulations are tabulated for use in the larger-scale predictive models of polymorphic thin film PVD.

Chapter 8 contains work discussing homophase and heterophase alumina interfaces modeled

with ReaxFF [52]. The contained study was specifically limited to molecular statics simulations performed at 0 K after observing limitations in the surface study in Chapter 7 that more greatly affect simulations at temperature when using the ReaxFF interatomic potential. ReaxFF shows good agreement to prior studies in its predicted interface structures and energies for most homophase α-Al_2O_3 twins providing confidence to the novel study of metastable Al_2O_3 homophase boundaries and heterophase Al_2O_3 interfaces. Here, virtual diffraction is used to aid the construction of low energy heterophase interfaces as well as to provide further validation of select modeled interfaces through experimental comparison.

Lastly, Chapter 9 summarizes the major findings and makes recommendations for future research. Specifically, this includes recommendation for further analysis of nanoscale mechanisms leading to phase transformation though simulated ion bombardment on alumina surfaces as well as an in-depth study highlighting the use of virtual diffraction characterization to optimize interface misorientation. Preliminary results for such studies are included in this chapter. The conclusion includes discussions of the broader impact of the virtual diffraction algorithm addressing its ability to act as a bridge between materials simulation and experiments.

References

[1] Mahan JE. (2000) Physical Vapor Deposition of Thin Films. New York: John Wiley & Sons, Inc.

[2] Mattox DM. (2010) Handbook of Physical Vapor Deposition (PVD) Processing, second ed. Oxford: Elsevier Inc.

[3] Villars P and Calvert LD. (1991) Pearson's Handbook of Crystallographic Data for Intermetallic Phases, second ed. Materials Park, OH: ASM International.

[4] Alvarez LJ, Sanz JF, Capitán MJ, and Odriozola JA. (1992) Molecular dynamics studies of the structure of γ-alumina, Chemical Physics Letters, **192**, 463–468.

[5] Husson E and Repelin Y. (1996) Structural studies of transition aluminas: Theta alumina, European Journal of Solid State and Inorganic Chemistry, **33**, 1223–1231.

[6] Levin I and Brandon DG. (1998) A new metastable alumina polymorph with monoclinic symmetry, Philosophical Magazine Letters, **77**, 117–124.

[7] Dinman BD. (1990) Aluminas and Health, in: Alumina Chem. Sci. Technol. Handb. Westerville, OH: American Ceramic Society Inc.

[8] Hart LD and Lense E, editors. (1990) Alumina Chemicals: Science and Technology Handbook. Westerville, Ohio: Wiley-American Ceramic Society.

[9] Allen MP and Tildesley DJ. (1990) Computer Simulation of Liquids. Oxford: Claredon Press.

[10] Kelchner CL, Plimpton SJ, and Hamilton JC. (1998) Dislocation nucleation and defect structure during surface indentation, Physical Review B, **58**, 11085–11088.

[11] Tsuzuki H, Branicio PS, and Rino JP. (2007) Structural characterization of deformed crystals by analysis of common atomic neighborhood, Computer Physics Communications, **177**, 518–523.

[12] Morrissey KJ, Czanderna KK, Merrill RP, and Carter CB. (1985) Transition alumina structures studied using HREM, Ultramicroscopy, **18**, 379–386.

[13] Yourdshahyan Y, Ruberto C, Halvarsson M, Bengtsson L, Langer V, and Lundqvist BI. (1999) Theoretical Structure Determination of a Complex Material: κ-Al2O3, Journal of the American Ceramic Society, **82**, 1365–1380.

[14] Yourdshahyan Y, Ruberto C, Bengtsson L, and Lundqvist BI. (1997) First-principles calculations on the atomic and electronic structure of κ-Al2O3, Physical Review B, **56**,

8553–8558.

[15] Yourdshahyan Y, Engberg U, Bengtsson L, Lundqvist BI, and Hammer B. (1997) Theoretical investigation of the structure of κ-Al2O3, Physical Review B, **55**, 8721–8725.

[16] Gutiérrez G, Taga A, and Johansson B. (2001) Theoretical structure determination of γ-Al2O3, Physical Review B, **65**, 1–4.

[17] Wolverton C and Hass KC. (2000) Phase stability and structure of spinel-based transition aluminas, Physical Review B, **63**, 024102.

[18] Kelber JA. (2007) Alumina surfaces and interfaces under non-ultrahigh vacuum conditions, Surface Science, **62**, 271–303.

[19] Lee C-K, Cho E, Lee H-S, Seol KS, and Han S. (2007) Comparative study of electronic structures and dielectric properties of alumina polymorphs by first-principles methods, Physical Review B, **76**, 1–7.

[20] Paglia G, Buckley CE, Rohl AL, Hunter BA, Hart RD, Hanna J V., and Byrne L. (2003) Tetragonal structure model for boehmite-derived γ-alumina, Physical Review B, **68**, 1–11.

[21] Paglia G, Rohl AL, Buckley CE, and Gale JD. (2005) Determination of the structure of γ-alumina from interatomic potential and first-principles calculations: The requirement of significant numbers of nonspinel positions to achieve an accurate structural model, Physical Review B, **71**, 1–16.

[22] Zhou RS and Snyder RL. (1991) Structures and transformation mechanisms of the η, γ and θ transition aluminas, Acta Crystallographica Section B, **47**, 617–630.

[23] Borosy AP, Silvi B, Allavena M, and Nortier P. (1994) Structure and bonding of bulk and surface θ-Alumina from periodic Hartree-Fock calculations, The Journal of Physical Chemistry, **98**, 13189–13194.

[24] Santos PS, Santos H de S, and Toledo SP. (2000) Standard transition aluminas. Electron microscopy studies, Materials Research, **3**, 104–114.

[25] Wilson SJ. (1979) Phase transformations and development of microstructure in boehmite-derived transition aluminas, Proceedings from the British Ceramic Society, **28**, 281–294.

[26] Ollivier B, Retoux R, Lacorre P, Massiot D, and Férey G. (1997) Crystal structure of κ-alumina: an X-ray powder diffraction, TEM and NMR study, Journal of Material Chemistry, **7**, 1049–1056.

[27] Kohn J. A, Katz G, and Broder JD. (1956) Characterization of β-Ga2O3 and its isomorph, θ-Al2O3, Proceedings from the Fourteenth Annual Pittsburg Diffraction Conference, 398–407.

[28] Repelin Y and Husson E. (1990) Transitional aluminas structural study. I. γ- and δ-aluminas, Materials Research Bulletin, **25**, 611–621.

[29] Jamting A, Ring M, Ruppi S, and Swain M V. (1995) Mechanical characterization of kappa and alpha alumina films on hard metals using indentation methods, Journal of Hard Materials, **6**, 67–87.

[30] Kathrein M, Schintlmeister W, Wallgram W, and Schleinkofer U. (2003) Doped CVD Al2O3 coatings for high performance cutting tools, Surface and Coatings Technology, **163-164**, 181–188.

[31] Dragoo AL and Diamond JJ. (1967) Transitions in vapor deposed alumina from 300° to 1200°C, Journal of the American Ceramic Society, **50**, 538–574.

[32] Levin I and Brandon DG. (1998) Metastable alumina polymorphs: Crystal structures and transition sequences, Journal of the American Ceramic Society, **81**, 1995–2012.

[33] Paglia G, Buckley CE, Rohl AL, Hart RD, Winter K, Studer AJ, Hunter BA, and Hanna J V. (2004) Boehmite derived γ-alumina system. 1 . Structural evolution with temperature, with the identification and structural determination of a new transition phase, γ′-alumina, Chemistry of Materials, **16**, 220–236.

[34] Coelho ACV, Santos H de S, and Kiyohara PK. (2007) Surface area, crystal morphology and characterization of transition alumina powders from a new gibbsite precursor, Material Research, **10**, 183–189.

[35] Ohring M. (2002) The Materials Science of Thin Films: Deposition and Structure, second ed. San Diego, CA: Academic Press.

[36] Aryasomayajula A, Canovic S, Bhat DG, Gordon MH, and Halvarsson M. (2007) Transmission electron microscopy and X-ray diffraction analysis of alumina coating by alternate-current inverted magnetron-sputtering technique, Thin Solid Films, **516**, 397–401.

[37] Pulugurtha SR, Bhat DG, and Gordon MH. (2007) CrN(x) and Cr(1−x)Al(x)N as template films for the growth of α-alumina using ac reactive magnetron sputtering, Journal of Vacuum Science & Technology A, **25**, 1367–1372.

[38] Movchan BA and Demchishin A V. (1969) Investigation of the structure and properties of thick vacuum-deposited films of nickel, titanium, tungsten, alumina and zirconium dioxide, Fizika Metallov i Metallovedenie,, **28**, 653–660.

[39] Thornton JA. (1977) High rate thick film growth, Annual Review of Materials Science, **7**, 239–260.

[40] Grovenor CRM, Hentzell HTG, and Smith DA. (1984) The development of grain structure

during growth of metallic films, Acta Metallurgica, **32**, 773–781.

[41] Hentzell HTG, Grovenor CRM, and Smith DA. (1984) Grain structure variation with temperature for evaporated metal films, Journal of Vacuum Science & Technology A, **2**, 218–219.

[42] Messier R, Giri AP, and Roy RA. (1984) Revised structure zone model for thin film physical structure, Journal of Vacuum Science & Technology A, **2**, 500–503.

[43] Kelly PJ and Arnell RD. (1999) Control of the structure and properties of aluminum oxide coatings deposited by pulsed magnetron sputtering, Journal of Vacuum Science & Technology A, **17**, 945–953.

[44] Kelly PJ and Arnell RD. (2000) Magnetron sputtering: a review of recent developments and applications, Vacuum, **56**, 159–172.

[45] Coleman SP, Spearot DE, and Foiles SM. (2014) The effect of synthetic driving force on the atomic mechanisms associated with grain boundary motion below the interface roughening temperature, Computational Materials Science, **86**, 38–42.

[46] Coleman SP, Spearot DE, and Capolungo L. (2013) Virtual diffraction analysis of Ni [0 1 0] symmetric tilt grain boundaries, Modelling and Simulation in Materials Science and Engineering, **21**, 055020.

[47] Coleman SP, Sichani MM, and Spearot DE. (2014) A computational algorithm to produce virtual x-ray and electron diffraction patterns of interfaces from atomistic simulations, JOM, **66**, 408–416.

[48] Plimpton S. (1995) Fast parallel algorithms for short-range molecular dynamics, Journal of Computational Physics, **117**, 1–19.

[49] Van Duin ACT, Dasgupta S, Lorant F, and Goddard WA. (2001) ReaxFF: A Reactive Force Field for Hydrocarbons, The Journal of Physical Chemistry A, **105**, 9396–9409.

[50] Sen FG, Qi Y, van Duin ACT, and Alpas AT. (2013) Oxidation induced softening in Al nanowires, Applied Physics Letters, **102**, 051912.

[51] Coleman SP and Spearot DE. (2014) Atomistic simulation and virtual diffraction characterization of stable and metastable alumina surfaces, Acta Materialia, Submitted.

[52] Coleman SP and Spearot DE. (2014) Atomistic simulation and virtual diffraction characterization of homophase and heterophase alumina interfaces, Acta Materialia, Submitted.

[53] Warren BE. (1990) X-Ray Diffraction, first ed. New York: Dover Publications.

[54] Ishizawa N, Miyata T, Minato I, Marumo F, and Iwai S. (1979) A structural investigation of α-Al203 at 2170K, Acta Crystallographica Section B, **36**, 228–230.

[55] Verwey EJW. (1935) The structure of the electrolytic oxide layer on aluminium, Zeitschrift für Kristallographie, **91**, 317–320.

[56] Verwey EJW. (1935) Incomplete atomic arrangement in crystals, The Journal of Chemical Physics, **3**, 592–593.

Chapter 2: Background

2.1 Atomistic Simulations

This research utilizes molecular dynamics (MD) and molecular statics (MS) simulations to model alumina surfaces and interfaces as well as to identify the atomic mechanisms that drive phase formation and transformation during physical vapor deposition. In the MD and MS frameworks, each atom is represented by a single point mass in space that encompasses both the nucleus and the orbiting electrons. Interactions between atoms are governed by an interatomic potential that describes the conformational (potential) energy of the system. The accuracy of these atomic models depends on the choice of interatomic potential, which depends on the material system and phenomena of interest.

In the MD and MS frameworks, the forces acting on an atom, $\mathbf{F}_i$, are computed from the specified interatomic potential function $\mathbf{U}_i$, using the spatial gradient operator ∇ via

$$\mathbf{F}_i = -\nabla \mathbf{U}_i \quad , \tag{2.1}$$

where $\mathbf{U}_i$ is written as a function of the atom positions within the simulation. There are many types of interatomic potentials that are created and optimized to model specific materials or phenomena. In its simplest form, interatomic potentials will contain repulsion terms that increase in energy when atomic nuclei overlap and attraction terms that seek to bring atoms together due to the interactions between the negatively charged electron cloud of one atom and the positively charged atomic nuclei of another atom. Together, the repulsive and attractive terms will have energy minima that bring atoms to an ideal separation distance and confirmation. The atomic forces, $\mathbf{F}_i$, computed through the interatomic potential are conservative and thus are not specific on the path taken by the atoms. More details concerning interatomic potentials and

the interatomic potential chosen to model the alumina phases in this work are included in Section 2.1.3 and Section 2.2 respectively.

Atomistic simulations commonly use periodic boundary conditions, introduced by Born and von Kármán in 1912 [1], to mimic infinite systems while modeling a finite collection of atoms. Periodic boundary conditions are constructed from 26 (in three-dimensions) replicated simulation cells surrounding a primary simulation model. The atom positions within each replica are identical after making appropriate adjustments for the periodic length defined by the dimensions of the primary simulation model. Atom velocities within each cell are also identical among the replicas and atom motion across replica boundaries results in symmetric motion of atoms across the mirroring boundaries

This research utilizes the classical atomistic simulation package LAMMPS, which is distributed by Sandia National Laboratories under the terms of the GNU Public License [2]. LAMMPS runs in serial or in parallel using message-passing techniques (MPI) and a spatial-decomposition of the atomistic simulation domain. LAMMPS is easily extendable with “plug-and-play” functionality so that new interatomic potentials, new atomistic computations, or new integration schemes can be easily integrated without modifying the core of the atomistic simulation package. This "plug-and-play" functionality serves as the framework for an enhanced virtual diffraction computation, discussed in detail in Chapters 3-5, which computes diffraction intensity data concurrently while the atomistic simulation progresses.

2.1.1 *Molecular Dynamics*

In MD simulations, the forces acting on each atom $\mathbf{F}_i$, calculated with Eq. (2.1), are incorporated with a set of equations of motion to compute the atomic trajectories (position and momentum) over time. To solve the equations of motion, an integration algorithm requires

initial positions, $\mathbf{r}_i$, velocities $\dot{\mathbf{r}}_i$, and acceleration, $\ddot{\mathbf{r}}_i$ for the N atoms contained within the simulation. Initial atom positions, $\mathbf{r}_i$, are determined by the crystal structure of the material of interest. Initial atom velocities, $\dot{\mathbf{r}}_i$, are typically randomized to achieve a predefined temperature, T, computed through the equipartition formula [3],

$$\frac{1}{2}\sum_{i=1}^{\mathrm{N}} m_i \left|\dot{\mathbf{r}}_i\right|^2 = \frac{3}{2}\mathrm{N}k_B\mathrm{T} \tag{2.2}$$

where m_i is the atomic mass and k_B is the Boltzmann constant. The acceleration for each atom, $\ddot{\mathbf{r}}_i$, is computed from the forces acting on an atom by coupling the forces $\mathbf{F}_i$ computed through Eq. (2.1) with Newton's 2nd Law of Motion (for the microcanonical ensemble)

$$\mathbf{F}_i = m_i\ddot{\mathbf{r}}_i \quad . \tag{2.3}$$

Using initial values for atom positions $\mathbf{r}_i$, velocities $\dot{\mathbf{r}}_i$, and acceleration $\ddot{\mathbf{r}}_i$, the integration algorithm solves the $6\mathrm{N}$ coupled differential equations in an iterative manner to determine the $3\mathrm{N}$ atom positions and $3\mathrm{N}$ atom velocities over time. The microcanonical ensemble (NVE) conserves the number of atoms, the system volume, and total energy throughout the simulation.

A common integration algorithm for NVE dynamics used in LAMMPS is the velocity-Verlet method. The algorithm described by the velocity-Verlet method computes updated atom trajectories at time $(t+\Delta t)$ from the initial trajectories at time t through the sequence of equations [4]:

$$\dot{\mathbf{r}}_i\left(t+\frac{\Delta t}{2}\right) = \dot{\mathbf{r}}_i(t) + \frac{\Delta t}{2}\ddot{\mathbf{r}}_i(t) \quad , \tag{2.4}$$

$$\mathbf{r}_i(t+\Delta t) = \mathbf{r}_i(t) + \dot{\mathbf{r}}_i(t)\Delta t \quad , \tag{2.5}$$

$$\mathbf{F}_i = -\nabla \mathbf{U}_i\left(\mathbf{r}_i^N(t+\Delta t)\right) \quad , \text{ and} \tag{2.6}$$

$$\dot{\mathbf{r}}_i\left(t+\Delta t\right)=\dot{\mathbf{r}}_i\left(t+\frac{\Delta t}{2}\right)+\frac{1}{2}\ddot{\mathbf{r}}_i\left(t\right)\Delta t \tag{2.7}$$

where Δt is the duration of the timestep. For MD simulations, the duration of the timestep is often on the order of 1 femtosecond (10^{-15} s) such that the simulation accurately captures the atomic vibrations critical to represent temperature within a collection of atoms.

If desired, augmented versions of Newton's second law can be implemented into the integration algorithm to couple the system dynamics to the surrounding environment. The augmented versions can incorporate thermodynamic boundary conditions such as temperature and pressure control into the simulation [5–9]. For example, this work utilizes the canonical ensemble (NVT), which is designed to maintain a constant number of particles, volume, and system temperature within the simulation. LAMMPS implements the NVT ensemble using the equations developed by Shinoda et al. [10] which are based on a Nosé-Hoover [7] style thermostat. Nosé-Hoover [7] style thermostats augment the equations of motion by adding an additional frictional term, ζ , that effectively connects the system to an eternal thermal reservoir of constant temperature, T_0 , by using the equations

$$\mathbf{F}_i = m_i\ddot{\mathbf{r}}_i + \zeta m_i\dot{\mathbf{r}}_i \quad \text{and} \tag{2.8}$$

$$\zeta = v_T^2\left(\frac{\mathrm{T}}{\mathrm{T}_0}-1\right) \tag{2.9}$$

where, v_T is the thermostat rate. Application of the Nosé-Hoover thermostat dynamically adjusts the system temperature to the desired thermal reservoir temperature, T_0 , by scaling the atomic velocities.

2.1.2 *Molecular Statics*

Molecular statics simulations seek to find the minimum energy conformation of a system at

0 K. In MS simulations, the forces acting on each atom $\mathbf{F}_i$, calculated with Eq. (2.1), are incorporated into numerical algorithms that search for atom coordinates, $\mathbf{r}_\mathrm{N}$, that minimize a defined objective function. For the microcanonical ensemble, MS simulations seek to minimize the potential energy of the system as computed by the interatomic potential, $\mathbf{U}_i(\mathbf{r}_\mathrm{N})$. Commonly, MS simulations use iterative methods to displace the atoms within the simulation along a specified search direction to find a lower energy state,

$$\mathbf{r}_\mathrm{N}{}^{(k+1)} = \begin{cases} \mathbf{r}_\mathrm{N}{}^{(0)} & \text{if } k = 0 \\ \mathbf{r}_\mathrm{N}{}^{(k)} + \alpha^{(k)}\mathbf{d}^{(k)} & \text{if } k > 0 \end{cases} . \tag{2.10}$$

Here, k is a particular iteration representing an arbitrary state of the system, $\alpha^{(k)}$ is the magnitude of the step, and $\mathbf{d}^{(k)}$ is the search direction.

The choice of search direction depends on the type of minimization routine used. For the microcanonical ensemble, the search direction employs the forces acting on the atoms within the simulation, $\mathbf{F} = -\nabla\mathbf{U}_i(\mathbf{r}_\mathrm{N})$, which represents the direction of greatest decrease of potential energy function as calculated through the gradient operator. At each iteration, the search directions are computed through,

$$\mathbf{d}^{(k+1)} = \begin{cases} \mathbf{F}^{(0)} & \text{if } k = 0 \\ \mathbf{F}^{(k+1)} + \beta^{(k+1)}\mathbf{d}^{(k)} & \text{if } k > 0 \end{cases} \tag{2.11}$$

where $\beta^{(k)}$ is an update parameter that scales the input from the previous search direction. If $\beta^{(k)} = 0$, which is known as the method of steepest decent, no input from the previous search direction is included and step directions follow normal to the contour lines of the potential energy surface. For most atomistic simulations, the simplicity of the method of steepest decent is overwhelmed by the complexity of the potential energy surfaces, which slows the convergence

of this method. To handle the complex potential energy surfaces found in atomistic simulations efficiently, MS simulations will commonly utilize a non-linear conjugate gradient method that incorporates values for the update parameter $\beta^{(k)}$ and thus utilizes information from the previous search direction. For example, the LAMMPS implementation of the non-linear conjugate gradient method uses the update parameter introduced by Polak and Ribière [11],

$$\beta^{(k+1)} = \frac{\mathbf{F}^{(k+1)^T}\left(\mathbf{F}^{(k+1)} - \mathbf{F}^{(k)}\right)}{\mathbf{F}^{(k)^T}\mathbf{F}^{(k)}} \quad . \tag{2.12}$$

Using this update parameter, the successive search direction is conjugate [12] to the previous which the improves convergence to a minimum energy configuration when examining complex potential energy surfaces.

The magnitude of the step size $\alpha^{(k)}$ is chosen to minimize the objective function defined by the MS simulation, which for the microcanonical system is,

$$\mathbf{U}_i\left(\mathbf{r}_{\mathrm{N}}{}^{(k)} + \alpha^{(k)}\mathbf{d}^{(k)}\right) \quad . \tag{2.13}$$

In LAMMPS, the step size $\alpha^{(k)}$ is evaluated through an iterative line search algorithm. The line search algorithm moves the atoms along the search directions until an energy minimum is attained. More details about specific minimization routines can be found in [12].

2.1.3 *Interatomic Potentials*

As shown in the prior sections, the specified interatomic potential function, $\mathbf{U}_i$, plays a key role in modeling the interactions between atoms and thus effects the prediction of material behavior. Interatomic potentials can take many forms in order to describe different material behavior, and are often decomposed as a summation of unique terms describing individual atomic interactions,

$$\mathbf{U}_i = \sum E_{\text{Interaction}} \ . \tag{2.14}$$

The most simple of interatomic potentials will consist of a single formula that describes the pair-wise interaction of atoms, E_{Pair}, based solely on the interatomic distance r_{ij} between atom i and atom j. An example pair potential is the Buckingham potential, described by [13],

$$E_{\text{Pair}} = A\exp\left(\frac{-r_{ij}}{\rho}\right) - \frac{C}{r_{ij}^6} \qquad r_{ij} < r_c \ . \tag{2.15}$$

In the Buckingham potential, the first term describes the repulsive interaction of atoms as their interatomic distances decreases and atomic nuclei begin to overlap. This repulsion has spherical symmetry, with a magnitude based on the energy coefficient A and a radius related to the distance parameter ρ. In Eq. (2.15), the second term represents the energy due to attractive van der Waals forces between atomic nuclei and electron clouds that are optimized for a particular material through the C parameter.

For materials that have ionic bonding, additional terms maybe added to the interatomic potential to account for the energy due to Coulombic forces (electrostatic interactions), E_{Coulomb}. The standard Coulombic interaction potential takes the form,

$$E_{\text{Coulomb}} = \frac{Cq_i q_j}{\varepsilon r_{ij}} \qquad r_{ij} < r_c \ , \tag{2.16}$$

where q_i and q_j are the charges associated with atom i and atom j respectively, C is an energy-conversion constant, and ε is the dielectric constant. Summed together, Eqs. (2.15) and (2.16) will describe an energy minima, like that shown in Figure 2.1, at the ideal interatomic separation between atom i and atom j.

Interatomic potentials with greater complexity are derived from similar principles as the two-

body potential in order to model specific phenomena found in a material system. For example, many-body potentials will include additional angular terms that describe the energetics caused by bending and torsional interactions that can be calculated between groups of atoms. These types of interactions are important to describe the potential energy surface in hydrocarbon systems [14,15] as well as other complex material systems [16]

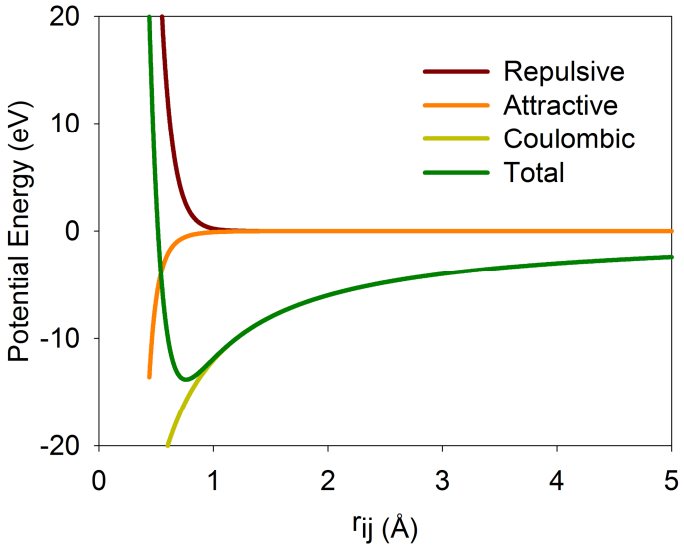

Figure 2.1: Representative Buckingham-Coulombic interatomic potentials made with fictitious parameters.

2.1.4 *First-Principles Methods*

Because of its important material properties and wide industrial use, the alumina material system has been studied extensively using atomistic simulations modeled using first-principles frameworks, as will be discussed in Chapter 7 and 8. First-principles methods are similar to molecular statics simulations in that they are used to study atomic structure and energetics at 0 K. However, unlike molecular statics simulations, first-principles methods rely on a quantum mechanical approach that models electron interactions explicitly (cf. [17–19]). Briefly, first-principles methods compute molecular energy and determine optimized atomic structures by

finding approximate solutions to the many-body Schrödinger equation for all electrons within the model. The approximations used in the prior alumina studies can be divided into two classes: (1) Hartree-Fock (HF) theory and (2) density functional theory (DFT). Methods based on HF theory attempt to find approximate solutions directly to the Schrödinger equation by posing a linear combination of functions that form a basis set approximating the interactions of all individual atoms. Whereas methods based on DFT attempt to find exact solutions to a set of modified equations which approximate the Schrödinger equation based on electronic density. The DFT methods also subdivide into two general classes that differ in how each represents the interactions between the different electrons (exchange-correlation). In DFT, the exchange-correlation can be modeled by functions relying on the local electron density alone, called the local density approximation (LDA), or by functions that also take into account non-local effects posed by gradients of the electronic density, called the generalized gradient approximations (GGA). The accuracy of first-principles models depends on the chosen method, basis set, and exchange-correlation; however, generally accuracy increases with DFT approaches compared to HF and in particular the greatest accuracy is achieved when using GGA exchange-correlation [20].

2.2 Alumina Interatomic Potentials

2.2.1 *Pair-wise Potentials*

Three pair-wise interatomic potentials are examined for use in this work developed by Matsui [21], Van Hoang [22], and Sun [23]. The Matsui potential was created to be transferable to several metal oxide materials and has been used to study amorphous alumina [24–26], melting α-Al_2O_3 [27,28], liquid alumina [27–29], as well as atomic layer deposition of Al_2O_3 [30]. The Van Hoang potential is of the Born-Mayer type [31] and has been used to study amorphous

alumina [32], liquid alumina [33], and super cooled alumina [34,35]. Sun developed a modified Matsui potential that is transferable to other binary metal oxides. Sun's modified Matsui potential has been used to study bulk α-Al_2O_3 [23] and the α-Al_2O_3 (0001) surface [36,37].

Nonlinear conjugate gradient potential energy minimizations are performed on each phase at 0 K to determine the predicted structure and potential energy of each simulation as a function of the interatomic potential, shown in Table 2.1. Here, all three pair-wise potentials fail to represent the critical thermodynamic stability of α-Al_2O_3. Instead, each potential predicts a lower potential energy γ-Al_2O_3 phase, which is inconsistent with experimental results.

Table 2.1: Minimized potential energy (kcal/mol) for various Al_2O_3 crystalline phases as a function of pair-wise interatomic potentials.

Potential	**α-Al_2O_3**	**γ-Al_2O_3**	**κ-Al_2O_3**	**θ-Al_2O_3**
Sun	-24.027	-25.911	-23.628	-25.605
Van Hoang	-30.349	-31.185	-29.392	-30.707
Matsui	-8.334	-8.853	-8.448	-8.334

The inability to accurately predict the thermodynamic stability of α-Al_2O_3 likely stems from the simplicity of these pair-wise models, specifically concerning the manner in which electrostatic interactions are described. The pair-wise interatomic potentials for alumina developed by Matsui, Van Hoang, and Sun all represent electrostatic interactions as simple point charges which cannot account for ion polarization effects. Wilson et al. [38] have noted that accurate modeling of oxygen polarization is a key element in the development of a valid transferable alumina interatomic potential. The results from the pair-wise interatomic potential study clearly show a more complex interatomic potential is needed to model the varying atomic environments within the different alumina phases.

2.2.2 *Reactive Force Field Potential (ReaxFF)*

In this work, the reactive force field (ReaxFF) potential is implemented to describe the interactions between the aluminum and oxygen atoms. ReaxFF was first developed by van Duin, Goddard, and coworkers [39] for use in hydrocarbon systems, but has since been expanded to many other material systems. To be transferable to a wide set of material systems, ReaxFF includes ten terms to represent various phenomena related to different atomic interactions [40],

$$\begin{aligned}\mathbf{U}_i = E_{\text{Bond}} + E_{\text{Over}} + E_{\text{Under}} + E_{\text{val}} + E_{\text{lp}} \\ E_{\text{pen}} + E_{\text{tors}} + E_{\text{conj}} + E_{\text{vdWaals}} + E_{\text{Coulomb}}\end{aligned} \tag{2.17}$$

However, when describing the aluminum and oxygen interactions, only four of these interactions are considered [41,42],

$$\mathbf{U}_i^{\text{Al}_2\text{O}_3} = E_{\text{Bond}} + E_{\text{Over}} + E_{\text{vdWaals}} + E_{\text{Coulomb}} \tag{2.18}$$

where E_{Bond} , E_{Over} , E_{vdWaals} , and E_{Coulomb} account for the energy contributions due to bonding energies, overcoordination penalties, non-bonded van der Waals interactions, and electrostatic interactions respectively. These four contributions allow ReaxFF to accurately model dynamic bond breaking and formation as well as the polarization of charged atomic species.

In ReaxFF, the bond energy term, E_{Bond} , gives the potential its ability to capture bond formation and breakage dynamically without explicitly determining connectivity. Dynamic bonding is made possible using a continuous bond order parameter, BO'_{ij} , computed as a function of the interatomic distance, r_{ij} . The bond order parameter contains three terms to provide different functional forms for σ, π, and ππ (single, double, and triple bonds respectively) [40],

$$\begin{aligned}\mathrm{BO}'_{ij} &= \mathrm{BO}'^{\sigma}_{ij} + \mathrm{BO}'^{\pi}_{ij} + \mathrm{BO}'^{\pi\pi}_{ij} \\ &= \exp\left[p_{\mathrm{bo},1} \cdot \left(\frac{r_{ij}}{r_o^{\sigma}} \right)^{p_{\mathrm{bo},2}} \right] + \exp\left[p_{\mathrm{bo},3} \cdot \left(\frac{r_{ij}}{r_o^{\pi}} \right)^{p_{\mathrm{bo},4}} \right] \\ &\quad + \exp\left[p_{\mathrm{bo},5} \cdot \left(\frac{r_{ij}}{r_o^{\pi\pi}} \right)^{p_{\mathrm{bo},6}} \right]\end{aligned} , \tag{2.19}$$

where $p_{\mathrm{bo},n}$ ($n = 1,2,3...6$) are parameters used to optimize the potential for the various atomic interactions. The bond order parameter is corrected for overcoordination, described in detail in the seminal publication [39], which accounts for atomic configurations exceeding their expected number of max bonds. This corrected bond order term, BO_{ij} , is used to compute the bond energy contribution through [40],

$$\begin{aligned}E_{\mathrm{Bond}} = -D_e^{\sigma} \cdot \mathrm{BO}_{ij}^{\sigma} \cdot \exp\left[p_{\mathrm{be},1} \left(1 - \left(\mathrm{BO}_{ij}^{\sigma} \right)^{p_{\mathrm{be},2}} \right) \right] - \\ D_e^{\pi} \cdot \mathrm{BO}_{ij}^{\pi} - D_e^{\pi\pi} \cdot \mathrm{BO}_{ij}^{\pi\pi}\end{aligned} , \tag{2.20}$$

where the D_e and p_{be} are parameters that are optimized to describe the dissociation energy for the various bond types found in the material system.

Considerations for atom overcoordination are further addressed through an energy penalty, E_{Over} , which is added to atoms exceeding their expected number of bonds based on their valency. The overcoordination energy is computed through [40],

$$E_{\mathrm{Over}} = \frac{\sum_{j=1}^{\mathrm{nbond}} p_{\mathrm{be},3} \mathrm{BO}_{ij}}{\Delta'_i + \mathrm{Val}_i} \cdot \Delta'_i \cdot \left(\frac{1}{1 + \exp\left(\lambda_6 \cdot \Delta_i \right)} \right) , \tag{2.21}$$

where Δ'_i is the corrected difference between the bond order and the expected from its valency,

Val_i, and the variables $p_{\mathrm{be},3}$ and λ_6 are bond energy and general parameters, respectively, optimized for a particular material system. For non-hydrocarbon systems, $\Delta_i^{'}$ is influenced by the presence of lone pair electrons, as shown in its computation [40],

$$\Delta_i^{'} = -\Delta_{\mathrm{lp},i}^{'} \cdot \frac{1}{1+\lambda_{33}\exp\left(\lambda_{33}\mathrm{SOV}\right)} + \sum_{j=1}^{\mathrm{nbond}} \mathrm{BO}_{ij} - \mathrm{Val}_i \quad , \tag{2.22}$$

where,

$$\mathrm{SOV} = \sum_{j=1}^{\mathrm{neighbors}(j)} \left(\Delta_j - \Delta_{\mathrm{lp},j}\right)\mathrm{BO}_{ij}^{\pi} \quad . \tag{2.23}$$

Here, $\Delta_{\mathrm{lp},i}^{'}$ is the difference between the number of lone pair electrons, $n_{\mathrm{lp},i}$, around an atom from the expected value based on its coordination. ReaxFF computes the number of lone pair electrons for each atom through [40],

$$n_{\mathrm{lp},i} = \mathrm{int}\left(\frac{\Delta_i^e}{2}\right) + \exp\left[-\lambda_{16}\cdot\left(2+\Delta_i^e - 2\cdot\mathrm{int}\left(\frac{\Delta_i^e}{2}\right)\right)^2\right] \tag{2.24}$$

where Δ_i^e is the difference between the number of valence electrons in the outer shell and the sum of the bond orders. In Eqs. (2.22) and (2.24), the λ variables are general parameters optimized for a particular material system. Note that in the alumina material system, overcoordination penalties are added to all atoms types; however, considerations for lone pair electrons primarily influences the expected valency of the oxygen atoms only.

In ReaxFF, non-bonded van der Waals interactions and Coulombic contributions are computed between all atom pairs within the simulation due to the consideration of dynamic bond breaking and formation through the bond energy. This differs from other bonded interatomic potentials that exclude bonded atoms when computing non-bonded van der Waals interactions

and Coulombic contributions. The van der Waals interactions describe the repulsive forces that atoms experience as their atomic nuclei begin to overlap. In ReaxFF, the van der Waals interaction energy, E_{vdWaals} , is computed through [40],

$$E_{\text{vdWaals}} = D_{ij} \cdot \left\{ \exp\left[\alpha_{ij} \cdot \left(1 - \frac{f_{13}(r_{ij})}{r_{\text{vdW}}} \right) \right] - 2 \cdot \exp\left[\frac{1}{2} \cdot \alpha_{ij} \cdot \left(1 - \frac{f_{13}(r_{ij})}{r_{\text{vdW}}} \right) \right] \right\}, \quad (2.25)$$

where

$$f_{13}(r_{ij}) = \left[r_{ij}^{\lambda_{29}} + \left(\frac{1}{\lambda_W} \right)^{\lambda_{28}} \right]^{1/\lambda_{28}} \quad . \quad (2.26)$$

Here the parameters D_{ij} describes the magnitude of the van der Waals energy, α_{ij} describes the width of the minima well, and r_{vdW} describes the ideal interatomic distance for the interaction. For the van der Waals energy, the interatomic distances are augmented through Eq. (2.26) to account for shielding interactions that decreases the repulsive interaction between bonded atoms. The shielding interactions are optimized using the λ_W and general λ parameters in Eq. (2.26).

Electrostatic interactions are modeled with the Coulomb energy contribution, computed in ReaxFF through [39],

$$E_{\text{Coulomb}} = C \cdot \frac{q_i \cdot q_j}{\left[r_{ij}^3 + (1/\gamma_{ij})^3 \right]^{1/3}} \quad , \quad (2.27)$$

where C relates the magnitude of the energy and γ_{ij} is an overlap parameter that adjusts for shielding effects. An important feature of the ReaxFF interatomic potential is its incorporation of dynamic charge calculations. The atomic charges q_i and q_j in Eq. (2.27), are not fixed; rather, they are continuously optimized based on atomic geometry at each timestep using the electron equilibration method [43]. The dynamic charge calculation allows modeling of

polarization effects; however, to maintain numerical stability of this charge equilibrium scheme, MD simulations incorporating the ReaxFF potential generally require sub-femtosecond timesteps.

The ReaxFF parameters used in this study were first optimized by Zhang et al. in 2004 for Al and α-Al_2O_3 using *ab inito* calculations on Al-O clusters [41] then further tailored by Sen et al. in 2013 to better incorporate varying Al oxidation states during oxidation simulations [42]. The ReaxFF interatomic potential is much more computationally demanding and memory intensive when compared to other standard pair-wise and many-body potentials [44]. However, these additional computational costs are necessary to accurately describe the structures and thermodynamics of multiple metastable and stable alumina phases.

Because of its important material properties and wide industrial use, the alumina material system has been studied extensively using atomistic simulations modeled from first-principles and Newtonian physics frameworks. However, none of these previous atomistic studies has attempted to catalog the structural and thermodynamic properties of interfaces and surface structures with more than a couple alumina phases using the same method. Instead, the majority of prior atomistic studies sought to identify the minimum energy structures of select bulk alumina phases, surfaces, and interfaces. By narrowing the focus on select alumina components, prior atomistic simulation studies have avoided the challenges of uniquely characterizing the subtle structural differences among the various alumina phases as well as the distortion created by atomic relaxations at the interfaces. In addition, because the various methods used previously to study alumina rely on different assumptions; direct comparisons between the results (especially quantitative thermodynamic values) across the different studies cannot be made.

2.3 Atomistic Simulation Characterization

2.3.1 *Traditional Methods*

The characterization techniques discussed in this section are described as "traditional methods" because they are well established and used extensively by researchers in the atomistic simulation community. A unique advantage of atomistic simulations is that they provide the coordinates and velocities (if performing dynamics) of every atom within the simulation. This allows researchers to study material phenomena by explicitly visualizing atomic structure and atomic velocities through time as well as enabling computation of spatially dependent properties. For example, using the coordinates of the atoms, researchers can compute the radial distribution function (RDF) [45] to describe atom density as a function of separation distance from a reference atom. The radial distribution function is calculated through a binning procedure that counts the number of atoms that surround the reference atom within a thin shell region as shown in Figure 2.2. Binned amounts are computed for each atom and are normalized through spatial averaging to provide a unique description of the local atomic geometry up to the maximum separation distance examined.

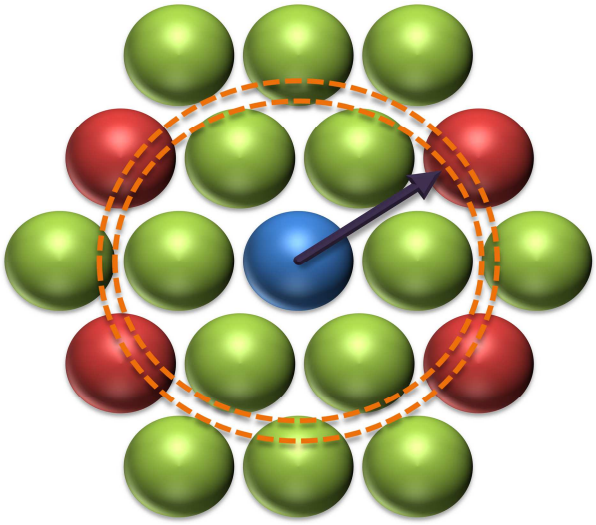

Figure 2.2: Schematic of radial distribution function calculation [9].

To elucidate other material phenomenon, researchers will often employ various color-coding techniques to provide more insight into their visualizations. As a simple example, researchers may color-code atoms within a simulation by their per-atom potential energy to locate defect regions within the simulations where atoms possess elevated energy. Other per-atom quantities, such as centrosymmetry [46] and the common neighbor-analysis parameter [47], have been developed to provide further insights into material phenomena through similar color-coding visualization techniques.

Centrosymmetry is a per-atom quantity developed by Kelchner et al. [46] to uncover defect structures associated with dislocation nucleation in face-centered cubic Au during nanoindention. This technique takes advantage of a special centrosymmetric property defined by the bonding within face-centered cubic (FCC) and body centered cubic (BCC) materials. In centrosymmetric materials, the lattice is constructed from atoms with bond pairs that are equal and opposite in direction. The centrosymmetry parameter defined by Kelchener et al. measures the distortion of these bonds through,

$$P = \sum_{i=1,6} \left| \mathbf{R}_i + \mathbf{R}_{i+6} \right|, \tag{2.28}$$

where $\mathbf{R}_i$ and $\mathbf{R}_{i+6}$ are the vectors describing the bond pairs. Under homogenous elastic deformation, bond pairs in centrosymmetric materials within the bulk will remain equal and opposite in direction, thus showing no distortion in the centrosymmetry parameter ($P = 0$). However, atoms located at interfaces and near defects as well as bulk atoms experiencing non-homogenous elastic deformation will have positive centrosymmetry values ($P > 0$). A benefit of the centrosymmetry parameter is its ease of implementation and concept. However, the disadvantage of this method is that it is only useful and valid for materials with centrosymmetric

structures, which alumina is not as shown in Figure 1.1.

A more general per-atom characterization technique is the common neighbor-analysis (CNA) parameter, which identifies disorder found in arbitrary local environments. The common neighbor-analysis parameter was defined by Tsuzuki et al. [47] through,

$$Q = \frac{1}{n_i} \sum_{j=1}^{n_i} \left| \sum_{k=1}^{n_{ij}} \mathbf{R}_{ik} + \mathbf{R}_{jk} \right|^2 , \tag{2.29}$$

where n_i is the number of nearest neighbors of atom i, n_{ij} is the number of common nearest neighbors between atom i and atom j, and $\mathbf{R}$ are vectors describing the bonds between the atoms identified through the subscript. The common neighbor-analysis parameter identifies deformation in many crystal systems and can distinguish between different types of defects such as stacking fault, dislocations, interface, etc. by relating these features to the common FCC, BCC, hexagonal closed packed (HCP), and "other" crystal systems.

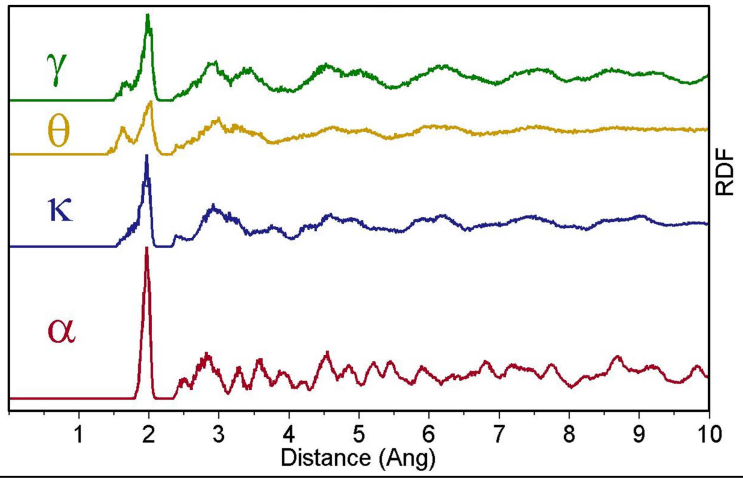

Figure 2.3: Computed radial distribution functions (RDF) for select alumina phases at 0 K do not clearly identify the different crystal structures.

The traditional characterization methods discussed here have had great success in describing material structure and phenomena in metallic materials; however, they fall short to uniquely characterize the complex structures and phenomena found within the alumina material system

due to the asymmetric placement of Al ions. The radial distribution functions computed for 0 K energy minimized structures using the ReaxFF potential [42], shown in Figure 2.3, show no clear distinction between the metastable phases. The complex, non-symmetric structures of the metastable phases have similar atomic densities within the 10 Å maximum cut-off distance explored; however, the specific placement of the aluminum interstitials within each phase is not clearly apparent.

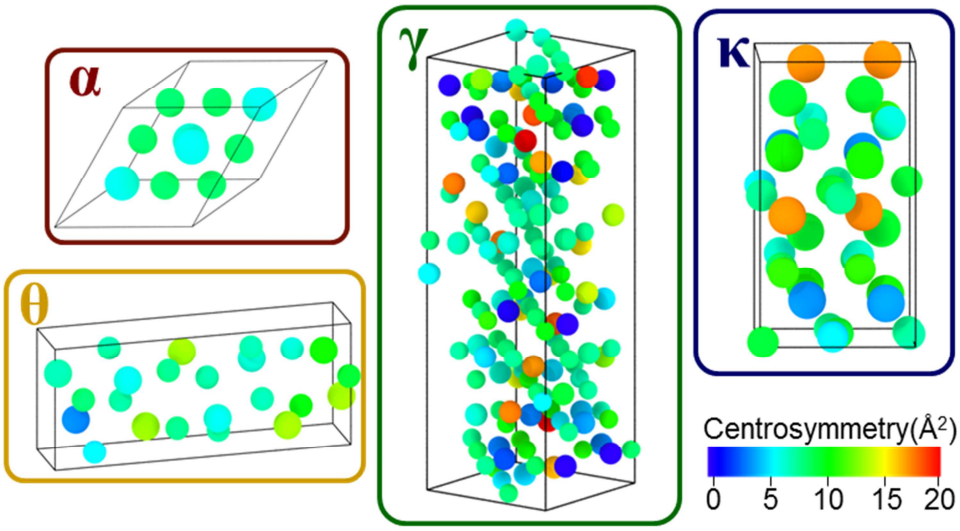

Figure 2.4: Select alumina phases color-coded by the computed centrosymmetry parameter – here, the larger atoms are Al and smaller atoms are O.

Computed centrosymmetry and common neighbor analysis parameters are also unable to uniquely identify the various alumina phases. Figure 2.4 shows the unit cell for each alumina phase studied in this research colored by the centrosymmetry parameter. In general, the α-Al_2O_3 and γ-Al_2O_3 phases are more centrosymmetric as seen by the lower magnitude of the centrosymmetry parameter for each atom; however, there is no clear differentiation among the phases. The common neighbor analysis conducted on the alumina unit cells did not identify any specific crystal system within the various phases; therefore, all atoms were declared as "other" using this method.

2.3.2 *Kinematic vs. Dynamic Virtual Diffraction Methods*

Because the traditional characterization methods used in atomistic simulations are unable to uniquely identify and differentiate the alumina phases, more advanced characterization methods based upon diffraction techniques are explored for his work. Diffraction is a common experimental method used to study the atomic scale structure of materials by examining the interaction between a beam of electromagnetic radiation (e.g. x-rays and electrons) and the periodic pattern of atoms within a material sample. Specifically, experimental diffraction patterns have been used to successfully identify and differentiate alumina phases [48–52]. Several previous virtual diffraction methods have been developed to analyze atomistic simulations; however, these prior methods have limited functionality and require *a prori* knowledge of the crystal system. Therefore, an advanced virtual diffraction technique is developed and implemented for this work that overcome these prior limitations, as will be discussed in Chapters 4-6.

Virtual diffraction methods utilize equations from diffraction theory in order to produce equivalent diffraction patterns in an effort to bridge atomistic simulations and experimental studies. More information on diffraction theory can be compiled from books by Warren [53] and Guinier [54]. Briefly, there are two classes of diffraction theory, (1) kinematic and (2) dynamic, that were developed starting in the early 1900s by W. H. Bragg, W. L. Bragg, Laue, Ewald, and Darwin soon after the discovery of coherent x-ray diffraction scattering in metals [55]. Kinematic diffraction theory models the interference patterns of diffracted radiation created by scattering off individual atoms. Similarly, dynamical diffraction theory models interference patterns; however, more rigorously incorporates the effects of reflected radiation. Figure 2.5 shows a schematic of diffracted versus reflected radiation related to the two classes of theory.

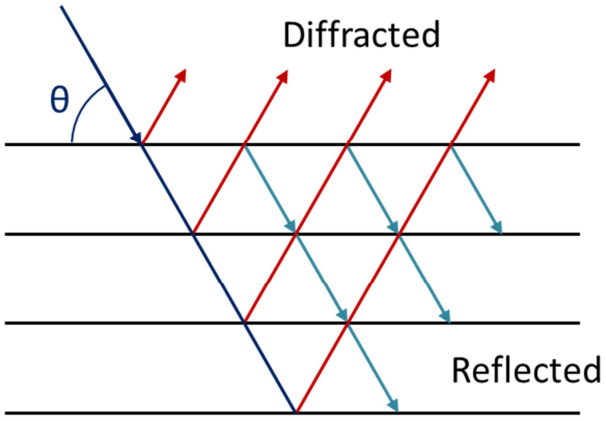

Figure 2.5: Diagram showing diffracted versus reflected radiation to illustrate capabilities of kinematic versus dynamic diffraction. [53]

When studying large or perfect crystals, the dynamical theory is a more appropriate model for diffraction because the contributions from reflections become much more important. However, the computational cost to evaluate diffraction intensities via the dynamic diffraction theory is much larger as compared to kinematic diffraction theory due to the considerations of reflected radiation. When studying small volumes or imperfect crystal structures, such in the case for MD and MS simulations, reflected radiation becomes less important and a good approximation for diffraction is made by using kinematic diffraction theory. The virtual diffraction technique developed for this work utilizes equations based on kinematic diffraction theory. Details regarding its implantation are contained in Chapters 4-6 alongside various case studies to validate the method and showcase its versatility. Virtual diffraction methods are used to study alumina in Chapters 7 and 8 which focus on bulk and surface simulations as well as interface structures, respectively.

References

[1] Born M and von Kármán T. (1912) On vibrations in space lattices, Physikalische Zeitschrift, **13**, 297–309.

[2] Plimpton SJ. (1995) Fast parallel algorithms for short-range molecular dynamics, Journal of Computational Physics, **117**, 1–19.

[3] Kundt A and Warburg E. (1875) Über Reibung und Wärmeleitung verdünnter Gase, Annalen der Physik, 525–550.

[4] Swope WC, Andersen HC, Berens PH, and Wilson KR. (1982) A computer simulation method for the calculation of equilibrium constants for the formation of physical clusters of molecules: Application to small water clusters, The Journal of Chemical Physics, **76**, 637.

[5] Andersen HC. (1980) Molecular dynamics simulations at constant pressure and/or temperature, The Journal of Chemical Physics, **72**, 2384.

[6] Berendsen HJC, Postma JPM, van Gunsteren WF, DiNola A, and Haak JR. (1984) Molecular dynamics with coupling to an external bath, The Journal of Chemical Physics, **81**, 3684.

[7] Hoover WG. (1985) Canonical dynamics: Equilibrium phase-space distributions, Physical Review A, **31**, 1695–1697.

[8] Melchionna S, Ciccotti G, and Holian BL. (1993) Hoover NPT dynamics for systems varying in shape and size, Molecular Physics, **78**, 533–544.

[9] Nosé S. (1984) A molecular dynamics method for simulations in the canonical ensemble, Molecular Physics, **52**, 255–268.

[10] Shinoda W, Shiga M, and Mikami M. (2004) Rapid estimation of elastic constants by molecular dynamics simulation under constant stress, Physical Review B, **69**, 134103.

[11] Polak E and Ribière G. (1969) Note sur la convergence de méthodes de directions conjuguées, Revue Française d'Informatique et de Recherche Operationelle, **43**, 35–43.

[12] Shewchuk JR. (1994) An Introduction to the Conjugate Gradient Method Without the Agonizing Pain, 1–58.

[13] Buckingham RA. (1938) The classical equation of state of gaseous helium , neon and argon, Proceedings of the Royal Society of London Series A, Mathematical and Physical Sciences, **168**, 264–283.

[14] Tersoff J. (1988) New empirical approach for the structure and energy of covalent systems, Physical Review B, **37**, 6991–7000.

[15] Tersoff J. (1988) Empirical Interatomic Potential for Carbon, with Applications to Amorphous Carbon, Physical Review Letters, **61**, 2879–2882.

[16] Tersoff J. (1986) New empirical model for the structural properties of silicon, Physical Review Letters, **56**, 632–635.

[17] Capelle K. (2006) A bird's-eye view of density-functional theory, Brazilian Journal of Physics, **36**, 1318–1343.

[18] Allan NL and Mackrodt WC. (1994) Density functional theory and interionic potentials, Philosophical Magazine B, **69**, 871–878.

[19] Yates JT and Johnson JK. (2007) Molecular Physical Chemistry for Engineers. Sausalito, CA: University Science Books.

[20] Yates JT and Johnson JK. (2007) Molecular Physical Chemistry for Engineers. Sausalito, CA: University Science Books.

[21] Matsui M. (1996) Molecular dynamics simulation of structures, bulk moduli, and volume thermal expansivities of silicate liquids in the system CaO-MgO-Al2O3-SiO2, Geophysical Research Letters, **23**, 395–398.

[22] Hoang V Van and Oh SK. (2004) Simulation of structural properties and structural transformation of amorphous Al2O3, Physica B: Condensed Matter, **352**, 73–85.

[23] Sun J, Stirner T, Hagston WE, Leyland A, and Matthews A. (2006) A simple transferable interatomic potential model for binary oxides applied to bulk α-Al2O3 and the (0001) α-Al2O3 surface, Journal of Crystal Growth, **290**, 235–240.

[24] Adiga SP, Zapol P, and Curtiss LA. (2007) Structure and Morphology of Hydroxylated Amorphous Alumina Surfaces, The Journal of Physical Chemistry C, **111**, 7422–7429.

[25] Adiga SP, Zapol P, and Curtiss LA. (2006) Atomistic simulations of amorphous alumina surfaces, Physical Review B, **74**, 1–8.

[26] Gutiérrez G and Johansson B. (2002) Molecular dynamics study of structural properties of amorphous Al2O3, Physical Review B, **65**, 1–9.

[27] Ahuja R, Belonoshko AB, and Johansson B. (1998) Melting and liquid structure of aluminum oxide using a molecular-dynamics simulation, Physical Review E, **57**, 1673–1676.

[28] Belonoshko AB. (1998) Melting of corundum using conventional and two-phase

molecular dynamic simulation method, Physics and Chemistry of Minerals, **25**, 138–141.

[29] Gutiérrez G, Belonoshko AB, Ahuja R, and Johansson B. (2000) Structural properties of liquid Al2O3: A molecular dynamics study, Physical Review E, **61**, 2723–2729.

[30] Hu Z, Shi J, and Turner CH. (2009) Molecular dynamics simulation of the Al2O3 film structure during atomic layer deposition, Molecular Simulation, **35**, 270–279.

[31] Born M and Mayer JE. (1932) Lattice theory of ionic crystals, Zeitschrift für Physikalische Chemie, **75**, 1–18.

[32] Hoang V Van and Kun Oh S. (2005) Annealing effects on structure in amorphous Al2O3 models, Physica B: Condensed Matter, **364**, 225–232.

[33] Hoang V Van and Kun Oh S. (2004) Structure and diffusion simulation of liquid Al2O3, Physica B: Condensed Matter, **352**, 342–352.

[34] Hoang V Van and Oh SK. (2005) Dynamical heterogeneities in supercooled Al2O3, Journal of Physics: Condensed Matter, **17**, 5179–5185.

[35] Hoang V Van. (2006) Spatial correlations of most mobile or immobile particles in supercooled Al2O3, physica status solidi (a), **203**, 478–484.

[36] Sun J, Stirner T, and Matthews A. (2006) Calculation of native defect energies in α-A12O3 and α-Cr2O3 using a modified Matsui potential, Surface and Coatings Technology, **201**, 4201–4204.

[37] Sun J, Stirner T, and Matthews A. (2007) Molecular dynamics simulation of the (0001) α-Al2O3 and α-Cr2O3 surfaces, Surface Science, **601**, 1358–1364.

[38] Wilson M, Exner M, Huang Y-M, and Finnis MW. (1996) Transferable model for the atomistic simulation of Al2O3, Physical Review B, **54**, 15683–15689.

[39] Van Duin ACT, Dasgupta S, Lorant F, and Goddard WA. (2001) ReaxFF: A Reactive Force Field for Hydrocarbons, The Journal of Physical Chemistry A, **105**, 9396–9409.

[40] Van Duin ACT, Strachan A, Stewman S, Zhang Q, Xu X, and Goddard WA. (2003) ReaxFF SiO Reactive Force Field for Silicon and Silicon Oxide Systems, The Journal of Physical Chemistry A, **107**, 3803–3811.

[41] Zhang Q, Çağın T, van Duin ACT, Goddard WA, Qi Y, and Hector LG. (2004) Adhesion and nonwetting-wetting transition in the Al/α-Al2O3 interface, Physical Review B, **69**, 045423.

[42] Sen FG, Qi Y, van Duin ACT, and Alpas AT. (2013) Oxidation induced softening in Al nanowires, Applied Physics Letters, **102**, 051912.

[43] Rappe AK and Goddard WA. (1991) Charge equilibration for molecular dynamics simulations, The Journal of Physical Chemistry, **95**, 3358–3363.

[44] Aktulga HM, Fogarty JC, Pandit SA, and Grama AY. (2012) Parallel reactive molecular dynamics: Numerical methods and algorithmic techniques, Parallel Computing, **38**, 245–259.

[45] Allen MP and Tildesley DJ. (1990) Computer Simulation of Liquids. Oxford: Claredon Press.

[46] Kelchner CL, Plimpton SJ, and Hamilton JC. (1998) Dislocation nucleation and defect structure during surface indentation, Physical Review B, **58**, 11085–11088.

[47] Tsuzuki H, Branicio PS, and Rino JP. (2007) Structural characterization of deformed crystals by analysis of common atomic neighborhood, Computer Physics Communications, **177**, 518–523.

[48] Santos PS, Santos H de S, and Toledo SP. (2000) Standard transition aluminas. Electron microscopy studies, Materials Research, **3**, 104–114.

[49] Wilson SJ. (1979) Phase transformations and development of microstructure in boehmite-derived transition aluminas, Proceedings from the British Ceramic Society, **28**, 281–294.

[50] Ollivier B, Retoux R, Lacorre P, Massiot D, and Férey G. (1997) Crystal structure of κ-alumina: an X-ray powder diffraction, TEM and NMR study, Journal of Material Chemistry, **7**, 1049–1056.

[51] Kohn J. A, Katz G, and Broder JD. (1956) Characterization of β-Ga2O3 and its isomorph, θ-Al2O3, Proceedings from the Fourteenth Annual Pittsburg Diffraction Conference, 398–407.

[52] Repelin Y and Husson E. (1990) Transitional aluminas structural study. I. γ- and δ-aluminas, Materials Research Bulletin, **25**, 611–621.

[53] Warren BE. (1990) X-Ray Diffraction, first ed. New York: Dover Publications.

[54] Guinier A. (1963) X-Ray Diffraction In Crystals, Imperfect Crystals, and Amorphous Bodies, second ed. San Francisco: W. H. Freeman and Company.

[55] Eckert M. (2012) Disputed discovery: the beginnings of X-ray diffraction in crystals in 1912 and its repercussions., Acta Crystallographica Section A, **68**, 30–9.

Chapter 3: The Effect of Synthetic Driving Force on the Atomic Mechanisms Associated with Grain Boundary Motion Below the Interface Roughening Temperature

Shawn P. Coleman[a,b], Douglas E. Spearot[a], Stephen M. Foiles[b]

[a] Department of Mechanical Engineering, University of Arkansas, Fayetteville, AR 72701

[b] Computational Materials Science and Data Analysis Department, Sandia National Laboratories, Albuquerque, NM 87185

Abstract

The mechanisms associated with grain boundary motion induced by synthetic, crystal-orientation-dependent driving forces are investigated for a large-angle [001] Ni symmetric tilt grain boundary. The application of non-physical forces by this method brings legitimate concern that it could lead to non-physical results. This concern is especially relevant below the interface roughening transition temperature where there is a substantial drop in grain boundary mobility and large driving force dependence. Using slip-vector analysis and examining continuum metrics for microrotation and strain, this work shows that the application of synthetic-driving forces does not alter the fundamental mechanisms leading to grain boundary motion. Results in this work are compared directly to shear driven simulations which reveal that the path and deformation history of grain boundary motion is unbiased by the non-physical nature of the driving force acting on the boundary. Nudged elastic band calculations show that the transition path for grain boundary motion is independent of the driving force magnitude and the energy barriers for motion are not appreciably altered by the application of the synthetic driving force.

3.1 Introduction

A fundamental understanding of grain boundary motion and mobility is necessary to advance mesoscale predictive models of grain growth in polycrystalline materials [1]. Grain boundary motion has been simulated in recent years using synthetic driving force molecular dynamics simulations, first introduced by Janssens et al. in 2006 [2]. In these simulations [2], flat grain boundaries constructed from bicrystal models are driven by a crystal-orientation-dependent driving force superimposed on an embedded atom method (EAM) potential. This driving force stems from a continuous potential energy term that is added to all atoms which varies in magnitude based on the relative orientation of neighboring atoms as compared to a reference grain. Using this method, extra potential energy is added to the atoms of the reference grain resulting in a synthetic driving force that biases the motion of the grain boundary towards the higher energy grain in order to reduce the total system potential energy. The synthetic driving force stimulates motion of flat grain boundaries within the timescale of molecular dynamics simulations and allows any grain boundary misorientation to be studied independently. This facilitates high-throughput studies of grain boundary motion as a function of grain boundary crystallography and temperature such as the study by Olmsted, et al. [3].

Prior studies have applied the synthetic driving force method to a variety of grain boundaries spanning a wide misorientation range, but researchers have limited their analysis to the collective motion of the atoms at the grain boundary [2–7]. Here we include studies [4–6] which utilized the adapted interface-random-walk method introduced by Deng and Schuh in 2011 [4] as a hybrid method that combines synthetic driving force and statistical analysis of boundary fluctuations in order to analyze slow moving grain boundaries. By focusing the analysis on the collective motion of the atoms at the grain boundary, prior researchers [2–7] were able to

compute grain boundary velocity and mobility as well as compare their results to experimental values [3,5] and conventional molecular dynamics simulations with physically based driving forces such as shear and strain [6,7].

Studies of grain boundary motion have also reported an interface roughening transition which significantly impacts the motion of grain boundaries. Interfacial roughening is a thermodynamic phase transition where the spatial variation of the position of the interfacial plane is finite below the transition temperature and diverges with the interfacial area above the transition temperature. The transition temperature reflects the energy cost of a local fluctuation of the interfacial position normal to the interface. It has been shown that there is an abrupt increase in grain boundary mobility as the temperature is increased above the transition temperature for that interface [7]. Simulations that applied synthetic driving force methods revealed large driving force dependence for the smooth grain boundary configurations below the roughening transition temperature [3,7]. Since the synthetic driving force method applies non-physical forces, there is a legitimate concern that this approach might lead to non-physical results, especially below the roughening transition temperature.

While prior work [7] shows that the computed mobility agrees with physical driving force simulations, studies have not yet analyzed the effect of synthetic driving forces on the atomic mechanisms associated with the motion of smooth interfaces, nor has any study examined the effect of synthetic driving forces on the transition energy barriers for grain boundary motion. The purpose of the synthetic driving force method is to bias the system such that the grain boundary will move from its current position towards a region with artificially added energy without purposely raising the basins on the potential energy surface in an attempt to lower the transition energy barriers, as is done in the hyperdynamics method [8]. In this work, we

investigate the effect of synthetic driving forces on the atomic mechanisms associated with low-temperature grain boundary motion and compare these mechanisms to those observed in simulations driven by shear. In addition, we study the effect of applied synthetic driving forces on the potential energy surfaces revealing how transition energy barriers are affected by the synthetic driving force method.

3.2 Methods

The ∑37 (570) [001] symmetric tilt grain boundary (STGB) modeled in this study was constructed originally by Olmsted et al. as part of their large survey of grain boundary energy and mobility [3,9]. The interface was chosen as a representative large-angle STGB constructed from sets of C type kite structural units [10] that zigzag at the interface. The initial studies by Olmsted et al. on this boundary provided evidence of grain boundary roughening at elevated temperatures and demonstrated motion-coupled shear when applying synthetic driving forces. Motion-coupled shear is the phenomenon whereby atoms in the neighboring grains collectively move parallel to the grain boundary plane in response to the synthetic driving force acting normal to the interface [11]. This phenomena is analogous to shear-coupled motion recently described in detail by Cahn et al. [12]. Boundaries experiencing motion-coupled shear are likely candidates for shear driven grain boundary motion, and would allow for direct mechanistic comparison.

The simulations conducted throughout this study use the LAMMPS molecular dynamics simulator [13] with the Foiles and Hoyt EAM potential for Ni [14]. To determine the roughening transition temperature, mobility calculations for the ∑37 (570) [001] STGB are performed at 300-1200 K using synthetic driving forces of 0.001-0.025 eV/atom. In this study, we are able to extend into lower temperature and driving force regimes than originally studied by

Olmsted et al. [3] by increasing the effective statistical sampling size in order to reduce error in the computed mobility. Increased statistical sampling is achieved by using 25 independent simulations and offsetting initial conditions in a similar manner as described by Cheng and Schuh [4]. For each temperature and driving force, grain boundary displacement data are collected every 1 ps using an 2 fs offset. The combined 12,500 displacement data points collected are fit to a Gaussian distribution to determine the mean grain boundary displacement for each time interval. Using enhanced effective sampling, the minimum 10 Å grain boundary displacement criteria used by Olmsted et al. is relaxed in this study such that all simulations with computed grain boundary mobility greater than 1 GPa^{-1} m/s are analyzed.

The effects of the synthetic driving forces below the roughening transition temperature are explored through direct comparisons with shear driven grain boundary motion simulations. Simple shear simulations are constructed at 300 and 400 K such that the normal grain boundary velocities closely match those of the simulations using synthetic driving forces of 0.025 and 0.005 eV/atom. The shear simulations are designed similar to those by Tucker et al. [15], where grain boundary motion is induced by moving rigid edges on both sides of the bicrystal model at a constant (opposing) velocity parallel to the grain boundary plane. To avoid shock wave generation, a linearly ramped velocity profile is imposed on the atoms positioned between the rigid edges. Low-temperature simulations driven by shear and the synthetic driving force method are analyzed and compared using slip-vector analysis and continuum metrics of microrotation and strain as described by Zimmerman et al. [16] and Tucker et al. [17] respectively.

The energy barriers and transition states associated with the motion of the smooth $\sum 37$ (570) [001] Ni STGB are investigated using the nudged elastic band (NEB) method extracting data

from climbing images [18]. NEB calculations determine the 0 K minimum energy configurations along the path from an initial to a final state. In this study, a series of six NEB calculations are performed applying synthetic driving forces in the range of 0.000 - 0.025 eV/atom. It is important to note that the NEB calculations with no applied driving force are comparable to conditions observed for shear driven simulations; thus, providing a baseline for comparing the synthetically driven methods.

3.3 Results and Discussion

Figure 3.1 displays an Arrhenius plot of log(mobility) versus inverse temperature for the ∑37 (570) [001] STGB revealing an interface roughening transition between 400 and 500 K. From 500-1200 K, synthetic driving forces have minimal effect on the grain boundary mobility and log(mobility) remains nearly constant between 5.5-6.9 log(GPa^{-1} m/s). However, from 300 to 400 K the mobility decreases significantly with application of lower driving forces, which is indicative of a transition into a smooth grain boundary configuration. Mobility data for the 300 K simulations driven by 0.0010 and 0.0025 eV/atom are not included as they fall below the minimum 1 GPa^{-1} m/s criteria used in this study.

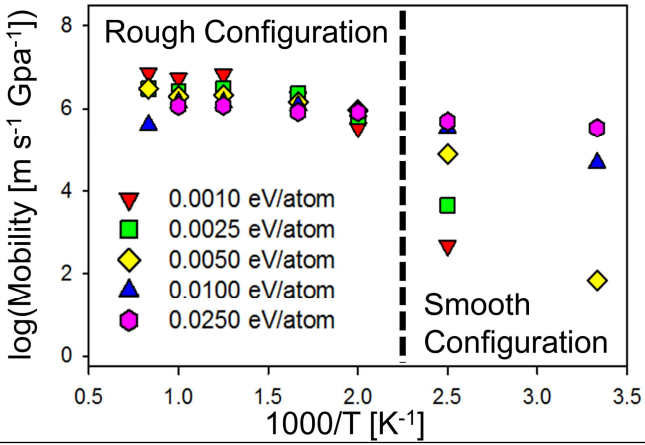

Figure 3.1: Arrhenius plot of log(mobility) versus inverse temperature for a ∑37 (570) [001] STGB computed with various driving forces. Grain boundary roughening occurs between 400 and 500 K as identified by a substantial drop in driving force dependence.

Shear-driven simulations are performed below the interface roughening transition temperature to directly compare the collective and individual atomic mechanisms associated with grain boundary motion. Table 3.1 shows the shear strain rates used to match the normal grain boundary velocity obtained using 0.005 and 0.025 eV/atom synthetic driving forces at 300 and 400 K. The effect of the different driving force types on the collective motion of the atoms near the grain boundary are presented in Figure 3.2, which displays the displacement of the grain boundaries normal (x*) and parallel (z*) to interface plane in dimensionless parameters. Here, the characteristic length is defined as 10 Å and the characteristic time, τ_{10}, is equal to the time required for the grain boundary to move 10 Å in the direction normal to the grain boundary. Characteristic times used to generate the plots in Figure 3.2 are reported in Table 3.2.

Table 3.1: Shear strain rates used to match normal grain boundary velocity obtained through synthetic driving force molecular dynamics simulations.

	300 K (s^{-1})	400 K (s^{-1})
0.005 eV/atom	$1.107\ 10^{7}$	$2.527\ 10^{8}$
0.025 eV/atom	$3.159\ 10^{9}$	$3.790\ 10^{9}$

Table 3.2: Characteristic time, τ_{10}, required for the grain boundary to move 10 Å in the direction normal to the interface.

	300 K (ps)	400 K (ps)
0.005 eV/atom	1455[a], 1685[b]	100[a], 98[b]
0.025 eV/atom	10.2[a], 10.8[b]	8.5[a],8.7[b]

[a] Synthetic driving force simulation
[b] Shear simulation

Simulations driven by 0.005 eV/atom and the corresponding shear strain rates are dominated by stick-slip behavior, which provides sufficient time for the shear-coupled motion and motion couple-shear to traverse through the bicrystal models. This stick-slip motion shows some

discontinuous jumps in Figure 3.2, but the normal and shear velocity remain relatively constant throughout the simulation. Differently, the shear and normal motion of the 0.025 eV/atom driven and corresponding shear simulations experience lag. Shear motion is delayed when applying 0.025 eV/atom synthetic diving forces because the driving force initiates motion at the grain boundary and requires time to propagate away from the boundary. Eventually, the shear motion in the 0.025 eV/atom driven simulations traverses through the simulation and recovers a similar velocity as the shear models. Likewise, motion normal to the grain boundary for shear simulations is delayed because the sheared regions are located a minimum of 75 Å away from the grain boundary at the edges of the bicrystal models. Thus, it takes time for the shear simulations to move the grain boundary, as compared to the synthetically driven simulations that act directly at the boundary and almost immediately initiate grain boundary motion.

The atomic mechanisms associated with grain boundary motion below the interface

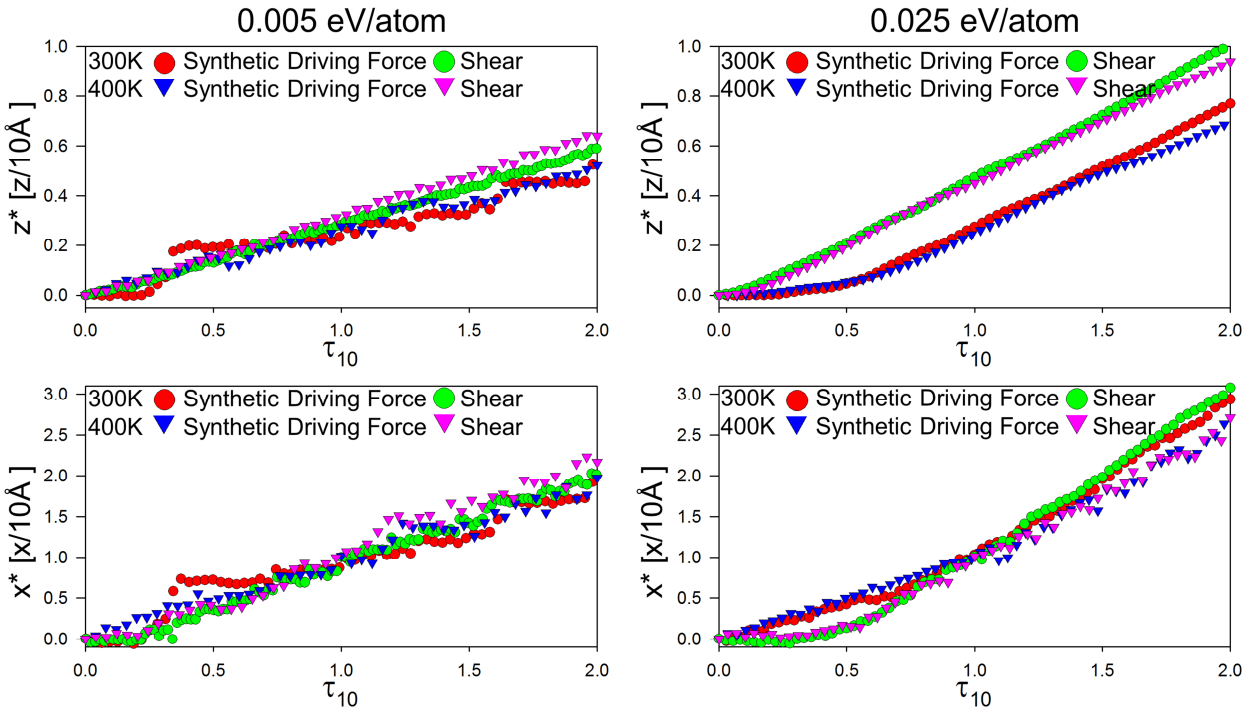

Figure 3.2: Comparison of dimensionless shear (z*) and normal (x*) grain boundary motion for synthetically driven and sheared simulations at 300 and 400 K.

roughening transition temperature are analyzed using slip-vector analysis and continuum metrics of microrotation and strain as described by Zimmerman et al. [16] and Tucker et al. [17]. Application of these metrics shows that the path and deformation history created by the ∑37 (570) [001] STGB motion is independent of the type of driving force and its magnitude. Example results for the 300 K simulation driven by 0.005 eV/atom are presented in Figure 3.3, but can be generalized for the eight cases studied. Slip vector analysis shown in Figure 3.3(a) reveals bands of inhomogeneous deformation within the region formerly associated with the structural units. The orientation of these slip bands clearly identifies the sheared path of the structural units; however, it does not clearly elucidate the mechanisms associated with grain

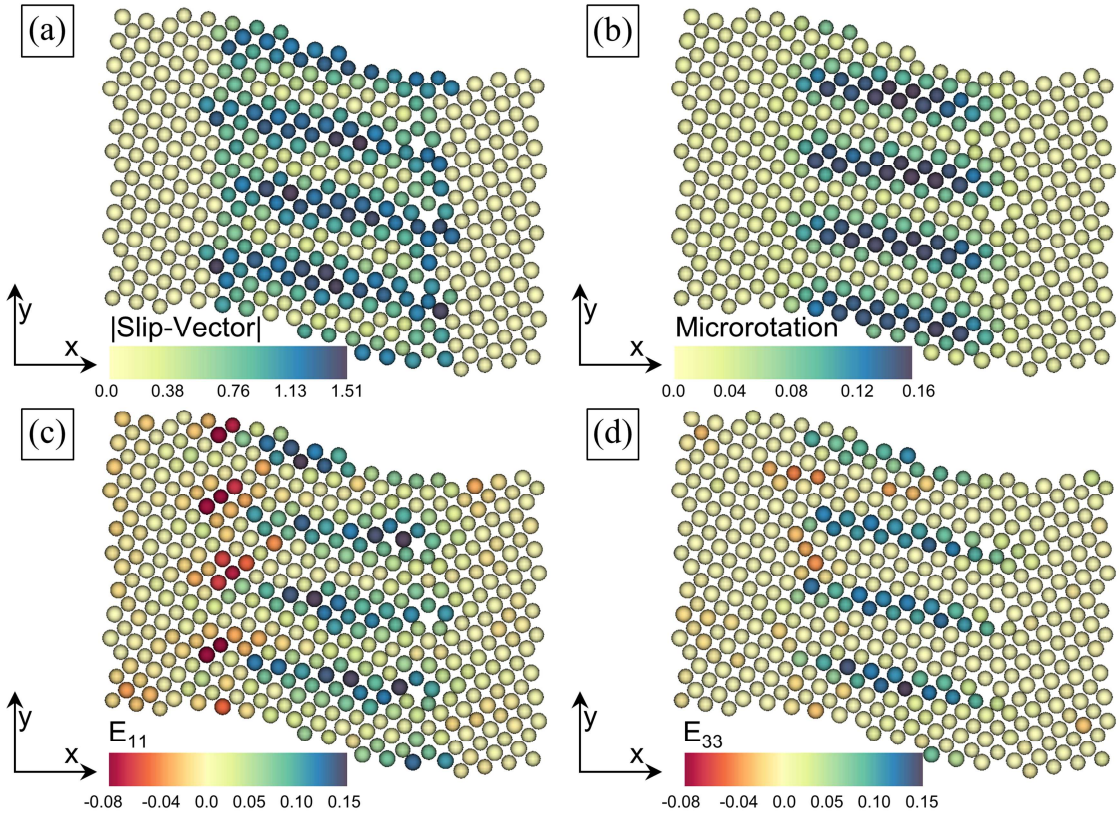

Figure 3.3: : Metrics analyzing (a) slip-vector magnitude, (b) microrotation, (c) E_{11} strain normal to the grain boundary plane, and (d) E_{33} strain parallel to the grain boundary plane for the 300 K simulations induced by a 0.005 eV/atom synthetic driving force. The results are independent of the driving force type and magnitude and can be generalized for the eight, low-temperature boundary conditions studied

boundary motion.

Analysis of the microrotation results, shown in Figure 3.3(b), indicates that the motion of the ∑37 (570) [001] STGB is caused by a rotation of the atoms adjacent to the structural units. To accommodate the rotation, the region formerly associated with the structural units is strained both normal and parallel to the grain boundary plane. Figure 3.3(c) shows an atomistic estimation of the strain normal to grain boundary plane, which strongly affects the atoms along the deformation path as well as the current structural units within the grain boundary. At the start of the deformation path, atomic rotations also cause atoms associated with the regions containing the initial structural units to be compressed normal to the grain boundary plane. An estimation of strain parallel to the grain boundary is displayed in Figure 3.3(d) and is less severe compared to strain normal to the grain boundary plane. This lower relative impact is further evidence pointing to a rotational mechanism causing motion parallel to the grain boundary plane.

Nudged elastic band results are reported in Figure 3.4. In each NEB calculation, four energy barriers are computed from the saddle-energy associated with the individual reconstruction of the four C structural units from their ideal kite-shaped to a heart-shaped transition state, as shown in Figure 3.4(a). Analysis of the atom motion during NEB shows that the transition path and the structure of the transition phases are independent of the added synthetic energy in the range studied. The energy barriers associated with the reconstruction of the four C structural units are computed by first subtracting the extra energy associated with the synthetic driving force, then comparing the potential energy of the transition states to that of the initial configuration. These adjustments to the potential energy surface for simulations driven by synthetic driving forces produce a similar energy landscape that closely matches that of the sheared simulation with no added synthetic driving force, as shown in Figure 3.4(b). The transition energy barriers

associated with grain boundary motion are not significantly altered by the addition of a synthetic energy, as shown in Figure 3.4(c). The computed energy barriers range from 0.53-0.69 eV for each of the transition states with application of 0.000-0.0250 eV/atom synthetic driving force.

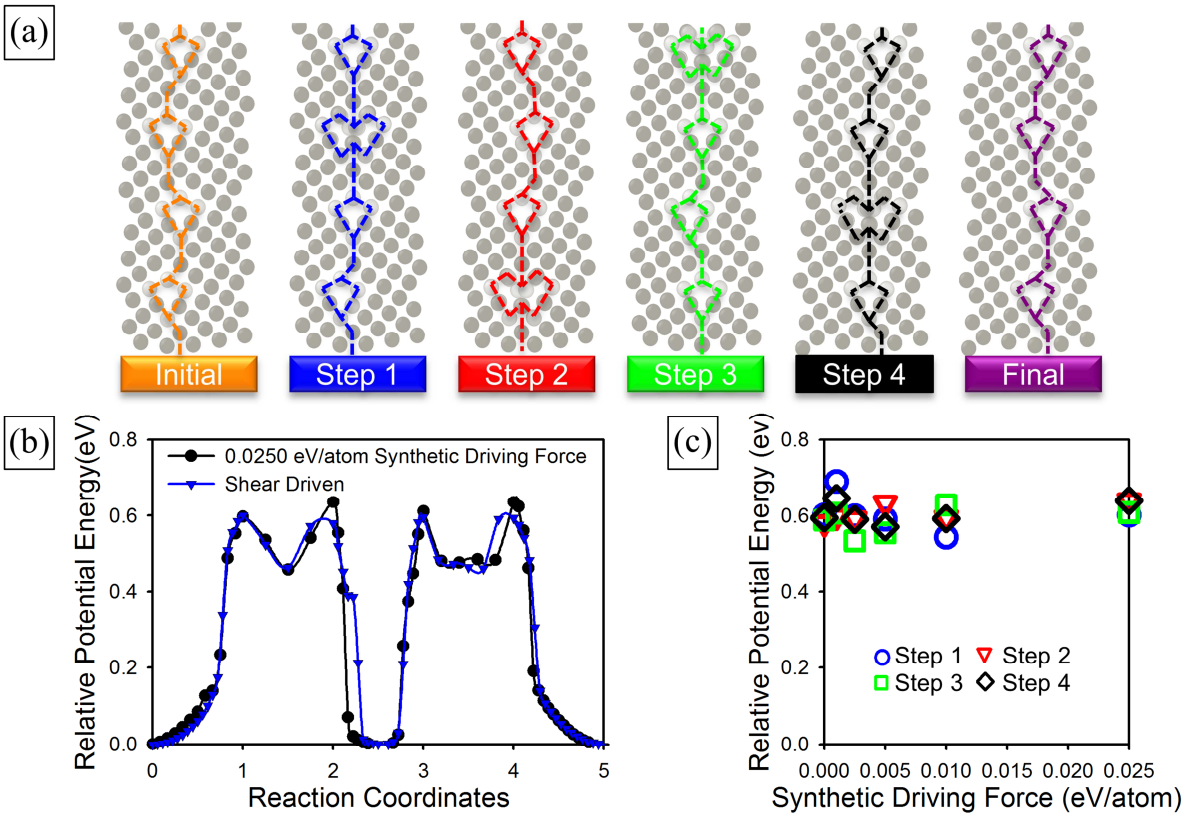

Figure 3.4: Nudged elastic band results showing (a) the four transition states to move the grain boundary, (b) NEB results for the 0.025 eV/atom driven simulation adjusted for the added synthetic energy compared to results from sheared driven simulations, and (c) the energy barriers relative to the energy of the initial grain boundary structure without the synthetic driving force energy.

3.4 Conclusion

In summary, this work identifies the grain boundary roughening temperature for the ∑37 (570) [001] Ni STGB and studies the mechanisms associated with motion in the low-temperature, smooth interface regime. At temperatures below the interface roughening transition, synthetic driving forces greatly affect the grain boundary mobility; however, the atomic mechanisms for grain boundary motion are not altered as shown through slip-vector

analysis and by examining continuum metrics of microrotation and strain. Additionally, comparison of these metrics with shear simulations shows that the synthetic driving force method induces the same mechanisms for motion as the physically based approach. NEB calculations confirm that synthetic driving forces do not alter the transition path for grain boundary motion and do not substantially change the transition energy barriers. The observation of consistent energy barriers, transition paths, and atomic mechanisms associated with grain boundary motion indicates the use of synthetic driving force molecular dynamics method does produce physically significant results.

Acknowledgements

The authors thank Garritt Tucker for his assistance with continuum metric analysis. SPC and DES acknowledge the support of the National Science foundation under grant #0954505. SMF and SPC acknowledge support from the U.S. Department of Energy, Office of Basic Energy Sciences, Division of Materials Sciences and Engineering. Sandia is a multi-program laboratory operated by Sandia Corporation, a Lockheed Martin Company, for the United States Department of Energy's National Nuclear Security Administration under contract DE-AC0494AL85000.

References

[1] Holm EA and Foiles SM. (2010) How grain growth stops: a mechanism for grain-growth stagnation in pure materials., Science, **328**, 1138–41.

[2] Janssens KGF, Olmsted DL, Holm EA, Foiles SM, Plimpton SJ, and Derlet PM. (2006) Computing the mobility of grain boundaries, Nature Materials, **5**, 124–7.

[3] Olmsted DL, Holm EA, and Foiles SM. (2009) Survey of computed grain boundary properties in face-centered cubic metals—II: Grain boundary mobility, Acta Materialia, **57**, 3704–3713.

[4] Deng C and Schuh C a. (2011) Atomistic Simulation of Slow Grain Boundary Motion, Physical Review Letters, **106**, 045503.

[5] Deng C and Schuh CA. (2011) Diffusive-to-ballistic transition in grain boundary motion studied by atomistic simulations, Physical Review B, **84**, 1–10.

[6] Mendelev MI, Deng C, Schuh CA, and Srolovitz DJ. (2013) Comparison of molecular dynamics simulation methods for the study of grain boundary migration, Modelling and Simulation in Materials Science and Engineering, **21**, 045017.

[7] Olmsted DL, Foiles SM, and Holm EA. (2007) Grain boundary interface roughening transition and its effect on grain boundary mobility for non-faceting boundaries, Scripta Materialia, **57**, 1161–1164.

[8] Voter AF. (1997) A method for accelerating the molecular dynamics simulation of infrequent events, The Journal of Chemical Physics, **106**, 4665–4677.

[9] Olmsted DL, Foiles SM, and Holm EA. (2009) Survey of computed grain boundary properties in face-centered cubic metals: I. Grain boundary energy, Acta Materialia, **57**, 3694–3703.

[10] Sutton AP and Vitek V. (1984) A computer simulation study of 〈001〉 and 〈111〉 tilt boundaries: the multiplicity of structures, Acta Metallurgica, **32**, 1093–1104.

[11] Homer ER, Foiles SM, Holm EA, and Olmsted DL. (2012) Phenomenology of shear-coupled grain boundary motion in symmetric tilt and general grain boundaries, Acta Materialia, **61**, 1048-1060.

[12] Cahn JW, Mishin YM, and Suzuki A. (2006) Coupling grain boundary motion to shear deformation, Acta Materialia, **54**, 4953–4975.

[13] Plimpton SJ. (1995) Fast parallel algorithms for short-range molecular dynamics, Journal of Computational Physics, **117**, 1–19.

[14] Foiles SM and Hoyt JJ. (2006) Computation of grain boundary stiffness and mobility from boundary fluctuations, Acta Materialia, **54**, 3351–3357.

[15] Tucker GJ, Zimmerman JA, and McDowell DL. (2010) Shear deformation kinematics of bicrystalline grain boundaries in atomistic simulations, Modelling and Simulation in Materials Science and Engineering, **18**, 015002.

[16] Zimmerman JA, Kelchner CL, Klein PA, Hamilton JC, and Foiles SM. (2001) Surface Step Effects on Nanoindentation, Physical Review Letters, **87**, 165507.

[17] Tucker GJ, Zimmerman JA, and McDowell DL. (2011) Continuum metrics for deformation and microrotation from atomistic simulations: Application to grain boundaries, International Journal of Engineering Science, **49**, 1424–1434.

[18] Henkelman G and Jónsson H. (2000) Improved tangent estimate in the nudged elastic band method for finding minimum energy paths and saddle points, The Journal of Chemical Physics, **113**, 9978.

Appendix 3.1

College of Engineering
Department of Mechanical Engineering
(479) 575-3153
(479) 575-6982 (FAX)

UNIVERSITY OF ARKANSAS

Mechanical Engineering Building
Fayetteville, Arkansas 72701

Coleman, S.P., Spearot, D.E., Foiles, S.M. (2014) The effect of synthetic driving force on the atomic mechanisms associated with grain boundary motion below the interface roughening temperature, Computational Materials Science, 86, 38-42.

I certify that Mr. Shawn Coleman is the first author of the paper and completed greater than 51% of the work in this publication. This work was done in collaboration with Dr. Stephen Foiles at Sandia National Laboratories, Albuquerque, NM.

Sincerely,

Douglas E. Spearot, Ph.D.
Dissertation Director
Associate Professor and 21st Century Professorship
Department of Mechanical Engineering
University of Arkansas
Fayetteville, AR 72701
Office: 479-575-3040
E-mail: dspearot@uark.edu

Appendix 3.2

Author Rights

Elsevier supports the need for authors to share, disseminate and maximize the impact of their research. We take our responsibility as stewards of the online record seriously, and work to ensure our policies and procedures help to protect the integrity of scholarly works.

Author's rights to reuse and post their own articles published by Elsevier are defined by Elsevier's copyright policy. For our proprietary titles, the type of copyright agreement used depends on the author's choice of publication:

For subscription articles: These rights are determined by a copyright transfer, where authors retain scholarly rights to post and use their articles.

For open access articles: These rights are determined by an exclusive license agreement, which applies to all our open access content.

In both cases, the fundamental rights needed to publish and distribute an article remain the same and Elsevier authors will be able to use their articles for a wide range of scholarly purposes.

Details on how authors can reuse and post their own articles are provided below.

Help and support

For reuse and posting not detailed below, please see our posting policy, or for authors who would like to:

- Include material from other sources in your work being published by Elsevier, please visit: Permission seeking guidelines for Elsevier authors.
- Obtain permission to re-use material from Elsevier books, journals, databases, or other products, please visit: Obtaining permission to reuse Elsevier material
- Or if you are an Elsevier author and are contacted by a requestor who wishes to re-use all or part of your article or chapter, please also refer them to our Obtaining Permission to Re-Use Elsevier Material page.
- See our FAQ on posting and copyright queries.
- Contact us directly, please email our Permissions Help Desk.

How authors can use their own journal articles

Authors can use their articles for a wide range of scholarly, non-commercial purposes as outlined below. These rights apply for all Elsevier authors who publish their article as either a subscription article or an open access article.

We require that all Elsevier authors always include a full acknowledgement and, if appropriate, a link to the final published version hosted on Science Direct.

For open access articles these rights are separate from how readers can reuse your article as defined by the author's choice of Creative Commons user license options.

Authors can use either their accepted author manuscript or final published article for:	
	Use at a conference, meeting or for teaching purposes
	Internal training by their company
	Sharing individual articles with colleagues for their research use* (also known as 'scholarly sharing')
	Use in a subsequent compilation of the author's works
	Inclusion in a thesis or dissertation
	Reuse of portions or extracts from the article in other works
	Preparation of derivative works (other than for commercial purposes)

*Please note this excludes any systematic or organized distribution of published articles.

http://www.elsevier.com/journal-authors/author-rights-and-responsibilities

Chapter 4: Virtual Diffraction Analysis of Ni [010] Symmetric Tilt Grain Boundaries

S. P. Coleman[a], D. E. Spearot[a] and L. Capolungo[a]

[a] Department of Mechanical Engineering, University of Arkansas, Fayetteville, AR 72701

[b] George W. Woodruff School of Mechanical Engineering, Georgia Institute of Technology, and UMI 2958 Georgia Tech–CNRS, 57070 Metz, France

Abstract

Electron and x-ray diffraction are well-established experimental methods used to explore the atomic scale structure of materials. In this work, a computational method is implemented to produce virtual electron and x-ray diffraction patterns directly from atomistic simulations without *a priori* knowledge of the unit cell. This method is applied to study the structure of [010] symmetric tilt low-angle and large-angle grain boundaries in Ni. Virtual electron diffraction patterns and x-ray diffraction 2θ line profiles show that this method can distinguish between low-angle grain boundaries with different misorientations and between low-angle boundaries with the same misorientation but different dislocation configurations. For large-angle Σ5 (210), Σ29 (520), and Σ5 (310) coincident site lattice [010] symmetric tilt grain boundaries, virtual diffraction methods can identify the misorientation of the grain boundary and show subtle differences between grain boundaries in the x-ray 2θ line profiles. A thorough analysis of the effects of simulation size on the relrod structure in the electron diffraction patterns is presented.

4.1 Introduction

Grain boundaries are planar defects accommodating the misorientation and elastic incompatibilities between two lattice regions of uniform crystallographic orientation [1]. Quantification and comprehension of the atomic scale structures within grain boundaries, such as full and partial dislocations, disclinations, etc., have greatly benefited from the use and interpretation of diffraction measures and simulations. Experimental work by Sass and coworkers [2–5] on grain boundaries used selected area diffraction (SAD) patterns from electron and x-ray sources to confirm that the atomic structure near grain boundaries is periodic. X-ray and electron diffraction patterns of low-angle twist grain boundaries in gold bicrystals showed weak subsidiary reflections caused by the regularly spaced screw dislocation grid within the grain boundary unit cell [5]. In studies of large-angle twist grain boundaries with low Σ coincident site lattice (CSL) [6] designations, Tan et al. [7] observed subsidiary reflections and indexed these reflections in terms of the CSL unit cell. For [001] symmetric tilt boundaries, Guan and Sass [8] found extra reflections in the vicinity of the (200) relrod tails caused by the spacing of the edge dislocation array. Careful characterization of the extra reflections allowed researchers to identify the structure and misorientation of different grain boundaries [7–9].

To supplement these experimental studies, virtual diffraction models based on kinematic diffraction theory were developed to connect atomistic simulations of large-angle symmetric twist grain boundaries to the experimental SAD patterns [10–12]. In these models, the structure factor equation was computed over a region of reciprocal space constructed from a grain boundary unit cell known *a priori*. Work by Bristowe and Sass [10] showed that small displacements of the atoms within the unit cell can create identifiable changes to the diffraction pattern allowing researchers [11–14] to use the virtual SAD patterns to accurately predict grain

boundary structure validated by experimental comparisons. In these early virtual diffraction models [10–12], computational limitations restricted the resolution of the reciprocal space explored and the number of atoms included within each simulation. *A priori* knowledge of the symmetric twist grain boundary unit cell facilitated a significant reduction in computational demand during structural optimization by reducing the degrees of freedom through symmetry [11]. As computational capabilities increased, higher resolution scans of reciprocal space were performed by Bristowe and Balluffi [12] revealing more subtle diffraction reflections stemming from secondary relaxations that were more difficult to match with experimental SAD patterns. To reconcile the effects of secondary relaxations, studies using larger simulations were performed on symmetric twist grain boundaries [13–15] examining the effects of multiple grain boundary unit cells within the simulation.

In addition to the SAD studies of grain boundary structure, x-ray diffraction line profile analysis has been used to study grain boundary structure in bicrystal and nanocrystalline samples. Several experimental x-ray diffraction studies have attempted to isolate the effects of grain boundaries on peak broadening [16–18]. Work by Eastman et al. [16,17] on nanocrystalline nickel found evidence of a reduction in line profile broadening due to relaxations in the grain boundary structure. Additionally, Gaudig et al. [18] showed that modulations in the lattice spacing near the grain boundary structure created subsidiary peaks primarily along the direction normal to the grain boundary plane.

Several researchers have applied virtual diffraction models based on the Debye scattering equation to study 2θ x-ray diffraction line profiles from atomistic models of nanocrystalline materials [19–22]. Derivation of the Debye scattering equation involves a spherical integration of the structure factor equation, which allows the diffraction intensity at a chosen scattering

angle to be related solely to the interatomic separation between pairs of atoms [23]. These researchers [19–22] verified the fidelity of the virtual diffraction line profiles using experimental comparisons. However, the complex structure of nanocrystalline materials and the assumptions inherent to the integration used to derive the Debye equation made isolating the influence of specific atomic scale defects on peak broadening difficult. Specifically, studies [19–21] have disputed the relative influence on peak broadening of the local displacement fields near grain boundaries versus the longer-range displacement fields associated with the nanocrystalline microstructure. Work by Stukowski et al. [19] found that the underlying cause for microstrain line broadening stems from longer-range coordinated displacements between grains. Whereas Alexsandrov et al. [20] and Derlet et al. [21] conclude that x-ray diffraction line profile broadening stems from the disorder around dislocations within the grain boundaries.

Together, experimental and virtual diffraction techniques have revealed important information regarding the atomic structure of grain boundaries and have enriched atomistic simulations by allowing a direct link between atomistic simulations and experimental results. This paper advances virtual diffraction methods by presenting an algorithm for performing virtual diffraction during an atomistic simulation via explicit evaluation of the structure factor equation without *a priori* knowledge of the grain boundary unit cell. The algorithm is sufficiently generic to be applicable to both electron and x-ray diffraction conditions and is integrated into the LAMMPS molecular dynamics simulator [24]. Within LAMMPS, the algorithm is capable of performing diffraction analyses either statically (after energy minimization) or dynamically during a molecular dynamics simulation to produce time averaged diffraction patterns at finite temperature. A visualization procedure is developed to create SAD patterns and 2θ x-ray diffraction line profiles from the intensities computed using the atomistic

simulation data. In this work, this algorithm is applied to study the structure of [010] symmetric tilt low-angle and large-angle CSL grain boundaries in face-centered cubic (FCC) Ni, differentiating from the previous literature on virtual diffraction which has primarily focused on the analysis of twist grain boundaries. Analogous to previous results in the literature, the virtual diffraction method is capable of extracting critical details related to the misorientation and structure of low-angle and large-angle CSL symmetric tilt grain boundaries.

4.2 Methodology

4.2.1 *Virtual Diffraction Algorithm and Visualization*

The diffraction algorithm implemented into LAMMPS generates a three-dimensional mesh of points filling a volume of reciprocal space constructed from the entire domain of the atomistic simulation cell. The mesh of reciprocal lattice points is built on a rectilinear grid with spacing $c_n \left|\mathbf{A}_n\right|^{-1}$ along each reciprocal lattice axis $\mathbf{B}_n$. Each reciprocal lattice axis $\mathbf{B}_n$ is determined from the associated vector $\mathbf{A}_n$ corresponding to the n = 1, 2, or 3 edge of the simulation cell. The parameters c_n control the spacing of the reciprocal lattice points, as shown schematically in Figure 4.1, and determine the resolution within the reciprocal space volume explored. Specific values of c_n used in this work are provided in Section 4.2.2.

During electron or x-ray diffraction, each reciprocal lattice point is associated with a reciprocal lattice vector $\mathbf{K}$ describing the deviation between the diffracted and incident wave vectors $\mathbf{k_D}$ and $\mathbf{k_I}$ [25],

$$\mathbf{K} = \mathbf{k_D} - \mathbf{k_I} = \xi \mathbf{B}_1 + \eta \mathbf{B}_2 + \zeta \mathbf{B}_3 \quad , \tag{4.1}$$

where ξ, η, and ζ can be any real number. Assuming monochromatic incident radiation of wavelength λ, the angle of diffraction θ is computed utilizing the geometric relationship

between $\mathbf{k_I}$, $\mathbf{k_D}$, $\mathbf{K}$, and λ through Bragg's law [25],

$$\frac{\sin(\theta)}{\lambda} = \frac{|\mathbf{K}|}{2} \quad . \tag{4.2}$$

At certain reciprocal lattice points throughout the mesh, the Bragg condition is satisfied $(\mathbf{K} = \mathbf{K_B})$ and the magnitude of the reciprocal lattice vectors is related to interplanar distances d_{hkl} of the associated {hkl} through [26],

$$\frac{1}{d_{hkl}} = |\mathbf{K_B}| \quad . \tag{4.3}$$

At these points, the atomic structure allows constructive interference of the radiation producing strong diffraction intensity.

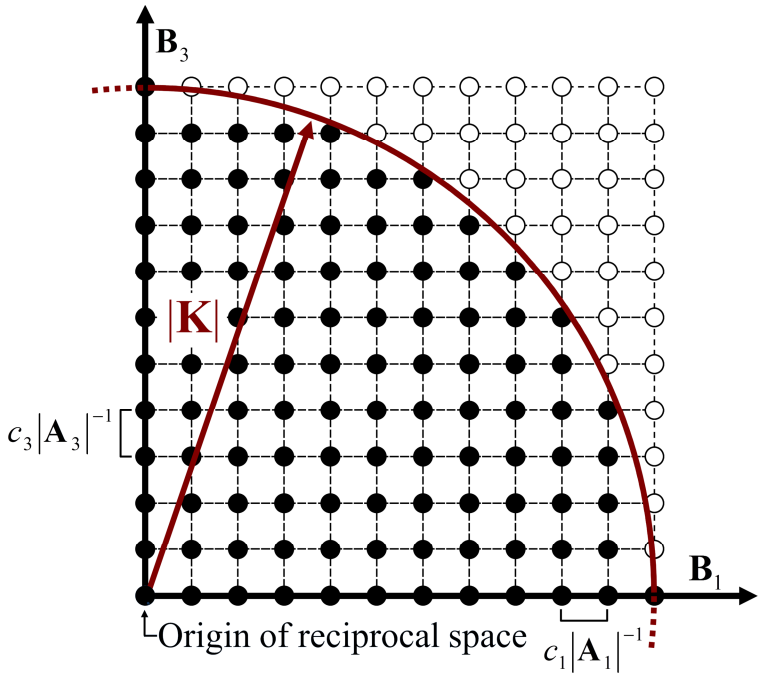

Figure 4.1: Diagram of the reciprocal space mesh illustrating the rectilinear spacing and criteria set on |K| to increase the computational efficiency of the algorithm by limiting the number or reciprocal lattice points explored.

The diffraction intensity at each reciprocal lattice point is calculated differently for electron and x-ray radiation; however, both require evaluation of the structure factor $F(\mathbf{K})$. For each

type of radiation, the structure factor $F(\mathbf{K})$ is computed utilizing the atomic positions $\mathbf{r}_j$ via [23],

$$\mathrm{F}(\mathbf{K}) = \sum_{\mathrm{j}=1}^{\mathrm{N}} f_{\mathrm{j}} \exp\left(2\pi i\, \mathbf{K} \cdot \mathbf{r}_{\mathrm{j}}\right) \quad . \tag{4.4}$$

Here, f_j are the atomic scattering factors which account for the reduction in diffracted intensity from an individual atom due to Compton scattering and vary by atom type, angle of diffraction θ, and type of radiation [23].

At each diffraction angle, the atomic scattering factors f_j are computed using analytical approximations parameterized for the specific atom type. For electron diffraction, the analytical approximation of the atomic scattering factor is the summation of five Gaussian functions of the form [27],

$$f_j\left(\frac{\sin\theta}{\lambda}\right) = \sum_{i}^{5} a_i \exp\left(-b_i \frac{\sin^2\theta}{\lambda^2}\right) \quad , \tag{4.5}$$

which have been parameterized for the majority of neutral elements by Peng et al. [28]. For x-ray diffraction, the analytical approximation of the atomic scattering factor is found from a summation of four Gaussian functions plus a constant of the form [29],

$$f_j\left(\frac{\sin\theta}{\lambda}\right) = \sum_{i}^{4} a_i \exp\left(-b_i \frac{\sin^2\theta}{\lambda^2}\right) + c \quad , \tag{4.6}$$

and has been parameterized by Fox et al. for most atom types [30].

For electron diffraction, the diffraction intensity $I_e(\mathbf{K})$ at each reciprocal lattice point is computed from the product of the structure factor and its complex conjugate $F^*(\mathbf{K})$ normalized by the number of atoms in the simulation N via [23],

$$I_e(\mathbf{K}) = \frac{F(\mathbf{K})F^*(\mathbf{K})}{N} \quad . \tag{4.7}$$

To compute x-ray diffraction intensities $I_x(\mathbf{K})$, an additional Lorentz-polarization factor $\mathrm{Lp}(\theta)$ is applied to account for the relative distribution of the reciprocal lattice points and the change in scatter intensity when using non-polarized incident radiation. The Lorentz-polarization factor is computed via [23],

$$\mathrm{Lp}(\theta) = \frac{1+\cos^2(2\theta)}{\cos(\theta)\sin^2(\theta)} \quad , \tag{4.8}$$

and thus the diffraction intensity from x-rays is computed through [23],

$$I_x(\mathbf{K}) = \mathrm{Lp}(\theta)\frac{F(\mathbf{K})F^*(\mathbf{K})}{N} \quad . \tag{4.9}$$

In general, virtual selected area electron diffraction (SAED) patterns are created by examining the region in reciprocal space intersecting the Ewald sphere of radius λ^{-1}. For a particular zone axis, the Ewald sphere is centered at the tail of the associated incident wave vector and intersects the origin of reciprocal space. To construct the electron diffraction pattern, a thin hemispherical slice of the reciprocal lattice mesh lying near the surface of the Ewald sphere is isolated and viewed parallel to the zone axis. The thickness of this slice is dependent on the resolution of the reciprocal space mesh and is chosen such that between one and five reciprocal lattice points are contained within the slice parallel to the zone axis at each point along the curvature of the Ewald sphere. To enhance features within the diffraction pattern, low intensity reciprocal lattice points are removed and the remaining points are coloured by intensity on a $\log_{10}$ scale. X-ray diffraction line profiles are created by virtually rotating the Ewald sphere around the origin of reciprocal space to all possible orientations, mimicking powder diffraction conditions [31]. By making all diffraction orientations equally probable, all reciprocal lattice

points will intersect the surface of the Ewald sphere. Line profiles simulating x-ray powder diffraction are constructed by collecting all reciprocal lattice points into bins corresponding to their scattering angle 2θ calculated using Eq. (4.2) and summing the intensity data. The scattering angle bin size is optimized through trials to reduce the noise within the line profile while maximizing peak features. Specific discussion of the parameters used to construct SAED and 2θ x-ray diffraction line profiles on simulated low-angle and large-angle CSL [010] symmetric tilt grain boundaries is provided in Section 4.2.2.

4.2.2 *Application to Grain Boundaries*

The virtual diffraction algorithm is applied to six FCC Ni [010] symmetric tilt grain boundaries (STGBs) modeled with the Foiles-Hoyt Ni embedded-atom method (EAM) potential [32]. The grain boundaries are constructed utilizing the methods described by Spearot et al. [33] with periodic boundary conditions applied in all directions forming bicrystal models with specific misorientations. For each bicrystal, minimum energy grain boundary structures are attained at 0 K by aligning the opposing lattice regions with the intended tilt and removing atoms that are inside specified cutoff distances. This procedure effectively samples multiple starting configurations with different relative displacements. Each grain boundary structure is optimized to best minimize the potential energy using a nonlinear conjugate gradient method implemented in LAMMPS [24]. Electron and x-ray virtual diffraction data are computed using the atomic positions in the minimum energy structures.

In this study, three low-angle (dislocation) [010] STGBs and three large-angle CSL [010] STGBs with low Σ values are studied. The low-angle bicrystal models consist of one 5.00° [010] STGB and two 10.39° [010] STGBs created by specifying different initial conditions during energy minimization. These boundaries are chosen for this work to validate the ability of the

virtual diffraction algorithm to differentiate between different low-angle tilt boundaries and to compare the results to prior experimental work [8]. The large-angle CSL bicrystal models studied in this investigation are the Σ5 (210), Σ29 (520), and Σ5 (310) [010] STGBs. In the CSL notation, the Σ values correspond to the inverse density of the coincidence lattice sites between the misoriented lattice regions and the Miller indices indicate the grain boundary plane [6]. These boundaries are chosen for this work because they exhibit the |B.B|, |BC.BC|, and |C| grain boundary structures consistent with the structural unit model [34]. In the context of the structural unit model, the Σ5 boundaries used in this study correspond to special grain boundaries at equilibrium while the Σ29 boundary is non-special. From the point of view of continuum mechanics, the transition between B and C structural units can be seen as a perturbation in an otherwise uniform array of structural units. Such perturbations can be represented via either secondary grain boundary dislocations or disclination dipoles [35]. For reference, descriptions of all boundaries used in this study are listed in Table 4.1.

Table 4.1: Description of the [010] STGBs studied in this work collected after energy minimization.

	Tilt Angle	Σ	Boundary Plane	$\lvert\mathbf{A}_1\rvert$ (Å)	$\lvert\mathbf{A}_2\rvert$ (Å)	$\lvert\mathbf{A}_3\rvert$ (Å)	N (atoms)	GB Energy (J/m^2)
Low-Angle	5.00°	265	23 1 0	161.63	28.16	81.01	33,760	0.789
	10.39°	61	11 1 0	233.23	28.16	38.89	23,392	1.050[a]
				231.87	28.17	38.87	23,232	1.138[b]
Large-Angle	36.87°	5	2 1 0	237.07	28.14	31.48	19,200	1.285
	43.60°	29	5 2 0	226.18	28.16	37.89	22,080	1.219
	53.13°	5	3 1 0	244.59	28.15	33.38	21,024	1.344

[a] Full dislocation grain boundary
[b] Partial dislocation grain boundary

Simulated 200 kV electron radiation (λ = 0.0251 Å [27]) and Cu K_α x-rays (λ = 1.54178 Å [23]) are used to create SAED patterns and 2θ x-ray line profiles. Table 4.2 lists the parameters used to compute analytical approximations of the Ni electron and x-ray atomic scattering factors.

For the SAED patterns, a very fine resolution of the reciprocal space lattice, approximately $5x10^7$ reciprocal lattice points per $Å^{-3}$, is achieved by using c_n = 0.10. This resolution is necessary to eliminate the mesh sensitivity in the analysis of relrods and subsidiary peaks. To increase the computational efficiency, the volume of reciprocal space that is explored is decreased by setting criteria on $|\mathbf{K}|$, as illustrated in Figure 4.1. In this study, the SAED patterns are focused on regions where $h^2 + k^2 + l^2 < 20$ limiting the explored volume of reciprocal space such that $0 < |\mathbf{K}| < 1.70$ $Å^{-1}$. SAED patterns aligned on the [010] misorientation axis are constructed by selecting reciprocal lattice points intersecting a 0.01 $Å^{-1}$ thick Ewald sphere slice centered at (0 39.8406 0) $Å^{-1}$ in reciprocal space. Initial SAED patterns are constructed by removing reciprocal lattice points with intensities less than 0.5% of the maximum intensity $I_e^{\max}$ outside the transmitted beam area. For more detailed patterns, this threshold is decreased to 0.2% of $I_e^{\max}$. Relrod profiles are created by isolating a cylindrical region of radius 0.004 $Å^{-1}$ centered on a specific (002) reflection with the average intensity of the reciprocal lattice points binned based on their position along the l-axis in reciprocal space.

For x-ray diffraction line profiles, the resolution of reciprocal space is set using c_n = 0.25 resulting in approximately $2x10^7$ reciprocal lattice points per $Å^{-3}$. Knowing that the ideal 2θ scattering angles associated with {111}, {002}, and {220} planes of FCC Ni are located at 44.59°, 51.96°, and 76.55° respectively (assuming an equilibrium lattice parameter of 3.52 Å [32]) the range of $|\mathbf{K}|$ is restricted such that $35° < 2\theta < 80°$ as computed via Eq. (4.2). For each boundary, x-ray diffraction line profiles are created using an optimal 2θ bin size of 0.067° determined through several trials.

Table 4.2: Parameters used to compute analytical approximations of the Ni atomic scattering factors for electron and x-ray diffraction as calculated via Eq. (4.5) and Eq. (4.6) respectively with $\sin(\theta)/\lambda$ ($Å^{-1}$).

Electron [a]	a_1	a_2	a_3	a_4	a_5	b_1	b_2	b_3	b_4	b_5
Eq. (4.5)	0.3860	1.1765	1.5451	2.0730	1.3814	0.2478	1.7660	6.3107	25.2204	74.3146
X-ray [b]	a_1	a_2	a_3	a_4	b_1	b_2	b_3	b_4	c	
Eq. (4.6)	12.8376	3.8785	7.2920	0.2565	4.4438	12.1763	2.3800	66.3421	1.0341	

[a] Peng et al. [28]
[b] Fox et al. [30]

4.3 Results and Discussion

4.3.1 *Low-Angle Symmetric Tilt Grain Boundaries*

The virtual diffraction methods are used initially to examine the structures of low-angle (dislocation) [010] STGBs to validate the algorithm implementation and to make comparison with the available literature that has previously discussed diffraction from low-angle tilt grain boundaries [8]. Figure 4.2(a) - (c) show the energy-minimized structure of each low-angle [010] STGB coloured by the centro-symmetry parameter [36]. The predicted structure of the 5.0^{o} [010] STGB from energy minimization calculations includes periodic sets of partial dislocations along the interface plane. Energy minimization calculations predict two different structures for the 10.39^{o} [010] STGB. In Figure 4.2(b) each dislocation in the periodic array along the grain boundary has dissociated into partial dislocations resulting in a boundary with slightly higher energy than that shown in Figure 4.2(c) where the edge dislocation array along the grain boundary plane remains intact. In Figure 4.2(b) the partial dislocations are spaced 7.74 Å apart within each grouping and separated from the neighboring group of partial dislocations by 11.69 Å, making the primary spacing of the dislocation array 19.43 Å. Similarly, the spacing of the primary array of intact edge dislocations in Figure 4.2(c) is 19.45 Å.

Selected area electron diffraction patterns with zone axis aligned along the [010] misorientation axis for each low-angle STGB are shown in Figure 4.2(d) - (e). Each SAED pattern explores approximately six million reciprocal lattice points and is indexed denoting the plane and the lattice region responsible for the diffraction reflection. Squares are drawn around the {220} reflections as guides to identify the misorientation between the two lattice regions in each low-angle grain boundary model. Figure 4.3 shows magnified portions of the SAED pattern in the vicinity of the (002) reflections for the two 10.39^{o} [010] STGBs. In this figure, the

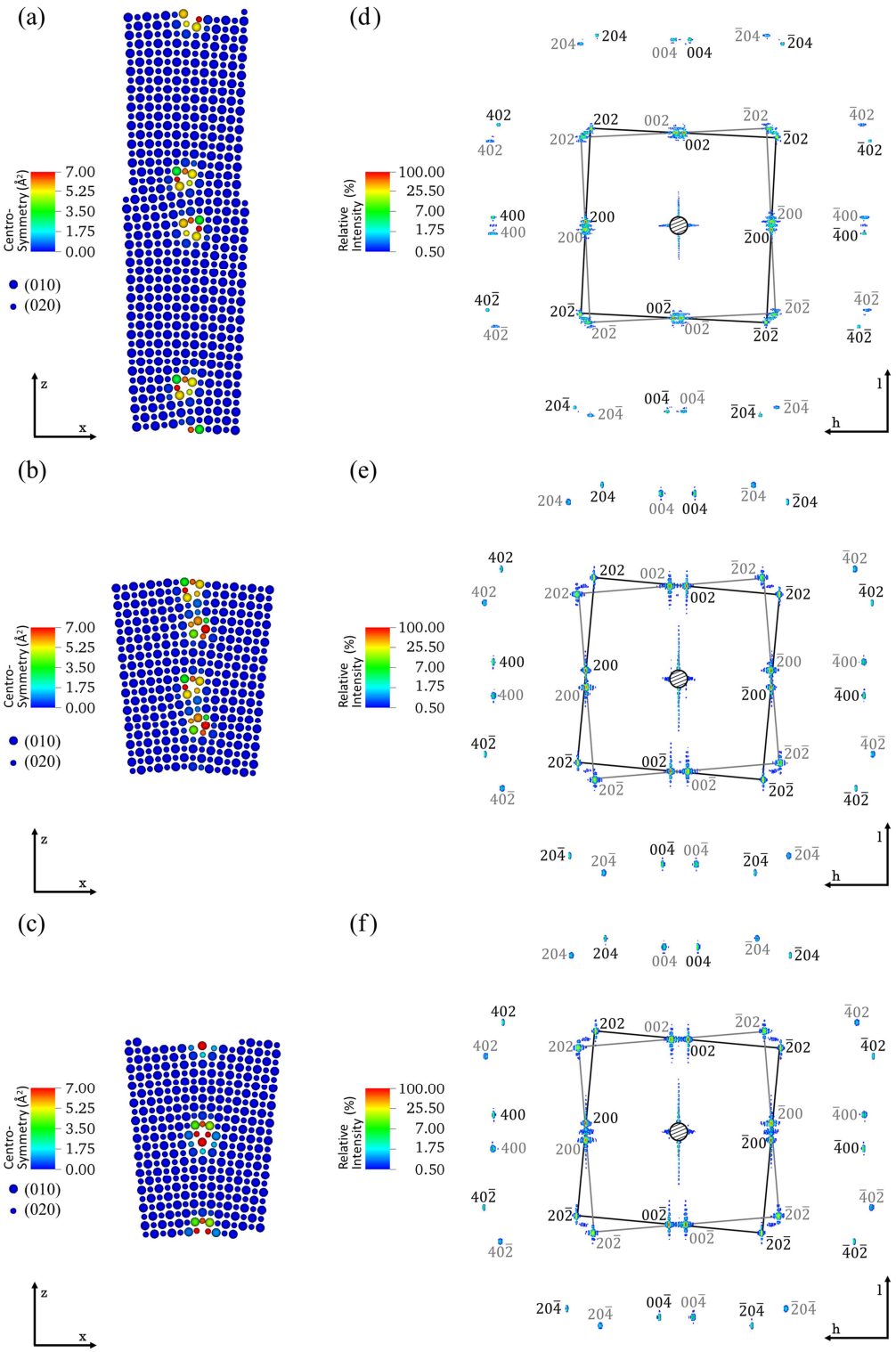

Figure 4.2: Low-angle [010] STGB structures for (a) {23 1 0} 5.0° (b) {11 1 0} 10.39° with partial dislocations, and (c) {11 1 0} 10.39° with full dislocations. SAED patterns aligned with the [010] misorientation axis are shown in (d) - (f) for each corresponding grain boundary. The squares are included as a guide to distinguish the orientations of bicrystal regions.

lower intensity threshold is reduced to 0.2% of I_e^{max} to better capture the presence of relrods and subsidiary reflections due to the grain boundary. The SAED patterns in Figure 4.3 show relrods orientated parallel to the grain boundary plane (vertical direction) and oriented normal to the grain boundary (horizontal direction) as well as subsidiary reflections in the vicinity of the FCC reflections.

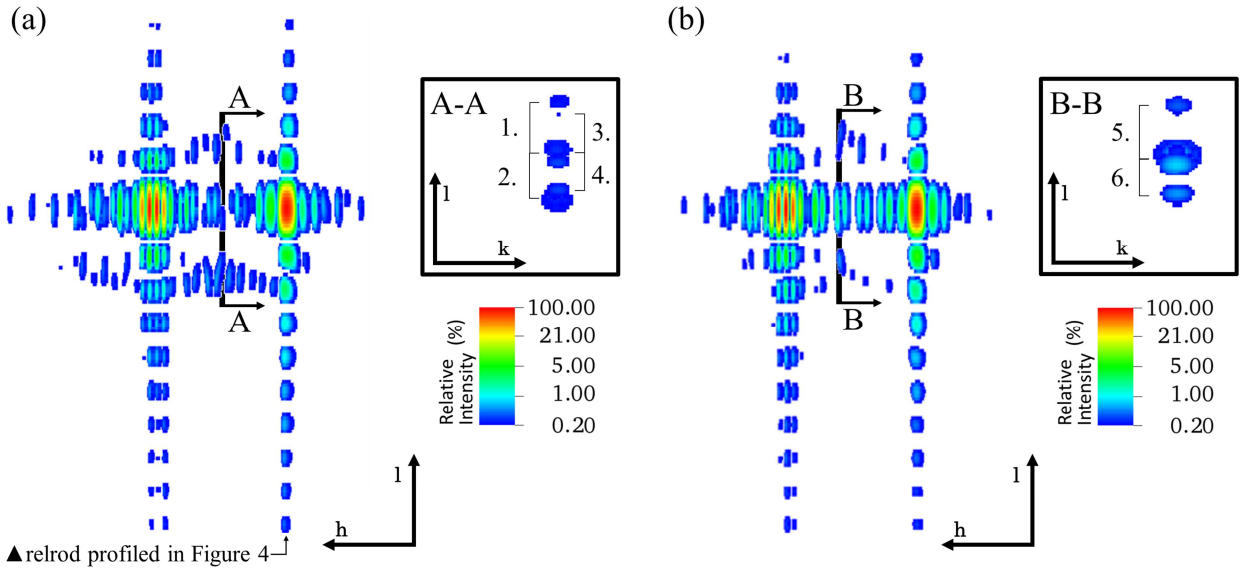

Figure 4.3: Magnified view of SAED patterns near the (002) reflections for (a) 10.39^o [010] STGB with partial dislocations and (b) 10.39^o [010] STGB with full dislocations. In (a) and (b) the zone axis is aligned with the [010] misorientation axis while in the insets the zone axis is aligned with the [100] normal to the grain boundary.

The subsidiary reflections in Figure 4.3 are the result of the periodic lattice strain created by the dislocations within the grain boundary analogous to those studied in detail in previous experimental works [2-14]. Specifically, studies on low-angle [001] STGBs indicated that the spacing between the extra reflections and the tails of the (002) reflections corresponds to the spacing of the primary dislocation array [8]. Rotating the zone axis to match the experimental results of Guan and Sass [8], the insets in Figure 4.3 correspond to SAED patterns aligned normal to the grain boundary plane and more clearly show the spacing between the extra

reflections and (002) tails. In the Figure 4.3(a) inset (corresponding to the 10.39^{o} [010] STGB with partial dislocations) four extra peaks are observed due to the grain boundaries. The spacing between the reflections and the center of the (002) tails labeled 1-4 are 0.058, 0.055, 0.045, and 0.040 Å^{-1} (17.28, 18.08, 22.22, and 25.08 Å) respectively. In the Figure 4.3(b) inset (corresponding to the 10.39^{o} [010] STGB with intact dislocations) two extra reflections are observed and the associated spacing labeled 5 and 6 are 0.059 and 0.044 Å^{-1} (16.90 and 22.87 Å) to the center of the (002) tails. As suggested by the experimental results of Guan and Sass [8], the average of these distances between the extra peaks and the (002) tails for each simulation is a close match to the primary spacing of the dislocation (19.43 and 19.45 Å) in the simulations.

In bicrystal models, relrods are expected to appear in the direction normal to each low-angle grain boundary; in this direction, the distortion field decays as a function of distance away from the interface providing a finite size effect. However, Figure 4.2 and Figure 4.3 show that the strongest relrods are those parallel to the grain boundary. Recall that the atomistic simulation model used in this work includes periodic boundary conditions in all directions meaning that atoms on or near the model surface interact via the interatomic potential through the periodic boundary with atoms on the opposing side of the model. However, the algorithm implemented to compute diffraction intensity from the structure factor equation does not account for an infinite size simulation model in the same way and thus the oscillating distortion field due to the dislocation structure at the low-angle grain boundary is truncated in the intensity calculation.

To illustrate the role of length scale on the relrod structure, traces of the (002) relrod along the l-axis are constructed, shown in Figure 4.4, using different simulation model sizes of the 10.39^{o} partial dislocation [010] STGB. Here, only $|\mathbf{A}_3|$ (parallel to the grain boundary plane and perpendicular to the dislocation cores) is increased from 38.87 Å in the original study (Figure 4.2

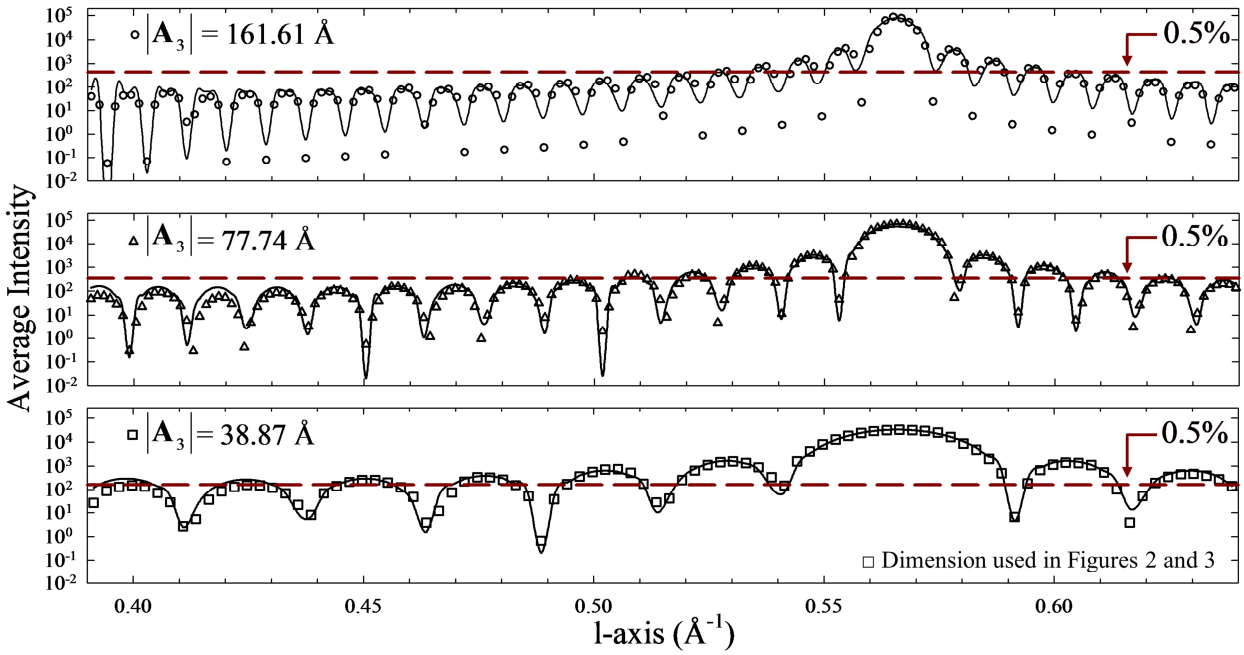

Figure 4.4: Intensity profiles tracing the (002) relrods indicated in Figure 4.3(a) for the 10.39° [010] STGB containing partial dislocations with increasing $|\mathbf{A}_3|$ as labeled. The 0.5% minimum intensity cutoff is plotted to show the threshold used in the SAED pattern shown in Figure 4.2.

and Figure 4.3) to 77.74 Å and 116.61 Å. The data computed from the relrod profiles are fit to [23],

$$I = |F|^2 \left(\frac{\sin^2(\pi\, N_1 \mathbf{K} \bullet \mathbf{a}_1)}{\sin^2(\pi\, \mathbf{K} \bullet \mathbf{a}_1)} \right) \left(\frac{\sin^2(\pi\, N_2 \mathbf{K} \bullet \mathbf{a}_2)}{\sin^2(\pi\, \mathbf{K} \bullet \mathbf{a}_2)} \right) \left(\frac{\sin^2(\pi\, N_3 \mathbf{K} \bullet \mathbf{a}_3)}{\sin^2(\pi\, \mathbf{K} \bullet \mathbf{a}_3)} \right) , \qquad (4.10)$$

which describes the predicted diffraction intensity observed from a small crystal constructed from many unit cells. For a single crystal $\mathbf{a}_1$, $\mathbf{a}_2$, and $\mathbf{a}_3$ in Eq. (4.10) are the lattice vectors describing the unit cell; however, because the bicrystal models are constructed using two unit cell orientations the vectors $\mathbf{a}_1$, $\mathbf{a}_2$, and $\mathbf{a}_3$ represents an averaged periodic repeating unit along each simulation cell axis. In Eq. (4.10), the variables N_1, N_2, and N_3 are the number of units cells in each direction within the grain boundary model. An excellent fit is achieved between the

computed relrod profile and the fundamental equation describing the shape of relrods during electron diffraction from finite volumes. From the fit, the magnitudes of $\mathbf{a}_3$ for the three simulations are 3.53, 3.53, and 3.54 Å with N_3 equal to 11, 22, and 33 respectively. These fitted parameters correspond to $|\mathbf{A}_3|$ of length 38.86, 77.70, and 116.66 Å, which closely match $|\mathbf{A}_3|$ in the simulations studied. In Figure 4.4, the 0.5% of $I_e^{\max}$ threshold is illustrated showing the subsidiary maxima not visible in Figure 4.2. As $|\mathbf{A}_3|$ in the simulations increases, the visible relrods become more concentrated around the (002) reflections.

Virtual 2θ x-ray diffraction line profiles for each low-angle [010] STGB are shown in Figure 4.5. To the authors' knowledge, no prior studies report experimental or virtual 2θ x-ray diffraction line profiles created from isolated STGBs for comparison; however, insights into the profile features are gained via comparison with the virtual SAED patterns. Clearly, the {111} and {220} peaks show a broadening due to the presence of the low-angle grain boundaries. In the line profiles, smooth broadening of a peak is the result of gradual changes to the spacing between a particular set of crystallographic planes. However, discrete peaks (roughness) in the broadening and secondary peaks emerge as the result of non-continuous displacement fields corresponding to the dislocation cores and periodic secondary relaxations within the grain boundary region. In the virtual 2θ line profiles, the {002} peak shows less significant broadening and subsidiary peaks with higher intensity as compared to the {111} and {220} peak maxima. While some of these peaks are created from secondary periodic relaxations, analysis of the SAED patterns indicates the main source for these distinct peaks are the relrods associated with the finite size of the simulation cell and the implementation of the virtual diffraction algorithm.

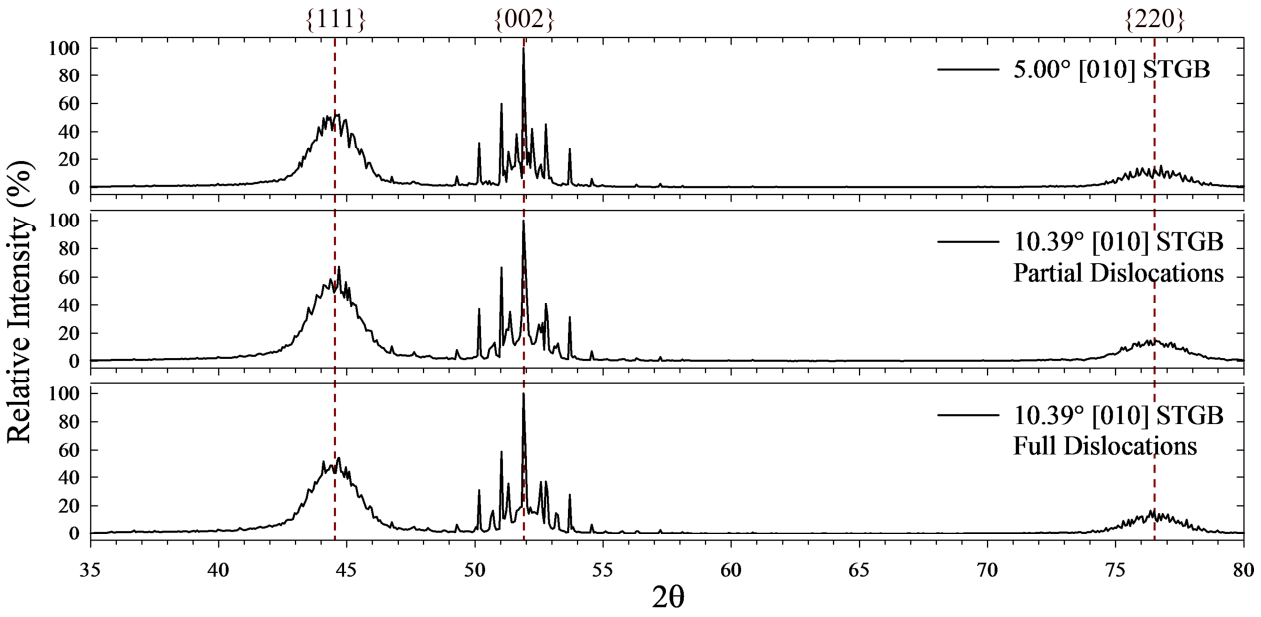

Figure 4.5: X-ray diffraction profiles for low-angle [010] STGBs constructed using a 2θ bin size of 0.067°. The extra high intensity peaks near the {002} peak are the result of relrod structures due to the finite size effect of the simulations.

4.3.2 *Large-Angle Symmetric Tilt CSL Grain Boundaries*

The virtual diffraction methods are applied to three large-angle CSL [010] STGBs to explore the capability of these methods to identify atomic scale structure, specifically the different structural units and their repeating pattern along the grain boundary. Previous experimental and virtual diffraction studies have not focused on isolated large-angle symmetric tilt CSL grain boundaries, thus no direct comparison can be made. Figure 4.6(a) - (c) show the energy-minimized structures of the Σ5 (210), Σ29 (520), and Σ5 (310) [010] STGBs respectively, coloured by the centrosymmetry parameter. The energy minimization routine successfully converges on the |B.B|, |BC.BC|, and |C| structural units as predicted by the structural unit model [34]. Selected area electron diffraction patterns with zone axis aligned along the [010] misorientation direction for each large-angle CSL grain boundary are shown in Figure 4.6(d) - (e). Each SAED pattern is indexed denoting the plane and the lattice region responsible for the

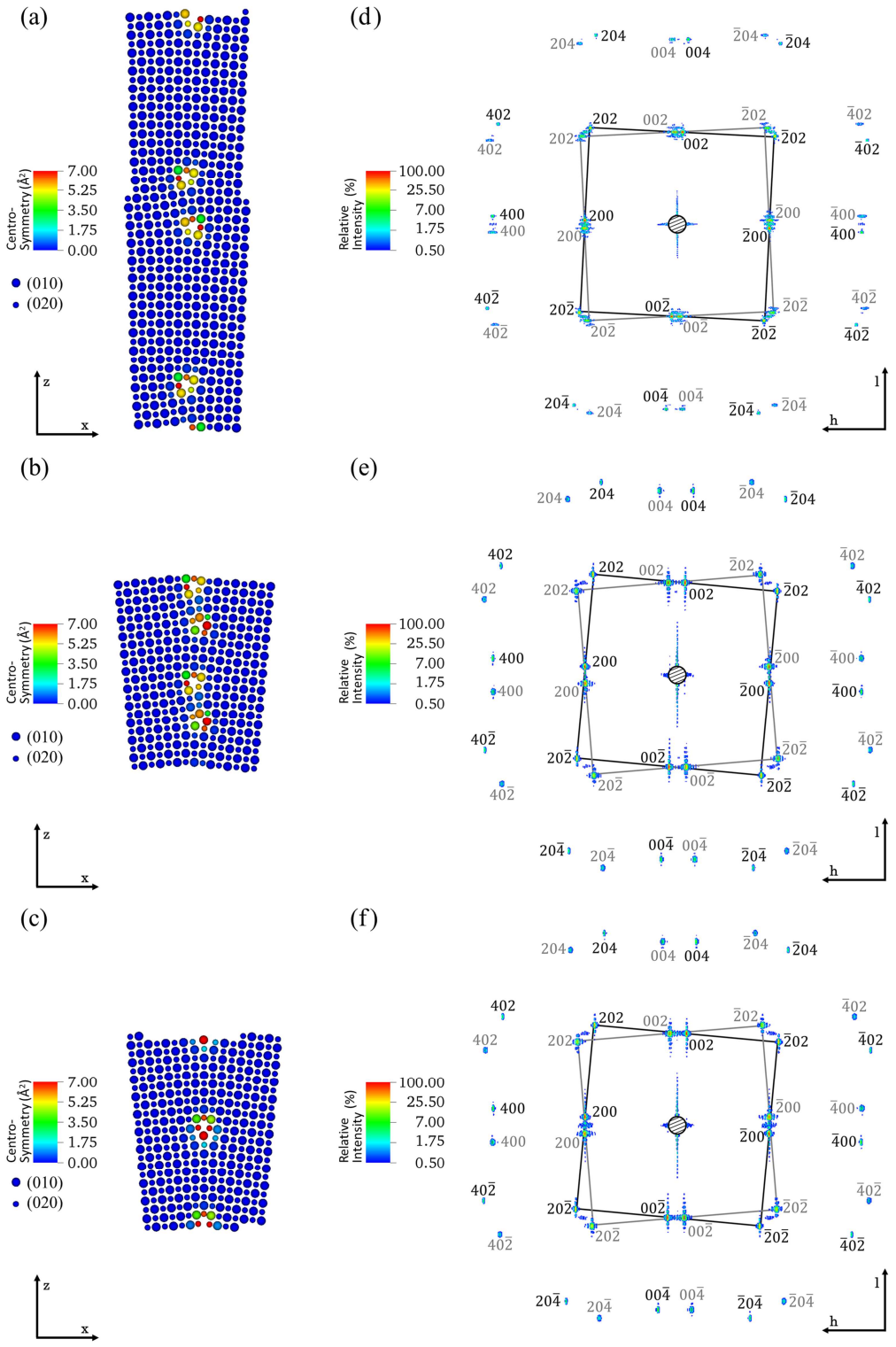

Figure 4.6: Large-angle [010] STGB structures for (a) Σ5 {210} 36.87°, (b) Σ29 {520} 43.60°, and (c) Σ5 {310} 53.13° as well as corresponding virtual electron diffraction patterns (d) - (f) with beam aligned along the [010] misorientation axis. The squares are included as a guide to distinguish the orientations of bicrystal regions.

diffraction reflection and squares are drawn as a guide to successfully identify the misorientation between the two lattice regions. The SAED patterns for the large-angle CSL [010] STGBs, using a 0.5% of $I_e^{\max}$ threshold, do not contain obvious subsidiary reflections that can be linked directly to dislocations or atomic structure. However, in Figure 4.6(d) and Figure 4.6(f), the SAED patterns do show the alignment of the {204} reflections from both lattice regions stemming from the special orientations of these Σ5 boundaries. Attempts at lowering the minimum intensity threshold to reveal subsidiary reflections were unsuccessful due to more pronounced vertical and horizontal relrods in the SAED patterns and extra reflections due to relrods originating from FCC peaks off the reciprocal lattice plane viewed in Figure 4.6.

Figure 4.7 presents a size effect study, analogous to that performed on a low-angle [010] STGB in Figure 4.4, for a (002) relrod profile created by the Σ5 (310) STGB with increasing $|\mathbf{A}_3|$. In this study, $|\mathbf{A}_3|$ is extended from 33.38 Å in the original study (Figure 4.5) to 66.77 Å

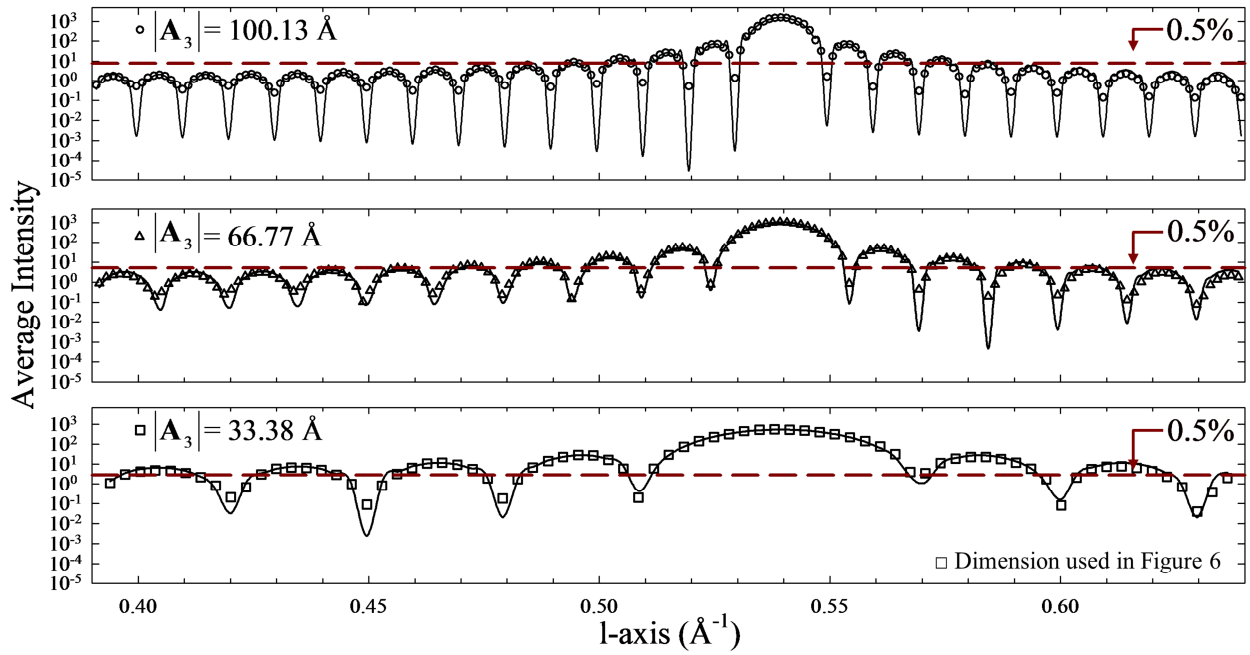

Figure 4.7: Average intensity profile of the Σ5 {310} [010] STGB (002) relrod from simulations with increasing $|\mathbf{A}_3|$ as labeled.

and 100.13 Å. Figure 4.7 shows that the relrod profiles for the three simulation sizes exhibit an excellent fit to the predicted diffraction intensity computed from Eq. (4.10). The fitted magnitude of $\mathbf{a}_3$ for all three simulations is 3.71 Å with N_3 equal to 9, 18, and 27 respectively. These fitted parameters correspond to $|\mathbf{A}_3|$ of length 33.38, 66.74, and 100.11 Å, which closely match the $|\mathbf{A}_3|$ used in the simulations. The larger magnitude of the fitted $\mathbf{a}_3$ parameter compared to those determined from the 10.39^o [010] STGB with partial dislocations compensates for the greater misorientation in the Σ5 (310) [010] STGB.

Virtual x-ray diffraction line profiles of the three large-angle CSL [010] STGBs are presented in Figure 4.8. Similar to the diffraction patterns presented in this study for low-angle symmetric tilt grain boundaries, these patterns show broadening of the {111} and {220} peaks as well as distinct secondary peaks emerging near the {002} peak. For each large-angle CSL [010] STGB, the broadening surrounding the {111} peak contains more discrete roughness, compared to the line profiles in Figure 4.5, indicating the presence of a secondary periodic structure within the grain boundaries impacting the {111} planar spacing. Further, there are subtle differences in the relative intensities of the secondary peaks on either side of the primary {111} peak between the different grain boundaries. Similarly, differences in the relative intensities of the discrete secondary peaks surrounding the {002} peak could indicate the presence of secondary structure that is buried beneath the relrod structure observed in Figure 4.6 and analyzed in detail in Figure 4.7. These observations provide motivation for future work to (1) explore long-range displacement field corrections to the virtual diffraction algorithm to minimize the role of simulation cell size on relrod structure and (2) explore a wide variety of zone axes in the SAED data, such as around the {111} reflections, as the virtual diffraction algorithm is capable of generating the full three dimensional reciprocal space map of each grain boundary. In addition,

reduction of the relrod structures that stem from the simulation size effects will aid in future comparisons of the virtual diffraction results to experimental efforts.

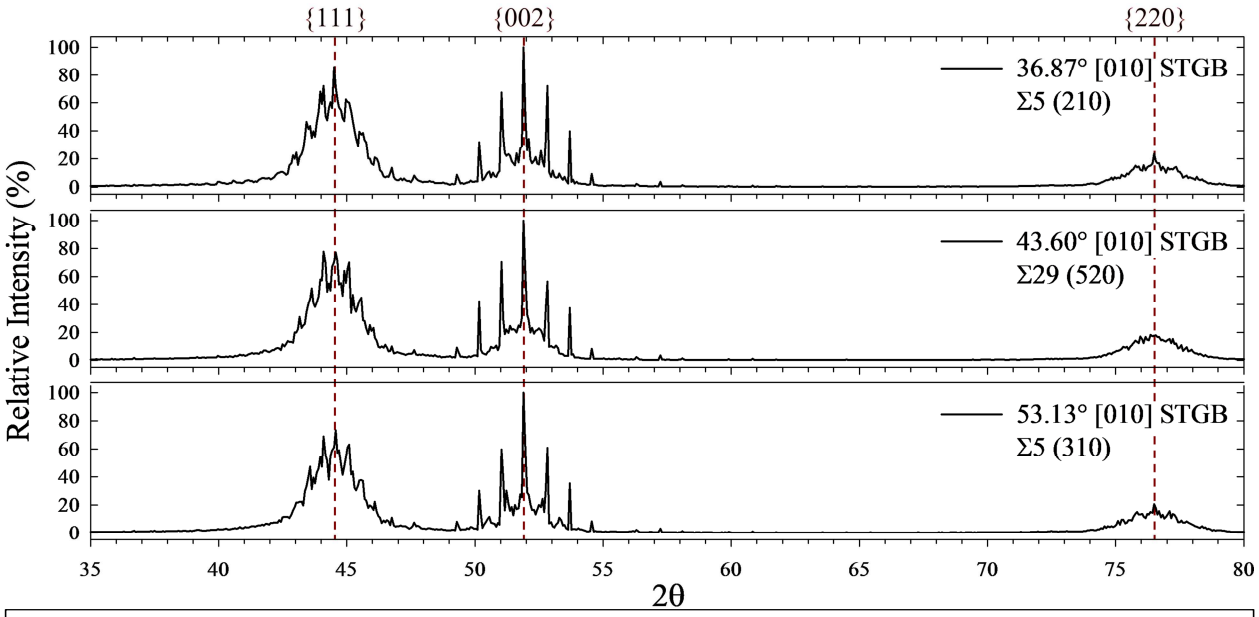

Figure 4.8: X-ray diffraction patterns for large-angle CSL [001] STGBs constructed using a 2θ bin size of 0.067°. The extra high intensity peaks near the {002} peak are the result of relrod structures due to the finite size effect of the simulations; however, the roughness of the {111} peak broadening stems from periodic secondary relaxations within the boundaries

4.4 Conclusion

This work presents a general method to compute and visualize virtual diffraction patterns from atomistic simulation data; this method is applied to study select low-angle and large-angle CSL Ni [010] symmetric tilt grain boundaries. For each STGB, the virtual diffraction algorithm produces SAED patterns and 2θ x-ray diffraction line profiles via explicit evaluation of the structure factor equation without *a priori* knowledge of the grain boundary unit cell. The virtual SAED patterns of the low-angle [010] STGBs differentiate the misorientation between the grain boundary regions and contain subsidiary peaks linked to the edge dislocation array within the simulations. Similarly, virtual SAED patterns of the large-angle CSL [010] STGBs, are successful in differentiating the misorientation between regions; however, subsidiary peaks are

not visible on these SAED patterns aligned with the misorientation axis due to prominent relrod structures. Thorough analysis on the effects of simulation size on computed relrod structures is performed for both low-angle and large-angle grain boundaries, which confirms their origin to be the finite size of the simulation cell. Virtual 2θ x-ray diffraction line profiles of the low-angle STGBs show smooth peak broadening around the {111} and {220} peaks due to gradual changes to their associated planar spacing, as well as discrete secondary peaks near the {002} linked to the relrods originating from the finite simulation cell size. For the large-angle CSL [010] STGBs, the {111} peak broadening contains small discrete peaks indicating the presence of a secondary periodic structure impacting this family of lattice planes.

Results from this work suggest that further virtual diffraction studies of bicrystal models can advance the understanding of non-local and non-homogeneous elasticity around grain boundaries which can be incorporated into constitutive models constructed for meso-scale simulations [37]. Non-locality and inhomogeneity in the elastic stiffness is typically associated with defects leading to incompatible strain and curvatures [38,39]. To treat this complex problem at the continuum scale, higher order and higher-grade constitutive laws have been proposed (cf. [38–43]). These necessarily introduce higher-order elastic-type stiffness tensors of rank fifth and higher, which are unknown. Their identification could be reached via fitting of virtual diffraction peaks between a continuum mechanics based representation of grain boundaries and those presented in this work.

Acknowledgements

We appreciate fruitful discussions with Dr. Mike Hawkridge at the University of Arkansas. DES and SPC acknowledge support of the National Science Foundation under grant #0954505. Simulations in this work were performed on resources supported in part by the National Science

Foundation under grants #0963249, #0959124, #0918970, managed by the Arkansas High Performance Computing Center.

References

[1] Howe JM. (1997) Introduction to Solid-Solid Interfaces, in: Interfaces Mater. At. Struct. Thermodyn. Kinet. Solid-Vaopr, Solid-Liquid Solid-Solid Interfaces. New York: John Wiley & Sons, Inc.

[2] Gaudig W and Sass SL. (1979) X-ray diffraction study of the structure of large-angle twist grain boundaries in gold, Philosophical Magazine A, **39**, 725–741.

[3] Balluffi RW, Sass SL, and Schober T. (1972) Grain boundary dislocation networks as electron diffraction gratings, Philosophical Magazine, **26**, 585–592.

[4] Sass SL and Bristowe PD. (1980) Boundaries, Diffraction Studies of the Atomic Structure of Grain. Metals Park, OH: American Society for Metals.

[5] Sass SL, Tan TY, and Balluffi RW. (1975) The detection of the periodic structure of high-angle twist boundaries: I. Electron diffraction study, Philosophical Magazine, **31**, 559–573.

[6] Randle V. (1993) The Measurement of Grain Boundary Geometry, first ed. Bristol: Taylor & Francis.

[7] Tan TY, Sass SL, and Balluffi RW. (1975) The detection of the periodic structure of high-angle twist boundaries: II. High resolution electron microscopy study, Philosophical Magazine, **31**, 575–585.

[8] Guan DY and Sass SL. (1979) X-ray diffraction study of the structure of small- and large-angle [001] tilt boundaries in gold, Philosophical Magazine A, **39**, 293–315.

[9] Sass SL. (1980) The study of the structure of grain boundaries using diffraction techniques, Journal of Applied Crystallography, **13**, 109–127.

[10] Bristowe PD and Sass SL. (1980) The atomic structure of a large angle [001] twist boundary in gold determined by a joint computer modelling and X-ray diffraction study, Acta Metallurgica, **28**, 575–588.

[11] Budai J, Bristowe PD, and Sass SL. (1983) The projected atomic structure of a large angle [001] $\Sigma = 5$ ($\theta = 36.9°$) twist boundary in gold: Diffraction analysis and theoretical predictions, Acta Metallurgica, **31**, 699–712.

[12] Bristowe PD and Balluffi RW. (1984) Effect of secondary relaxations on diffraction from high-Σ [001] twist boundaries, Surface Science, **144**, 14–27.

[13] Oh Y and Vitek V. (1986) Structural multiplicity of $\Sigma=5$(001) twist boundaries and interprtation of x-ray diffraction from these boundaries, Acta Metallurgica, **34**, 1941–

1953.

[14] Fitzsimmons MR and Sass SL. (1988) Quantitative x-ray diffraction study of the atomic structure of the Σ=5 (θ=36.9°) [001] twist boundary in gold, Acta Metallurgica, **36**, 3103–3122.

[15] Fitzsimmons MR, Vaudin MD, and Sass SL. (1988) Structural multiplicity and the interpretation of X-ray diffraction observations from grain boundaries, Scripta Metallurgica, **22**, 105–110.

[16] Eastman JA, Beno MA, Knapp GS, and Thompson LJ. (1995) X-ray diffraction characterization of defect behavior in nanocrystalline nickel during annealing, Nanostructured Materials, **6**, 543–546.

[17] Fitzsimmons MR, Eastman JA, Muller-Stach M, and Wallner G. (1991) Structural characterization of nanometer-sized crystalline Pd by x-ray-diffraction techniques, Physical Review B, **44**, 2452–2460.

[18] Gaudig W, Guan DY, and Sass SL. (1976) X-ray diffraction study of large-angle twist grain boundaries, Philosophical Magazine, **34**, 923–928.

[19] Stukowski A, Markmann J, Weissmüller J, and Albe K. (2009) Atomistic origin of microstrain broadening in diffraction data of nanocrystalline solids, Acta Materialia, **57**, 1648–1654.

[20] Alexandrov I V. and Valiev RZ. (2000) X-ray analysis of bulk nanostructured metals, Materials Science Forum, **321-324**, 577–582.

[21] Derlet PM, Van Petegem S, and Van Swygenhoven H. (2005) Calculation of x-ray spectra for nanocrystalline materials, Physical Review B, **71**, 1–8.

[22] Markmann J, Yamakov V, and Weissmüller J. (2008) Validating grain size analysis from X-ray line broadening: A virtual experiment, Scripta Materialia, **59**, 15–18.

[23] Warren BE. (1990) X-Ray Diffraction, first ed. New York: Dover Publications.

[24] Plimpton SJ. (1995) Fast parallel algorithms for short-range molecular dynamics, Journal of Computational Physics, **117**, 1–19.

[25] Williams DB and Carter CB. (2009) Thinking in Reciprocal Space, in: Transm. Electron Microsc. Part 2 Diffr., second ed. New York: Springer.

[26] Williams DB and Carter CB. (2009) Diffraction in TEM, in: Transm. Electron Microsc. Part 2 Diffr., second ed. New York: Springer.

[27] Colliex C, Cowley JM, Dudarev SL, Fink M, Gjønnes K, Hilderbrandt R, Howie A, Lynch

DF, Peng L-M, Ren G, Ross AW, Smith VH, Spence JCH, Steeds J, Wang J, Whelan MJ, and Zvyagin BB. (2004) Electron Diffraction, in: Prince E (Ed.). Int. Tables Crystallogr. Vol. C Math. Phys. Chem. Tables, third ed. Norwell, MA: Kluwer Academic Publishers.

[28] Peng L-M, Ren G, Dudarev SL, and Whelan MJ. (1996) Robust Parameterization of Elastic and Absorptive Electron Atomic Scattering Factors, Acta Crystallographica Section A, **52**, 257–276.

[29] Brown PJ, Fox AG, Maslen EN, O'Keefe MA, and Willis BTM. (2004) Intensity of Diffraction Intensities, in: Prince E (Ed.). Int. Tables Crystallogr. Vol. C Math. Phys. Chem. Tables, third ed. Norwell, MA: Kluwer Academic Publishers.

[30] Fox AG, O'Keefe MA, and Tabbernor MA. (1989) Relativistic Hartree–Fock X-ray and electron atomic scattering factors at high angles, Acta Crystallographica Section A, **45**, 786–793.

[31] Warren BE. (1969) The Powder Method, in: Cohen M (Ed.). X-Ray Diffr. Reading, MA: Addison-Wesley Publishing Company.

[32] Foiles SM and Hoyt JJ. (2006) Computation of grain boundary stiffness and mobility from boundary fluctuations, Acta Materialia, **54**, 3351–3357.

[33] Spearot DE, Jacob KI, and McDowell DL. (2005) Nucleation of dislocations from [001] bicrystal interfaces in aluminum, Acta Materialia, **53**, 3579–3589.

[34] Sutton AP and Vitek V. (1983) On the structure of tilt grain boundaries in cubic metals I. Symmetrical tilt boundaries, Philosophical Transactions of the Royal Society A: Mathematical, Physical and Engineering Sciences, **309**, 1–36.

[35] Upadhyay M, Capolungo L, Taupin V, and Fressengeas C. (2011) Grain boundary and triple junction energies in crystalline media: A disclination based approach, International Journal of Solids and Structures, **48**, 3176–3193.

[36] Kelchner CL, Plimpton SJ, and Hamilton JC. (1998) Dislocation nucleation and defect structure during surface indentation, Physical Review B, **58**, 11085–11088.

[37] Fressengeas C, Taupin V, and Capolungo L. (2011) An elasto-plastic theory of dislocation and disclination fields, International Journal of Solids and Structures, **48**, 3499–3509.

[38] Kröner E. (1963) On the physical reality of torque stresses in continuum mechanics, International Journal of Engineering Science, **1**, 261–278.

[39] Simmons JA, DeWit R, and Bullough R. (1969) Fundamental aspects of dislocation theory: A conference report with abstracts, Journal of Research of the National Bureau of Standards Section A: Physics and Chemistry, **73A**, 517.

[40] Mindlin RD and Tiersten HF. (1962) Effects of couple-stresses in linear elasticity, Archive for Rational Mechanics and Analysis, **11**, 415–448.

[41] Cosserat EMP and Cosserat F. (1909) Théorie Des Corps Déformables. Paris: A. Hermann et Fils.

[42] Eringen AC and Suhubi ES. (1964) Nonlinear theory of simple micro-elastic solids—I, International Journal of Engineering Science, **2**, 189–203.

[43] Lazar M and Maugin GA. (2004) Defects in gradient micropolar elasticity-I: screw dislocation, Journal of the Mechanics and Physics of Solids, **52**, 2263–2284.

Appendix 4.1

College of Engineering
Department of Mechanical Engineering
(479) 575-3153
(479) 575-6982 (FAX)

UNIVERSITY OF ARKANSAS

Mechanical Engineering Building
Fayetteville, Arkansas 72701

Coleman, S., Spearot, D.E., Capolungo, L. (2013) Virtual diffraction analysis of Ni [010] symmetric tilt grain boundaries, Modeling and Simulation in Materials Science and Engineering, 21, 055020.

I certify that Mr. Shawn Coleman is the first author of the paper and completed greater than 51% of the work in this publication. This work was done in collaboration with Dr. Laurent Capolungo at the Georgia Institute of Technology.

Sincerely,

Douglas E. Spearot, Ph.D.
Dissertation Director
Associate Professor and 21st Century Professorship
Department of Mechanical Engineering
University of Arkansas
Fayetteville, AR 72701
Office: 479-575-3040
E-mail: dspearot@uark.edu

Appendix 4.2

Author's rights after publication by IOP (articles not published on an open access basis)

- **After the copyright in my article has transferred to IOP, may I still use the article for teaching or in a thesis or dissertation?**
  Yes - upon transfer of copyright, IOP and/or the copyright owner grants back to authors a number of rights. These include the right to copy the article for teaching purposes, and to include the article in research theses or dissertations. Please include citation details and for online use, a link to the Version of Record. IOP's permission will be required for commercial use of an article published as part of your thesis.
- **After the copyright in my article has transferred to IOP, may I still use it for lecturing and at conferences?**
  Yes, you may make oral presentations of the article and, subject to adequate citation, include a summary and/or highlights of it in papers distributed at presentations or in conference proceedings. You may not submit a work which is substantially similar to one published in an IOP journal for inclusion in conference proceedings.
- **As the author of an IOP published article, may I provide a pdf of my paper to a colleague or third party?**
  Authors may send the Final Published Version of their article to colleagues on specific request provided no fee is charged and it is not done systematically through, for example, mass-mailings, posting on listservs or other open websites.
- **May I re-use the abstract of my article?**
  Yes, article abstracts and video abstracts can be freely re-used. No changes may be made to the abstract. Any links, brands, trademarks, or copyright notices embedded in the abstract must remain intact. Wherever possible the abstract should provide a link back to the Version of Record.
- **May I re-use supplementary material forming part of my article?**
  Yes, you may re-use supplementary material. Authors retain copyright in supplementary material, granting IOP a non-exclusive licence to reproduce it. IOP adheres to STM's 2006 Statement **Databases, Datasets, and Data Accessibility – Views and Practices of Scholarly Publishers**.

http://authors.iop.org/atom/help.nsf/LookupJournalSpecific/WebPermissionsFAQ~**

Chapter 5: A Computational Algorithm to Produce Virtual X-Ray and Electron Diffraction Patterns From Atomistic Simulations

Shawn P. Coleman[a], Mehrdad M. Sichani[a], Douglas E. Spearot[a]

[a] Department of Mechanical Engineering, University of Arkansas, Fayetteville, AR 72701

Abstract

Electron and x-ray diffraction are well-established experimental methods used to explore the atomic scale structure of materials. In this work, a computational algorithm is developed to produce virtual electron and x-ray diffraction patterns directly from atomistic simulations. This algorithm advances beyond previous virtual diffraction methods by utilizing a high-resolution mesh of reciprocal space which eliminates the need for *a priori* knowledge of the crystal structure being modeled or other assumptions concerning the diffraction conditions. At each point on the reciprocal space mesh, the diffraction intensity is computed via explicit computation of the structure factor equation. To construct virtual selected area electron diffraction patterns, a hemispherical slice of the reciprocal lattice mesh lying on the surface of the Ewald sphere is isolated and viewed along a specified zone axis. X-ray diffraction line profiles are created by binning the intensity of each reciprocal lattice point by its associated scattering angle, effectively mimicking powder diffraction conditions. The virtual diffraction algorithm is sufficiently generic to be applied to atomistic simulations of any atomic species. In this article, the capability and versatility of the virtual diffraction algorithm is exhibited by presenting findings from atomistic simulations of <100> symmetric tilt Ni grain boundaries, nanocrystalline Cu models, and a heterogeneous interface formed between α-Al_2O_3 (0001) and γ-Al_2O_3 (111).

5.1 Introduction

Virtual diffraction is a simulation technique that generates experimentally comparable diffraction patterns from atomistic simulation data using equations from diffraction theory. For over thirty years, researchers have used virtual diffraction methods to make direct connections between atomistic simulations and experimentation [1–11]; however, computational limitations inherent to the time of these early studies restricted their capability and required researchers to make assumptions about the crystal structure or the diffraction conditions. The virtual diffraction algorithm discussed in this article advances these earlier studies by leveraging modern computational power in order to eliminate the need for assumptions related to the crystal structure of the material, allowing a single algorithm to produce both x-ray diffraction line profiles and selected area electron diffraction (SAED) patterns from atomistic simulation [12]. The virtual diffraction algorithm offers new routes to connect atomistic simulations directly to experimental studies in order to investigate the structure and deformation of nanoscale materials and offers new capability to characterize complex materials within the framework of atomistic simulations.

Virtual diffraction models based on kinematic diffraction theory were developed in the 1980s to characterize atomistic simulations of large-angle symmetric twist grain boundaries using area diffraction patterns [1–3]. In kinematic models, the diffraction intensity, I, is computed for N atoms as the product of the structure factor, $F(\mathbf{K})$, with its complex conjugate, $F^*(\mathbf{K})$,

$$I(\mathbf{K}) = F^*(\mathbf{K})F(\mathbf{K}) \tag{5.1}$$

where

$$F(\mathbf{K}) = \sum_{j=1}^{N} f_j \exp\left(2\pi i\, \mathbf{K}\cdot\mathbf{r}_j\right) \quad . \tag{5.2}$$

Here, $\mathbf{K}$ is the location of the diffraction peak in reciprocal space, $\mathbf{r}_j$ is the position of the atom in real space, and f_j is the atomic scattering factor (often simplified as unity [1–5]). In the seminal studies [1–3], computational limitations restricted both the number of atoms used to compute diffraction intensities and the range of reciprocal space that could be explored. To improve computational efficiency, diffraction intensities were computed over a limited region of reciprocal space known to be important based on *a priori* knowledge of the grain boundary unit cell. Using these techniques, work by Bristowe and Sass [1] showed that small displacements of the atoms within the grain boundary unit cell can create identifiable changes to the diffraction patterns. This breakthrough prompted several researchers [2–5] to incorporate virtual diffraction patterns in their subsequent studies to verify predicted grain boundary structures.

Following the early kinematic diffraction studies, a second method to generate virtual diffraction patterns became popular among researchers modeling nanocrystalline materials that utilized assumptions based on powder diffraction conditions [6–11]. These researchers used formulations of the Debye scattering equation to compute diffraction intensity based on the interatomic distance between atoms, r_{ij}, via [13],

$$I(k) = \sum_{i=1}^{N}\sum_{j=1}^{N} f_i f_j \frac{\sin(2\pi k r_{ij})}{2\pi k r_{ij}} \quad . \tag{5.3}$$

Here, $k = 2\sin(\theta)/\lambda$ represents a spherically averaged position in reciprocal space that is related to the diffraction angle, θ, and monochromatic radiation of wavelength, λ. By spherical averaging the positions in reciprocal space, all orientations of the simulated crystals are mathematically represented mimicking the random distribution associated with powder diffraction conditions. Using this relationship, researchers [6–11] constructed x-ray diffraction line profiles to investigate peak shift and peak broadening in order to extract data on the mean

grain size and microstrain in nanocrystalline models with different grain diameters.

The virtual diffraction algorithm discussed in this work advances beyond these previous methods to create both SAED and x-ray diffraction line profiles using the same algorithm without any *a priori* knowledge of the crystal structure. The algorithm is sufficiently generic for all atomic species and is integrated into the LAMMPS molecular dynamics simulator [14] as a user-defined compute; it can also be implemented into other atomistic simulation packages. Following a concise discussion of the computational algorithm, this article presents three unique applications of the virtual diffraction method, displaying its versatility and its capability to connect atomistic simulations with experimental studies.

5.2 Computational Algorithm

The diffraction algorithm generates a high-resolution, three-dimensional mesh of points filling a volume of reciprocal space constructed from the entire domain of the atomistic simulation cell. Each point on the reciprocal lattice mesh is associated with a reciprocal lattice vector $\mathbf{K}$ describing the deviation between the diffracted and incident wave vectors $\mathbf{k_D}$ and $\mathbf{k_I}$ [13],

$$\mathbf{K} = \mathbf{k_D} - \mathbf{k_I} = \xi\,\mathbf{B}_1 + \eta\,\mathbf{B}_2 + \zeta\,\mathbf{B}_3 \quad , \tag{5.4}$$

where ξ, η, and ζ can be any real number. The mesh of reciprocal lattice points is built on a rectilinear grid with spacing, $c_n\left|\mathbf{A}_n\right|^{-1}$, along each reciprocal lattice axis $\mathbf{B}_n$, as shown in Figure 5.1. Each reciprocal lattice axis, $\mathbf{B}_n$, is determined from its associated vector, $\mathbf{A}_n$, corresponding to the n = 1, 2, or 3 edge of the simulation cell. The parameters c_n control the spacing of the reciprocal lattice points, and tune the resolution within the reciprocal space volume explored. To increase the computational efficiency, the volume of reciprocal space that is explored is reduced by setting criteria on $\left|\mathbf{K}\right|$ as shown in Figure 5.1. By constructing a high-

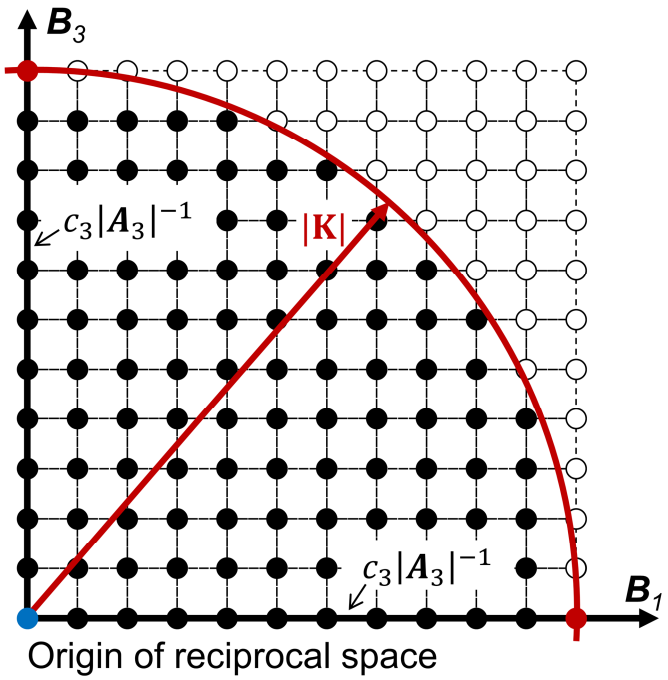

Figure 5.1: Schematic of the reciprocal space mesh variables and bounds.

resolution reciprocal space mesh, strong intensity peaks associated with the constructive interference of Bragg reflections are intuitively captured without *a priori* knowledge of the crystal structure. The interplanar distances d_{hkl} associated with these Bragg reflections can be computed at each reciprocal lattice point utilizing the geometric relationships between $\mathbf{k}_I$, $\mathbf{k}_D$, $\boldsymbol{\kappa}$, and λ described in Bragg's Law [13],

$$\frac{2\sin(\theta)}{\lambda} = \frac{1}{d_{hkl}} = |\mathbf{K}| \quad . \tag{5.5}$$

Diffraction intensity at each reciprocal lattice point is computed using the structure factor equation, Eq. (5.2), with the variations described below to differentiate between electron and x-ray diffraction. In the diffraction algorithm, atomic scattering factors f_j are explicitly computed for each atomic species to account for the reduction in diffracted intensity from an individual atom due to Compton scattering and vary by angle of diffraction and type of radiation [15]. At

each diffraction angle, the atomic scattering factors f_j are computed using analytical approximations parameterized for the specific atomic species. For electron diffraction, the analytical approximation of the atomic scattering factor is taken as the summation of five Gaussian functions of the form [16],

$$f_j\left(\frac{\sin\theta}{\lambda}\right)=\sum_i^5 a_i \exp\left(-b_i\frac{\sin^2\theta}{\lambda^2}\right) \quad , \tag{5.6}$$

which have been parameterized for the majority of neutral elements by Peng et al. [17]. For x-ray diffraction, the analytical approximation of the atomic scattering factor is found from a summation of four Gaussian functions plus a constant of the form [18],

$$f_j\left(\frac{\sin\theta}{\lambda}\right)=\sum_i^4 a_i \exp\left(-b_i\frac{\sin^2\theta}{\lambda^2}\right)+c \quad , \tag{5.7}$$

and have been parameterized by Fox et al. for most atomic species [19].

For electron diffraction, the diffraction intensity, $\mathrm{I_e}(\mathbf{K})$, at each reciprocal lattice point is computed from the product of the structure factor and its complex conjugate normalized by the number of atoms being studied within the simulation via [15],

$$\mathrm{I_e}(\mathbf{K})=\frac{\mathrm{F}(\mathbf{K})\mathrm{F}^*(\mathbf{K})}{\mathrm{N}} \quad . \tag{5.8}$$

To compute x-ray diffraction intensities, $\mathrm{I_x}(\mathbf{K})$, the Lorentz-polarization factor, $\mathrm{Lp}(\theta)$, is applied to account for the relative distribution of the reciprocal lattice points and the change in scatter intensity when using non-polarized incident radiation. The Lorentz-polarization factor is computed via [15],

$$\mathrm{Lp}(\theta)=\frac{1+\cos^2(2\theta)}{\cos(\theta)\sin^2(\theta)} \quad , \tag{5.9}$$

and thus the diffraction intensity from x-rays is computed at each reciprocal lattice point through [15],

$$I_x(\mathbf{K}) = Lp(\theta)\frac{F(\mathbf{K})F^*(\mathbf{K})}{N} \quad . \tag{5.10}$$

Virtual SAED patterns are created by examining the region in reciprocal space intersecting the Ewald sphere of radius λ^{-1}. For a particular zone axis, the Ewald sphere is centered at the tail of the associated incident wave vector and intersects the origin of reciprocal space. To construct the electron diffraction pattern, a hemispherical slice of the reciprocal lattice mesh lying on the surface of the Ewald sphere is isolated and viewed along the zone axis. Using visualization software, intensity values are interpolated between points on the reciprocal space mesh allowing the slice to take on no thickness while maintaining a continuous intensity field along the hemisphere. To enhance features within the diffraction pattern, reciprocal lattice points are colored by intensity on a $\log_{10}$ scale. To achieve higher computational efficiency when creating SAED patterns for a user-specified zone axis, the diffraction algorithm can be augmented to limit the intensity calculation to only those reciprocal mesh points that lie near the surface of the Ewald sphere.

X-ray diffraction line profiles are created by virtually rotating the Ewald sphere around the origin of reciprocal space to all possible orientations, mimicking powder diffraction conditions [20]. By making all diffraction orientations equally probable, every reciprocal lattice point will intersect the surface of the Ewald sphere. Line profiles simulating x-ray powder diffraction are constructed by collecting reciprocal lattice points into bins corresponding to their scattering angle 2θ calculated using Eq. (5.5) and summing the intensity data. The scattering angle bin size is optimized through trials to reduce the noise within the line profile while maximizing peak features. To achieve higher computational efficiency while computing x-ray diffraction line

profiles within known 2θ limits, additional criteria on $|\mathbf{K}|$ can be assigned using Bragg's law, Eq. (5.5), to associate 2θ with $|\mathbf{K}|$.

The new diffraction algorithm leverages parallelization techniques and modern computing hardware to compute diffraction intensities using a much larger number of atoms and a much larger number of reciprocal lattice points compared to any prior study. The diffraction algorithm is implemented into LAMMPS as a user-defined compute and uses message passing interface (MPI) parallelization of the atoms matching the standard spatial decomposition built within the LAMMPS framework. To further increase computational efficiency, the diffraction compute uses shared memory parallelization over the reciprocal space mesh via OpenMP and is capable of offloading computation to external multicore hardware.

5.3 Applications

The capability and versatility of the virtual diffraction algorithm is illustrated via three applications: (1) low-angle Ni <100> symmetric tilt grain boundaries, (2) Cu nanocrystalline models, and (3) a complex heterogeneous alumina interface. These studies highlight the flexibility of the virtual diffraction technique to successfully model different material systems. In the following applications, simulated 200 kV electron radiation (λ = 0.0251 Å [16]) and Cu K_α x-rays (λ = 1.54178 Å [15]) are used to create SAED patterns and x-ray line profiles, respectively. In the electron diffraction studies, the SAED patterns are produced limiting $\mathbf{K}$ from $0 \leq |\mathbf{K}| \leq 0.85$ Å^{-1} and restricting mesh points to a 0.01 Å^{-1} hemispherical slice from the associated Ewald sphere in the intensity calculation. X-ray diffraction line profiles utilize a 2θ bin size of 0.07 degrees.

5.3.1 *Ni Bicrystals*

Virtual diffraction SAED patterns are constructed to analyze two bicrystal samples

containing low-angle symmetric tilt grain boundaries (STGBs) with a [010] tilt axis modeled using the Foiles-Hoyt Ni embedded-atom method (EAM) potential [21]. Here, low-angle [010] STGBs with tilt angles of 10.39^o and 12.68^o are constructed utilizing the methods described by Spearot et al. [22] with periodic boundary conditions applied in all directions. For each bicrystal, minimum energy grain boundary structures are attained at 0 K by aligning the opposing lattice regions with the intended tilt and removing atoms that are inside specified cutoff distances. This procedure effectively samples multiple starting configurations with different relative displacements. Each grain boundary structure is optimized according to the minimum potential energy using a nonlinear conjugate gradient method implemented in LAMMPS. Electron and x-ray diffraction data are computed using the atomic positions of the minimum energy grain boundary structures.

The two energy minimized [010] Ni STGB structures contain a periodic array of edge dislocations separated by a distance, $d_{D,}$ of 19.45 Å and 15.94 Å for the 10.39^o and 12.68^o tilts, respectively, as shown in Figure 5.2(a-b). Computed SAED patterns with the zone axis aligned along the [010] tilt axis are shown in Figure 5.2(c-f). Figure 5.2(c-d) are viewed such that Bragg reflections in the range of $h^2+k^2+l^2 <= 8$ are visible in order to capture the misorientation between the two grains. The figures also show the presence of relrods near the Bragg reflections orientated parallel to the grain boundary plane (vertical direction) and oriented normal to the grain boundary (horizontal direction). Relrods are a locus of non-negligible intensity peaks encompassing Bragg reflections that occur during diffraction within a finite volume [23]. The size and shape of the relrods are dependent on the size and shape of the finite volume, which correspond to the number of atoms included within the summation of the structure factor equation.

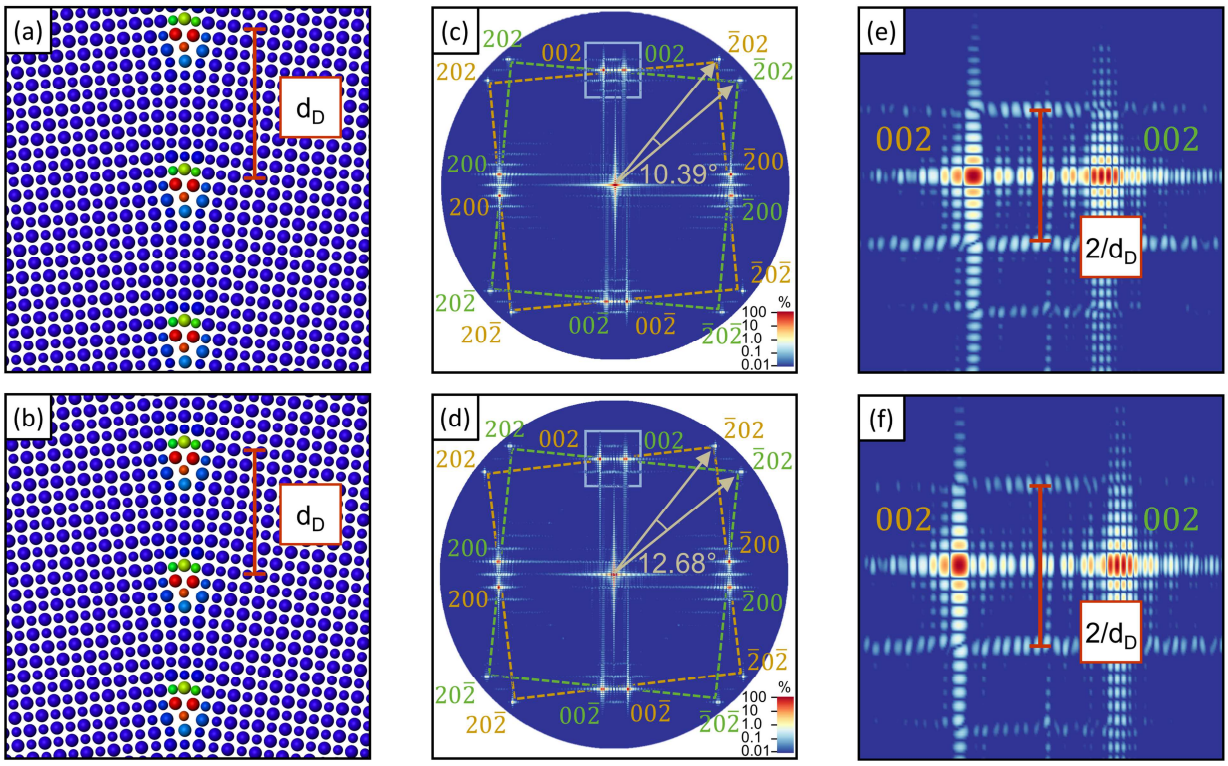

Figure 5.2: The structure of minimum energy Ni [010] STGBs with tilt angles of (a) 10.39° and (b) 12.68° each created by an array of dislocation cores separated a distance d_D. SAED patterns aligned on the tilt axis show the (c,d) corresponding misorientation of and (d,e) subsidiary peaks associated with the dislocation array near the (002) reflections.

Figure 5.2(e-f) show magnified regions near the (002) reflections and highlight the presence of two sets of subsidiary reflections within each SAED pattern not attributed to the relrod structures. These subsidiary peaks were observed in previous experimental works and have been related to the periodic spacing of the dislocation cores within the grain boundary [24]. In this work, the average spacing between the subsidiary peaks and the (002) relrod tail is calculated as 1/19.89 $Å^{-1}$ and 1/15.94 $Å^{-1}$ which is in very good agreement with the spacing between the dislocations in the bicrystal models.

5.3.2 *Cu Nanocrsytals*

X-ray diffraction line profiles and SAED patterns are created for nanocrystalline Cu samples with different grain diameters and number of grains. The different nanocrystalline samples are

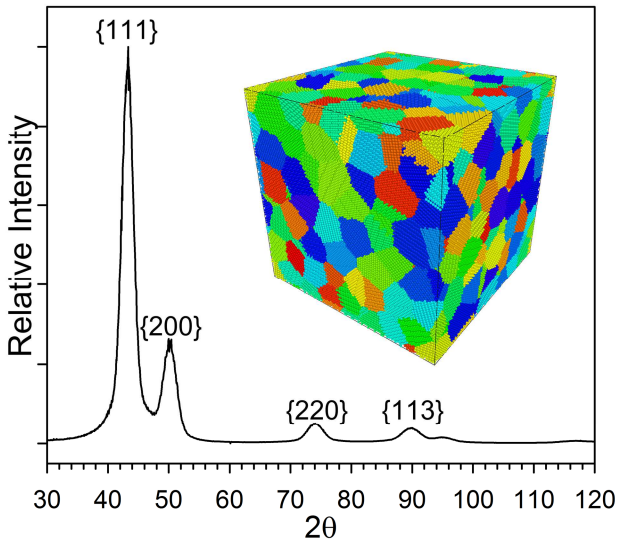

Figure 5.3: XRD pattern for a nanocrystalline Cu samples with 300 grains and 5 nm mean grain diameter. The nanocrystalline sample is shown in the inset colored by grain number.

constructed using the Voronoi method to create a random distribution of grain orientations within fully periodic, cubic simulation cells. The Voronoi method requires the user to specify a target mean grain size and uses this value to determine the number and distribution of grain centers within the simulation cell. There is no guarantee that the true mean grain diameter resulting from the Voroni construction algorithm will be exactly equal to the user-defined target value. Within each nanocrystalline sample, the atomic interactions are modeled using the Cu EAM potential parameterized by Mishin et al. [25]. Before computing the virtual diffraction patterns, the atomic structures are relaxed at 0 K using a non-linear conjugate gradient method.

X-ray diffraction line profiles are constructed for each nanocrystalline Cu sample using a mesh resolution of approximately 4.7×10^7 reciprocal lattice points per $Å^{-3}$,which is achieved by appropriately scaling the c_n parameters for the different simulation dimensions. Figure 5.3 shows a representative x-ray diffraction line profile for a nanocrystalline sample containing 300 grains with a target mean grain diameter of 5 nm. Four peaks are observed at 2θ locations 43.29°, 50.43°, 74.15°, and 89.96° which correspond to the interplanar distances associated with

{111}, {200}, {220}, and {311} planes, respectively. These peak locations are a close match to the predicted locations computed using Bragg's law for single crystal Cu with a lattice parameter of 3.615 Å [25], indicating that there is no net tensile or compressive strain in the nanocrystalline samples after the Voronoi construction and energy minimization procedures.

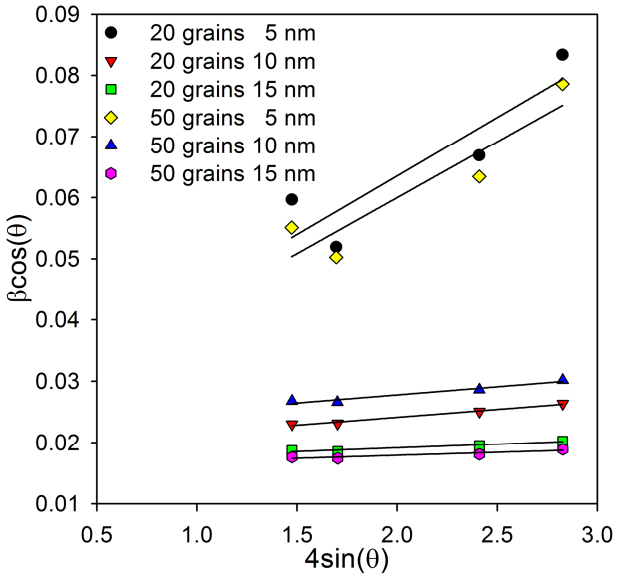

Figure 5.4: Williamson-Hall analysis for six different samples using Lorentzian-Gaussian fitting of the diffraction peaks.

Peak locations and broadening from the virtual x-ray diffraction line profiles are used to perform a Williamson-Hall analysis [26] to predict microstrain in the lattice due to the grain boundaries as well as the true mean grain diameter of the nanocrystalline samples. This analysis is performed for six samples containing 20 and 400 grains with target mean grain diameters of 5, 10, and 15 nm. Both Lorentzian and Lorentzian-Gaussian distributions are fit to the x-ray diffraction peaks using the Fityk software [27], which provides peak location and peak broadening information. It is found that the Lorentzian-Gaussian distribution provides a closer approximation to the peak maxima and shapes through minimization of the residuals between the computed diffraction data and each fitted distribution. Figure 5.4 shows a Williamson-Hall plot

using the Lorentzian-Gaussian fit to the virtual diffraction data. The true mean grain diameter and the microstrain are extracted via a linear fit and are reported in Table 5.1 for the six different samples using both Lorentzian and Lorentzian-Gaussian fittings. For the 5 nm model, the true mean grain diameter is larger than the target grain diameter used during Voronoi construction and the microstrain within each nanocrystalline model is non-homogeneous as evident by the non-linearity of the data. On the other hand, for the 10 and 15 nm samples, the true mean grain diameter predicted with the Lorentzian-Gaussian distribution is smaller than the target grain diameter and data is linear, implying that the root-mean-squared microstrain is isotropic. These observations are consistent with work of Derlet et al. [10]. For simulations containing the same number of grains, the magnitude of the microstrain decreases in models built with increasing target grain diameter. This is attributed to the smaller fraction of atoms within the larger nanocrystalline samples whose lattice potions are distorted by the grain boundaries. Models constructed with the same target mean grain diameter show negligible dependence of the microstrain on the number of grains.

Table 5.1 True mean grain diameter (nm) and microstrain predicted from the Williamson-Hall analysis using different peak fitting functions

Target Grain	**20 grains**				**50 grains**			
Diameter	**Microstrain**		**True Diameter**		**Microstrain**		**True Diameter**	
5 nm	0.0188[a],	0.0192[b]	6.64[a],	6.12[b]	0.0186[a],	0.0183[b]	7.79[a],	6.59[b]
10 nm	0.0040[a],	0.0026[b]	10.85[a],	8.11[b]	0.0040[a],	0.0026[b]	8.43[a],	6.85[b]
15 nm	0.0020[a],	0.0012[b]	11.01[a],	9.23[b]	0.0018[a],	0.0010[b]	11.59[a],	9.70[b]

[a] X-ray diffraction peaks fit to a Lorentizain distribution.
[b] X-ray diffraction peaks fit to a Lorentzian-Gaussian distribution.

Figure 5.5 shows SAED patterns generated with zone-axes oriented along the [100] direction for simulations containing 50 and 400 grains using target mean grain diameters of 5 and 10 nm. Each SAED pattern contains three rings associated with the {111}, {200}, and {220} planes, as

expected from experimental results which were performed on a thin copper film containing 45 nm grains [28]. In the 400 grain models the rings are more complete as compared with the 50 grain models implying that models with a larger number of grains are statistically more representative of nanocrystalline samples with random grain orientations. In addition, the rings in the 10 nm samples are thinner than the rings in the 5 nm samples because of microstrain effects, analogous to the role of microstrain on peak broadening in the x-ray diffraction line profiles.

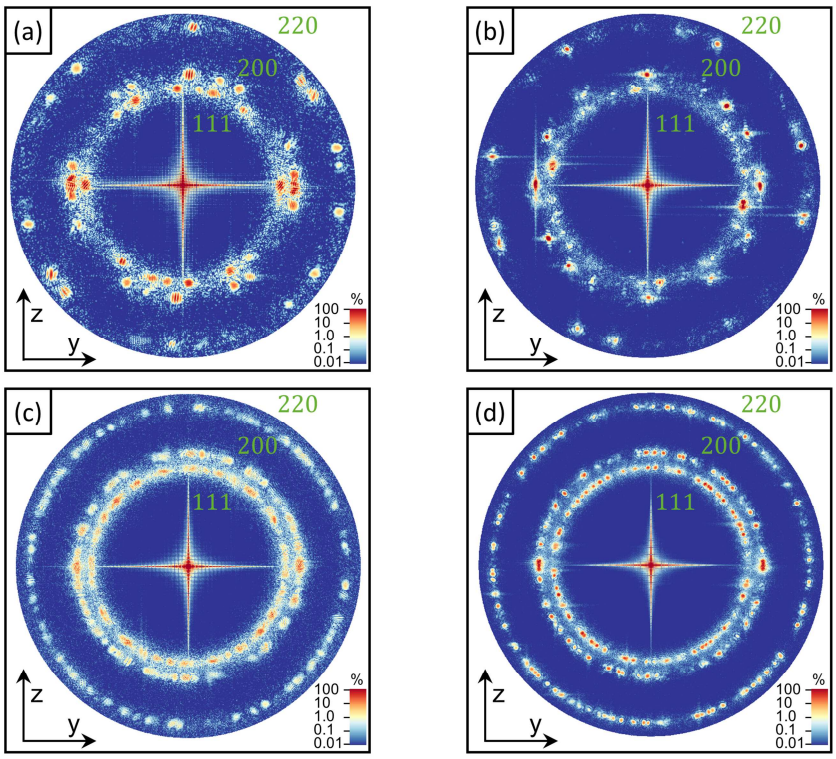

Figure 5.5: SAED pattern for nanocrystalline Cu models containing 50 grains having (a) 5 nm and (b) 10 nm grain diameter as well as 400 grain models with (c) 5 nm and (d) 10 nm grain diameter.

5.3.3 *Heterogeneous Al_2O_3 interfaces*

Finally, virtual diffraction methods are used to characterize a complex interface formed between α-Al_2O_3 (0001) and γ-Al_2O_3 (111). Here, both the individual components and combined

interface are constructed using fully periodic boundary conditions with a large vacuum region separating free surfaces normal to the grain boundary. The boundary dimensions along the grain boundary plane are chosen to minimize the strain associated with joining the α-Al_2O_3 (0001) and γ-Al_2O_3 (111) components forming the interface. The Al_2O_3 phases are modeled using the ReaxFF potential [29] and the structures associated with the individual components and the combined interface are relaxed at 0 K to their minimum potential energy structures using a nonlinear conjugate gradient method implemented in LAMMPS.

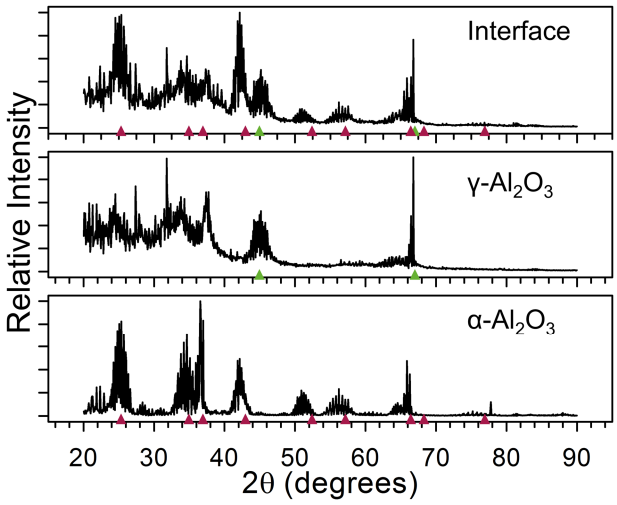

Figure 5.6: X-ray diffraction line profiles identifying an α-Al_2O_3 slab (bottom), a γ-Al_2O_3 slab (middle), and a α-Al_2O_3 (0001), and γ-Al_2O_3 (111) interface (top). The colored triangles are positioned at experimentally determined peak locations for bulk α-Al_2O_3 (red) [54] and γ-Al_2O_3 (green) [55].

Prior to this work, identification of different Al_2O_3 phases, much less interfaces, has not been possible in atomistic simulations using traditional computational methods (radial distribution functions, centrosymmetry [30], common neighbor-analysis [31], energy-filtration methods, etc.) due to their non-cubic nature and subtle differences between their atomic structures. However, virtual x-ray diffraction line profiles of the individual components and the combined interface, shown in Figure 5.6, uniquely identify the phases. These virtual x-ray

diffraction results are further validated through direct comparisons to experimental results (colored triangles, in Figure 5.6) [32,33]. Peak locations for the simulated alumina models are skewed relative to the experimental reference indicating a uniform expansion of the lattice structure. This expansion is related to the equilibrium lattice parameter predicted by the ReaxFF potential [29] as well as the relaxation of the lattice due to the free surfaces in the simulations being modeled.

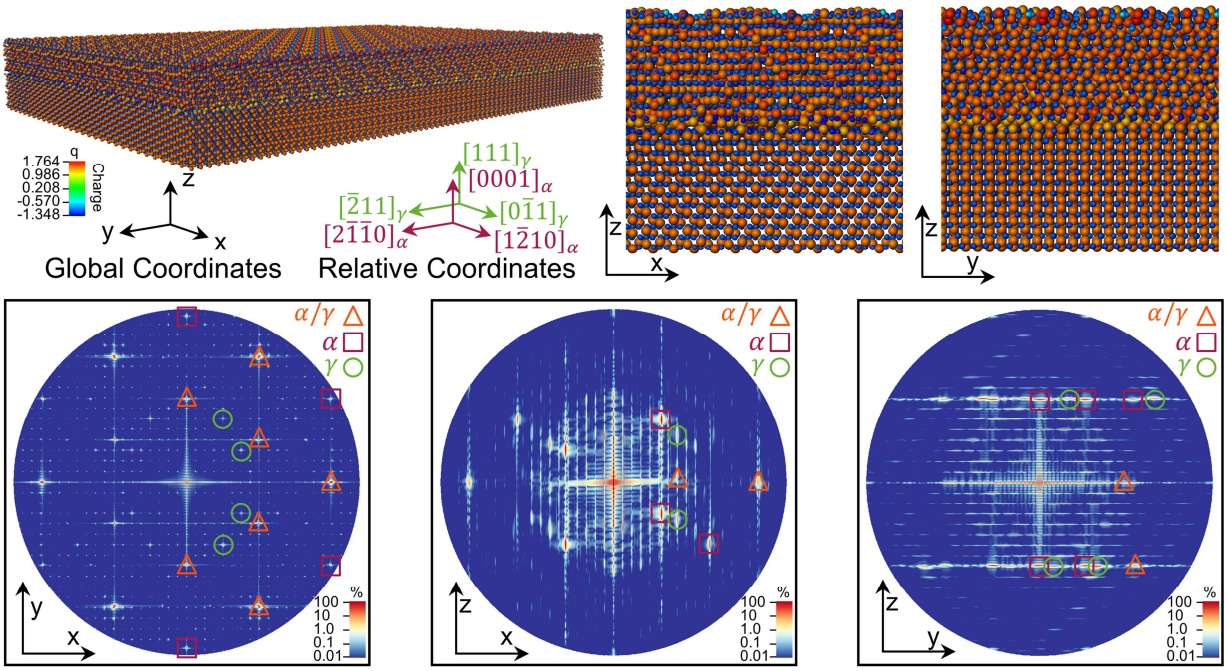

Figure 5.7: Minimum energy structure of a heterogonous α-Al_2O_3 (0001) - γ-Al_2O_3 (111) interface shown in (a) and its corresponding virtual SAED patterns aligned on the primary global axes shown in (b-d). Overlapping SAED reflections are identified in (b-d) which assisted in the optimization of a minimum energy interface.

The complex crystal structures associated with α-Al_2O_3 and γ-Al_2O_3 makes optimization of the five macroscopic degrees of freedom required for the construction of their interface difficult [34]. During this study, virtual SAED patterns assisted in the search for an ideal interface structure by identifying orientations that achieve higher orders of crystallographic compatibility, as shown by the overlapping diffraction peaks in Figure 5.7. Interfaces constructed with more

overlapping peaks, as identified by analyzing patterns created by the individual components as well as comparisons to prior experimental work [35], were lower in energy compared to those with disregistry

5.4 Conclusions

The virtual diffraction algorithm introduced in this article computes diffraction intensities via the structure factor equation at each point within a high-resolution reciprocal space mesh. The three-dimensional intensity data are used to construct both SAED and x-ray diffraction line profiles from atomistic simulations without *a priori* knowledge of the crystal structure. The diffraction algorithm is implemented within the LAMMPS molecular dynamics simulator and is capable of being integrated into other atomistic simulation packages in order to take advantage of modern parallelization techniques and computing hardware.

Three unique applications discussed in this article show the versatility of this algorithm to produce diffraction patterns using different atomic species and model configurations as well as its capability to link virtual diffraction work directly to experimental findings. In addition, the study shows a new route virtual diffraction offers in the characterization and optimization of complex material structures within atomistic simulations.

Acknowledgments

The authors acknowledge support of the National Science Foundation under grant #0954505. Additional support is provided by the 21st Century Professorship in Mechanical Engineering at the University of Arkansas. Most simulations in this work were performed on resources supported in part by the National Science Foundation under grants #0963249, #0959124, #0918970, managed by the Arkansas High Performance Computing Center. Select simulations were performed using the National Science Foundation support XSEDE Network. The authors

also acknowledge support of Y. Wang at the Pittsburgh Supercomputing Center for assistance parallelizing the reciprocal space mesh in the virtual diffraction compute.

References

[1] Bristowe PD and Sass SL. (1980) The atomic structure of a large angle [001] twist boundary in gold determined by a joint computer modelling and X-ray diffraction study, Acta Metallurgica, **28**, 575–588.

[2] Budai J, Bristowe PD, and Sass SL. (1983) The projected atomic structure of a large angle [001] Σ= 5 (θ=36. 9°) twist boundary in gold: Diffraction analysis and theoretical predictions, Acta Metallurgica, **31**, 699–712.

[3] Bristowe PD and Balluffi RW. (1984) Effect of secondary relaxations on diffraction from high-Σ [001] twist boundaries, Surface Science, **144**, 14–27.

[4] Oh Y and Vitek V. (1986) Structural multiplicity of Σ=5(001) twist boundaries and interprtation of x-ray diffraction from these boundaries, Acta Metallurgica, **34**, 1941–1953.

[5] Fitzsimmons MR and Sass SL. (1988) Quantitative x-ray diffraction study of the atomic structure of the Σ=5 (θ=36.9°) [001] twist boundary in gold, Acta Metallurgica, **36**, 3103–3122.

[6] Brandstetter S, Derlet PM, Van Petegem S, and Van Swygenhoven H. (2008) Williamson–Hall anisotropy in nanocrystalline metals: X-ray diffraction experiments and atomistic simulations, Acta Materialia, **56**, 165–176.

[7] Stukowski A, Markmann J, Weissmüller J, and Albe K. (2009) Atomistic origin of microstrain broadening in diffraction data of nanocrystalline solids, Acta Materialia, **57**, 1648–1654.

[8] Markmann J, Yamakov V, and Weissmüller J. (2008) Validating grain size analysis from X-ray line broadening: A virtual experiment, Scripta Materialia, **59**, 15–18.

[9] Markmann J, Bachurin D, Shao L, Gumbsch P, and Weissmüller J. (2010) Microstrain in nanocrystalline solids under load by virtual diffraction, EPL (Europhysics Letters), **89**, 66002.

[10] Derlet PM, Van Petegem S, and Van Swygenhoven H. (2005) Calculation of x-ray spectra for nanocrystalline materials, Physical Review B, **71**, 1–8.

[11] Van Swygenhoven H, Budrovie Ž, Derlet PM, Froseth AG, and Van Petegem S. (2005) In situ diffraction profile analysis during tensile deformation motivated by molecular dynamics, Materials Science and Engineering: A, **400**, 329–333.

[12] Coleman SP, Spearot DE, and Capolungo L. (2013) Virtual diffraction analysis of Ni [0 1 0] symmetric tilt grain boundaries, Modelling and Simulation in Materials Science and

Engineering, **21**, 055020.

[13] Williams DB and Carter CB. (2009) Thinking in Reciprocal Space, in: Transm. Electron Microsc. Part 2 Diffr., second ed. New York: Springer.

[14] Plimpton SJ. (1995) Fast parallel algorithms for short-range molecular dynamics, Journal of Computational Physics, **117**, 1–19.

[15] Warren BE. (1990) X-Ray Diffraction, first ed. New York: Dover Publications.

[16] Colliex C, Cowley JM, Dudarev SL, Fink M, Gjønnes K, Hilderbrandt R, Howie A, Lynch DF, Peng L-M, Ren G, Ross AW, Smith VH, Spence JCH, Steeds J, Wang J, Whelan MJ, and Zvyagin BB. (2004) Electron Diffraction, in: Prince E (Ed.). Int. Tables Crystallogr. Vol. C Math. Phys. Chem. Tables, third ed. Norwell, MA: Kluwer Academic Publishers.

[17] Peng L-M, Ren G, Dudarev SL, and Whelan MJ. (1996) Robust Parameterization of Elastic and Absorptive Electron Atomic Scattering Factors, Acta Crystallographica Section A, **52**, 257–276.

[18] Brown PJ, Fox AG, Maslen EN, O'Keefe MA, and Willis BTM. (2004) Intensity of Diffraction Intensities, in: Prince E (Ed.). Int. Tables Crystallogr. Vol. C Math. Phys. Chem. Tables, third ed. Norwell, MA: Kluwer Academic Publishers.

[19] Fox AG, O'Keefe MA, and Tabbernor MA. (1989) Relativistic Hartree–Fock X-ray and electron atomic scattering factors at high angles, Acta Crystallographica Section A, **45**, 786–793.

[20] Warren BE. (1969) The Powder Method, in: Cohen M (Ed.). X-Ray Diffr. Reading, MA: Addison-Wesley Publishing Company.

[21] Foiles SM and Hoyt JJ. (2006) Computation of grain boundary stiffness and mobility from boundary fluctuations, Acta Materialia, **54**, 3351–3357.

[22] Spearot DE, Jacob KI, and McDowell DL. (2005) Nucleation of dislocations from [001] bicrystal interfaces in aluminum, Acta Materialia, **53**, 3579–3589.

[23] Williams DB and Carter CB. (2009) Diffraction of Small Volumes, in: Transm. Electron Microsc. Part 2 Diffr., second ed. New York: Springer.

[24] Guan DY and Sass SL. (1979) X-ray diffraction study of the structure of small- and large-angle [001] tilt boundaries in gold, Philosophical Magazine A, **39**, 293–315.

[25] Mishin YM, Mehl M, Papaconstantopoulos D, Voter AF, and Kress J. (2001) Structural stability and lattice defects in copper: Ab initio, tight-binding, and embedded-atom calculations, Physical Review B, **63**, 224106.

[26] Williamson GK and Hall WH. (1953) X-ray line broadening from filed aluminium and wolfram, Acta Metallurgica, **1**, 22–31.

[27] Wojdyr M. (2010) Fityk : a general-purpose peak fitting program, Journal of Applied Crystallography, **43**, 1126–1128.

[28] Simões S, Calinas R, Vieira MT, Vieira MF, and Ferreira PJ. (2010) In situ TEM study of grain growth in nanocrystalline copper thin films., Nanotechnology, **21**, 145701.

[29] Sen FG, Qi Y, van Duin ACT, and Alpas AT. (2013) Oxidation induced softening in Al nanowires, Applied Physics Letters, **102**, 051912.

[30] Kelchner CL, Plimpton SJ, and Hamilton JC. (1998) Dislocation nucleation and defect structure during surface indentation, Physical Review B, **58**, 11085–11088.

[31] Tsuzuki H, Branicio PS, and Rino JP. (2007) Structural characterization of deformed crystals by analysis of common atomic neighborhood, Computer Physics Communications, **177**, 518–523.

[32] Ishizawa N, Miyata T, Minato I, Marumo F, and Iwai S. (1979) A structural investigation of α-Al203 at 2170K, Acta Crystallographica Section B, **36**, 228–230.

[33] Verwey EJW. (1935) The structure of the electrolytic oxide layer on aluminium, Zeitschrift für Kristallographie, **91**, 317–320.

[34] Sutton AP and Balluffi RW. (1995) Interfaces in Crystalline Materials, in: Monogr. Phys. Chem. Mater. Vol. 51. Oxford and New York: Claredon Press.

[35] Chou TC and Nieh TG. (1992) Interface-controlled phase transformaiton and abnormal grian growth of α-Al2O3 in thin γ-alumina films, Thin Solid Films, **221**, 89–97.

Appendix 5.1

College of Engineering
Department of Mechanical Engineering
(479) 575-3153
(479) 575-6982 (FAX)

UNIVERSITY OF ARKANSAS

Mechanical Engineering Building
Fayetteville, Arkansas 72701

Coleman, S.P., Sichani, M.M., Spearot, D.E. (2014) A computational algorithm to produce virtual x-ray and electron diffraction patterns from atomistic simulations, JOM, 66, 408-416.

I certify that Mr. Shawn Coleman is the first author of the paper and completed greater than 51% of the work in this publication. This work was an invited submission in collaboration with Ph.D. candidate Mehrdad M. Sichani at the University of Arkansas.

Sincerely,

Douglas E. Spearot, Ph.D.
Dissertation Director
Associate Professor and 21st Century Professorship
Department of Mechanical Engineering
University of Arkansas
Fayetteville, AR 72701
Office: 479-575-3040
E-mail: dspearot@uark.edu

Appendix 5.2

SPRINGER LICENSE
TERMS AND CONDITIONS

Apr 29, 2014

This is a License Agreement between Shawn P Coleman ("You") and Springer ("Springer") provided by Copyright Clearance Center ("CCC"). The license consists of your order details, the terms and conditions provided by Springer, and the payment terms and conditions.

All payments must be made in full to CCC. For payment instructions, please see information listed at the bottom of this form.

License Number	3378430602680
License date	Apr 29, 2014
Licensed content publisher	Springer
Licensed content publication	JOM Journal of the Minerals, Metals and Materials Society
Licensed content title	A Computational Algorithm to Produce Virtual X-ray and Electron Diffraction Patterns from Atomistic Simulations
Licensed content author	Shawn P. Coleman
Licensed content date	Jan 1, 2013
Volume number	66
Issue number	3
Type of Use	Thesis/Dissertation
Portion	Full text
Number of copies	1
Author of this Springer article	Yes and you are the sole author of the new work
Order reference number	None
Title of your thesis / dissertation	Atomistic Simulation and Virtual Diffraction Characterization of Alumina Interfaces: Evaluating Structure and Stability for Predictive Physical Vapor Deposition Models
Expected completion date	Aug 2014
Estimated size(pages)	200
Total	0.00 USD

Terms and Conditions

Introduction

The publisher for this copyrighted material is Springer Science + Business Media. By clicking "accept" in connection with completing this licensing transaction, you agree that the following terms and conditions apply to this transaction (along with the Billing and

Payment terms and conditions established by Copyright Clearance Center, Inc. ("CCC"), at the time that you opened your Rightslink account and that are available at any time at http://myaccount.copyright.com).

Limited License

With reference to your request to reprint in your thesis material on which Springer Science and Business Media control the copyright, permission is granted, free of charge, for the use indicated in your enquiry.

Licenses are for one-time use only with a maximum distribution equal to the number that you identified in the licensing process.

This License includes use in an electronic form, provided its password protected or on the university's intranet or repository, including UMI (according to the definition at the Sherpa website: http://www.sherpa.ac.uk/romeo/). For any other electronic use, please contact Springer at (permissions.dordrecht@springer.com or permissions.heidelberg@springer.com).

The material can only be used for the purpose of defending your thesis limited to university-use only. If the thesis is going to be published, permission needs to be re-obtained (selecting "book/textbook" as the type of use).

Although Springer holds copyright to the material and is entitled to negotiate on rights, this license is only valid, subject to a courtesy information to the author (address is given with the article/chapter) and provided it concerns original material which does not carry references to other sources (if material in question appears with credit to another source, authorization from that source is required as well).

Permission free of charge on this occasion does not prejudice any rights we might have to charge for reproduction of our copyrighted material in the future.

Altering/Modifying Material: Not Permitted

You may not alter or modify the material in any manner. Abbreviations, additions, deletions and/or any other alterations shall be made only with prior written authorization of the author(s) and/or Springer Science + Business Media. (Please contact Springer at (permissions.dordrecht@springer.com or permissions.heidelberg@springer.com)

Reservation of Rights

Springer Science + Business Media reserves all rights not specifically granted in the combination of (i) the license details provided by you and accepted in the course of this licensing transaction, (ii) these terms and conditions and (iii) CCC's Billing and Payment terms and conditions.

Copyright Notice:Disclaimer

You must include the following copyright and permission notice in connection with any reproduction of the licensed material: "Springer and the original publisher /journal title, volume, year of publication, page, chapter/article title, name(s) of author(s), figure number(s), original copyright notice) is given to the publication in which the material was originally published, by adding; with kind permission from Springer Science and Business Media"

Warranties: None

Example 1: Springer Science + Business Media makes no representations or warranties with respect to the licensed material.

Example 2: Springer Science + Business Media makes no representations or warranties with respect to the licensed material and adopts on its own behalf the limitations and disclaimers established by CCC on its behalf in its Billing and Payment terms and conditions for this licensing transaction.

Indemnity

You hereby indemnify and agree to hold harmless Springer Science + Business Media and CCC, and their respective officers, directors, employees and agents, from and against any and all claims arising out of your use of the licensed material other than as specifically authorized pursuant to this license.

No Transfer of License

This license is personal to you and may not be sublicensed, assigned, or transferred by you to any other person without Springer Science + Business Media's written permission.

No Amendment Except in Writing

This license may not be amended except in a writing signed by both parties (or, in the case of Springer Science + Business Media, by CCC on Springer Science + Business Media's behalf).

Objection to Contrary Terms

Springer Science + Business Media hereby objects to any terms contained in any purchase order, acknowledgment, check endorsement or other writing prepared by you, which terms are inconsistent with these terms and conditions or CCC's Billing and Payment terms and conditions. These terms and conditions, together with CCC's Billing and Payment terms and conditions (which are incorporated herein), comprise the entire agreement between you and Springer Science + Business Media (and CCC) concerning this licensing transaction. In the event of any conflict between your obligations established by these terms and

conditions and those established by CCC's Billing and Payment terms and conditions, these terms and conditions shall control.

Jurisdiction

All disputes that may arise in connection with this present License, or the breach thereof, shall be settled exclusively by arbitration, to be held in The Netherlands, in accordance with Dutch law, and to be conducted under the Rules of the 'Netherlands Arbitrage Instituut' (Netherlands Institute of Arbitration).***OR:***

All disputes that may arise in connection with this present License, or the breach thereof, shall be settled exclusively by arbitration, to be held in the Federal Republic of Germany, in accordance with German law.

Other terms and conditions:

v1.3

If you would like to pay for this license now, please remit this license along with your payment made payable to "COPYRIGHT CLEARANCE CENTER" otherwise you will be invoiced within 48 hours of the license date. Payment should be in the form of a check or money order referencing your account number and this invoice number 501290678. Once you receive your invoice for this order, you may pay your invoice by credit card. Please follow instructions provided at that time.

Make Payment To:
Copyright Clearance Center
Dept 001
P.O. Box 843006
Boston, MA 02284-3006

For suggestions or comments regarding this order, contact RightsLink Customer Support:customercare@copyright.com or +1-877-622-5543 (toll free in the US) or +1-978-646-2777.

Gratis licenses (referencing $0 in the Total field) are free. Please retain this printable license for your reference. No payment is required.

Chapter 6: Performance Improvement and Workflow Development of Virtual Diffraction Calculations

Shawn P. Coleman[a], Yang Wang[b], Sudhakar Pamidighantam[c],

Lars Koesterke[d], Mark Van Moer[c], and Douglas E. Spearot[a]

[a] Department of Mechanical Engineering, University of Arkansas, Fayetteville, AR 72701

[b] Pittsburg Supercomputing Center Pittsburgh, PA 15213

[c] National Center for Supercomputing Applications, Urbana, IL 61801

[d] Texas Advanced Computing Center Austin, TX 78758

Abstract

Electron and x-ray diffraction are well-established experimental methods used to explore the atomic scale structure of materials. In this work, a computational algorithm is presented to produce electron and x-ray diffraction patterns directly from atomistic simulation data. This algorithm advances beyond previous virtual diffraction methods by utilizing an ultra high-resolution mesh of reciprocal space which eliminates the need for *a priori* knowledge of the material structure. This paper focuses on (1) algorithmic advances necessary to improve performance, memory efficiency and scalability of the virtual diffraction calculation, and (2) the integration of the diffraction algorithm into a workflow across heterogeneous computing hardware for the purposes of integrating simulations, virtual diffraction calculations and visualization of electron and x-ray diffraction patterns.

1.1 Introduction

Diffraction is a common experimental method used to study the atomic scale structure of a material [1]. In x-ray diffraction, for example, a sample is exposed to a beam of monochromatic x-rays with a wavelength on the same order as the spacing between atomic planes in the sample. X-rays scatter upon interacting with the atoms in the sample and the constructive interference of the scattered x-rays is collected and analyzed to determine the crystal structure and lattice constants of the material. Similarly, a beam of electrons can be used within a transmission electron microscope (TEM) to produce a selected area electron diffraction (SAED) pattern. Both x-ray and electron diffraction can be used to study lattice distortion due to defects within crystalline solids (cf. [2,3]).

Calculations of diffraction patterns based on kinematic diffraction theory were first developed in the 1980s to characterize atomistic simulations of large-angle symmetric twist grain boundaries [4–6]. In kinematic models, the diffraction intensity, I, is computed for N atoms as the product of the structure factor, $F(\mathbf{K})$, with its complex conjugate, $F^*(\mathbf{K})$,

$$I(\mathbf{K}) = F^*(\mathbf{K})F(\mathbf{K}) \tag{6.1}$$

where

$$F(\mathbf{K}) = \sum_{j=1}^{N} f_j \exp\left(2\pi i\, \mathbf{K}\cdot\mathbf{r}_j\right) \quad . \tag{6.2}$$

Here, $\mathbf{K}$ is the location of the diffraction peak in reciprocal space, $\mathbf{r}_j$ is the position of the atom in real space, and f_j is the atomic scattering factor. In [4–6], computational limitations inherent to the time restricted both the number of atoms in the calculation and the range of reciprocal space explored. To improve computational efficiency, diffraction intensities were computed over a limited region of reciprocal space known to be important based on *a priori* knowledge of

the grain boundary unit cell. Using these techniques, Bristowe and Sass [4] showed that small displacements of the atoms within the grain boundary unit cell can create identifiable changes to the diffraction patterns. This breakthrough motivated researchers [4–8] to incorporate virtual diffraction patterns in their subsequent studies to verify predicted grain boundary structures.

In the mid 2000s, a second method to compute diffraction patterns that utilized assumptions based on powder diffraction conditions became popular among researchers modeling nanocrystalline materials [9–14]. These researchers used formulations of the Debye scattering equation to compute diffraction intensity based on the interatomic distance between atoms, r_{ij}, via [1],

$$I(k) = \sum_{i=1}^{N} \sum_{j=1}^{N} f_i f_j \frac{\sin(2\pi k r_{ij})}{2\pi k r_{ij}}. \tag{6.3}$$

Here, $k = 2\sin(\theta)/\lambda$ represents a spherically averaged position in reciprocal space that is related to the diffraction angle, θ, and monochromatic radiation of wavelength, λ. By spherically averaging the positions in reciprocal space, all orientations of the simulated crystals are mathematically represented mimicking the random distribution associated with powder diffraction. Using this relationship, researchers [9–14] constructed x-ray diffraction line profiles to investigate peak shift and peak broadening in order to extract data on the mean grain size and lattice strain in nanocrystalline models with different grain diameters.

The virtual diffraction algorithm in this work advances beyond these previous methods to create both SAED and x-ray diffraction line profiles using the same algorithm without any *a priori* knowledge of the crystal structure. The algorithm is sufficiently generic for all atomic species and is integrated into the LAMMPS atomistic simulation package [15] as a user-defined compute; it can also be implemented into other atomistic simulation packages. Following a

concise discussion of the computational algorithm, this article presents advancements made to increase performance and scalability, and the integration of this algorithm into a workflow across heterogeneous computing hardware including visualization. A complete discussion of the virtual diffraction algorithm is provided in [16,17] along with application of this method to study grain boundary structure, nanocrystalline materials and interfaces between complex solids.

1.2 Virtual Diffraction Method

1.2.1 Diffraction Intensity

The diffraction algorithm generates a high-resolution, three-dimensional mesh of points filling a volume of reciprocal space constructed using the entire domain of the atomistic simulation cell. Each point on the reciprocal space mesh is associated with a reciprocal lattice vector $\mathbf{K}$ describing the deviation between the diffracted and incident wave vectors $\mathbf{k_D}$ and $\mathbf{k_I}$ [1],

$$\mathbf{K} = \mathbf{k_D} - \mathbf{k_I} \quad . \tag{6.4}$$

The mesh of reciprocal space points is built on a rectilinear grid with resolution defined by the user [16,17].By constructing a high-resolution reciprocal space mesh, strong intensity peaks associated with the constructive interference between the incoming x-ray or electron beam and the crystal lattice are intuitively captured without *a priori* knowledge of the crystal structure of the material. The interplanar distances d_{hkl} associated with each reflection can be computed at each reciprocal lattice point utilizing the geometric relationships described by Bragg's Law [1],

$$\frac{2\sin(\theta)}{\lambda} = \frac{1}{d_{\mathrm{hkl}}} = |\mathbf{K}| \quad . \tag{6.5}$$

The diffraction intensity at each reciprocal lattice point is computed using the structure factor equation, Eq. (6.1), with the modifications described below to differentiate between electron and x-ray diffraction. In the diffraction algorithm, atomic scattering factors are explicitly computed for each atomic species to account for the reduction in diffracted intensity from an individual atom due to Compton scattering [18]. Specifically, at each diffraction angle, the atomic scattering factors are computed using analytical approximations parameterized for each atomic species. For electron diffraction, the analytical approximation of the atomic scattering factor is taken as the summation of five Gaussian functions of the form [19],

$$f_j\left(\frac{\sin\theta}{\lambda}\right) = \sum_i^5 a_i \exp\left(-b_i \frac{\sin^2\theta}{\lambda^2}\right) \quad , \tag{6.6}$$

which have been parameterized for the majority of neutral elements by Peng et al. [20]. For x-ray diffraction, the analytical approximation of the atomic scattering factor is the summation of four Gaussian functions plus a constant of the form [21],

$$f_j\left(\frac{\sin\theta}{\lambda}\right) = \sum_i^4 a_i \exp\left(-b_i \frac{\sin^2\theta}{\lambda^2}\right) + c \quad , \tag{6.7}$$

which have been parameterized by Fox et al. [22] for most atom species. In addition, to compute x-ray diffraction intensities, the Lorentz-polarization factor, $\mathrm{Lp}(\theta)$, is applied to account for the relative distribution of the reciprocal lattice points and the change in scatter intensity when using non-polarized incident radiation. The Lorentz-polarization factor is computed via [18],

$$\mathrm{Lp}(\theta) = \frac{1+\cos^2(2\theta)}{\cos(\theta)\sin^2(\theta)} \quad . \tag{6.8}$$

1.2.2 Diffraction Pattern Generation

X-ray diffraction line profiles are created by virtually rotating the Ewald sphere around the

origin of reciprocal space to all possible orientations, mimicking powder diffraction conditions [18]. By making all diffraction orientations equally probable, every reciprocal space point will intersect the surface of the Ewald sphere. Line profiles are constructed by collecting reciprocal space points into bins corresponding to their scattering angle, using Eq. (6.5), and summing the intensity data within each bin. The scattering angle bin size is optimized through trials to reduce the noise within the line profile while maximizing peak features. For example, Figure 6.1 shows the calculated powder diffraction line profile for bulk α-alumina with comparison to experimental data [23].

Virtual SAED patterns are created by examining the region in reciprocal space intersecting the Ewald sphere of radius $1/\lambda$. For a particular zone axis, the Ewald sphere is centered at the tail of the associated incident wave vector and intersects the origin of reciprocal space. To construct the electron diffraction pattern, a hemispherical slice of the reciprocal space mesh lying on the surface of the Ewald sphere is isolated and viewed along the zone axis. Using VisIt [24], intensity values are interpolated between points on the reciprocal space mesh allowing the slice to take on no thickness while maintaining a continuous intensity field along the hemisphere. For

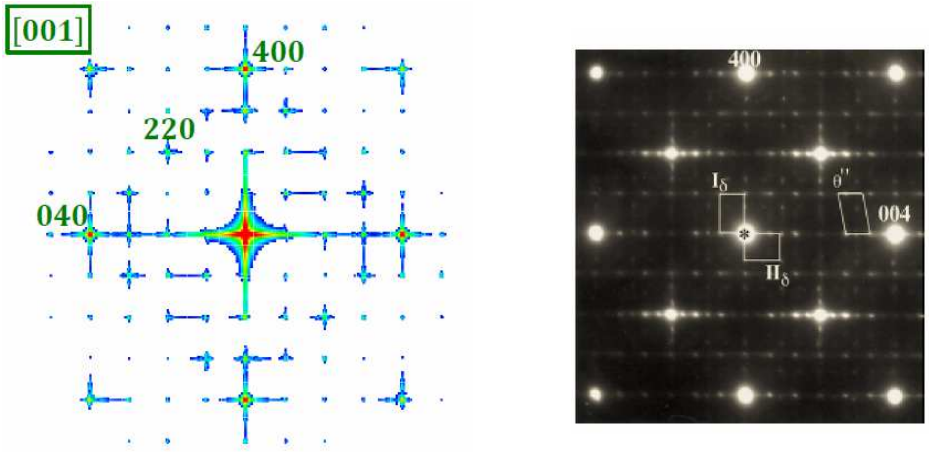

Figure 6.1: Calculated selected area electron diffraction pattern for the γ-alumina surface with comparison to experiment [25].

example, Figure 6.2 shows the calculated SAED pattern for a (001) γ-alumina surface with comparison to experimental data [25]. To enhance features within the diffraction pattern, the sampled reciprocal space nodes are colored by intensity on a $\log_{10}$ scale. To achieve higher computational efficiency when creating SAED patterns for a user-specified zone axis, the diffraction algorithm can be augmented to limit the intensity calculation to only those reciprocal space mesh points that lie near the surface of the Ewald sphere.

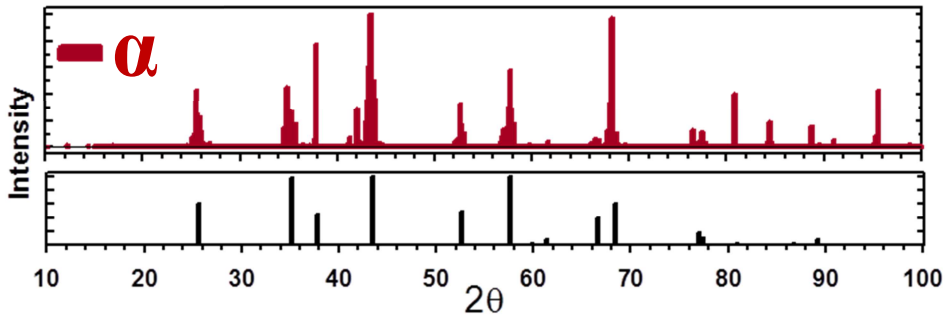

Figure 6.2: Calculated powder diffraction pattern of α-alumina with comparison to experiment [23].

1.3 Algorithm Scalability

1.3.1 Initial Scalability

The performance and scalability of the diffraction calculation was documented to provide benchmark data prior to the partnership with XSEDE Extended Collaborative User Services (ECSS). Benchmark diffraction computations were completed on the Texas Advance Computing Center (TACC) Stampede system, which is configured with compute nodes that host two 8-core Xeon E5-2680 processors and one Intel Xeon Phi SE10P coprocessor (MIC). The compute nodes are outfitted with 32 GB of memory (2GB/core) which is separate from the 8 GB of memory on the Xeon Phi coprocessor. The benchmark simulation contains 256,000 bulk Ni atoms and explores 9,006,316 reciprocal space nodes during a single x-ray diffraction computation of the static structure. The benchmark simulation is run within the LAMMPS

atomistic simulation package. The output of the compute is an x-ray diffraction line profile for Ni with 2θ ranging from 10° to 90°. Timing data and memory usage are extracted directly from primary x-ray diffraction compute to avoid any overlaying functionalities within LAMMPS.

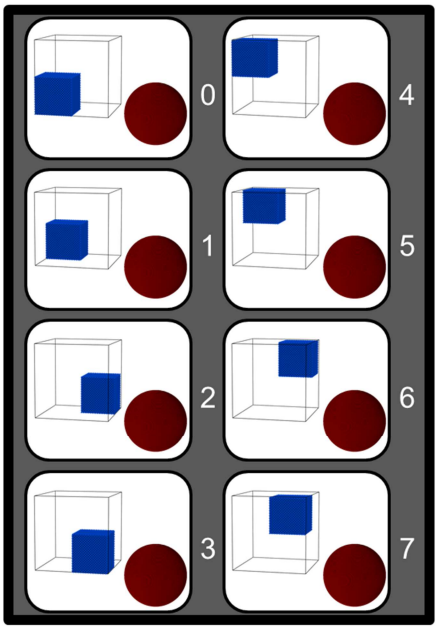

Figure 6.3: Schematic of the MPI parallelization technique in the initial diffraction code. The blue cube represents the atomistic simulation while the red sphere represents the reciprocal space nodes sampled in the diffraction calculation.

Initially, the code was parallelized via the native message passing interface (MPI) parallelization within the LAMMPS atomistic simulation package, which performs a spatial decomposition of the atoms in a simulation, illustrated in Figure 6.3. The benchmark simulations were used to determine the speedup and efficiency of the diffraction calculation over 1,2,4,8, and 16 nodes. Results of the initial scalability tests are shown in Table 6.1. The speedup values are determined by comparing the absolute time for the computation using multiple nodes, compared to the computation time run using one 16-core node. Efficiency is computed by comparing the computation core-time to the reference core-time using one 16-core node. The

results of the initial implementation of the code (prior to ECSS) show a 13.23 speedup with an efficiency reduction to 83% when scaled to 256 cores. The reduction in efficiency is primarily due to the finite number of atoms to parallelize over within the strong scaling study. An identified weakness of the initial implementation of the virtual diffraction code is its memory footprint. The initial code requires that both the locations of the atoms and the locations of the reciprocal space nodes are kept in memory throughout the entire calculation. More importantly, a copy of all these locations must be accessible to each MPI process. Therefore, as the simulation size and resolution of reciprocal space increases, the memory required to complete the calculation dramatically increases. For example, the modest size benchmark simulation requires 9.7 GB of the available 32 GB of memory per node to compute a single x-ray diffraction line profile.

Table 6.1: Initial scalability testing showing speedup, efficiency, and total memory usage.

Nodes	Cores	Speedup	Efficiency	Memory (GB)
1	16	1.00	100%	9.67
2	32	1.91	96%	19.34
4	64	3.65	91%	38.67
8	128	6.70	84%	77.35
16	256	13.23	83%	154.70

1.3.2 Scalability Improvements

Both speedup and efficiency of the diffraction calculation are improved through ECSS collaboration, resulting in a second generation of the code which has improved memory utilization and incorporated a second level of OpenMP parallelization shown schematically in Figure 6.4. Further, a third generation of the diffraction code is developed via ECSS collaboration to take advantage of offloading tasks to the available MIC coprocessors on Stampede. Speedup values for each generation of the diffraction code are evaluated using the

same benchmark simulation as in Section 6.3.1. The speedup value is computed from the absolute time of computation using the new code on multiple nodes as compared to the computation time run using the initial code on one 16-core node. Thus, speedup values are directly comparable across the different generations of the diffraction code. Differently, efficiency values are computed for each specific code generation and utilization of MPI/OpenMP. Results from the new scalability tests are shown in Table 6.2.

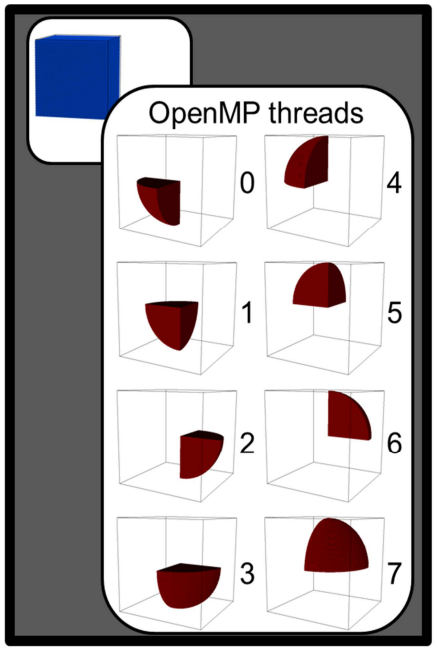

Figure 6.4: Schematic of the OpenMP parallelization technique of the reciprocal space nodes sampled in the diffraction calculation.

In the second generation of the virtual diffraction code, the MPI and OpenMP-based parallelization show speedup of 1.69 and 1.78, respectively, due to a reorganization of data structures and incorporation of more efficient calculations. MPI-based parallelization shows a similar efficiency drop (82% using 256 cores) as the initial code due to the strong scaling effects. To mitigate this effect, OpenMP threads are added to parallelize over the reciprocal lattice

points. As shown in Table 6.2, the efficiency of the OpenMP parallelized second generation code is less affected by the finite number of atoms due to its second level of parallelism over the reciprocal lattice nodes (95% using 256 cores). The MIC enabled third generation code shows approximately 2x speedup from the second generation code by offloading a section of computation to the MIC. The reported values are taken when 90% of the reciprocal lattices nodes are offloaded to the MIC to be used in the solution of the structure factor equation. The remaining 10% of the reciprocal lattice nodes are utilized within concurrent computations on the CPU.

Table 6.2: Scalability tests of the second and third generation diffraction code showing speedup compared to the original 16-core timing, efficiency relative to code generation and utilization of MPI/OpenMP, and total memory usage.

Nodes - MPI/OpenMP/MIC	**Speedup**	**Efficiency**	**CPU Memory (GB)**
Second Generation			
1 - 16/0/0	1.69	100%	8.1
2 - 32/0/0	3.21	95%	16.1
4 - 64/0/0	6.16	91%	32.2
8 - 128/0/0	11.71	86%	64.4
16 - 256/0/0	22.17	82%	128.9
1 - 1/16/0	1.78	100%	0.51
2 - 2/16/0	3.56	100%	1.01
4 - 4/16/0	7.12	100%	2.02
8 - 8/16/0	14.16	99%	4.05
16 - 16/16/0	26.94	95%	8.10
Third Generation (MIC – Enabled)			
1 - 1/16/240	4.61	100%	0.51
2 - 2/16/240	9.19	100%	1.01
4 - 4/16/240	17.43	95%	2.02
8 - 8/16/240	34.65	94%	4.05
16 - 16/16/240	60.93	83%	8.10
1 - 16/0/240	4.37	100%	8.1
2 - 32/0/240	8.38	96%	16.1
4 - 64/0/240	15.94	91%	32.2
8 - 128/0/240	29.51	84%	64.4
16 - 256/0/240	49.32	70%	128.9

1.4 Workflow Implementation and Visualization

1.4.1 SEAGrid Lammps_DS Workflow

The coupled execution of LAMMPS molecular dynamics followed by the simulation of x-ray diffraction or selected area electron diffraction calculations of the appropriately averaged system of interest and consequent visualization of the diffraction patterns required setting up of a workflow. The need for a workflow is particularly significant when multiple platforms for computing and visualization are to be used to address the large memory VSMP implementation of the visualization software required in the final step. The workflow problem is tackled by using an existing XSEDE SEAGrid science gateway, that supported the LAMMPS application and the corresponding tools to achieve the remote job submission, but in this case using a remote workflow submission and managing the data such that a single jobID handle can provide all the data at the end of the multi-resource computations. Additionally, a script-based high-throughput submission of multiple jobs is implemented in SEAGrid client, as shown in Figure 6.5. This uses an XML script with tags to specify job requirements and input files as needed and the system is equipped to execute each of the jobs specified as independent jobs. This is particularly useful for parameter sweep type runs and may benefit other communities that use the SEAGrid gateway as well.

The workflow implemented consists of coupled execution of three main tasks: Lammps_MD followed by Lammps_XRD, Lammps_SAED and a set of parallel VisIt executions as depicted in the schematic in the Figure 6.6. Initial implementations of the workflow used the same compute resource or a closely coupled resource at the same host site (such as Stampede and Ranch). A complete implementation involves execution of initial Lammps_MD at TACC's Stampede system and the latter two tasks in SDSC's Gordon system. The large memory

available for the Gordon system was critical for the second stage of the workflow and it is useful in distributing the computing and visualization tasks. This also facilitates interactive access to the VisIt service deployed on Gordon in the future.

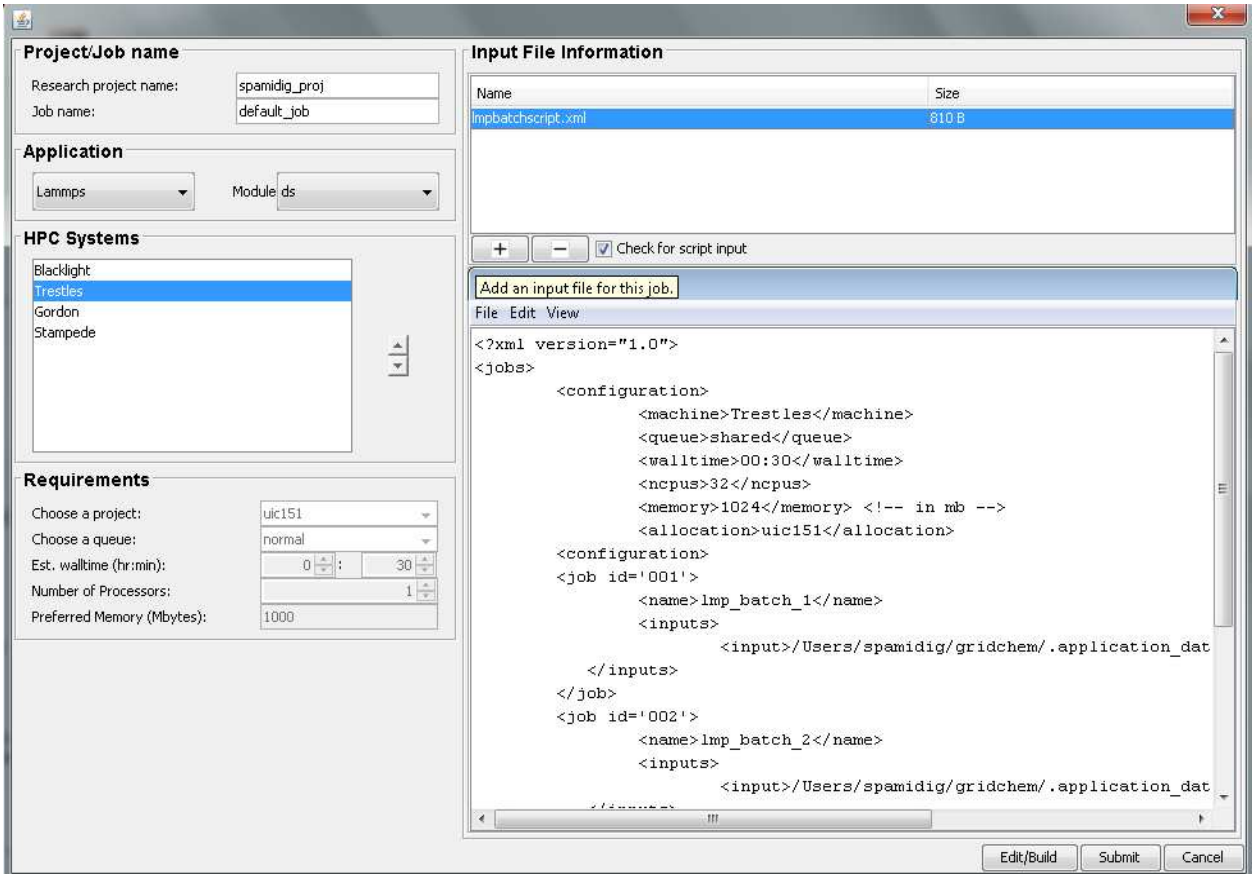

Figure 6.5: Job set up panel in DESSERT client with multi-job submission script.

The workflow execution required additional inputs to drive the latter tasks and the original LAMMPS input was modified with a remark line for this purpose. The initial LAMMPS execution ignores this line in the input while the same is parsed and the queue instructions are set using this data for the subsequent steps. SEAGrid uses GSISSH based execution of a local script for the execution of a job task at a remote HPC site (for details of SEAGrid operation please refer to [26]and [27]). The LAMMPS specific portion of the script is modified to include the

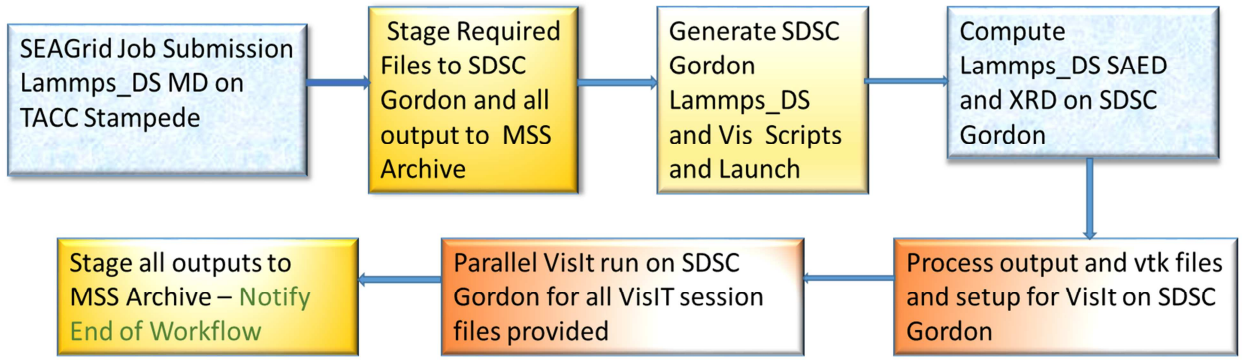

Figure 6.6: Schematic workflow depicting the tasks orchestrated from GridChem client of SEAGrid Science Gateway.

execution of the workflow transparently during this ECSS project. SEAGrid supported publicly released LAMMPS already, but a special module named DS (Doug Spearot's version) is implemented and currently restricted to the developer group to accommodate the special workflow version. The initial job is launched with the modified input on the Stampede system as a standard SEAGrid job. The Stampede job in turn prepares the inputs and provides the data required for the Lammps_XRD (and Lammps_SAED) and the VisIt components for the second stage. The script verifies the normal termination of the first stage, moves all the data and inputs for the subsequent jobs to the SDSC Gordon system and launches the jobs in Gordon. The path hierarchy is consistently managed and all the results are archived at the end of each stage into the mass storage device in SEAGrid organization. The entire workflow is tracked as a single job and all the corresponding result files can be retrieved based on the job handle through MyCCG job monitoring function in the client. The files retrieved can be further processed using the post processing tools available in the GridChem client. Though SEAGrid integrated the Apache Airavata based XBaya workflow execution system [28] which is described in detail in [27] for Paramchem project, this explicit implementation is chosen as the Gordon system did not support the Gram based orchestration of workflow available in XBaya. Currently, we are exploring the

Unicore [29] based orchestration of tasks on Gordon system through Airavata/Xbaya system.

1.4.2 Visualization

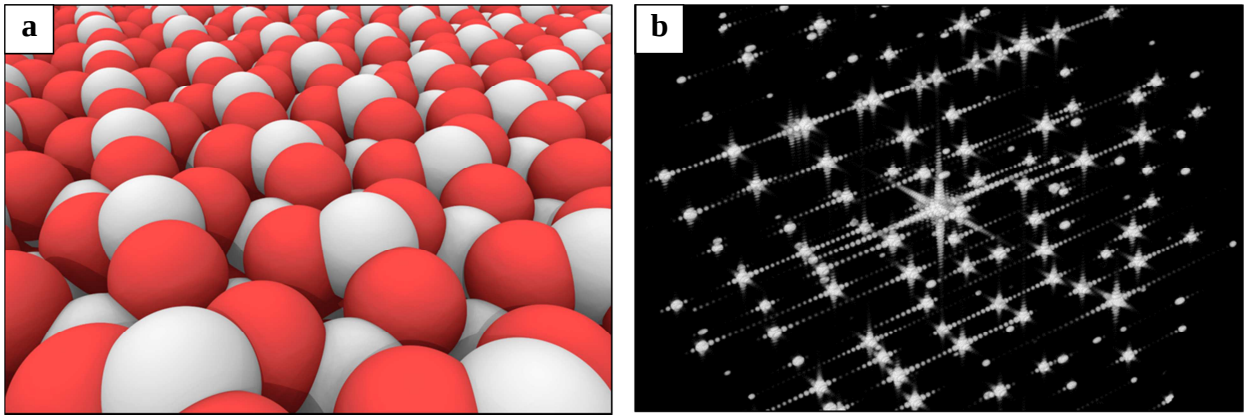

Figure 6.7: Visualization of the (a) Van der Waals model of an α-alumina surface using Ovito and (b) the 3D reciprocal space map of the calculated electron diffraction pattern of an α-alumina surface. Aluminum atoms are shaded white and oxygen atoms are shaded red in (a).

Visualization uses the VisIt program and utilizes either a session-less protocol or a set of session files supplied along with the LAMMPS input by the user. The session files are staged to the appropriate computer resource and used in the final task. A rendering python script drives the VisIt computation in a parallel batch job for each of the vtk files generated during the processing of the diffraction patterns that are provided as LAMMPS dump files in the Lammps_XRD compute step. The VisIt runs result in the images outputted in .png format. The visualization of the images from the simulation can be launched from the GridChem client automatically and an example set for an alumina surface is shown in Figure 6.7. Alternatively if the visualization programs are locally installed, such as Ovito used to generate Figure 6.7(a), appropriate files can be exported to these applications from the GridChem post processing tool.

1.5 Summary

In this work, a computational algorithm is presented to produce electron and x-ray diffraction

patterns directly from atomistic simulation data. First, through XSEDE ECSS support, the scalability and performance of the virtual diffraction algorithm has been considerably improved. The diffraction algorithm parallelization has been enhanced to support offloading to the MIC coprocessor on Stampede. Second, through XSEDE ECSS support, the virtual diffraction algorithm has been integrated into a workflow platform that allows for job submission across heterogeneous computing hardware at different sites within the XSEDE network. Specifically, atomistic simulations using LAMMPS, diffraction calculations using LAMMPS and visualization using VisIt are coupled in the workflow using the SEAGrid Science gateway. Ultimately, the diffraction algorithm provides a novel bridge between experiments and computation and will be of significant use to both communities to study the atomic-level structure of materials.

Acknowledgements

The authors acknowledge support of the National Science Foundation under grant #0954505. Additional support is provided by the 21st Century Professorship in Mechanical Engineering at the University of Arkansas. This work utilized the Extreme Science and Engineering Discovery Environment (XSEDE), which is supported by National Science Foundation grant #OCI-1053575. Consultant support was made possible through the XSEDE Extended Collaborative Support Services (ECSS) program. Beneficial discussions concerning FFT implementation with XSEDE Campus Champion Fellow Luis Cueva-Parra of Auburn University Montgomery are appreciated.

References

[1] Williams DB and Carter CB. (2009) Transmission Electron Microscopy, second ed. New York: Springer.

[2] Ungár T and Borbély A. (1996) The effect of dislocation contrast on x-ray line broadening: A new approach to line profile analysis, Applied Physics Letters, **69**, 3173.

[3] Meyer KE, Felcher GP, Sinha SK, and Schuller IK. (1981) Models of diffraction from layered ultrathin coherent structures, Journal of Applied Physics, **52**, 6608–6610.

[4] Bristowe PD and Sass SL. (1980) The atomic structure of a large angle [001] twist boundary in gold determined by a joint computer modelling and X-ray diffraction study, Acta Metallurgica, **28**, 575–588.

[5] Budai J, Bristowe PD, and Sass SL. (1983) The projected atomic structure of a large angle [001] Σ= 5 (θ=36. 9°) twist boundary in gold: Diffraction analysis and theoretical predictions, Acta Metallurgica, **31**, 699–712.

[6] Bristowe PD and Balluffi RW. (1984) Effect of secondary relaxations on diffraction from high-Σ [001] twist boundaries, Surface Science, **144**, 14–27.

[7] Oh Y and Vitek V. (1986) Structural multiplicity of Σ=5(001) twist boundaries and interprtation of x-ray diffraction from these boundaries, Acta Metallurgica, **34**, 1941–1953.

[8] Fitzsimmons MR and Sass SL. (1988) Quantitative x-ray diffraction study of the atomic structure of the Σ=5 (θ=36.9°) [001] twist boundary in gold, Acta Metallurgica, **36**, 3103–3122.

[9] Brandstetter S, Derlet PM, Van Petegem S, and Van Swygenhoven H. (2008) Williamson–Hall anisotropy in nanocrystalline metals: X-ray diffraction experiments and atomistic simulations, Acta Materialia, **56**, 165–176.

[10] Stukowski A, Markmann J, Weissmüller J, and Albe K. (2009) Atomistic origin of microstrain broadening in diffraction data of nanocrystalline solids, Acta Materialia, **57**, 1648–1654.

[11] Markmann J, Yamakov V, and Weissmüller J. (2008) Validating grain size analysis from X-ray line broadening: A virtual experiment, Scripta Materialia, **59**, 15–18.

[12] Markmann J, Bachurin D, Shao L, Gumbsch P, and Weissmüller J. (2010) Microstrain in nanocrystalline solids under load by virtual diffraction, EPL (Europhysics Letters), **89**, 66002.

[13] Derlet PM, Van Petegem S, and Van Swygenhoven H. (2005) Calculation of x-ray spectra for nanocrystalline materials, Physical Review B, **71**, 1–8.

[14] Van Swygenhoven H, Budrovie Ž, Derlet PM, Froseth AG, and Van Petegem S. (2005) In situ diffraction profile analysis during tensile deformation motivated by molecular dynamics, Materials Science and Engineering: A, **400**, 329–333.

[15] LAMMPS. (2014) Http://lammps.sandia.gov.

[16] Coleman SP, Spearot DE, and Capolungo L. (2013) Virtual diffraction analysis of Ni [0 1 0] symmetric tilt grain boundaries, Modelling and Simulation in Materials Science and Engineering, **21**, 055020.

[17] Coleman SP, Sichani MM, and Spearot DE. (2014) A computational algorithm to produce virtual x-ray and electron diffraction patterns of interfaces from atomistic simulations, JOM, **66**, 408–416.

[18] Warren BE. (1990) X-Ray Diffraction, first ed. New York: Dover Publications.

[19] Colliex C, Cowley JM, Dudarev SL, Fink M, Gjønnes K, Hilderbrandt R, Howie A, Lynch DF, Peng L-M, Ren G, Ross AW, Smith VH, Spence JCH, Steeds J, Wang J, Whelan MJ, and Zvyagin BB. (2004) Electron Diffraction, in: Prince E (Ed.). Int. Tables Crystallogr. Vol. C Math. Phys. Chem. Tables, third ed. Norwell, MA: Kluwer Academic Publishers.

[20] Peng L-M, Ren G, Dudarev SL, and Whelan MJ. (1996) Robust Parameterization of Elastic and Absorptive Electron Atomic Scattering Factors, Acta Crystallographica Section A, **52**, 257–276.

[21] Brown PJ, Fox AG, Maslen EN, O'Keefe MA, and Willis BTM. (2004) Intensity of Diffraction Intensities, in: Prince E (Ed.). Int. Tables Crystallogr. Vol. C Math. Phys. Chem. Tables, third ed. Norwell, MA: Kluwer Academic Publishers.

[22] Fox AG, O'Keefe MA, and Tabbernor MA. (1989) Relativistic Hartree–Fock X-ray and electron atomic scattering factors at high angles, Acta Crystallographica Section A, **45**, 786–793.

[23] Ishizawa N, Miyata T, Minato I, Marumo F, and Iwai S. (1979) A structural investigation of α-Al203 at 2170K, Acta Crystallographica Section B, **36**, 228–230.

[24] VisIt. (2014) Https://wci.llnl.gov/codes/visit/.

[25] Levin I and Brandon DG. (1998) Metastable alumina polymorphs: Crystal structures and transition sequences, Journal of the American Ceramic Society, **81**, 1995–2012.

[26] Dooley R, Milfeld K, Guiang C, Pamidighantam S, and Allen G. (2006) From Proposal to Production: Lessons Learned Developing the Computational Chemistry Grid

Cyberinfrastructure, Journal of Grid Computing, **4**, 195–208.

[27] Shen N, Y. F, and Pamidighantam S. (2014) E-science infrastructures for molecular modeling and parameterization, Journal of Computer Science, In Press.

[28] Marru S, Herath C, Tangchaisin P, Pierce M, Mattmann C, Singh R, Gunarathne T, Chinthaka E, Gardler R, Slominski A, Douma A, Perera S, Gunathilake L, and S. W. (2011) Apache Airavata : A framework for Distributed Applications and Computational Workflows, Proceedings of the 2011 ACM Workshop on Gateway Computing Environments, 21–28.

[29] UNICORE. (2014) Http://www.unicore.eu.

Appendix 6.1

College of Engineering
Department of Mechanical Engineering
(479) 575-3153
(479) 575-6982 (FAX)

UNIVERSITY OF ARKANSAS

Mechanical Engineering Building
Fayetteville, Arkansas 72701

Coleman, S.P., Pamidighantam, S., Van Moer, M., Wang, Y., Koesterke, L., Spearot, D.E. (2014) Performance Improvement and Workflow Development of Virtual Diffraction Calculations, Proceedings of XSEDE 2014.

I certify that Mr. Shawn Coleman is the first author of the paper and completed greater than 51% of the work in this publication. This work was an invited submission in collaboration with Drs. Sudhakar Pamidighantam and Mark Van Moer at the National Center for Supercomputing Applications (NCSA), Dr. Yang Wang at the Pittsburg Supercomputing Center (PSC), and Dr. Lars Koesterke at the Texas Advanced Computing Center (TACC), as part of a grant received from the XSEDE supercomputing network.

Sincerely,

Douglas E. Spearot, Ph.D.
Dissertation Director
Associate Professor and 21st Century Professorship
Department of Mechanical Engineering
University of Arkansas
Fayetteville, AR 72701
Office: 479-575-3040
E-mail: dspearot@uark.edu

Appendix 6.2

I. **Copyright Transfer, Reserved Rights and Permitted Uses**
* Your Copyright Transfer is conditional upon you agreeing to the terms set out below.

Copyright to the Work and to any supplemental files integral to the Work which are submitted with it for review and publication such as an extended proof, a PowerPoint outline, or appendices that may exceed a printed page limit, (including without limitation, the right to publish the Work in whole or in part in any and all forms of media, now or hereafter known) is hereby transferred to the ACM (for Government work, to the extent transferable) effective as of the date of this agreement, on the understanding that the Work has been accepted for publication by ACM.

Reserved Rights and Permitted Uses

(a) All rights and permissions the author has not granted to ACM are reserved to the Owner, including all other proprietary rights such as patent or trademark rights.

(b) Furthermore, notwithstanding the exclusive rights the Owner has granted to ACM, Owner shall have the right to do the following:

(i) Reuse any portion of the Work, without fee, in any future works written or edited by the Author, including books, lectures and presentations in any and all media.

(ii) Create a "Major Revision" which is wholly owned by the author

(iii) Post the Accepted Version of the Work on (1) the Author's home page, (2) the Owner's institutional repository, or (3) any repository legally mandated by an agency funding the research on which the Work is based.

(iv) Post an "Author-Izer" link enabling free downloads of the Version of Record in the ACM Digital Library on (1) the Author's home page or (2) the Owner's institutional repository;

(v) Prior to commencement of the ACM peer review process, post the version of the Work as submitted to ACM ("Submitted Version" or any earlier versions) to non-peer reviewed servers;

(vi) Make free distributions of the final published Version of Record internally to the Owner's employees, if applicable;

(vii) Make free distributions of the published Version of Record for Classroom and

Personal Use;

(viii) Bundle the Work in any of Owner's software distributions; and

(ix) Use any Auxiliary Material independent from the Work.
Authors should understand that consistent with ACMs policy of encouraging dissemination of information, each work published by ACM appears with a copyright and the following notice:

(c) 2014 Association for Computing Machinery. ACM acknowledges that this contribution was authored or co-authored by an employee, contractor or affiliate of the national government of United States. As such, the Government retains a nonexclusive, royalty-free right to publish or reproduce this article, or to allow others to do so, for Government purposes only.

Chapter 7: Atomistic simulation and virtual diffraction characterization of stable and metastable Al_2O_3 surfaces

Shawn P. Coleman[a] and Douglas E. Spearot[a]

[a] Department of Mechanical Engineering, University of Arkansas, Fayetteville, AR 72701

Abstract

The structures of select alumina surfaces are studied using molecular statics and molecular dynamics simulations and are characterized using virtual diffraction methods. First, bulk alumina simulations are performed to validate the transferability of the ReaxFF potential to model different alumina phases. Bulk alumina simulations accurately predict α-Al_2O_3 as the lowest energy crystalline phase; however, they unexpectedly predict an even lower energy amorphous phase. At 0 K, virtual x-ray diffraction patterns of the bulk crystalline phases and select alumina surfaces are validated by experimental studies. Molecular statics simulations of select alumina surfaces are consistent with prior first-principles studies. However, molecular dynamics simulations show that many surfaces experience significant reconstructions at temperatures below what is expected from experiments. It is believed that premature surface reconstructions are biased by the predicted lower energy amorphous phase and occur due to the extra degrees of freedom allowed by the free surfaces as well as the available thermal energy during dynamics. Discrete peaks appearing in virtual selected area electron diffraction patterns indicate that the reconstructions are not fully amorphous due to lattice constraints imposed by the internal bulk structure. Bulk and surface energies are tabulated for each simulation to be used in future predictive mesoscale models of polymorphic alumina.

7.1 Introduction

Alumina (Al_2O_3) is an abundant ceramic material that exhibits extraordinary structural flexibility [1–5]. The different Al_2O_3 phases display a range of unique physical properties which make them useful in a variety of coating applications [6,7]. These properties stem from only subtle differences within the crystal structure of its phases. In general, the alumina phases are composed of a close-packed O sublattice surrounded by Al interstitials filling 2/3 of the octahedral and tetrahedral sites to maintain stoichiometry [8]. The type of close-pack arrangement of the O sublattice and the degree of symmetry of the Al interstitials within each alumina unit cell determines the phase and properties of the material. Corundum, α-Al_2O_3, is the only thermodynamically stable alumina phase, which contains the most symmetric ordering of the Al interstitials [1]. High symmetry leads to the high density of α-Al_2O_3 compared to the other phases and promotes directionality and ionic bonding between the atoms leading to high hardness. The metastable alumina phases have decreasing symmetry of the Al interstitials, which decreases their density and weakens their bond strength by reducing bond directionality. Due to subtle structural differences, phase identification within atomistic simulations based solely on local atomic positions is difficult; however, experimental characterization techniques such as x-ray diffraction (XRD) and selected area electron diffraction (SAED) have proven successful in distinguishing between alumina phases [9–13].

Selective vapor deposition of single-phase alumina thin films is often desired in order to take advantage of specific material properties, but is difficult due to the complexity of the alumina material system. For example, κ- and α-Al_2O_3 surfaces are widely regarded as ideal protective coatings due to their wear resistance, chemical inertness, resistance to thermal shock, and high hardness [14,15]. However, several metastable alumina phases demonstrate properties less ideal

for these purposes and can form during deposition depending on the processing conditions [16]. For example, θ- and γ-Al_2O_3 metastable phases may form at lower processing temperatures (T_m~0.3) [16]. These metastable phases have lower surface energies and therefore exhibit higher surface areas making them more appropriate as catalytic supports. In addition, selective vapor deposition of single-phase alumina proves difficult due to alumina's complex phase transition series that is dependent on the material precursors and processing conditions [17–19]. To determine the current state under a particular synthesis process, researchers and manufacturers must continually characterize the surface structure.

Predictive mesoscale material simulations can aid in the search for the ideal processing conditions that produce tailored alumina coatings, similar to solidification studies of multicomponent systems [20–22]. By considering the mechanisms governing phase formation and evolution, predictive models can computationally explore the unique processing conditions that achieve single-phase coatings in polycrystalline materials. Analogous experimental approaches, such as those taken to develop structure zone diagrams [23,24], rely on phenomenological observations requiring an exhaustive experimental study for a polymorphic material system and are only predictive within the same processing space. Mesoscale models, such as phase-field methods [25], for physical vapor deposition of polymorphic materials will require energetic data (i.e., bulk, surface, and interface energies) that can be easily computed from atomistic simulations. However, to quantitatively compare these data the relevant energies need to be computed using the same computational model, as is done in this work.

Specifically, this work investigates select bulk and surface alumina structures using atomistic simulations modeled with the reactive force-field (ReaxFF) potential [26]. This article begins with a detailed discussion of previous atomistic simulations performed on alumina bulk and

surface structures highlighting the necessity for a consistent computational model to provide quantitatively comparable data. This is followed by a description of the current simulation methods using ReaxFF as well as the virtual diffraction method [27,28] used to characterize the nanoscale structure of the alumina simulations. Next, computed surface energies as well as characterization results are reported and analyzed. This article concludes with a summary and discussion of the future work needed to develop predictive mesoscale models of vapor deposition for polymorphic alumina.

7.2 Previous atomistic studies of alumina

Because of its important material properties and wide industrial use, the alumina system has been studied extensively using molecular dynamics (MD), molecular statics (MS), and first-principles computational models. However, none of these previous atomistic studies has attempted to catalog structural and energetic properties of bulk and surface structures across more than two alumina phases using the same computational model. By narrowing the focus on select alumina components, prior atomistic simulation studies have avoided the challenges of uniquely characterizing the subtle structural differences among the various alumina phases as well as the distortion created by atomic relaxations near surfaces. More importantly, because prior alumina studies used different computational models, direct comparisons between computed energetic values cannot be made.

First-principles simulations have studied alumina bulk and surface structures at 0 K using models based on quantum mechanics which rely on approximations to describe the electron interactions explicitly (cf. [29–31]). These approximations can be divided into three classes: (i) Hartree-Fock (HF) theory, (ii) density functional theory with local density approximations of the electron exchange-correlation (DFT-LDA), and (iii) density functional theory with generalized

gradient approximations of the electron exchange-correlation (DFT-GGA). Differently, MS and MD simulations use models based on Newtonian physics which represent atoms as point masses in space that encompass both the nucleus and the orbiting electrons. Interactions between atoms are governed by an interatomic potential to describe the potential energy of the system. Prior MS and MD simulations employed a variety of interatomic potentials with different approximations for electrostatic and non-electrostatic interactions (i.e., the styles describing pair, many-body, and bonded interactions). The approximations used to describe the electrostatic interactions in alumina can be divided into three different classes: (i) fixed point charges [32–43], (ii) charged shell models [44–48], or (iii) dynamic geometry dependent charges [49–52]. Each of these increases in complexity in an attempt to better represent the polarization of the O ions.

7.2.1 *Bulk Alumina Studies*

Prior atomistic simulations of alumina modeled bulk systems in order to assess the transferability of the computational model to multiple phases. Because α-Al_2O_3 is the only thermodynamically stable phase, transferable computational models should predict α-Al_2O_3 as the lowest potential energy structure per Al_2O_3 unit. Table 7.1 lists a sample of previous atomistic simulation studies that compared the predicted α-Al_2O_3 potential energy to a selection of metastable alumina phases as well as the bixbyite structure. Here, relative energies are measured as the difference between the predicted potential energy of the specified phase and α-Al_2O_3 such that positive values indicate lower energy α-Al_2O_3.

Table 7.1 shows different computational models predict a different ordering of the energetic stability among alumina phases and shows that some models fail to predict the stability of α-Al_2O_3. Wilson et al. [53] commented that some of the discrepancy among the various models

Table 7.1: Sample values of computed energy deviations from κ-, θ-, γ-, and bixbyite (B) Al_2O_3 compared to α-Al_2O_3. Values are reported in eV per formula unit.

Year	Comp. Model	ΔE(κ-α)	ΔE(θ-α)	ΔE(γ-α)	ΔE(B-α)	Ref.
2007	DFT-LDA	0.21	0.25	0.37	0.21	[54]
2004	MS[a]	---	0.19	---	0.66	[52]
2004	DFT-GGA	---	---	0.18	---	[55]
2003	DFT-GGA	---	0.03	---	---	[56]
2001	DFT-LDA	---	-0.01	---	0.08	[57]
2001	DFT-GGA	0.09	---	---	---	[58]
2001	DFT-LDA	0.15	---	---	---	[58]
2000	DFT-GGA	0.08	0.04	---	0.16	[59]
2000	DFT-LDA	0.21	0.25	---	0.21	[59]
1998	DFT-LDA	---	0.38	---	0.97	[60]
1999	DFT-LDA	0.15	---	---	---	[2]
1999	DFT-GGA	0.09	---	---	---	[2]
1996	MS[b]	---	0.29	---	-0.40	[53]
1996	DFT-LDA	---	0.56	---	0.77	[53]
1994	HF	---	0.44	---	---	[61]

[a] Bond Style –Geometry Dependent
[b] Pair Style – Charged Shell

stems from difficulties representing the polarization of the O ions. Another difficulty stems from uncertainty in the exact crystal structure of several of the metastable phases. In particular, the structure of the κ- and γ-Al_2O_3 phases has been the subject of much debate regarding the placement of the Al ions in the O interstitial sites. Using similar first-principles approaches, Yourdshahyan et al. [62,63] and Paglia et al. [64,65] studied the minimum energy structures of bulk κ-Al_2O_3 and γ-Al_2O_3, respectively. In their studies, candidate structures for the bulk phases were constructed using a chosen O sublattice and Al ions located in combinations of every possible interstitial site. The 40-atom κ-Al_2O_3 unit cell, studied by Yourdshahyan et al. [62,63], produced 169 candidate structures whose bulk energies could be computed directly from first-principles. Differently, the 160-atom γ-Al_2O_3 unit cell studied by Paglia et al. [64] produced ~1.47 billion candidate structures that could not be studied directly from first-principles due to computational costs. Instead, Paglia et al. used selection criteria to reduce the number of γ-Al_2O_3

candidates to 56,064 that were then modeled using less computationally expensive MS simulations. The MS simulations produced a subset of 1,161 lower-energy structures with more-optimal atomic configurations. Paglia et al. [64] computed bulk energies of select low-energy structures using first-principles methods and observed the same energy trends as the MS simulation results.

Low-energy bulk κ- and γ-Al_2O_3 structures found by Paglia and Yourdshahyan were further analyzed using virtual diffraction methods. In their work, Yourdshahyan et al. showed that the virtual XRD line profile generated from the lowest-energy unit cell was the best match to the experimentally obtained pattern [2]. Differently, Paglia et al. showed that simulated neutron diffraction line profiles from low-energy γ-Al_2O_3 structures did not match the experimental results; instead, a better experimental match was found from unit cells slightly altered from the ideal spinel structure [64].

7.2.2 *Alumina Surface Studies*

Many prior studies have independently examined select surface structures of several alumina phases. In particular, many studies focused on the α-Al_2O_3 (0001) surface due to its important industrial use in catalytic and electronic supports. Table 7.2 lists a sample of previous atomistic studies that explored the α-Al_2O_3 (0001) surface structure along with computed surface energy values. From Table 7.2, it is clear that the computational model can significantly influence the computed values for surface energy. Analysis of these studies shows that structural relaxations and size effects can further affect the results. Tasker [66] was the first to incorporate an energy minimization routine into his study, which revealed substantial structural relaxations of the α-Al_2O_3 (0001) surface. Verdozzi et al. [67] showed that the degree of structural relaxation is impacted by the number of layers contained in the surface model (i.e., the thickness

Table 7.2: Sample history of α-Al_2O_3 (0001) surface energy values computed using various atomistic simulation methods. Values in parenthesis are for non-relaxed surface structures.

Year	Comp. Model	E_{surf} (0001) [J/m^2]		Ref.
2008	DFT-GGA	(3.51)	1.54	[68]
2007	HF	(4.82)	1.85	[69]
2004	DFT-GGA		1.98	[70]
2004	MS[a]		1.00	[52]
2004	DFT-GGA	(3.15)	1.54	[55]
2004	DFT-GGA	(3.52)	1.55/1.57	[71]
2003	DFT-GGA	(3.58)	1.60	[72]
2003	DFT-LDA	(3.97)	1.94	[72]
2001	MS[b]	(6.5)	3.15 at 300K	[73]
1999	DFT-GGA	(3.5)	1.95	[74]
1999	DFT-LDA		1.98	[75]
1998	MS[c]		2.06 at 300K	[76]
1995	MS[b]	(4.48)	2.00	[77]
1995	MS[b]	(3.86)	1.70	[77]
1994	MS[d]	(3.67)	2.67	[49]
1994	DFT-LDA	(3.77)	1.76	[78]
1993	MS[e]	(5.04)	2.04 at 300K	[36]
1992	DFT-LDA	(3.7)	---	[79]
1992	HF	(3.30)	---	[80]
1989	HF	(6.53)	5.32	[81]
1987	MS[c]	(5.95)	2.03	[82]
1984	MS[c]	(6.53)	2.97	[66]
1980	MS[c]	(4.82)	---	[83]

[a] Bond Style – Geometry Dependent
[b] Pair Style – Charged Shell
[c] Pair Style – Point Charge
[d] Many-body Style – Geometry Dependent
[e] Many-body Style – Point Charge

of the simulation). In Table 7.2, size effects were not considered in earlier simulations as they focused on constructing a minimum size model to reduce the computational expense. Considering all the findings from the α-Al_2O_3 (0001) studies, it is clear that direct comparisons of computed energetic values cannot be easily made unless the same computational models are implemented and similar considerations for relaxations and size effects are taken into account, as

is done in this work.

Table 7.3 lists a sample of prior atomistic studies on select α-Al_2O_3 surfaces along with computed surface energies. For qualitative comparisons among the studies, relative surface energies are reported as a percentage value based on the ratio of the computed surface energy versus the α-Al_2O_3 (0001) surface. While the relative stability of the various α-Al_2O_3 surfaces deviates in early studies, the later HF results by Marmier and Parker [70] and DFT-GGA results by Sun et al. [84] agree that the ordering of surface energies for α-Al_2O_3 follows: $(0001)_\alpha < (10\bar{1}2)_\alpha < (11\bar{2}0)_\alpha < (10\bar{1}0)_\alpha < (10\bar{1}1)_\alpha$, indicating the basal surface as most stable.

Only a few prior atomistic studies have examined the structure and energetics of surfaces in metastable alumina phases. Table 7.4 list a sample of these studies along with computed surface energies. Of these, only one study by Blonski and Garofalni [36] used the same computational model to examine multiple surfaces in both α-Al_2O_3 and a metastable phase. Blonski and Garofalni utilized a many-body potential to study select α- and γ-Al_2O_3 surfaces [36]. The many-body potential modeled pair interactions with a Born-Mayer Huggins form [85], three-body interactions for Al-O-Al and O-Al-O triplets, and electrostatic interactions using fixed point charges. In their work, Blonski and Garofalni showed that the potential successfully predicted minimum energy structures for bulk α- and γ-Al_2O_3 when compared to experimental radial distribution functions. Additionally, the α-Al_2O_3 surface energy calculations predicted the ordering of surface energies to be $(0001)_\alpha < (11\bar{2}0)_\alpha < (10\bar{1}0)_\alpha$ similar to the more recent first-principles results [70,84]. Differently, the predicted ordering of γ-Al_2O_3 surface energies by Blonski and Garofalni [36] contradicts more recent DFT-GGA values computed by Pinto and Elliot [55]. The DFT-GGA study [55] predicted the ordering of γ-Al_2O_3 surface energies as $(111)_\gamma < (001)_\gamma < (110)_\gamma < (150)_\gamma$, indicating the $(111)_\gamma$ surface as most stable.

Table 7.3: Sample of previous α-Al_2O_3 surface energies computed using atomistic simulation methods. All values are in J/m^2. The values in parenthesis are for non-relaxed surface structures. For relaxed values, relative energy compared to the $(0001)_\alpha$ surface energy are reported.

Year	Comp. Model	$(0001)_\alpha$	$(10\bar{1}2)_\alpha$	$(11\bar{2}0)_\alpha$	$(10\bar{1}1)_\alpha$	$(10\bar{1}0)_\alpha$	Ref.
2006	HF	(4.82) 1.85 100%	(2.94) 2.14 116%	(3.36) 2.39 129%	(4.33) 2.53 137%	(4.57) 2.44 132%	[84]
2004	DFT-GGA	1.98 100%	2.04 103%	2.34 118%	2.57 130%	2.56 129%	[70]
1999	MS[a]	(6.03) 2.42 100%	2.38 98%	(4.83) 2.68 111%	(5.9) 3.19 132%	2.86 118%	[86]
1998	MD[b] (300 K)	2.06 100%	1.95 95%	2.08 101%	2.35 114%	--- ---	[76]
1998	MD[b] (1500 K)	2.09 100%	1.99 95%	2.12 101%	2.44 117%	--- ---	[76]
1998	MD[b] (1700 K)	2.09 100%	2.02 97%	2.27 109%	2.20 105%	--- ---	[76]
1995	MS[a]	(4.48) 2.00 100%	(4.45) 2.65 133%	(3.58) 2.20 110%	(2.77) 1.82 91%	(5.01) 2.25 113%	[77]
1995	MS[a]	(3.86) 1.7 100%	(3.24) 1.96 115%	(2.45) 1.68 99%	(1.91) 1.41 83%	(3.69) 2.1 124%	[77]
1994	MS[c]	(3.67) 2.67 100%	(2.42) 1.80 67%	(2.52) 1.81 68%	(3.22) 2.13 80%	(3.18) 1.28 48%	[49]
1994	DFT-LDA	(3.77) 1.76 100%	(2.51) 1.97 112%	(2.49) 1.86 106%	(3.64) 2.55 145%	(3.59) 1.40 80%	[78]
1994	DFT-LDA	(3.70) ---	(3.00) ---	(3.20) ---	---	---	[87]
1993	MD[d] (300 K)	5.04 (2.04) 100%	--- ---	(3.49) 2.27 111%	--- ---	(5.56) 2.35 115%	[36]
1989	HF	6.72 (5.32) 100%	--- ---	--- ---	--- ---	(5.65) 5.59 105%	[81]
1989	MS[a]	(5.95) 2.03 100%	(3.63) 2.29 113%	(4.37) 2.50 123%	(5.58) 2.52 124%	(6.46) 2.23 110%	[80]
1984	MS[b]	(6.53) 2.97 100%	(3.55) 2.57 87%	(5.17) 2.65 89%	(6.41) 3.27 110%	(6.87) 2.89 97%	[66]
1980	MS[b]	4.83	4.8	3.8	2.55	---	[88]

[a] Pair Style – Charged Shell
[b] Pair Style – Point Charge
[c] Many-body Style – Geometry Dependent
[d] Many-body Style – Point Charge

Table 7.4: Sample of computed surface energies from previous atomistic simulations of metastable alumina. Subscripts indicate the alumina phase and unrelaxed surface energy values are in denoted by parenthesis.

Year	Comp. Model	Metastable Alumina Surface Energies [J/m^2]				Ref.
		$(001)_\gamma$	**$(110)_\gamma$**	**$(111)_\gamma$**	**$(150)_\gamma$**	
2004	DFT-GGA	(2.97) 1.05	(3.43) 1.53	(1.62) 0.95	(2.79) 1.91	[55]
2002	DFT-GGA	0.97	1.54	---	---	[89]
1993	MS[a]	(3.37) 0.79	(4.62) 1.21	(9.45) 0.87		[90]
		$(100)_\theta$	**$(110)_\theta$**	**$(111)_\theta$**	**$(010)_\theta$**	
2004	DFT-GGA	0.70	1.65	1.00	---	[91]
1994	HF	3.88	---	---	4.41	[61]
		$(001)_\kappa$	**$(00\bar{1})_\kappa$**			
2003	DFT-GGA	(7.00) 5.20	(7.00) 5.80			[72]

[a] Many-body Style – Point Charge

Table 7.4 also lists previously computed surface energy values for a selection of θ- and κ-Al_2O_3 surfaces. While similar DFT-GGA models were used in these calculations, the authors did not match basis sets or use similar boundary conditions necessary for quantitative comparison with the other studies. Thus, direct comparison of the computed surface energy values among the various studies is not possible. However, the reported data do indicate the lowest energy surfaces for θ- and κ-Al_2O_3 are the $(100)_\theta$ and $(001)_\kappa$ surfaces, respectively.

It is important to note that the previously discussed studies were conducted for clean alumina surfaces. In experimental settings, alumina surfaces exposed to water can become hydroxylated. Several atomistic studies have examined hydroxylated alumina surfaces [91–96] and reported that hydroxylation increased the stability of alumina surfaces. For example, Łodziana et al. [91] computed negative surface energies for the $(110)_\theta$ surface in θ-Al_2O_3 caused by the generation of a new, more porous equilibrium surface structure that exhibits a lower energy than bulk θ-Al_2O_3.

7.3 Methods

7.3.1 *Simulation Details*

Atomistic simulations of alumina are performed with LAMMPS [97] using the ReaxFF potential [26]. ReaxFF is chosen for this work because of its hypothesized transferability to many alumina phases due to its use of a dynamic bond order term and geometry dependent charge optimization. Specifically, ReaxFF computes van der Waals and Coulombic contributions to the potential energy between all atom pairs and implements a continuous bond order term to allow dynamic bond formation and breaking. Additionally, ReaxFF uses an electron equilibration method [98] to optimize atomic charges based on the atomic geometry at each time step. Dynamic charge optimization has the potential to increase the transferability of ReaxFF by modelling different oxidation states within different alumina phases. The ReaxFF parameters used in this study were first optimized by Zhang et al. for Al and α-Al_2O_3 using first-principles simulations of Al-O clusters [52] then further tailored by Sen et al. to better incorporate varying Al oxidation states during oxidation simulations [51].

Slab models are created for the 11 surfaces described in Table 7.5. Each slab model is constructed using fully-periodic boundary conditions with a vacuum region normal to the surface greater than 50 Å, as shown in Figure 7.1. For each model, the simulation dimensions and terminating planes are chosen such that the correct stoichiometry of alumina is maintained. The simulation dimensions along the surface plane are chosen to minimize strain stemming from small misalignments of the periodic images created by the oriented crystals.

For each slab model, a series of initial structures are constructed by varying the terminating planes on each opposing surface. The initial structures are relaxed at 0 K using a non-linear conjugate gradient method. Surface energies for each structure are computed using two

Table 7.5: Description of the simulation size for alumina slabs modeled in this study. Here each subscript indicates a particular alumina phase associated with the surface plane.

Surface	L_x [Å]	L_y [Å]	L_z [Å]	N [atoms]
$(0001)_\alpha$	201.2721	203.6963	194.9318	885,600
$(11\bar{2}0)_\alpha$	197.9836	195.8093	197.7603	846,450
$(1\bar{1}00)_\alpha$	197.9786	195.8206	197.8010	846,450
$(001)_\gamma$	198.9950	199.0289	189.7136	800,000
$(110)_\gamma$	203.6746	190.2056	202.9786	829,440
$(111)_\gamma$	202.1025	175.9054	207.5978	777,600
$(001)_\kappa$	197.3578	201.6267	198.2140	844,800
$(010)_\kappa$	361.5524	118.2935	184.9249	844,800
$(100)_\kappa$	336.2477	217.3695	107.7260	844,800
$(001)_\theta$	201.3005	201.0150	194.7824	844,560
$(110)_\theta$	158.9278	191.0272	161.4515	512,085

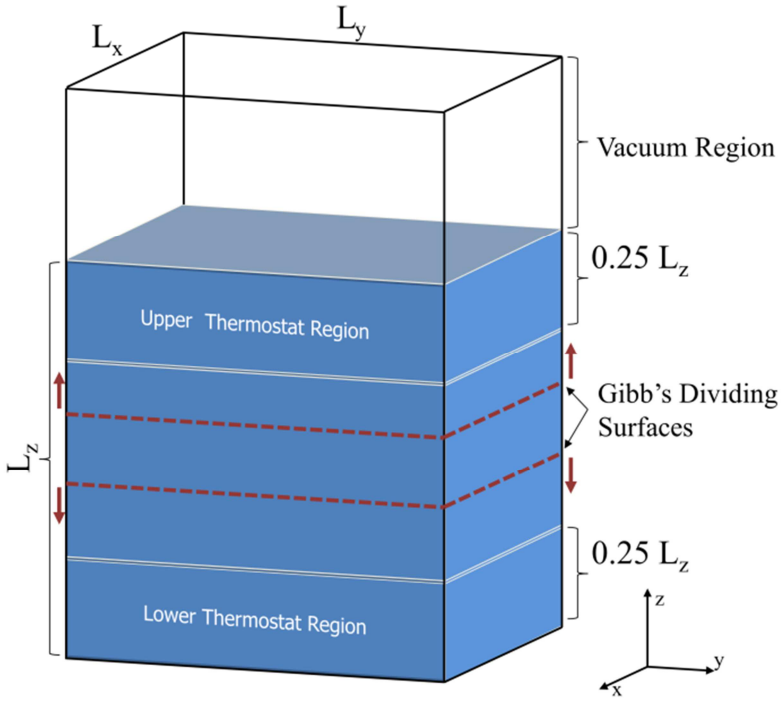

Figure 7.1: Schematic of slab model used in atomistic simulations of alumina surfaces showing the thermostat regions and placement of Gibb's dividing surfaces.

methods. The first method considers the entire slab and computes an average surface energy, γ_s^{ave} ,accounting for both the upper and lower surfaces via,

$$\gamma_s^{ave} = \frac{E_{\text{Slab}} - nE_{\text{Bulk}}}{2A} \quad . \tag{7.1}$$

Here, E_{Slab} is the minimized potential energy for a particular slab, E_{Bulk} is the minimized potential energy for the bulk alumina unit cell of the matching phase, n is the number of alumina unit cells contained within the slab, and A is the area of the slab surface. Note, the average surface energy γ_s^{ave} for a slab model with identical surface structures will be equivalent to the surface energy of the upper and lower surfaces. However, for complex non-symmetric alumina phases there is no guarantee the surface structures on opposing sides of the slab will be identical. Therefore, a second method of computing surface energies is employed that uses Gibbs dividing surfaces to divide the slab into upper and lower stoichiometric regions [99]. The Gibbs dividing surfaces are aligned parallel to the slab surfaces and are positioned within the slab through an iterative process that identifies stoichiometric regions exposed to the vacuum. The iterative process places an initial Gibbs dividing surface in the middle of slab and steps normal to the desired surface until the atoms within the region exposed to the vacuum are stoichiometric. Surface energies for the upper γ_s^U and lower γ_s^L regions are computed via,

$$\gamma_s^{U/L} = \frac{E_{\text{Region}} - mE_{\text{Bulk}}}{A} \tag{7.2}$$

where E_{Region} and m are the potential energy and equivalent number of unit cells contained within the Gibbs region, respectively. Surface energies are computed using both methods for each series of initial structures to determine the lowest energy configuration for each slab model.

For low-energy degenerate structures, slab models with the smallest deviation between upper and lower surface energies calculated from Eq. (7.2) are selected for the MD study as this indicates the presence of similar surface structures.

Molecular dynamics simulations are performed on the lowest-energy slab models for each surface using the canonical (NVT) ensemble at 300, 500, and 700 K. The MD simulations use a 0.5 fs time step with the Hoover damping parameter set to 100 fs. The NVT ensemble is chosen in order to decrease the time for equilibration and is sufficient for alumina models because of their low coefficient of thermal expansion [42]. To avoid localized temperature fluctuations near the surfaces caused by extra degrees of freedom experienced by atoms exposed to the vacuum, the slab models are divided into three NVT thermostat regions. Two thermostat regions are defined for the upper and lower surface regions by grouping all atoms exposed to the surfaces that are located within 25% of the direction normal to the surface (L_z) while the remaining atoms are grouped into the third thermostat region. Each region is coupled to a unique external thermal reservoir held at the desired temperature.

The MD simulations for each slab are performed at each temperature for 25 ps and equilibration is monitored by reporting the total potential energy every 0.05 ps. Energetic data are extracted over the last 5 ps of the simulation when the maximum deviation of the potential energy is less 0.1% of the average value. Surface energies are computed for each slab at each temperature via Eqs. (7.1) and (7.2) using the equilibrated potential energy values for the slab and from bulk alumina simulations equilibrated using the same procedures as discussed above.

7.3.2 *Virtual Diffraction Analysis*

Characterization of alumina atomistic simulations proves difficult due to the subtle structural differences observed among the phases. While traditional characterization methods used for

atomistic simulation results (i.e., radial distribution functions [100], centrosymmetry [101], common neighbor-analysis [102]) are successful in analyzing cubic or other high-symmetry crystal structures, none of these methods are capable of uniquely identifying alumina phases due to the subtle differences in the Al ion placement within the non-cubic crystal structures. Therefore, in this work, virtual diffraction methods developed by Coleman et al. [27,28] are chosen to identify the alumina models and characterize the stable and metastable alumina surfaces.

The virtual diffraction method developed by Coleman et al. [27,28] uses kinematic diffraction theory to create both SAED patterns and XRD line profiles from atomistic simulation data. Previously, other virtual diffraction methods based on kinematic diffraction theory have studied atomistic simulations of (i) grain boundary structures in bicrystals [103–108], (ii) grain size and microstrain in nanocrystals [109–114], (iii) defect formation and evolution during shock of nanocrystals [115–118], and (iv) bulk alumina simulations [2,64]. The virtual diffraction method developed by Coleman et al. [27,28] advances beyond these prior studies because it generates both SAED patterns and XRD line profiles without requiring *a priori* knowledge of the crystal structure. Additionally, the method by Coleman et al. takes advantage of modern computer hardware and external accelerators in order to directly compute the Fourier components in the structure factor equation [119]. The algorithm is generic for all atom species and is integrated into LAMMPS [97] which leverages multi-level parallelization techniques to rapidly compute diffraction intensities for large atomistic simulations [119].

Briefly, the method introduced by Coleman et al. [27,28] computes diffraction intensities, $I(\mathbf{K})$, for N atoms as the product of the structure factor, F(**K**), with its complex conjugate, $F^{*}(\mathbf{K})$, via

$$I(\mathbf{K}) = F^{*}(\mathbf{K})F(\mathbf{K})/N \quad (3)$$

where F(**K**) is computed by the structure factor equation [120],

$$F(\mathbf{K}) = \sum_{j=1}^{N} f_j \exp\left(2\pi i\, \mathbf{K}\cdot\mathbf{r}_j\right) \quad . \quad (4)$$

Here, $\mathbf{K}$ is the location of the diffraction peak in reciprocal space, $\mathbf{r}_j$, is the position of the atom in real space, and f_j is the atomic scattering factor computed for each atom species. Diffraction intensities are explored across a high-resolution, three-dimensional reciprocal space mesh that is constructed either based on the dimensions of the entire simulation or as a user defined value. The resolution of the reciprocal space mesh is tuned in order to ensure important peak locations are sampled. In this work, all atoms within the simulation box (except for select surface analyses as denoted) are used to compute the diffraction intensities. Reciprocal lattice nodes are spaced 0.00475 $Å^{-1}$ and 0.02 $Å^{-1}$ in each direction to generate SAED and XRD patterns, respectively. SAED patterns and XRD line profiles are constructed from the three-dimensional intensity data using simulated 200 keV electron radiation (λ = 0.0251 Å [121]) and Cu K_α x-rays (λ = 1.54178 Å [120]) by applying unique data analysis and visualization methods developed for each technique [27].

7.4 Results and Discussion

7.4.1 *Bulk Alumina*

The transferability of the ReaxFF potential is evaluated by modeling bulk γ-, κ-, θ-, and α-Al_2O_3 systems using MS and MD simulations. Potential energy values per Al_2O_3 unit extracted from these simulations are reported in Table 7.6. At all temperatures explored, the ReaxFF interatomic potential successfully predicts α-Al_2O_3 as more energetically stable (i.e., lower potential energy) than any other crystalline phase. Table 7.6 also shows the difference in

Table 7.6: Potential energy (eV per Al_2O_3 formula unit) for various Al_2O_3 crystalline phases computed using ReaxFF.

Temp.	**α-Al_2O_3**	**γ-Al_2O_3**	**κ-Al_2O_3**	**θ-Al_2O_3**
0 K	-28.607	-28.421	-28.406	-28.413
300 K	-28.417	-28.236	-28.211	-28.267
500 K	-28.292	-28.134	-28.101	-28.117
700 K	-28.157	-28.041	-28.056	-28.062

Method		**ΔE(γ-α)**	**ΔE(κ-α)**	**ΔE(θ-α)**
ReaxFF (0 K)	--	0.19	0.20	0.19
DFT-LDA [54]	--	0.37	0.21	0.25

potential energy per Al_2O_3 unit at 0 K for the metastable phases compared to α-Al_2O_3 computed using ReaxFF and for the most recent DFT-LDA study by Lee et al. [54]. ReaxFF predicts the metastable structures to be nearly energetically degenerate having potential energies each approximately 0.20 eV per Al_2O_3 unit greater than α-Al_2O_3. Lee et al. predict a similar magnitude for the energy deviation; however, their DFT-LDA results show the deviation for γ-Al_2O_3 to be nearly twice that as κ-Al_2O_3. The larger energy deviation in the prior DFT-LDA study could be the result of a different γ-Al_2O_3 initial structure as compared to that used in the current study [64,65].

A series of MS simulations are performed exploring an isotropic expansion of the α-Al_2O_3 lattice parameters to investigate the minimum energy lattice structure and to compute the predicted bulk elastic modulus. To calculate the bulk modulus, the minimized potential energies are fitted to the Birch-Murnaghan equation of state [122]. As seen in Table 7.7, the resulting minimum energy lattice parameters and the predicted bulk modulus closely match both experimental and first-principles computed values. Specifically, the a and c lattice constants calculated by ReaxFF for this work deviate from the reported experimental values data by only 0.1% while the bulk modulus deviates by 2.8%.

Table 7.7: Computed properties for α-Al_2O_3. Prior experimental data were observed at high pressure and 300 K.

α-Al_2O_3	**Expt.**	**DFT-GGA**	**ReaxFF**	**This Work**
a [Å]	4.758[a]	4.783[c]	4.810[c]	4.81
c [Å]	12.995[a]	13.252[c]	13.100[c]	13.13
B [Gpa]	253[b]	250[c]	248[c]	244

[a] Reference [123]
[b] Reference [124]
[c] Reference [52]

Due to the complexity of the metastable alumina phases, structural properties for these phases are unable to be computed using the same procedure. However, XRD patterns computed for each energy-minimized structure are shown in Figure 7.2. The virtual XRD line profiles

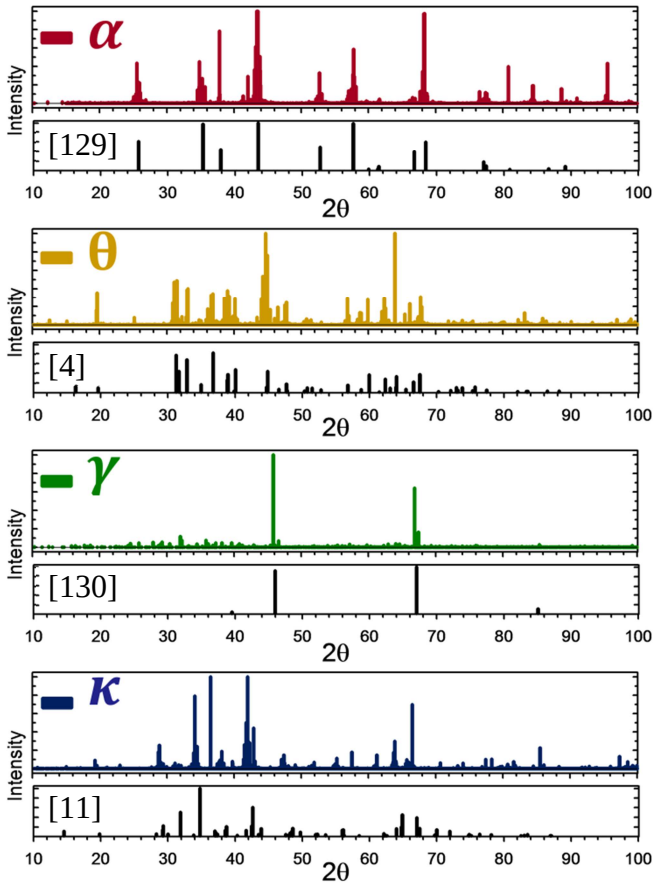

Figure 7.2: Computed XRD profiles (colored) compared to experimental references [4,11,129,130] (black) for various energy minimized phases using the ReaxFF potential.

uniquely identify each alumina phase. In addition, the virtual XRD line profiles (colored) show excellent agreement with experimental powder diffraction data (black). The ability of ReaxFF to predict the expected energetics and correct structures suggests good transferability of this potential to different alumina phases at 0 K.

7.4.2 *Alumina Surfaces*

Average surface energies evaluated at 0, 300, 500, and 700 K for each of the 11 alumina slab models are listed in Table 7.8. Among the α-Al_2O_3 surfaces, ReaxFF predicts the $(0001)_\alpha$ surface to be the lowest energy surface at all temperatures, which is consistent with previous HF [70] and DFT-GGA results [84]. Among the γ-Al_2O_3 surfaces, ReaxFF predicts the $(001)_\gamma$ surface to be the lowest surface energy at 0 and 700 K; however, at 300 and 500 K, the ReaxFF simulations predict an even lower energy for the $(110)_\gamma$ surface. The 0 K results for γ-Al_2O_3 are consistent with previous MD simulation results [90] but disagree with results found by DFT-GGA [55], which found the lowest surface to be the $(111)_\gamma$ surface. Among the κ-Al_2O_3 surfaces, ReaxFF predicts the $(010)_\kappa$ surface to be the lowest surface energy at 0, 500, and 700 K; however, at 300 K, the ReaxFF simulations predict an even lower surface energy for the $(001)_\kappa$ surface. Interestingly, a negative average surface energy is found for the $(010)_\kappa$ surface at 700 K indicating the presence of a lower-energy surface structure within the slab model as compared to the bulk. Negative values for the surface energies are also found for both θ-Al_2O_3

Table 7.8: Computed average surface energy values, Eq. (7.1), for select alumina surfaces using the ReaxFF potential [60]. Values are reported in J/m^2.

	α-Al_2O_3			**γ-Al_2O_3**			**κ-Al_2O_3**			**θ-Al_2O_3**	
Temp.	**(0001)**	**$(1\bar{1}00)$**	**$(11\bar{2}0)$**	**(001)**	**(110)**	**(111)**	**(001)**	**(010)**	**(100)**	**(001)**	**(110)**
0 K	0.749	1.756	1.767	2.166	2.897	2.826	0.434	0.189	0.773	-0.187	-1.948
300 K	0.768	1.505	1.524	1.853	1.131	1.456	0.238	0.294	0.604	-0.101	-1.012
500 K	0.805	1.174	1.158	1.751	1.254	1.574	0.786	0.254	0.620	-1.174	-0.812
700 K	0.913	0.948	0.961	0.507	0.536	1.025	0.574	-0.638	0.849	0.078	-1.946

surface structures at 0, 300, and 500 K and for the $(110)_\theta$ surface at 700 K. Between the θ-Al_2O_3 surfaces, ReaxFF predicts lower surface energy for the $(110)_\theta$ at 0, 300, and 700 K. The upper and lower surface energy values computed using Eq. (7.2) are tabulated in the supplementary materials. Of the 11 alumina slab model studied, only the $(001)_\gamma$, $(111)_\gamma$, and $(001)_\kappa$ surfaces showed significant deviation between the computed upper and lower surface energy values due to different terminating structures.

Figure 7.3 shows virtual SAED patterns observed normal to the α-Al_2O_3 (0001) and γ-Al_2O_3 (110) surface after the 0 K energy minimization as well as comparisons to prior experimental results obtained by Heffelfinger et al. [125] and Morrissey et al. [8], respectively. For visualization, low diffraction intensity data in the virtual SAED patterns are removed so that peak locations become more evident. The virtual SAED results show distinct diffraction peaks as well as regular vertical and horizontal relrod structures due to the finite volume of the simulation [27]. For the α-Al_2O_3 (0001) surface, the virtual SAED results clearly show the same hexagonal pattern as observed in the experimental results. For the γ-Al_2O_3 (110) surface, the underlying shape of the diffraction peaks is consistent with the experimental results; however many low-intensity diffraction peaks are evident in the virtual SAED pattern which are not observed experimentally. These low-intensity peaks arise from a regular placement of Al interstitials within the slab created by repeating the γ-Al_2O_3 unit cell when constructing the model. This periodicity of the Al interstitials is especially pronounced in the static structure. In general, the one-to-one comparison between experimental and virtual SAED patterns, shown in Figure 7.3, validate the computational methods used and provide confidence in the virtual SAED results when no experimental comparisons are available.

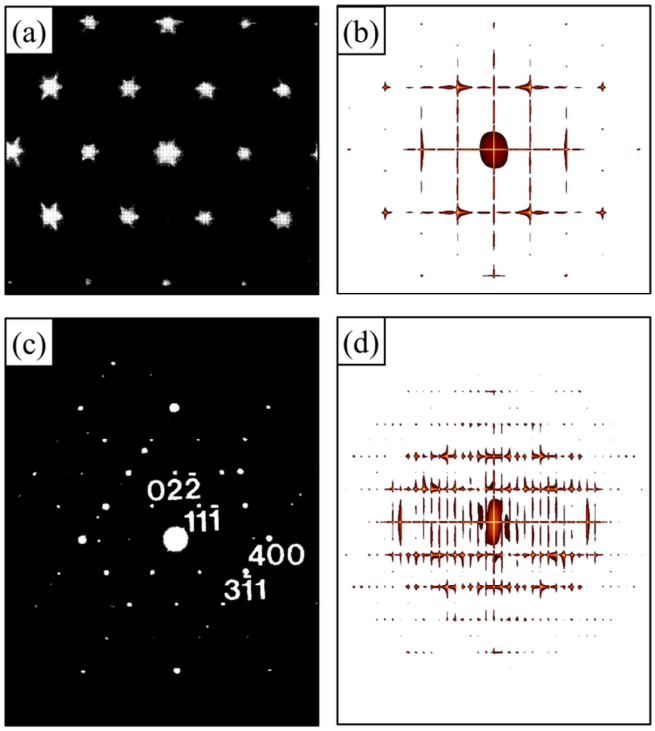

Figure 7.3: Comparison between experimental and 0 K virtual SAED patterns observed normal to (a-b) the α-Al_2O_3 (0001) and (c-d) the γ-Al_2O_3 (110) surfaces. Experimental results obtained from works by Heffelfinger et al. [96] and Morrissey et al. [8], respectively.

The nanoscale structure of the lowest average surface energy models (at 0 K) for each phase are characterized using virtual SAED patterns as well as by analyzing snapshots of the atomic positions within an approximate 2 x 2 x 1.25 nm^3 region near the upper and lower surfaces. Characterization results from all models are contained in the supplementary materials. At temperature, time averaged virtual SAED patterns are constructed by averaging diffraction data taken every 2.5 ps over the entire 25 ps equilibration period.

Figure 7.4 shows the characterization results of the (0001) surface in α-Al_2O_3 at 0, 300, 500, and 700 K. Here, both the SAED and atomic snapshots are viewed along the $[10\bar{1}2]$ direction. The upper and lower $(0001)_\alpha$ surfaces at 0, 300, and 500 K are cleaved with Al terminations that have displaced inwardly from their bulk configurations into the slab. However, at 700 K the $(0001)_\alpha$ surface experiences a reconstruction in which clusters of Al and O ions protruding from

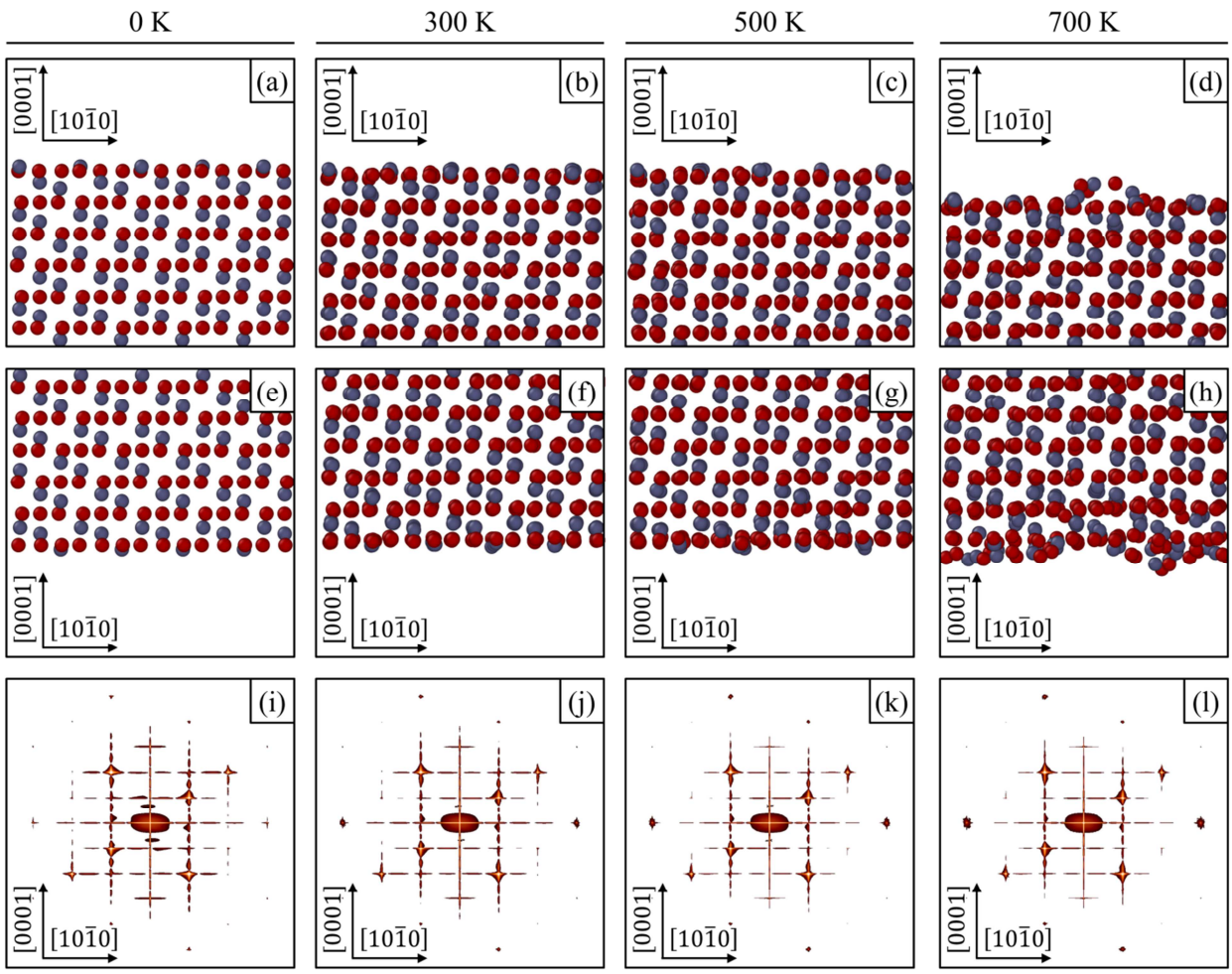

Figure 7.4: Characterization results for the α-Al_2O_3 (0001) surface viewed along the $[10\bar{1}2]$ direction showing snapshots of the (a-d) upper and (e-h) lower surfaces as well as (i-l) virtual SAED patterns.

the surface. At 0, 300, and 500 K, smearing of the diffraction peaks is minimal which is consistent with the lack of surface reconstructions at these temperatures; however, at 700 K, peak smearing occurs at the higher (hkl) peak locations due to the surface reconstruction.

Characterization results for the (001) surface in γ-Al_2O_3 at 0, 300, 500, and 700 K are shown in Figure 7.5 viewed along the [010] direction. At 0, 300, and 500 K, O ions terminate a nearly cleaved upper surface while the Al ions terminating the lower surface extend slightly into the vacuum region. At these temperatures, the Al terminated surface energy is approximately 1.4

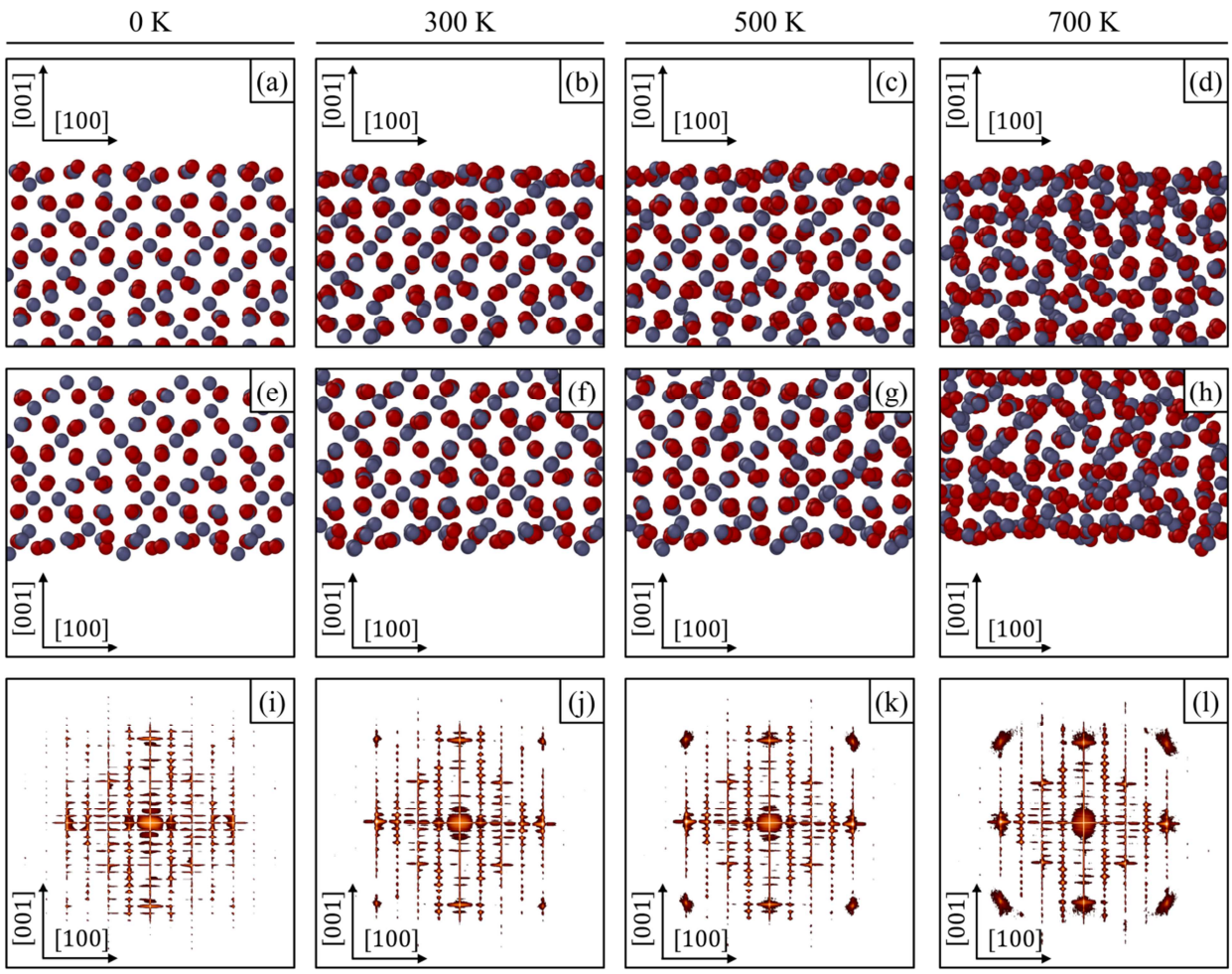

Figure 7.5: Characterization results for the γ-Al_2O_3 (001) surface viewed along the [010] direction showing snapshots of the (a-d) upper and (e-h) lower surfaces as well as (i-l) virtual SAED patterns.

J/m^2 than the O terminated surface. The 500 K surfaces show minimal surface relaxations in the outer layers. However, at 700 K both upper and lower surfaces experience significant reconstructions extending substantially into the slab models, which reduces the deviation between the upper and lower surface energies to 0.8 J/m^2. Virtual SAED patterns of the cleaved surfaces at 0 and 300 K show minimal peak smearing. However, relaxations and reconstructions at 500 and 700 K result in increased smearing of diffraction peaks as compared with the 700 K $(0001)_\alpha$ surface in Figure 7.4.

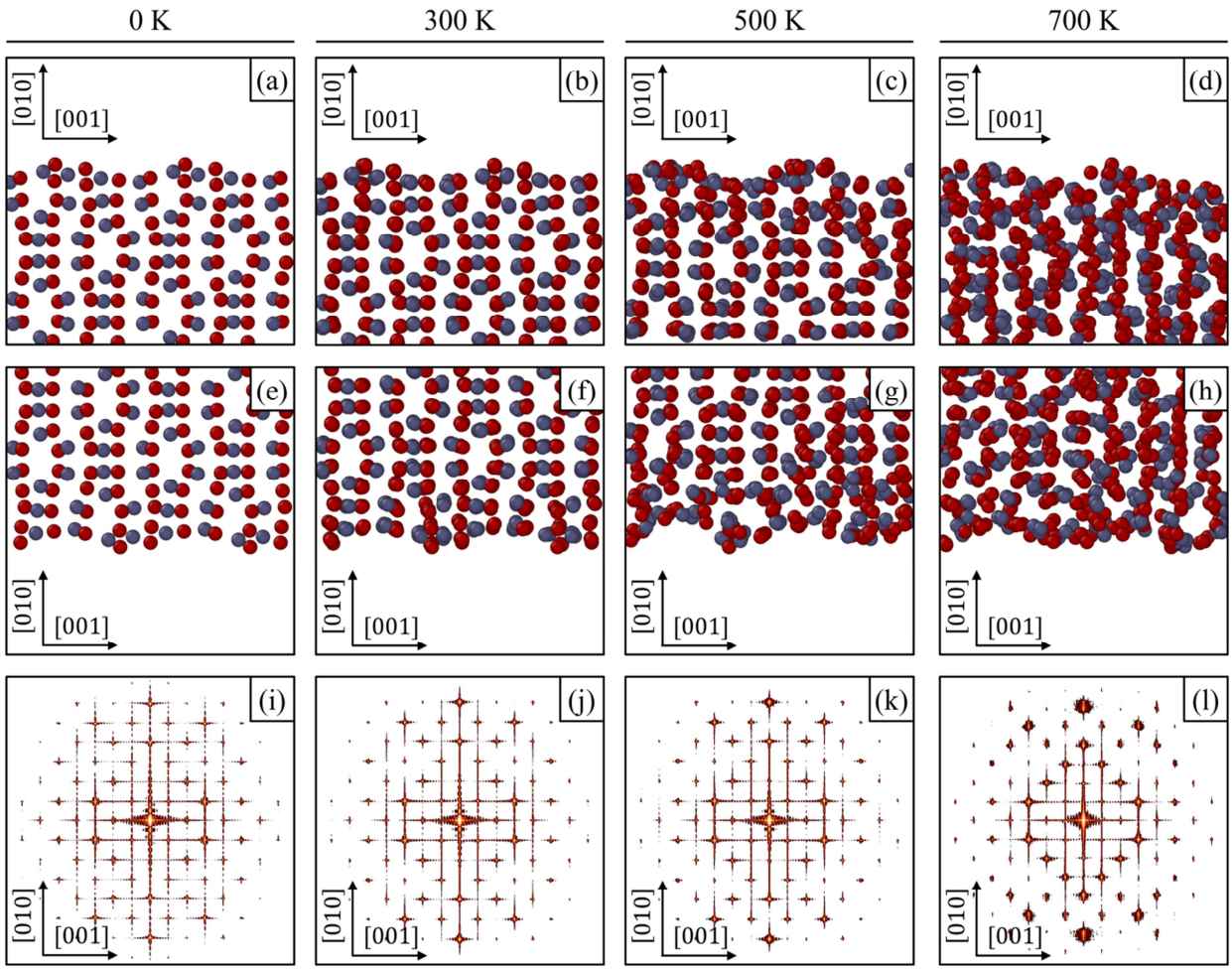

Figure 7.6: Characterization results for the κ-Al_2O_3 (010) surface viewed along the [100] direction showing snapshots of the (a-d) upper and (e-h) lower surfaces as well as (i-l) virtual SAED patterns.

Figure 7.6 shows characterization results for the (010) surface in κ-Al_2O_3 at 0, 300, 500, and 700 K viewed along the [100] direction. At 0 and 300 K both upper and lower surfaces form a regular concave structure with terminating O ions. Similar to the $(001)_\gamma$ surfaces, at 500 K the outermost layers of the $(010)_\kappa$ surfaces are relaxed, whereas substantial surface reconstruction is seen at 700 K. At 700 K, the surface reconstruction extends far beneath the surface of the slab creating a lower-energy configuration as compared to the bulk, which results in the negative average surface energies reported in Table 7.8. The virtual SAED patterns for $(010)_\kappa$ surfaces at

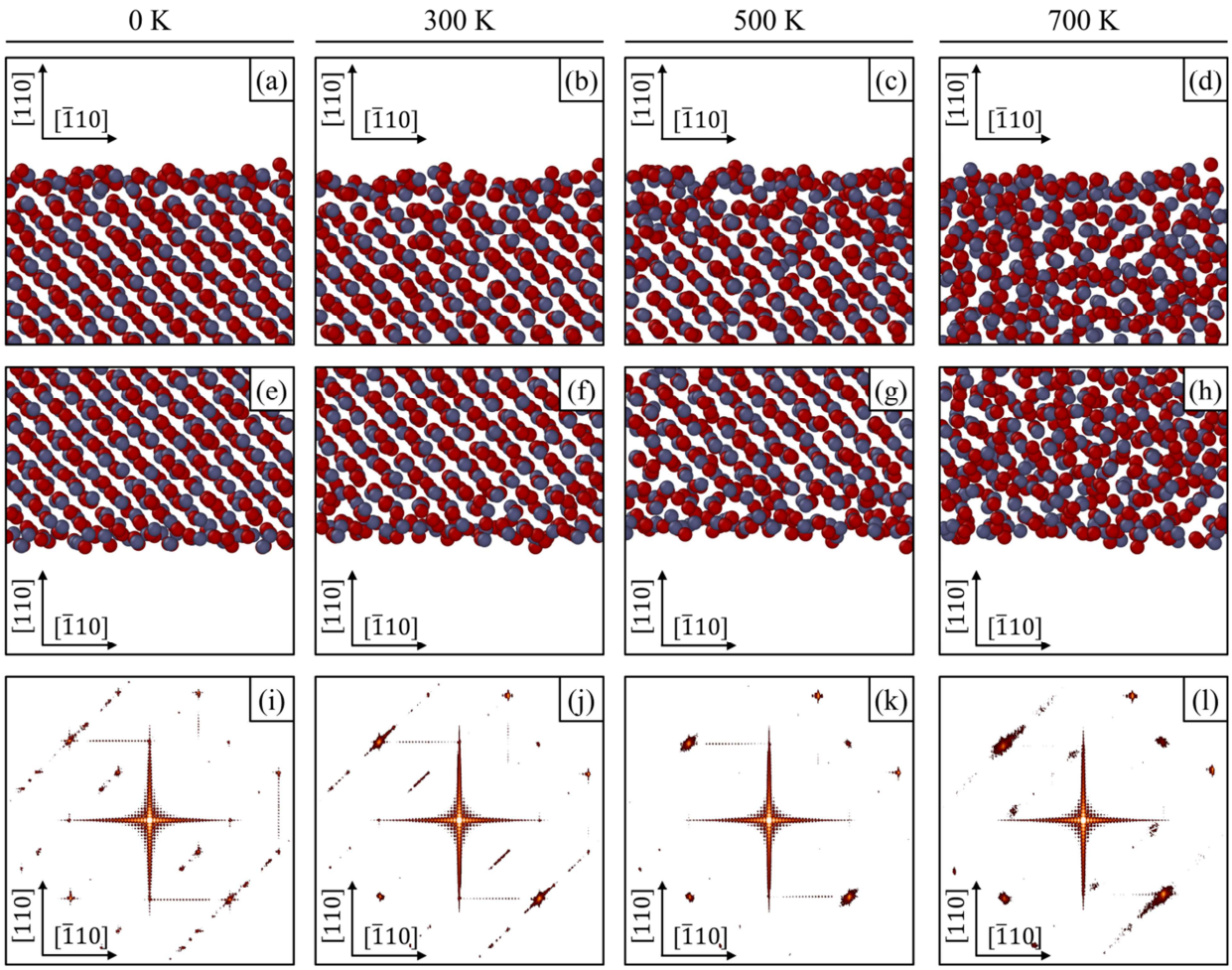

Figure 7.7: Characterization results for the θ-Al_2O_3 (110) surface viewed along the [001] direction showing snapshots of the (a-d) upper and (e-h) lower surfaces as well as (i-l) virtual SAED patterns.

0, 300, and 500 K show no significant smearing of the diffraction peaks; however at 700 K, substantial peak smearing is evident.

Characterization results for the (110) surface in θ-Al_2O_3 at 0, 300, 500, and 700 K are shown in Figure 7.7 viewed along the [001] direction. At 0 and 300 K, the outer layers of the surfaces are relaxed with a mixture of O and Al terminating ions. Substantial surface reconstructions are observed at 500 and 700 K appearing almost non-crystalline in nature. However, distinct diffraction peaks within the virtual SAED patterns indicate that some crystallinity is preserved at

all temperatures. With increasing temperature, certain diffraction peaks disappear and new peaks emerge while smearing of existing peaks becomes more substantial. To further investigate the negative surface energy computed for $(110)_\theta$ surfaces, slab models are analyzed using the virtual XRD patterns, as shown in Figure 7.8. XRD patterns produced from 0 K energy minimized slabs as well as at each temperature do not match the predicted or experimental XRD patterns for bulk θ-Al_2O_3, thus showing ReaxFF predicts a substantially different structure for $(110)_\theta$ slab models. XRD profiles for the $(110)_\theta$ slab models at 0, 500, and 700 K show the strongest reflection at $2\theta = 31.65°$ corresponding to an interplanar spacing of 2.83 Å. Additionally, diminishing peaks at larger 2θ values suggest a transformation towards an amorphous configuration.

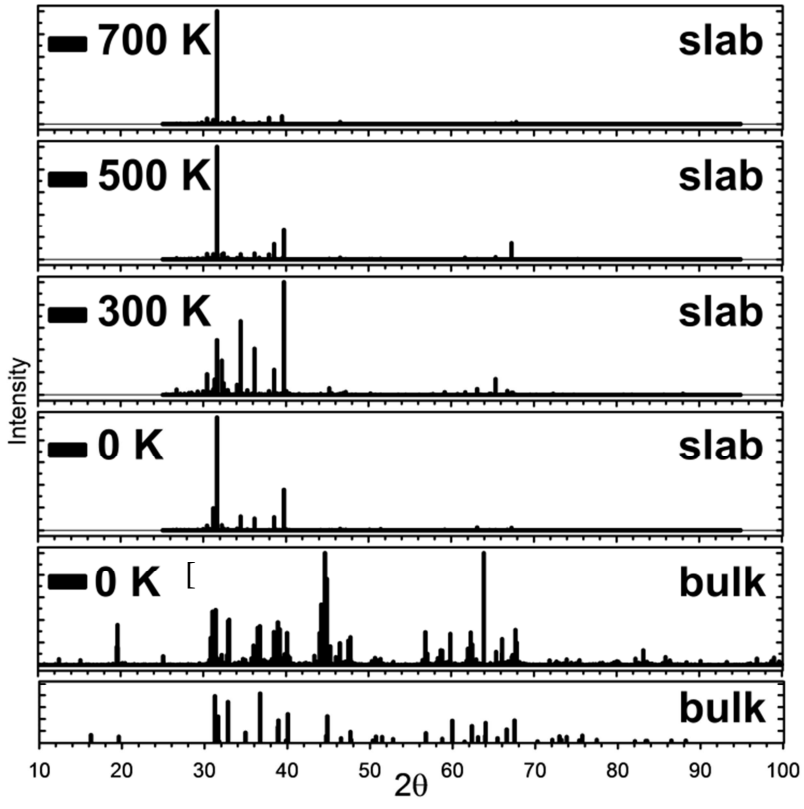

Figure 7.8: Virtual XRD patterns computed for bulk θ-Al_2O_3 and slab models of the $(110)_\theta$ surface at varying temperatures which show the prediction of a new low-energy phase in the slab modeled by the ReaxFF potential.

ReaxFF predicts substantial reconstructions of several alumina surfaces at temperatures below what is expected from experimental studies (c.f. [126–128]). To investigate the cause for the premature reconstructions, amorphous bulk alumina is modeled using ReaxFF. Samples of bulk amorphous alumina are constructed by heating models of each crystalline phase to 3,000 K using a NPT ensemble for 25 ps then cooling the amorphous melt to 30 K over an additional 25 ps. This is followed by a non-linear conjugate gradient minimization of the solidified amorphous system. Virtual SAED diffraction analysis performed on each relaxed amorphous structure shows similar diffuse ring patterns, as expected for an amorphous material, which indicates the final structures are independent of the original phase selected. Similarly, virtual XRD profiles show a single strong reflection at $2\theta = 25.57°$ corresponding to an interplanar spacing of 3.48 Å. A representative amorphous structure is equilibrated to each of the three temperatures via the NVT equilibration procedure described in Section 3.

Unexpectedly, at all temperatures explored ReaxFF predicts the potential energy of the amorphous alumina phase to be approximately 0.10 eV per Al_2O_3 unit lower than α-Al_2O_3. Therefore, it is believed that ReaxFF unnaturally biases surface reconstruction within slab models to a lower energy amorphous-like configuration, especially due to the extra degrees of freedom available to the exposed surfaces. Note, virtual SAED patterns constructed only using the reconstructed surface regions reveal distinct (but smeared) peaks signifying that these regions are not fully amorphous. It is believed the lattice constraints imposed by the bulk interior of the slab models prevents the formation of fully amorphous reconstructed surface structures. In addition, it is believed that the bias for reconstruction primarily affects surfaces modeled at temperatures when the available thermal energy increases the ability for transformation into a different surface configuration. Therefore, 0 K results from this study are believed to be more

appropriate for use in future predictive mesoscale simulations.

7.5 Conclusions

In this work, select bulk and surface alumina structures are modeled using the ReaxFF interatomic potential in order to characterize their nanoscale structure and to compute bulk and surface energies. In comparison to prior efforts, this work provides the widest study to date on alumina bulk and surface structures within a consistent computational model. ReaxFF accurately predicts bulk α-Al_2O_3 as the lowest energy crystalline phase; however, it also predicts an even lower energy amorphous phase. Virtual XRD patterns computed for each bulk crystalline structure uniquely identify alumina phases and are validated by experimental data.

Surface energies computed using ReaxFF of many alumina phases are consistent with prior atomistic simulation results. However, results from certain surfaces significantly deviate from prior experimental and atomistic results. For example, ReaxFF predicts negative surface energies for the θ-Al_2O_3 surfaces due to the creation of a new lower-energy Al_2O_3 surface structure within the slab models as determined by virtual XRD patterns. Several alumina surfaces also experience significant surface reconstructions at temperatures below what is expected from experiments. It is believed the premature surface reconstruction is biased by the lower energy amorphous phase predicted by ReaxFF. Free surfaces enable the premature surface reconstructions due to the extra degrees of freedom available, which is especially true during MD simulations when thermal energy increases the ability for the transformation to occur.

Because a consistent computational model is employed throughout this study, the computed energies can be quantitatively compared and used in future predicted mesoscale models of vapor deposition for polymorphic alumina. It is believed that the limitations found for the ReaxFF potential primarily affect simulations of surface properties at temperature. Therefore, data

extracted at 0 K is the most appropriate for use in predictive mesoscale models. A complete mesoscale model of vapor deposition for polymorphic alumina will require future work to investigate the structures and energetics of homogenous and heterogeneous (solid/solid) alumina interfaces. For quantitative comparison with data in this study, it is essential that this future work be conducted using the same computational model employed here.

Acknowledgements

The authors acknowledge support of the National Science Foundation under grant #0954505. Additional support is provided by the 21st Century Professorship in Mechanical Engineering at the University of Arkansas. This work utilized the Extreme Science and Engineering Discovery Environment (XSEDE), which is supported by National Science Foundation grant #OCI-1053575. The authors thank Prof. Adri van Duin for useful discussions concerning ReaxFF and equilibration procedures as well as Prof. C. Barry Carter for fruitful discussions concerning electron diffraction.

References

[1] Villars P and Calvert LD. (1991) Pearson's Handbook of Crystallographic Data for Intermetallic Phases, second ed. Materials Park, OH: ASM International.

[2] Yourdshahyan Y, Ruberto C, Halvarsson M, Bengtsson L, Langer V, and Lundqvist BI. (1999) Theoretical Structure Determination of a Complex Material: κ-Al2O3, Journal of the American Ceramic Society, **82**, 1365–1380.

[3] Alvarez LJ, Sanz JF, Capitán MJ, and Odriozola JA. (1992) Molecular dynamics studies of the structure of γ-alumina, Chemical Physics Letters, **192**, 463–468.

[4] Husson E and Repelin Y. (1996) Structural studies of transition aluminas: Theta alumina, European Journal of Solid State and Inorganic Chemistry, **33**, 1223–1231.

[5] Levin I and Brandon DG. (1998) A new metastable alumina polymorph with monoclinic symmetry, Philosophical Magazine Letters, **77**, 117–124.

[6] Dinman BD. (1990) Aluminas and Health, in: Alumina Chem. Sci. Technol. Handb. Westerville, OH: American Ceramic Society Inc.

[7] Hart LD and Lense E, editors. (1990) Alumina Chemicals: Science and Technology Handbook. Westerville, Ohio: Wiley-American Ceramic Society.

[8] Morrissey KJ, Czanderna KK, Merrill RP, and Carter CB. (1985) Transition alumina structures studied using HREM, Ultramicroscopy, **18**, 379–386.

[9] Santos PS, Santos H de S, and Toledo SP. (2000) Standard transition aluminas. Electron microscopy studies, Materials Research, **3**, 104–114.

[10] Wilson SJ. (1979) Phase transformations and development of microstructure in boehmite-derived transition aluminas, Proceedings from the British Ceramic Society, **28**, 281–294.

[11] Ollivier B, Retoux R, Lacorre P, Massiot D, and Férey G. (1997) Crystal structure of κ-alumina: an X-ray powder diffraction, TEM and NMR study, Journal of Material Chemistry, **7**, 1049–1056.

[12] Kohn J. A, Katz G, and Broder JD. (1956) Characterization of β-Ga2O3 and its isomorph, θ-Al2O3, Proceedings from the Fourteenth Annual Pittsburg Diffraction Conference, 398–407.

[13] Repelin Y and Husson E. (1990) Transitional aluminas structural study. I. γ- and δ-aluminas, Materials Research Bulletin, **25**, 611–621.

[14] Jamting A, Ring M, Ruppi S, and Swain M V. (1995) Mechanical characterization of

kappa and alpha alumina films on hard metals using indentation methods, Journal of Hard Materials, **6**, 67–87.

[15] Kathrein M, Schintlmeister W, Wallgram W, and Schleinkofer U. (2003) Doped CVD Al2O3 coatings for high performance cutting tools, Surface and Coatings Technology, **163-164**, 181–188.

[16] Dragoo AL and Diamond JJ. (1967) Transitions in vapor deposed alumina from 300° to 1200°C, Journal of the American Ceramic Society, **50**, 538–574.

[17] Levin I and Brandon DG. (1998) Metastable alumina polymorphs: Crystal structures and transition sequences, Journal of the American Ceramic Society, **81**, 1995–2012.

[18] Paglia G, Buckley CE, Rohl AL, Hart RD, Winter K, Studer AJ, Hunter BA, and Hanna J V. (2004) Boehmite derived γ-alumina system. 1 . Structural evolution with temperature, with the identification and structural determination of a new transition phase, γ′-alumina, Chemistry of Materials, **16**, 220–236.

[19] Coelho ACV, Santos H de S, and Kiyohara PK. (2007) Surface area, crystal morphology and characterization of transition alumina powders from a new gibbsite precursor, Material Research, **10**, 183–189.

[20] Ofori-Opoku N and Provatas N. (2010) A quantitative multi-phase field model of polycrystalline alloy solidification, Acta Materialia, **58**, 2155–2164.

[21] Tiaden J. (1999) Phase field simulations of the peritectic solidification of Fe–C, Journal of Crystal Growth, **198-199**, 1275–1280.

[22] Nestler B, Garcke H, and Stinner B. (2005) Multicomponent alloy solidification: Phase-field modeling and simulations, Physical Review E, **71**, 041609.

[23] Movchan BA and Demchishin A V. (1969) Investigation of the structure and properties of thick vacuum-deposited films of nickel, titanium, tungsten, alumina and zirconium dioxide, Fizika Metallov i Metallovedenie,, **28**, 653–660.

[24] Thornton JA. (1977) High rate thick film growth, Annual Review of Materials Science, **7**, 239–260.

[25] Steinbach I. (2009) Phase-field models in materials science, Modelling and Simulation in Materials Science and Engineering, **17**, 073001.

[26] Van Duin ACT, Dasgupta S, Lorant F, and Goddard WA. (2001) ReaxFF: A Reactive Force Field for Hydrocarbons, The Journal of Physical Chemistry A, **105**, 9396–9409.

[27] Coleman SP, Spearot DE, and Capolungo L. (2013) Virtual diffraction analysis of Ni [0 1 0] symmetric tilt grain boundaries, Modelling and Simulation in Materials Science and

Engineering, **21**, 055020.

[28] Coleman SP, Sichani MM, and Spearot DE. (2014) A computational algorithm to produce virtual x-ray and electron diffraction patterns of interfaces from atomistic simulations, JOM, **66**, 408–416.

[29] Capelle K. (2006) A bird's-eye view of density-functional theory, Brazilian Journal of Physics, **36**, 1318–1343.

[30] Allan NL and Mackrodt WC. (1994) Density functional theory and interionic potentials, Philosophical Magazine B, **69**, 871–878.

[31] Yates JT and Johnson JK. (2007) Molecular Physical Chemistry for Engineers. Sausalito, CA: University Science Books.

[32] Hoang V Van and Oh SK. (2004) Simulation of structural properties and structural transformation of amorphous Al2O3, Physica B: Condensed Matter, **352**, 73–85.

[33] Hoang V Van and Kun Oh S. (2004) Structure and diffusion simulation of liquid Al2O3, Physica B: Condensed Matter, **352**, 342–352.

[34] Hoang V Van and Hung NH. (2006) Temperature- induced phase transition in simulated amorphous Al2O3, physica status solidi (b), **243**, 416–423.

[35] Hoang V Van and Oh SK. (2005) Computer simulation of the structural transformation in liquid Al2O3, Journal of Physics: Condensed Matter, **17**, 3025–3033.

[36] Blonski S and Garofalini SH. (1993) Molecular dynamics simulations of α-alumina and γ-alumina surfaces, Surface Science, **295**, 263–274.

[37] Adiga SP, Zapol P, and Curtiss LA. (2006) Atomistic simulations of amorphous alumina surfaces, Physical Review B, **74**, 1–8.

[38] Adiga SP, Zapol P, and Curtiss LA. (2007) Structure and Morphology of Hydroxylated Amorphous Alumina Surfaces, The Journal of Physical Chemistry C, **111**, 7422–7429.

[39] Gutiérrez G and Johansson B. (2002) Molecular dynamics study of structural properties of amorphous Al2O3, Physical Review B, **65**, 1–9.

[40] Gutiérrez G, Belonoshko AB, Ahuja R, and Johansson B. (2000) Structural properties of liquid Al2O3: A molecular dynamics study, Physical Review E, **61**, 2723–2729.

[41] Hu Z, Shi J, and Turner CH. (2009) Molecular dynamics simulation of the Al2O3 film structure during atomic layer deposition, Molecular Simulation, **35**, 270–279.

[42] Sun J, Stirner T, and Matthews A. (2007) Molecular dynamics simulation of the (0001) α-

Al2O3 and α-Cr2O3 surfaces, Surface Science, **601**, 1358–1364.

[43] Sun J, Stirner T, and Matthews A. (2006) Calculation of native defect energies in α-A12O3 and α-Cr2O3 using a modified Matsui potential, Surface and Coatings Technology, **201**, 4201–4204.

[44] Baxter R, Reinhardt P, Lopez N, and Illas F. (2000) Extent of relaxation of the α-Al2O3 (0001) surface and the reliability of empirical potentials, Surface Science, **445**, 448–460.

[45] Catlow CRA, James R, Mackrodt WC, and Stewart RF. (1982) Defect energetics in α-Al2O3 and rutile TiO2, Physical Review B, **25**, 1006–1026.

[46] Gale JD, Catlow CRA, and Mackrodt WC. (1999) Periodic ab initio determination of interatomic potentials for alumina, Modelling and Simulation in Materials Science and Engineering, **73**, 73–81.

[47] Marmier A, Lozovoi A, and Finnis MW. (2003) The α-alumina(0001) surface: relaxations and dynamics from shell model and density functional theory, Journal of the European Ceramic Society, **23**, 2729–2735.

[48] Rambaut C, Jobic H, Jaffrezic H, Kohanoff J, and Fayeulle S. (1999) Molecular dynamics simulation of the α-Al2O3 lattice: dynamic properties, Journal of Physics: Condensed Matter, **10**, 4221–4229.

[49] Streitz FH and Mintmire JW. (1994) Electrostatic-based model for alumina surfaces, Thin Solid Films, **253**, 179–184.

[50] Streitz FH and Mintmire JW. (1994) Charge transfer and bonding in metallic oxides, Journal of Adhesion Science and Technology, **8**, 853–864.

[51] Sen FG, Qi Y, van Duin ACT, and Alpas AT. (2013) Oxidation induced softening in Al nanowires, Applied Physics Letters, **102**, 051912.

[52] Zhang Q, Çağın T, van Duin ACT, Goddard WA, Qi Y, and Hector LG. (2004) Adhesion and nonwetting-wetting transition in the Al/α-Al2O3 interface, Physical Review B, **69**, 045423.

[53] Wilson M, Exner M, Huang Y-M, and Finnis MW. (1996) Transferable model for the atomistic simulation of Al2O3, Physical Review B, **54**, 15683–15689.

[54] Lee C-K, Cho E, Lee H-S, Seol KS, and Han S. (2007) Comparative study of electronic structures and dielectric properties of alumina polymorphs by first-principles methods, Physical Review B, **76**, 1–7.

[55] Pinto HP, Nieminen RM, and Elliott SD. (2004) Ab initio study of γ-Al2O3 surfaces, Physical Review B, **70**, 125402.

[56] Łodziana Z and Parliński K. (2003) Dynamical stability of the α and θ phases of alumina, Physical Review B, **67**, 174106.

[57] Ouyang L and Ching W-YY. (2001) Geometry Optimization and Ground- State Properties of Complex Ceramic Oxides, Journal of the American Ceramic Society, **84**, 801–805.

[58] Ruberto C. (2001) Metastable Alumina from Theory: Bulk , Surface , and Growth of K-Al2O3. Chalmers University of Technology and Goteborg University.

[59] Wolverton C and Hass KC. (2000) Phase stability and structure of spinel-based transition aluminas, Physical Review B, **63**, 024102.

[60] Kenny SD, Nguyen-Manh D, Fujitani H, and Sutton AP. (1998) Ab initio modelling of alumina, Philosophical Magazine Letters, **78**, 469–476.

[61] Borosy AP, Silvi B, Allavena M, and Nortier P. (1994) Structure and bonding of bulk and surface θ-Alumina from periodic Hartree-Fock calculations, The Journal of Physical Chemistry, **98**, 13189–13194.

[62] Yourdshahyan Y, Ruberto C, Bengtsson L, and Lundqvist BI. (1997) First-principles calculations on the atomic and electronic structure of κ-Al2O3, Physical Review B, **56**, 8553–8558.

[63] Yourdshahyan Y, Engberg U, Bengtsson L, Lundqvist BI, and Hammer B. (1997) Theoretical investigation of the structure of κ-Al2O3, Physical Review B, **55**, 8721–8725.

[64] Paglia G, Rohl AL, Buckley CE, and Gale JD. (2005) Determination of the structure of γ-alumina from interatomic potential and first-principles calculations: The requirement of significant numbers of nonspinel positions to achieve an accurate structural model, Physical Review B, **71**, 1–16.

[65] Paglia G, Buckley CE, Rohl AL, Hunter BA, Hart RD, Hanna J V., and Byrne L. (2003) Tetragonal structure model for boehmite-derived γ-alumina, Physical Review B, **68**, 1–11.

[66] Tasker PW. (1984) Surfaces of magnesia and alumina, Advances in Ceramics, **10**, 176–189.

[67] Verdozzi C, Jennison DR, Schultz PA, and Sears MP. (1999) Sapphire (0001) Surface, Clean and with d-Metal Overlayers, Physical Review Letters, **82**, 799–802.

[68] Briquet LG V., Catlow CRA, and French SA. (2008) Comparison of the Adsorption of Ni, Pd, and Pt on the (0001) Surface of α-Alumina, The Journal of Physical Chemistry C, **112**, 18948–18954.

[69] Sun J, Stirner T, and Matthews A. (2007) Structure and electronic properties calculation of

ultrathin α-Al2O3 films on (0001) α-Cr2O3 templates, Surface Science, **601**, 5050–5056.

[70] Marmier A and Parker SC. (2004) Ab initio morphology and surface thermodynamics of α-Al2O3, Physical Review B, **69**, 115409.

[71] Carrasco J, Gomes JRB, and Illas F. (2004) Theoretical study of bulk and surface oxygen and aluminum vacancies in α-Al2O3, Physical Review B, **69**, 064116.

[72] Ruberto C, Yourdshahyan Y, and Lundqvist BI. (2003) Surface properties of metastable alumina: A comparative study of κ- and α-Al2O3, Physical Review B, **67**, 195412.

[73] Baudin M and Hermansson K. (2001) Metal oxide surface dynamics from molecular dynamics simulations: the α-Al2O3 (0001) surface, Surface Science, **474**, 107–113.

[74] Batirev IG, Alavi A, Finnis MW, and Deutsch T. (1999) First-principles calculations of the ideal cleavage energy of bulk niobium(111)/ α-alumina(0001) interfaces, Physical Review Letters, **82**, 1510–1513.

[75] Felice R Di and Northrup JE. (1999) Theory of the clean and hydrogenated Al2O3 (0001)-(1×1) surfaces, Physical Review B, **60**, R16287–R16290.

[76] Suzuki H, Matsubara H, Kishino J, and Kondoh T. (1998) Simulation of surface and grain boundary properties of alumina by molecular dynamics method, Journal of the Ceramic Society of Japan, **106**, 1215–1222.

[77] Gay DH and Rohl AL. (1995) MARVIN: a new computer code for studying surfaces and interfaces and its application to calculating the crystal morphologies of corundum and zircon, Journal of the Chemical Society, Faraday Transactions, **91**, 925.

[78] Manassidis I and Gillan MJ. (1994) Structure and energetics of alumina surfaces calculated from first principles, Journal of the American Ceramic Society, **77**, 335–338.

[79] Guo J, Ellis DE, and Lam D. (1992) Electronic structure and energetics of sapphire (0001) and ($11\bar{0}2$) surfaces, Physical Review B, **45**, 13647–13656.

[80] Mackrodt WC. (1989) Atomistic simulation of the surfaces of oxides, Journal of the Chemical Society, Faraday Transactions 2, **85**, 541.

[81] Causá M, Dovesi R, Pisani I, and Roetti C. (1989) Ab inito characterization of the (0001) and (101-0) crystal faces of α-alumina, Surface Science, **215**, 259–271.

[82] Mackrodt WC, Davey RJ, and Black SN. (1987) The morphology of α-Al2O3 and α-Fe2O3: The importance of surface relaxation, Journal of Crystal Growth, **80**, 441–446.

[83] Hartman P. (1980) The attachment energy as a habit controlling factor. III. Application to corundum, Journal of Crystal Growth, **49**, 166–170.

[84] Sun J, Stirner T, and Matthews A. (2006) Structure and surface energy of low-index surfaces of stoichiometric α-Al2O3 and α-Cr2O3, Surface and Coatings Technology, **201**, 4205–4208.

[85] Fumi FG and Tosi MP. (1964) Ionic sizes and born repulsive parameters in the NaCl-type alkali halides—I The Huggins-Mayer and Pauling forms, Journal of Physics and Chemistry of Solids, **25**, 31–43.

[86] De Leeuw NH, Higgins FM, and Parker SC. (1999) Modeling the Surface Structure and Stability of alpha-Quartz, Journal of Physical Chemistry B, **103**, 1270–1277.

[87] Ellis DE, Guo J, and Daniel J. (1994) Cluster models of bulk, surface, and impurity structure in alpha-Al2O3, Journal of the American Ceramic Society, **77**, 398–403.

[88] Hartman P. (1989) The effect of surface relaxation on crystal habit: cases of corundum (α-Al2O3) and hematite (α-Fe2O3), Journal of Crystal Growth, **96**, 667–672.

[89] Digne M, Sautet P, Raybaud P, Euzen P, and Toulhoat H. (2002) Hydroxyl Groups on γ-Alumina Surfaces: A DFT Study, Journal of Catalysis, **211**, 1–5.

[90] Blonski S and Garofalini SH. (1993) Molecular dynamics simulations of γ -alumina surface stabilization by depostied silicon ions, Chemical Physics Letters, **211**, 575–879.

[91] Łodziana Z, Topsøe N-Y, and Nørskov JK. (2004) A negative surface energy for alumina, Nature Materials, **3**, 289–93.

[92] Mason SE, Iceman CR, Trainor TP, and Chaka AM. (2010) Density functional theory study of clean, hydrated, and defective alumina (1102) surfaces, Physical Review B, **81**, 125423.

[93] Wang X-G, Chaka AM, and Scheffler M. (2000) Effect of the environment on α-Al2O3 (0001) surface structures, Physical Review Letters, **87**, 3650–3653.

[94] Ranea VA, Schneider WF, and Carmichael I. (2008) DFT characterization of coverage dependent molecular water adsorption modes on α-Al2O3(0001), Surface Science, **602**, 268–275.

[95] Trainor TP, Eng PJ, Brown GE, Robinson IK, and De Santis M. (2002) Crystal truncation rod diffraction study of the α-Al2O3 (1102) surface, Surface Science, **496**, 238–250.

[96] Eng PJ, Trainor TP, Brown GE, Waychunas GA, Newville M, Sutton SR, and Rivers ML. (2000) Structure of the Hydrated α-Al2O3 (0001) Surface, Science, **288**, 1029–1033.

[97] Plimpton SJ. (1995) Fast parallel algorithms for short-range molecular dynamics, Journal of Computational Physics, **117**, 1–19.

[98] Rappe AK and Goddard WA. (1991) Charge equilibration for molecular dynamics simulations, The Journal of Physical Chemistry, **95**, 3358–3363.

[99] Wolf DE and Nozières P. (1988) Interfacial properties of elastically strained materials, Zeitschrift für Physik B Condensed Matter, **70**, 507–513.

[100] Allen MP and Tildesley DJ. (1990) Computer Simulation of Liquids. Oxford: Claredon Press.

[101] Kelchner CL, Plimpton SJ, and Hamilton JC. (1998) Dislocation nucleation and defect structure during surface indentation, Physical Review B, **58**, 11085–11088.

[102] Tsuzuki H, Branicio PS, and Rino JP. (2007) Structural characterization of deformed crystals by analysis of common atomic neighborhood, Computer Physics Communications, **177**, 518–523.

[103] Bristowe PD and Sass SL. (1980) The atomic structure of a large angle [001] twist boundary in gold determined by a joint computer modelling and X-ray diffraction study, Acta Metallurgica, **28**, 575–588.

[104] Budai J, Bristowe PD, and Sass SL. (1983) The projected atomic structure of a large angle [001] Σ= 5 (θ=36. 9°) twist boundary in gold: Diffraction analysis and theoretical predictions, Acta Metallurgica, **31**, 699–712.

[105] Bristowe PD and Balluffi RW. (1984) Effect of secondary relaxations on diffraction from high-Σ [001] twist boundaries, Surface Science, **144**, 14–27.

[106] Oh Y and Vitek V. (1986) Structural multiplicity of Σ=5(001) twist boundaries and interprtation of x-ray diffraction from these boundaries, Acta Metallurgica, **34**, 1941–1953.

[107] Fitzsimmons MR and Sass SL. (1988) Quantitative x-ray diffraction study of the atomic structure of the Σ=5 (θ=36.9°) [001] twist boundary in gold, Acta Metallurgica, **36**, 3103–3122.

[108] Fitzsimmons MR, Vaudin MD, and Sass SL. (1988) Structural multiplicity and the interpretation of X-ray diffraction observations from grain boundaries, Scripta Metallurgica, **22**, 105–110.

[109] Stukowski A, Markmann J, Weissmüller J, and Albe K. (2009) Atomistic origin of microstrain broadening in diffraction data of nanocrystalline solids, Acta Materialia, **57**, 1648–1654.

[110] Alexandrov I V. and Valiev RZ. (2000) X-ray analysis of bulk nanostructured metals, Materials Science Forum, **321-324**, 577–582.

[111] Derlet PM, Van Petegem S, and Van Swygenhoven H. (2005) Calculation of x-ray spectra for nanocrystalline materials, Physical Review B, **71**, 1–8.

[112] Markmann J, Yamakov V, and Weissmüller J. (2008) Validating grain size analysis from X-ray line broadening: A virtual experiment, Scripta Materialia, **59**, 15–18.

[113] Markmann J, Bachurin D, Shao L, Gumbsch P, and Weissmüller J. (2010) Microstrain in nanocrystalline solids under load by virtual diffraction, EPL (Europhysics Letters), **89**, 66002.

[114] Van Swygenhoven H, Budrovie Ž, Derlet PM, Froseth AG, and Van Petegem S. (2005) In situ diffraction profile analysis during tensile deformation motivated by molecular dynamics, Materials Science and Engineering: A, **400**, 329–333.

[115] Kimminau G, Nagler B, Higginbotham A, Murphy WJ, Park N, Hawreliak JA, Kadau K, Germann TC, Bringa EM, Kalantar DH, Lorenzana HE, Remington BA, and Wark JS. (2008) Simulating picosecond x-ray diffraction from shocked crystals using post-processing molecular dynamics calculations, Journal of Physics: Condensed Matter, **20**, 505203.

[116] Higginbotham A, Suggit MJ, Bringa EM, Erhart P, Hawreliak JA, Mogni G, Park N, Remington BA, and Wark JS. (2013) Molecular dynamics simulations of shock-induced deformation twinning of a body-centered-cubic metal, Physical Review B, **88**, 104105.

[117] Hawreliak JA, Colvin JD, Eggert JH, Kalantar DH, Lorenzana HE, Stölken JS, Davies HM, Germann TC, Holian BL, Kadau K, Lomdahl PS, Higginbotham A, Rosolankova K, Sheppard J, and Wark JS. (2006) Analysis of the x-ray diffraction signal for the α-ϵ transition in shock-compressed iron: Simulation and experiment, Physical Review B, **74**.

[118] Mogni G, Higginbotham A, Gaál-Nagy K, Park N, and Wark JS. (2014) Molecular dynamics simulations of shock-compressed single-crystal silicon, Physical Review B, **89**, 064104.

[119] Coleman SP, Pamidighantam S, Van Moer M, Wang Y, Koesterke L, and Spearot DE. (2014) Performance improvement and workflow development of virtual diffraction calculations, XSEDE14, In Press.

[120] Warren BE. (1990) X-Ray Diffraction, first ed. New York: Dover Publications.

[121] Colliex C, Cowley JM, Dudarev SL, Fink M, Gjønnes K, Hilderbrandt R, Howie A, Lynch DF, Peng L-M, Ren G, Ross AW, Smith VH, Spence JCH, Steeds J, Wang J, Whelan MJ, and Zvyagin BB. (2004) Electron Diffraction, in: Prince E (Ed.). Int. Tables Crystallogr. Vol. C Math. Phys. Chem. Tables, third ed. Norwell, MA: Kluwer Academic Publishers.

[122] Murnaghan FD. (1944) The compressibility of media under extreme pressures,

Proceedings from the National Academy of Sciences of the United States of America, **30**, 244–247.

[123] Finger LW and Hazen RM. (1978) Crystal structure and compression of ruby to 46 kbar, Journal of Applied Physics, **48**, 5823–5826.

[124] D'Amour H, Schiferl D, Denner W, Schulz H, and Holzapfel WB. (1978) High-pressure single-crystal structure determinations for ruby up to 90 kbar using an automatic diffractometer, Journal of Applied Physics, **49**, 29–31.

[125] Heffelfinger JR, Bench MW, and Carter CB. (1997) Steps and the structure of the (0001) α-alumina surface, Surface Science, **370**, L168–L172.

[126] French TM and Somorjai GA. (1970) Composition and surface structure of the (0001) face of α-alumina by low-energy electron diffraction, The Journal of Physical Chemistry, **74**, 2489–2495.

[127] Barth C and Reichling M. (2001) Imaging the atomic arrangements on the high-temperature reconstructed α-Al2O3 (0001) surface, Nature, **414**, 54–57.

[128] Sohlberg K, Pantelides ST, and Pennycook SJ. (2001) Surface reconstruction and the difference in surface acidity between gamma- and eta-alumina., Journal of the American Chemical Society, **123**, 26–9.

[129] Ishizawa N, Miyata T, Minato I, Marumo F, and Iwai S. (1979) A structural investigation of α-Al203 at 2170K, Acta Crystallographica Section B, **36**, 228–230.

[130] Verwey EJW. (1935) Incomplete atomic arrangement in crystals, The Journal of Chemical Physics, **3**, 592–593.

Appendix 7.1

College of Engineering
Department of Mechanical Engineering
(479) 575-3153
(479) 575-6982 (FAX)

UNIVERSITY OF ARKANSAS

Mechanical Engineering Building
Fayetteville, Arkansas 72701

Coleman, S.P., Spearot, D.E. (2014) Atomistic simulation and virtual diffraction characterization of stable and metastable Al_2O_3 surfaces, Acta Materialia, submitted.

I certify that Mr. Shawn Coleman is the first author of the paper and completed greater than 51% of the work in this publication.

Sincerely,

Douglas E. Spearot, Ph.D.
Dissertation Director
Associate Professor and 21st Century Professorship
Department of Mechanical Engineering
University of Arkansas
Fayetteville, AR 72701
Office: 479-575-3040
E-mail: dspearot@uark.edu

Appendix 7.2

Author Rights

Elsevier supports the need for authors to share, disseminate and maximize the impact of their research. We take our responsibility as stewards of the online record seriously, and work to ensure our policies and procedures help to protect the integrity of scholarly works.

Author's rights to reuse and post their own articles published by Elsevier are defined by Elsevier's copyright policy. For our proprietary titles, the type of copyright agreement used depends on the author's choice of publication:

For subscription articles: These rights are determined by a copyright transfer, where authors retain scholarly rights to post and use their articles.

For open access articles: These rights are determined by an exclusive license agreement, which applies to all our open access content.

In both cases, the fundamental rights needed to publish and distribute an article remain the same and Elsevier authors will be able to use their articles for a wide range of scholarly purposes.

Details on how authors can reuse and post their own articles are provided below.

Help and support

For reuse and posting not detailed below, please see our posting policy, or for authors who would like to:

- Include material from other sources in your work being published by Elsevier, please visit: Permission seeking guidelines for Elsevier authors.
- Obtain permission to re-use material from Elsevier books, journals, databases, or other products, please visit: Obtaining permission to reuse Elsevier material
- Or if you are an Elsevier author and are contacted by a requestor who wishes to re-use all or part of your article or chapter, please also refer them to our Obtaining Permission to Re-Use Elsevier Material page.
- See our FAQ on posting and copyright queries.
- Contact us directly, please email our Permissions Help Desk.

How authors can use their own journal articles

Authors can use their articles for a wide range of scholarly, non-commercial purposes as outlined below. These rights apply for all Elsevier authors who publish their article as either a subscription article or an open access article.

We require that all Elsevier authors always include a full acknowledgement and, if appropriate, a link to the final published version hosted on Science Direct.

For open access articles these rights are separate from how readers can reuse your article as defined by the author's choice of Creative Commons user license options.

Authors can use either their accepted author manuscript or final published article for:	
✓	Use at a conference, meeting or for teaching purposes
✓	Internal training by their company
✓	Sharing individual articles with colleagues for their research use* (also known as 'scholarly sharing')
✓	Use in a subsequent compilation of the author's works
✓	Inclusion in a thesis or dissertation
✓	Reuse of portions or extracts from the article in other works
✓	Preparation of derivative works (other than for commercial purposes)

*Please note this excludes any systematic or organized distribution of published articles.

http://www.elsevier.com/journal-authors/author-rights-and-responsibilities

Appendix 7.3 : Supplementary Materials:

7.3.1 Local Surface Energies

Computed surface energies for the upper γ_s^U and lower γ_s^L regions are evaluated through

$$\gamma_s^{U/L} = \frac{E_{\text{Region}} - mE_{\text{Bulk}}}{A}$$

in the manner discussed in the text are reported in Table 7.9.

Table 7.9: Computed upper and lower surface energy values (Eq. 7.2) for select alumina surfaces using the ReaxFF potential [60]. Values are reported in J/m^2.

	α-Al_2O_3			**γ-Al_2O_3**			**κ-Al_2O_3**			**θ-Al_2O_3**	
0 K	**(0001)**	**(1$\bar{1}$00)**	**(11$\bar{2}$0)**	**(001)**	**(110)**	**(111)**	**(001)**	**(010)**	**(100)**	**(001)**	**(110)**
Upper	0.749	1.754	1.721	2.881	2.800	1.629	0.199	0.189	0.773	-0.181	-1.936
Lower	0.749	1.756	1.794	1.450	2.936	3.730	0.701	0.189	0.773	-0.194	-1.942
	α-Al_2O_3			**γ-Al_2O_3**			**κ-Al_2O_3**			**θ-Al_2O_3**	
300 K	**(0001)**	**(1$\bar{1}$00)**	**(11$\bar{2}$0)**	**(001)**	**(110)**	**(111)**	**(001)**	**(010)**	**(100)**	**(001)**	**(110)**
Upper	0.771	1.496	1.482	2.479	0.940	0.361	-0.471	0.293	0.600	-0.101	-0.997
Lower	0.765	1.510	1.548	1.226	1.337	2.453	0.969	0.295	0.607	-0.101	-1.017
	α-Al_2O_3			**γ-Al_2O_3**			**κ-Al_2O_3**			**θ-Al_2O_3**	
500 K	**(0001)**	**(1$\bar{1}$00)**	**(11$\bar{2}$0)**	**(001)**	**(110)**	**(111)**	**(001)**	**(010)**	**(100)**	**(001)**	**(110)**
Upper	0.806	1.169	1.116	2.487	1.033	0.307	-0.002	0.243	0.615	-1.176	-0.810
Lower	0.803	1.176	1.180	1.015	1.529	2.662	1.567	0.264	0.625	-1.172	-0.803
	α-Al_2O_3			**γ-Al_2O_3**			**κ-Al_2O_3**			**θ-Al_2O_3**	
700 K	**(0001)**	**(1$\bar{1}$00)**	**(11$\bar{2}$0)**	**(001)**	**(110)**	**(111)**	**(001)**	**(010)**	**(100)**	**(001)**	**(110)**
Upper	0.908	0.935	0.915	0.900	0.333	-0.408	0.135	-0.626	0.863	0.121	-1.957
Lower	0.918	0.959	0.984	0.114	0.800	2.342	0.996	-0.650	0.835	0.034	-1.918

7.3.1 Characterization Results

The characterization results for alumina surfaces studied but not reported in the text are shown here in the supplementary materials.

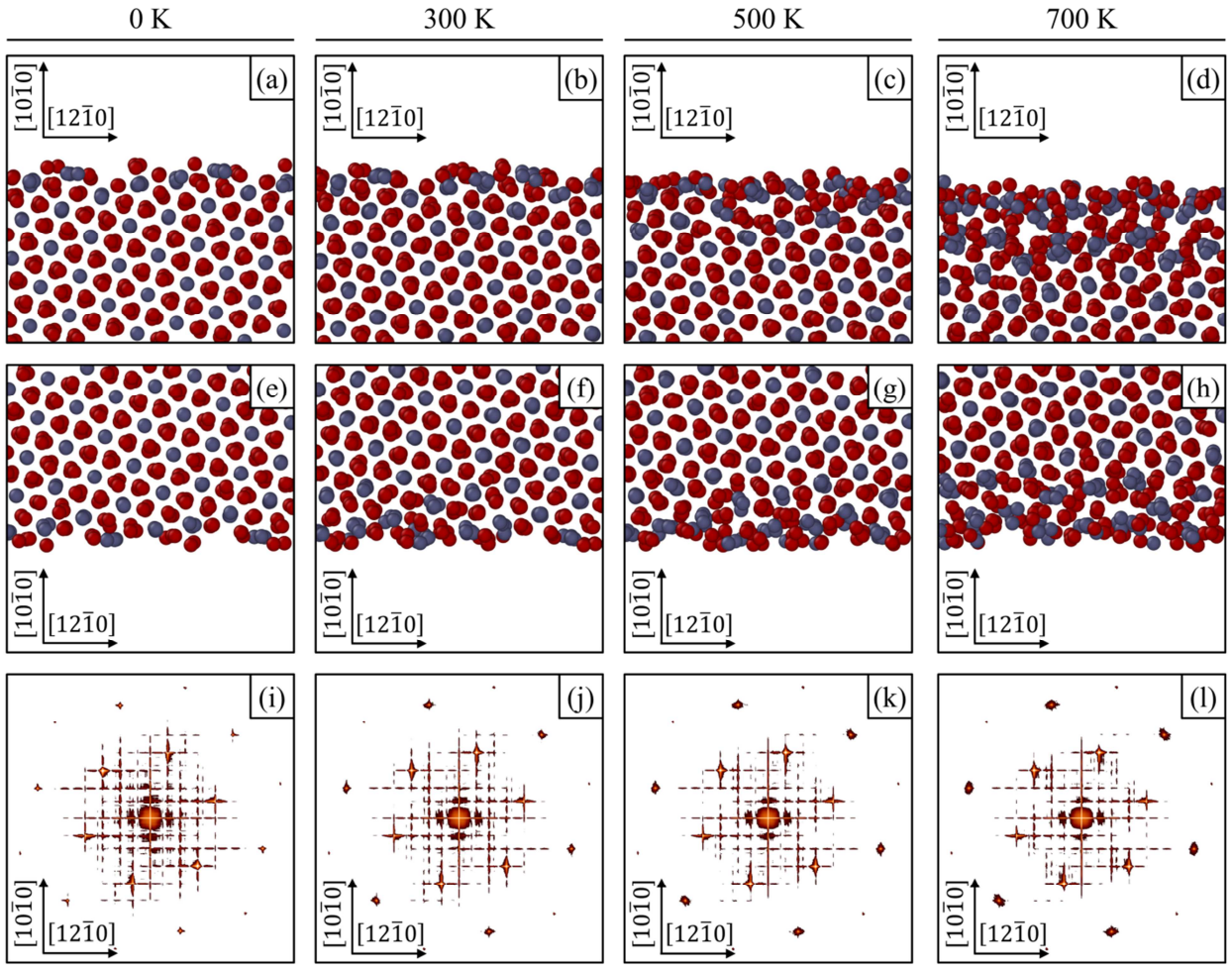

Figure 7.9: Characterization results for the α-Al_2O_3 ($1\bar{1}00$) surface viewed along the [0001] direction showing snapshots of the (a-d) upper and (e-h) lower surfaces as well as (i-l) virtual SAED patterns.

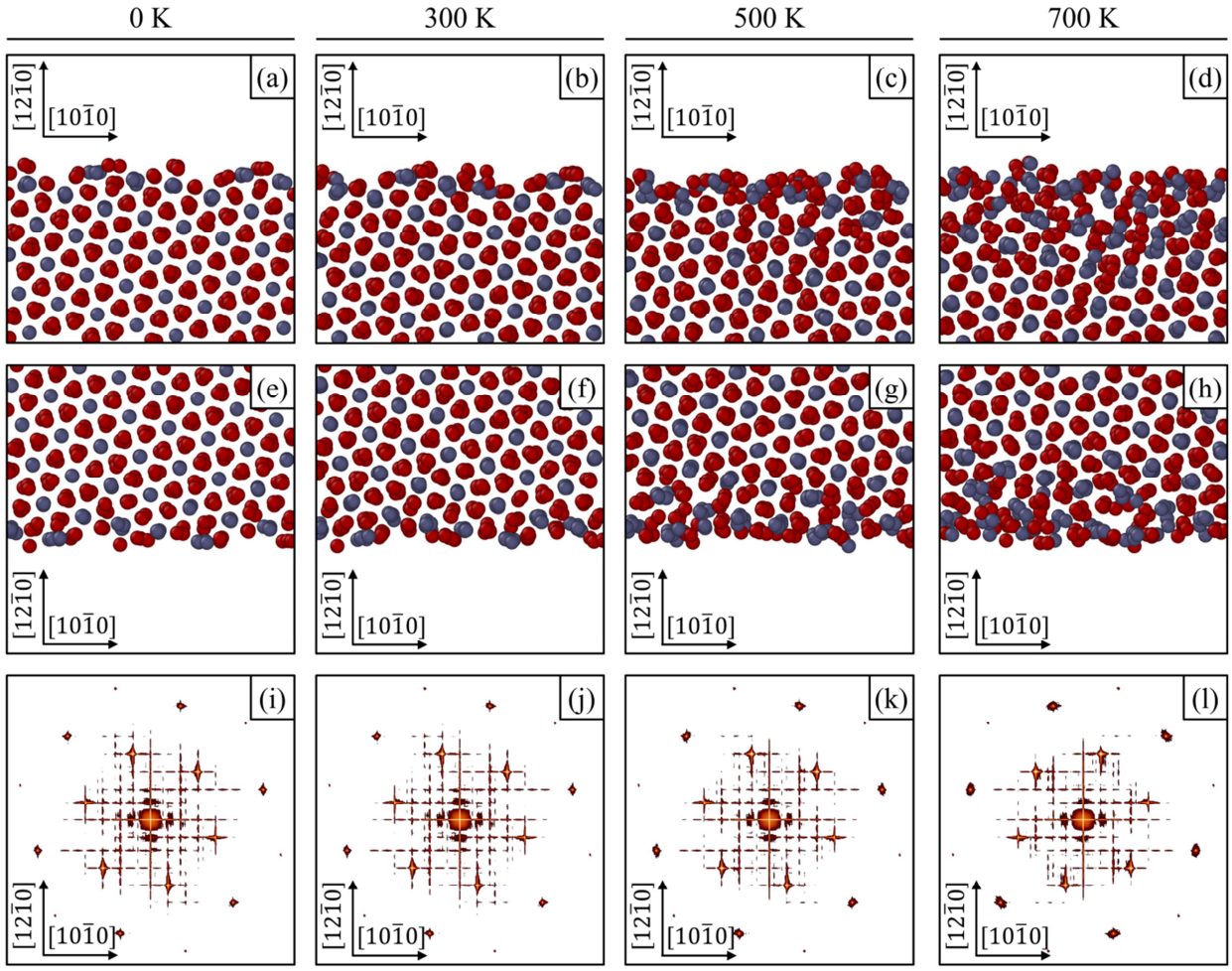

Figure 7.10: Characterization results for the α-Al_2O_3 $(11\bar{2}0)$ surface viewed along the [0001] direction showing snapshots of the (a-d) upper and (e-h) lower surfaces as well as (i-l) virtual SAED patterns.

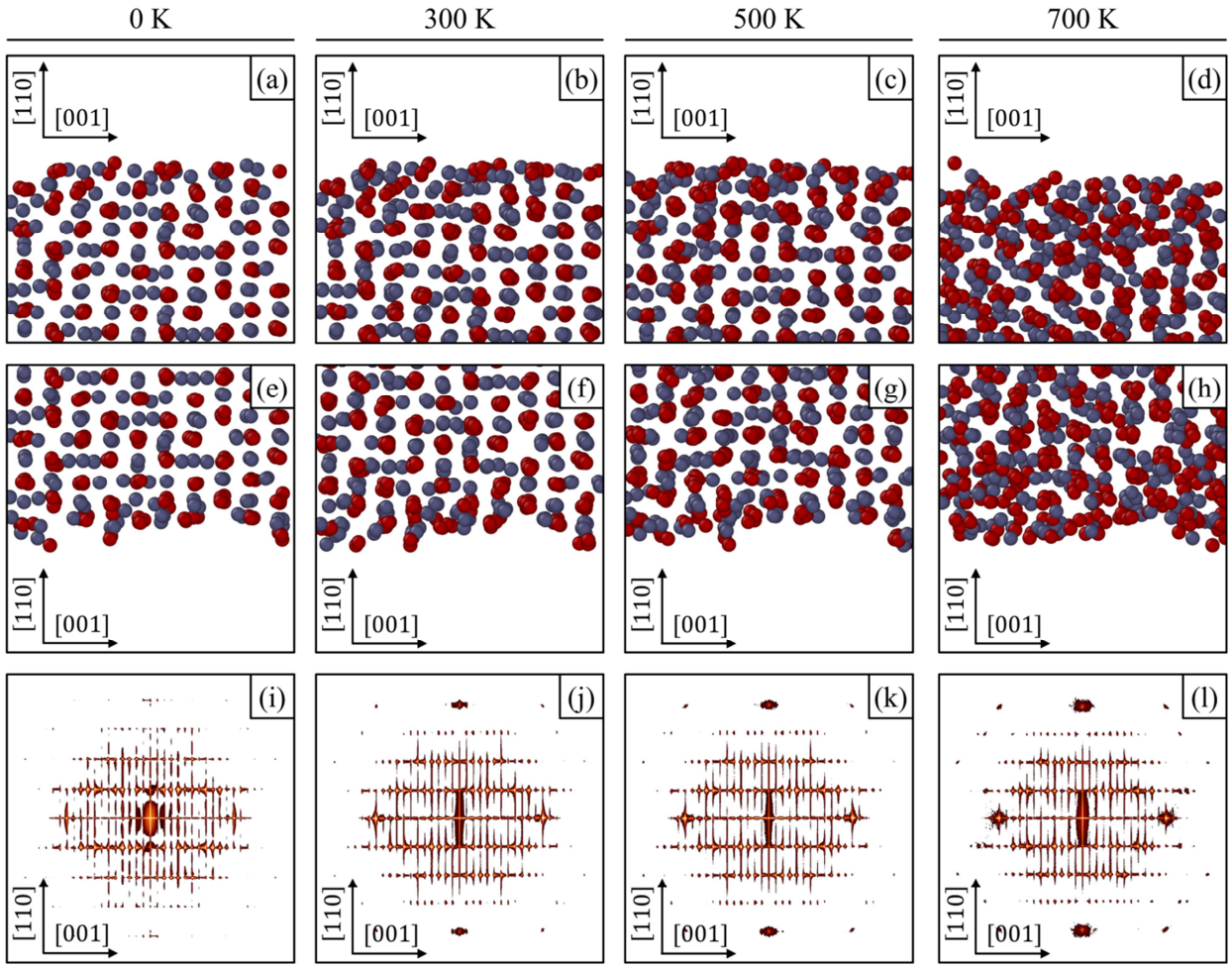

Figure 7.11: Characterization results for the γ-Al_2O_3 (110) surface viewed along the $[\bar{1}10]$ direction showing snapshots of the (a-d) upper and (e-h) lower surfaces as well as (i-l) virtual SAED patterns.

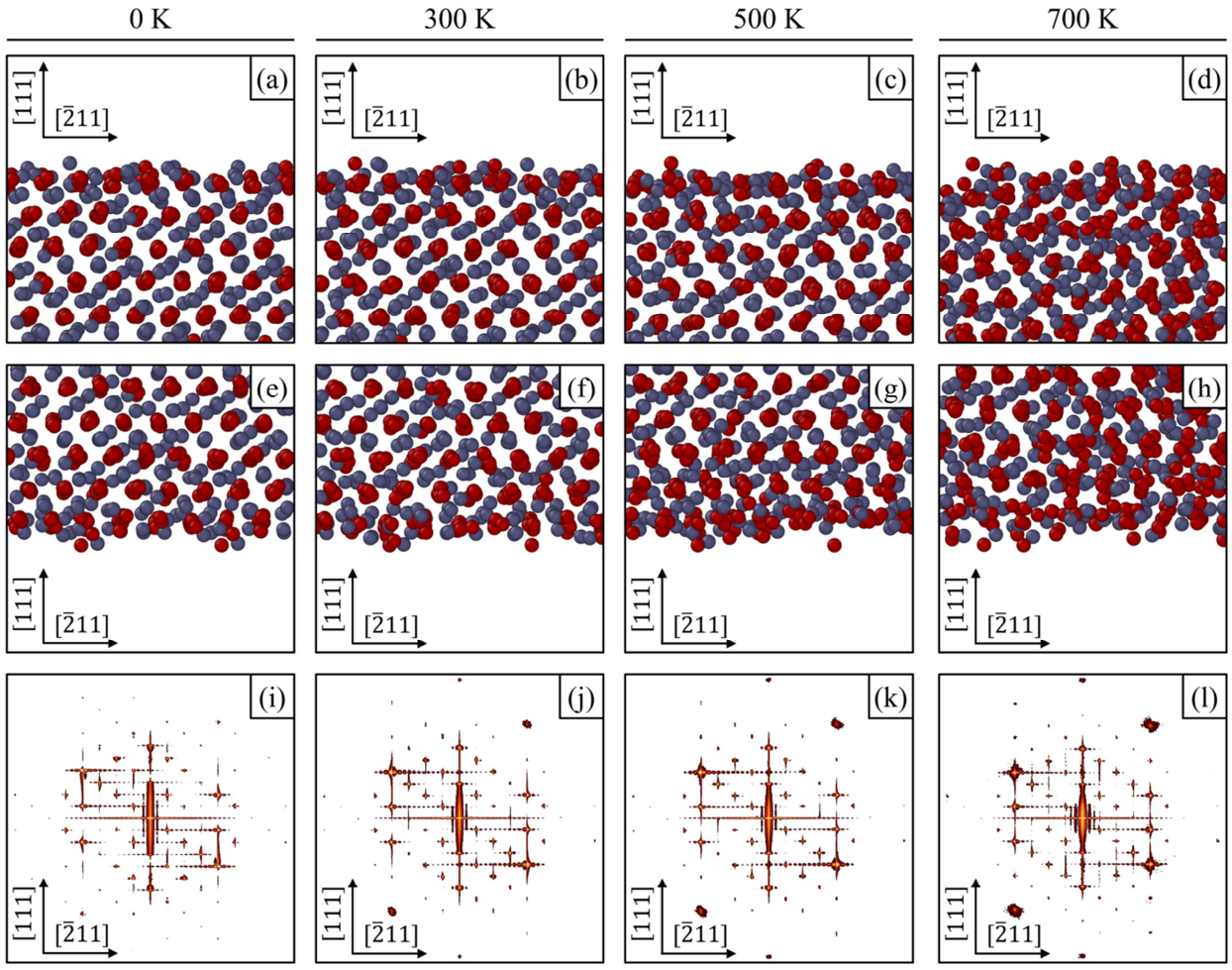

Figure 7.12: Characterization results for the γ-Al_2O_3 (111) surface viewed along the $[0\bar{1}\bar{1}]$ direction showing snapshots of the (a-d) upper and (e-h) lower surfaces as well as (i-l) virtual SAED patterns.

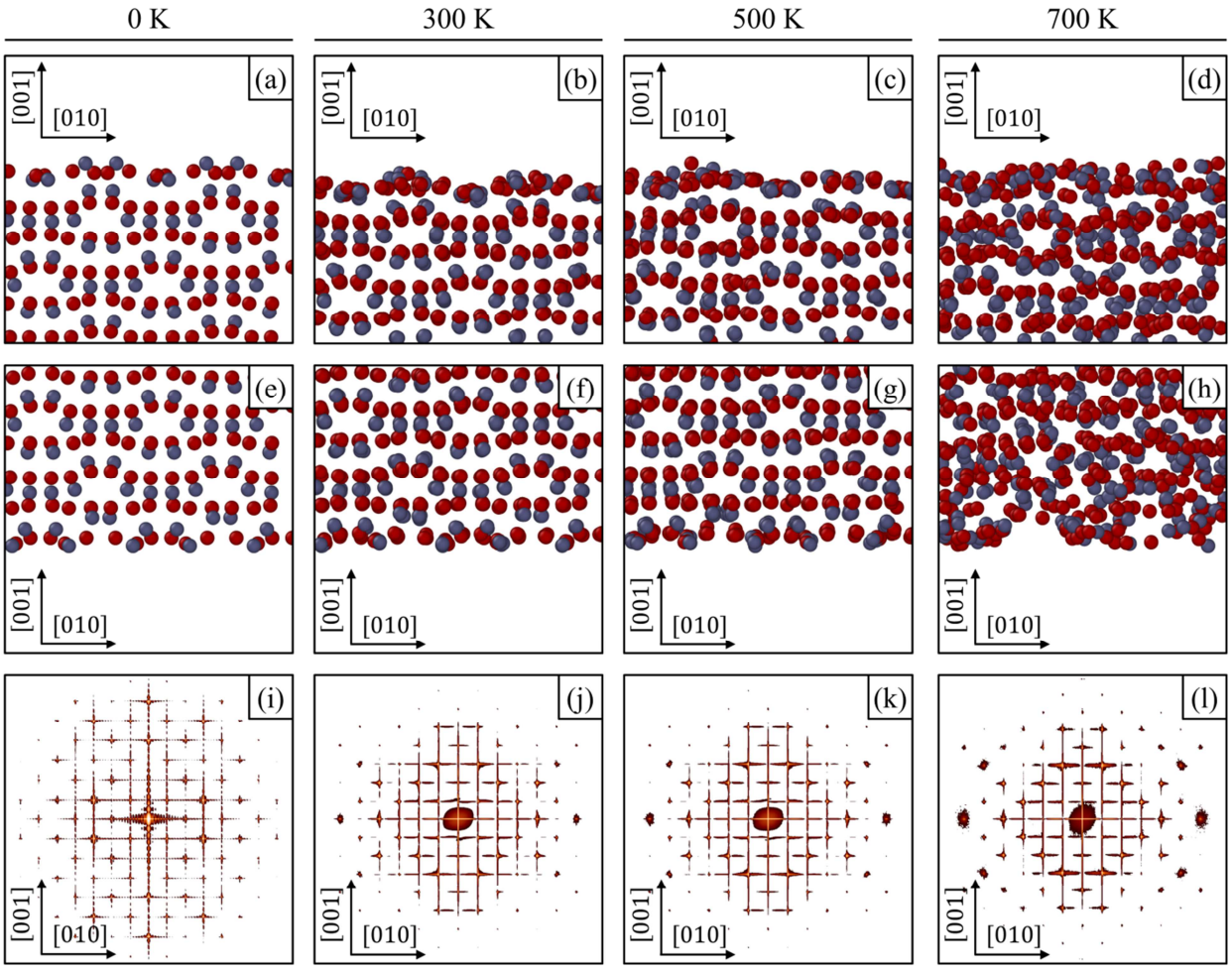

Figure 7.13: Characterization results for the κ-Al_2O_3 (001) surface viewed along the [100] direction showing snapshots of the (a-d) upper and (e-h) lower surfaces as well as (i-l) virtual SAED patterns.

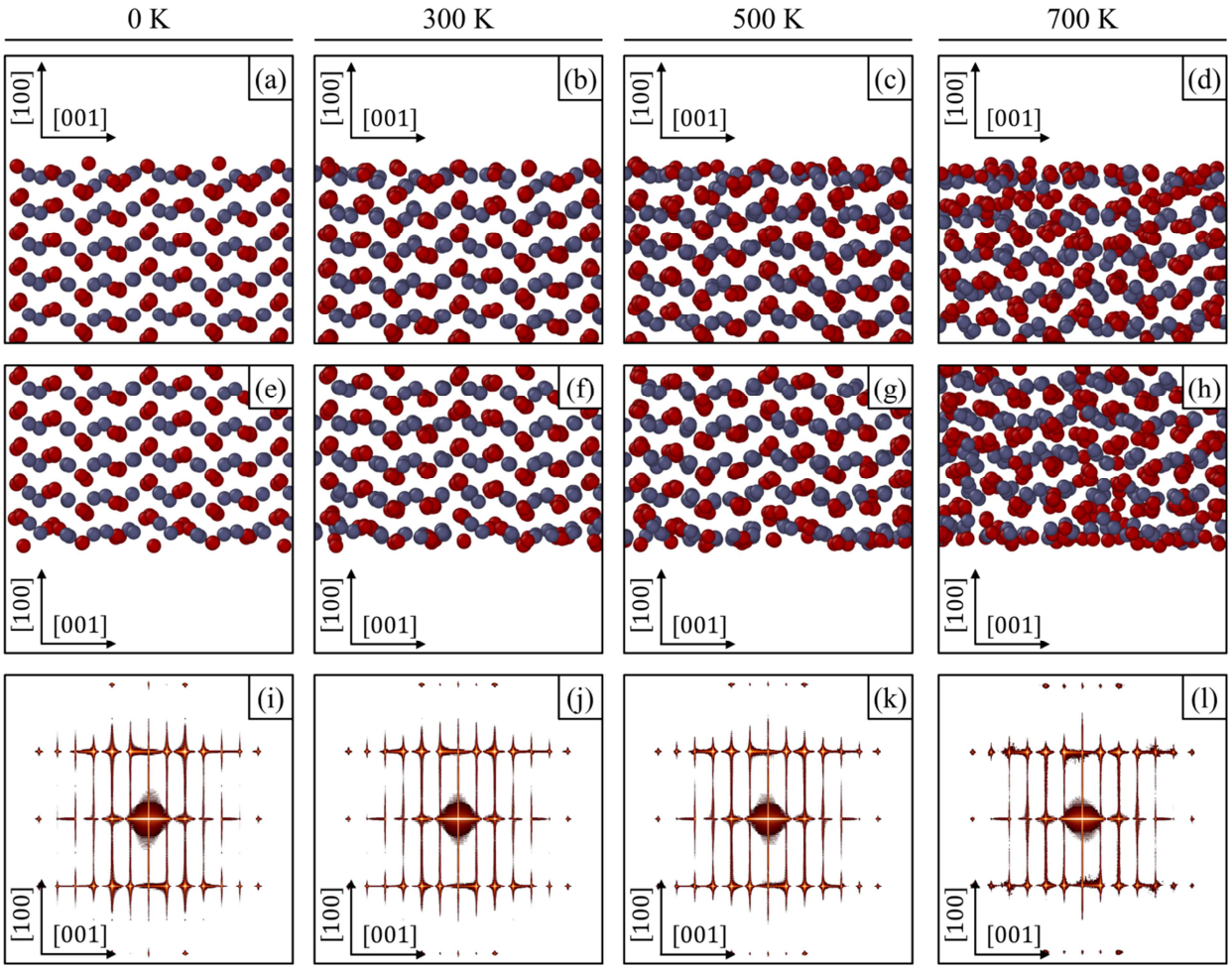

Figure 7.14: Characterization results for the κ-Al_2O_3(100) surface viewed along the [010] direction showing snapshots of the (a-d) upper and (e-h) lower surfaces as well as (i-l) virtual SAED patterns.

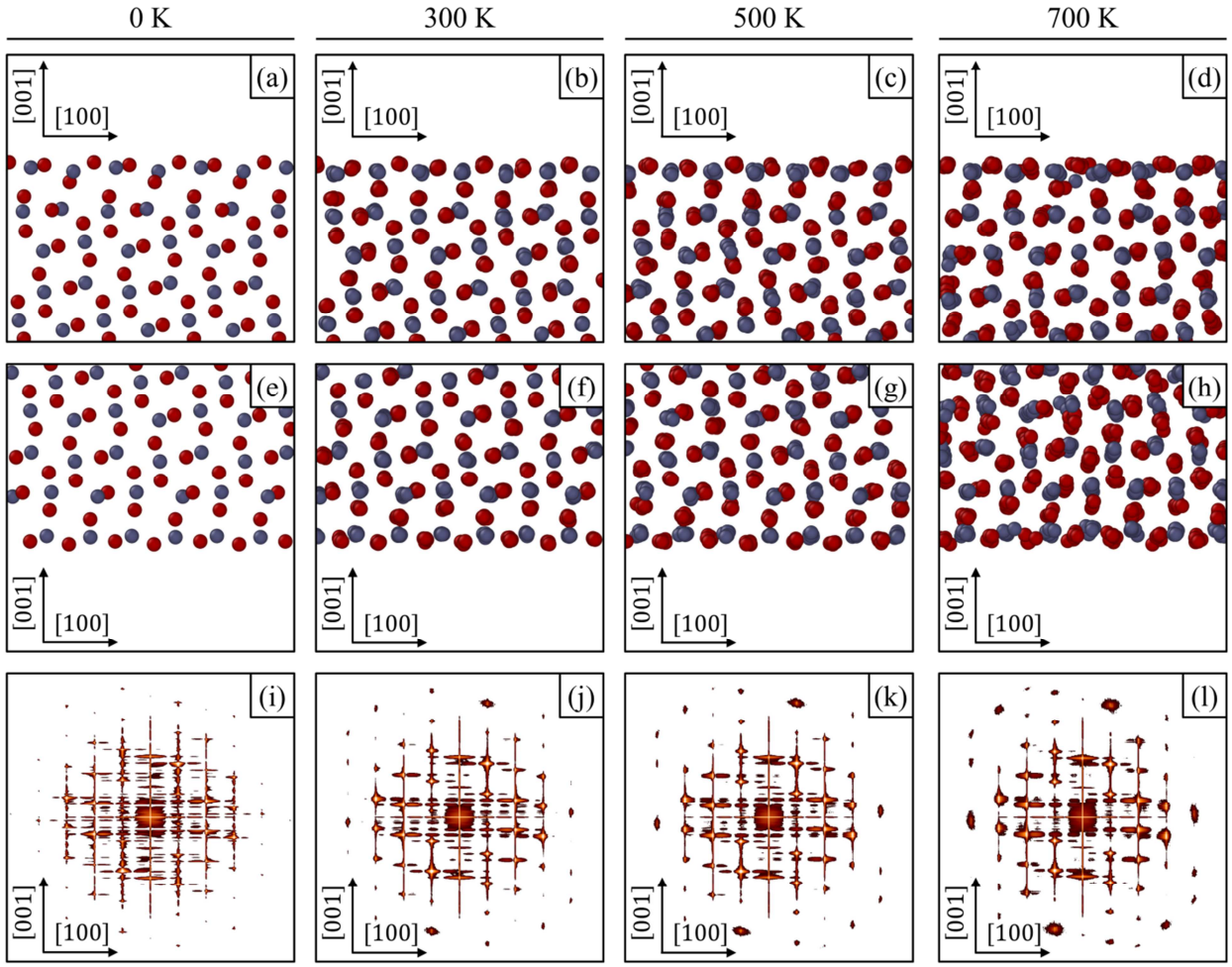

Figure 7.15: Characterization results for the θ-Al_2O_3(001) surface viewed along the [010] direction showing snapshots of the (a-d) upper and (e-h) lower surfaces as well as (i-l) virtual SAED patterns. (Color online)

Chapter 8: Atomistic Simulation and Virtual Diffraction Characterization of Homophase and Heterophase Alumina Interfaces

Shawn P. Coleman[a] and Douglas E. Spearot[a]

[a] Department of Mechanical Engineering, University of Arkansas, Fayetteville, AR 72701

Abstract

The minimum energy structures of twelve homophase and heterophase alumina interfaces are studied using the ReaxFF potential. First, the computational methods are validated by exploring a set of five α-Al_2O_3 symmetric tilt twin interfaces that have been studied in depth through prior simulations. The interface structures and energies for most homophase α-Al_2O_3 twins are in good agreement with prior atomistic studies; however, small deviations from prior works occur in select α-Al_2O_3 interfaces due to the larger interface areas explored in this work. Next, select experimentally observed κ-Al_2O_3, γ-Al_2O_3, and θ-Al_2O_3 homophase interfaces as well as heterophase α-Al_2O_3 // γ-Al_2O_3 and θ-Al_2O_3 // γ-Al_2O_3 interfaces are investigated for the first time using atomistic simulations. The computed interface energies for the γ-Al_2O_3 {111} twin and the θ-Al_2O_3 {200} twin interfaces are on the same order as that found for the lowest energy α-Al_2O_3 prismatic twin boundary. ReaxFF predicts the α-Al_2O_3 (0001) // γ-Al_2O_3 (111) interface to have the lowest energy of the structures studied. Lastly, virtual selected area diffraction patterns of select interfaces are used to experimentally validate the modeled interface structures. Because a consistent computational method is implemented throughout this work, the tabulated interface energies can be incorporated in future predictive mesoscale simulations of polymorphic alumina.

8.1 Introduction

Alumina (Al_2O_3) films are used in a variety of applications, ranging from electronic and catalytic supports [1,2] to thermal barrier and protective coatings [3,4], due the wide range of material properties exhibited by its various polymorphs. Deposition methods and processing conditions influence the microstructure and morphology of the alumina films, which influence the overall performance of the coatings. Both physical vapor deposition (PVD) and chemical vapor deposition (CVD) processes commonly result in the formation of mixtures of γ-Al_2O_3, θ-Al_2O_3, κ-Al_2O_3, and α-Al_2O_3 phases [5–13]. Generally, higher percentages of γ-Al_2O_3 and θ-Al_2O_3 metastable phases form using PVD methods or at lower processing temperatures [5–8], whereas higher percentages of κ-Al_2O_3 and α-Al_2O_3 phases form using CVD methods or at elevated temperatures [9–12]. The γ-Al_2O_3 and θ-Al_2O_3 metastable phases are desired in catalytic support applications due to their high surface area and acid-basic properties [14,15]. Differently, κ-Al_2O_3 and α-Al_2O_3 phases are desired in protective coating applications due to their wear resistance, chemical inertness, resistance to thermal shock, and high hardness [16,17]. Because α-Al_2O_3 is the only thermodynamically stable alumina phase, researchers and manufacturers seeking protective coatings will often employ thermal treatments to induce the necessary phase transformations to form α-Al_2O_3 [18,19]. Of course, the morphology of heat-treated films is dependent on the microstructure of the as-deposited polymorphic coatings [18,20].

As-deposited alumina films can be fully amorphous, nanocrystalline, or coarse-grained depending on the processing conditions used to create the coating [21]. Internal interfaces within polycrystalline alumina films can affect the properties and performance of the coating [22–26] as well as influence microstructure evolution during thermal treatment [27–29]. It is

known that abnormal grain growth in alumina occurs due to the presence of impurities and pores at the interfaces [30,31]. However, the effects of interface misorientation on grain growth in polycrystalline alumina films is not fully known [32–34], in particular for heterophase interfaces constructed from different adjoining alumina polymorphs. Despite not fully understanding the role of interfaces, researchers and manufacturers commonly create interfaces through deposition of multilayers which have been shown to be more wear resistant and easier to manufacture than single phase coatings [35,36].

Predictive mesoscale simulations of alumina vapor deposition can help determine the processing conditions needed to produce tailored film morphology and properties. To perform mesoscale simulations, such as phase-field modelling [37–39], extensive knowledge of alumina energetic data (i.e., bulk, surface, and interface energies) is needed. Atomistic simulations can easily compute the relevant energies required, but care must be taken to utilize the same computational method in order for these values to be used quantitatively. The current work utilizes the reactive force-field (ReaxFF) potential [40] to study homophase and heterophase alumina interfaces. An identical computational method has been used in a previous atomistic simulation study by the authors on bulk and surface alumina structures [41]. Together, these works tabulate the energetic data necessary to enable predictive mesoscale models to explore the unique processing conditions that achieve a desired tailored morphology and properties in polycrystalline and polymorphic alumina coatings.

This article begins with a detailed discussion of previous studies performed on alumina interfaces, focusing on prior atomistic simulations and the need for a consistent computational method to provide quantitatively comparable data. This is followed by a description of the current simulation and analysis methods imposed to extract interface energies and characterize

the atomic geometry near the alumina interfaces. Here, virtual diffraction methods [42,43] are implemented for the first time to aid in the construction of complex, heterophase alumina interfaces. Next, the computed interface energies are tabulated and reported alongside characterization results. Select alumina interfaces in this work are characterized using virtual selected area electron diffraction (SAED) patterns [42,43] that are directly comparable to experimental studies.

8.2 Previous alumina interface studies

Alumina interfaces have been studied using a variety of experimental and computational methods. The majority of previous atomistic simulation studies focused on five twin interfaces formed within α-Al_2O_3, as described in Table 8.1, using (i) molecular dynamics (MD), (ii) molecular statics (MS), (iii) density functional theory with local density approximations of the electron exchange-correlation (DFT-LDA), and (iv) density functional theory with generalized gradient approximations of the electron exchange-correlation (DFT-GGA). Each of these interfaces is created by a rotation of the basal plane about the $[1\bar{2}10]$ axis as shown schematically in Figure 8.1. Computed α-Al_2O_3 interface energies collected from previous atomistic simulations are listed in Table 8.2. Four previous research studies examined multiple α-Al_2O_3 interface structures using a consistent computational method within each study. These results

Table 8.1: Description of α-Al_2O_3 twin interfaces studied using atomistic simulation. Rotation is about the $[1\bar{2}10]$ tilt axis and measured from the $[10\bar{1}0]$ direction in the basal plane.

ID	Interface Planes	Rotation	Σ	Description
A	$(0001) // (0001)$	0°	3	Basal Twin
B	$(10\bar{1}0) // (10\bar{1}0)$	90°	3	Prismatic Twin
C	$(\bar{1}10\bar{2}) // (\bar{1}10\bar{2})$	56.9°	7	Rhombohedral Twin
D	$(10\bar{1}4) // (10\bar{1}4)$	142.5°	13	Pyramidal Twin
E	$(10\bar{1}1) // (10\bar{1}\bar{1})$	79.1°	11	General Twin

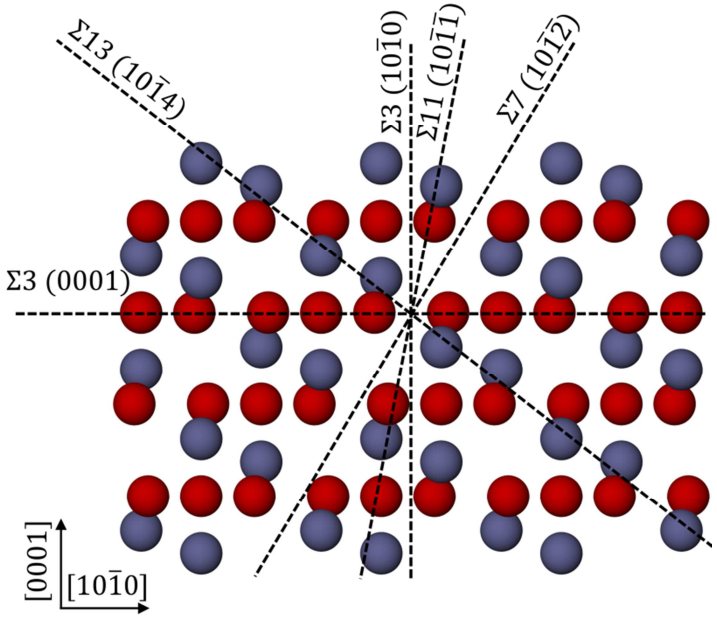

Figure 8.1: Diagram of five α-Al_2O_3 twin interface planes explored, viewed along the [$1\bar{2}10$] direction. In all figures within this work, the O and Al ions are colored red and gray, respectively.

showed that the ordering of interface energy can depend on several factors, including the computational method. For example, molecular statistics simulations performed by Galmarini et al. predicted the lowest interface energy in the basal twin structure (A) whereas the first-principles study performed by Elsässer et al. [44–51] and the molecular dynamics studies performed by Suzuki et al. [52], predicted the prsimatic twin structure (B) to have the lowest energy.

Deviations among the computed interface energies result partially from the different approximations used to model electrostatic interactions. The different approximations for electrostatic interactions affect the ability of the compuational method to capture the correct polarization of the O ions, which directly affects the accuracy of the energy calculation [62]. In addition, some of the deviations among the computed interface energies result from the construction of different energy-minimized interface structures created when different periodic

Table 8.2: Sample of computed α-Al_2O_3 interface energies from previous atomistic simulation studies.

Year	Method	A	B	C	D	E	Ref.
2014	DFT-GGA	---	---	---	1.70	---	[53]
2011	MS[a]	2.66	0.50	0.27	2.42	1.88	[54]
2010	DFT-GGA	---	---	---	1.65	---	[55]
2008	DFT-GGA	---	---	---	---	2.71	[56]
2007	DFT-GGA	---	---	---	1.25	---	[57]
2005	DFT-GGA	---	0.42	---	---	---	[58]
2003	MS[b]	---	---	0.40	---	---	[59]
2003	DFT-LDA	0.73	0.30	0.63	1.88	---	[45–51]
2003	MS[a]	1.71	0.10	---	---	---	[45–51]
1998	MD[b] (300 K)	1.66	0.19	0.95	---	1.97	[52]
1998	MD[b] (1500 K)	1.48	0.15	1.04	---	2.13	[52]
1998	MD[b] (1700 K)	1.62	0.19	1.04	---	2.54	[52]
1996	MS[a]	---	---	---	1.54	---	[60]
1994	MS[a]	1.50	---	---	1.10	1.70	[61]
1994	MS[a]	1.30	---	---	2.30	---	[61]
1994	MS[b]	1.00	---	---	1.70	---	[61]

[a] Pair Style – Charged Shell
[b] Pair Style – Point Charge

simulation cell dimensions are used. Different periodic simulation cell dimensions impose different image forces that affect the interface structure. Both the computational method and available resources can limit the simulation cell dimensions, which restricts the number of interface structures capable of being modeled. To the authors' knowledge, no prior atomistic study has examined homophase interfaces constructed from a metastable alumina phase nor has any atomistic study examined heterophase interfaces constructed from multiple alumina polymorphs, as is done in this work.

A much wider scope of alumina interface structures has been studied using experimental methods, such as high-resolution transmission electron microscopy and electron diffraction. Several research groups have characterized the structure [63–67], analyzed impurities [68,69], and determined interface energies [70,71] in diffusion bonded α-Al_2O_3 bicrystals, while others have performed similar analyses using polycrystalline α-Al_2O_3 [72–74]. Experimentally

measured interface energies for α-Al_2O_3 are reflective of the type of samples considered. For example, the 0.85 J/m^2 interface energy measured by Shin et al. [74] using polycrystalline α-Al_2O_3 represented an averaged value for all interfaces sampled. Differently, analysis of α-Al_2O_3 [0001] symmetric tilt bicrystals conducted by Sakuma and coworkers [70,71] revealed three classifications of interfaces with different energy values: (i) special Σ7 $(2\bar{3}10)$ // $(\bar{3}210)$ and Σ3 prismatic twin boundaries with low-energy interfaces approximately 0.054 J/m^2, (ii) low-angle, Σ21 $(45\bar{1}0)$ // $(\bar{5}410)$ and Σ13 $(34\bar{1}0)$ // $(\bar{4}310)$ boundaries with interface energies approximately 0.4 J/m^2, and (iii) large-angle and Σ19 $(3\bar{5}20)$ // $(\bar{5}320)$ boundaries with interface energies approximately 0.7 J/m^2.

Table 8.3: Sample of experimentally observed homophase and heterophase alumina interfaces containing metastable Al_2O_3.

ID	GB Planes	Ref.
F	γ-Al_2O_3 {111} Twins	[75,76]
G	κ-Al_2O_3 {001} 120° Twins	[77]
H	θ-Al_2O_3 {200} Twins	[78]
I	θ-Al_2O_3 {110} Twins	[79]
J	$(110)_\theta$ // $(100)_\gamma$	[80]
K	$(010)_\theta$ // $(0\bar{1}1)_\gamma$	[82,84]
L	$(0001)_\alpha$ // $(111)_\gamma$	[80,81]
M	$(10\bar{1}0)_\alpha$ // $(110)_\gamma$	[80]
N	$(11\bar{2}0)_\alpha$ // $(11\bar{2})_\gamma$	[82,84]

Homophase interfaces constructed from a metastable alumina phase and heterophase interfaces constructed from multiple alumina phases have also been studied experimentally, as described Table 8.3. Multiple {111} γ-Al_2O_3 twins (F) were observed during CVD, which promoted texture within the films grown [75,76]. An analysis of pure κ-Al_2O_3 observed platelet like crystal formations oriented along {001} containing 120° twinning (G) of three crystal

regions, which mimicked pseudo-hexagonal structures [77]. Twinning also occurred in θ-Al_2O_3 on the {200} [78] and the {110} [79] mirror planes (H and I, respectively). Five heterophase alumina interfaces were identified from studies exploring the phase transition series of alumina which exhibit good crystallographic compatibility [75–83]. These commensurate interphases included two θ-Al_2O_3 // γ-Al_2O_3 interfaces (J-K) and three α-Al_2O_3 // γ-Al_2O_3 interfaces (L-N).

8.3 Methods

Atomistic simulations of alumina are performed with LAMMPS [85] using the ReaxFF potential [40]. ReaxFF is chosen for this work because of its transferability to many alumina phases, as shown in a previous study by the authors on bulk and surface alumina [41]. The ReaxFF parameters used in the previous [41] and the current study were first optimized by Zhang et al. [86] for Al and α-Al_2O_3 using first-principles simulations of Al-O clusters, then further tailored by Sen et al. [87] to better incorporate varying Al oxidation states during oxidation simulations. In the previous study [41], the authors showed that ReaxFF [87] correctly predicts α-Al_2O_3 as the lowest energy crystalline alumina phase; however, it unexpectedly predicts an even lower energy amorphous phase. The lower energy amorphous phase biased substantial surface reconstructions during MD simulations at temperatures well below what is expected from experiments. However, because no substantial surface reconstructions were observed at 0 K, it was concluded that the added thermal energy during MD helped promote the surface transformations. Thus, to avoid unnatural reconstructions, the current study on alumina interface structures is restricted to MS simulations performed at 0 K. Further, interface structures in this work are validated by experiment, when possible, using virtual SAED to ensure ReaxFF provides accurate results.

Alumina interfaces are studied using stoichiometric fully periodic bicrystal models and

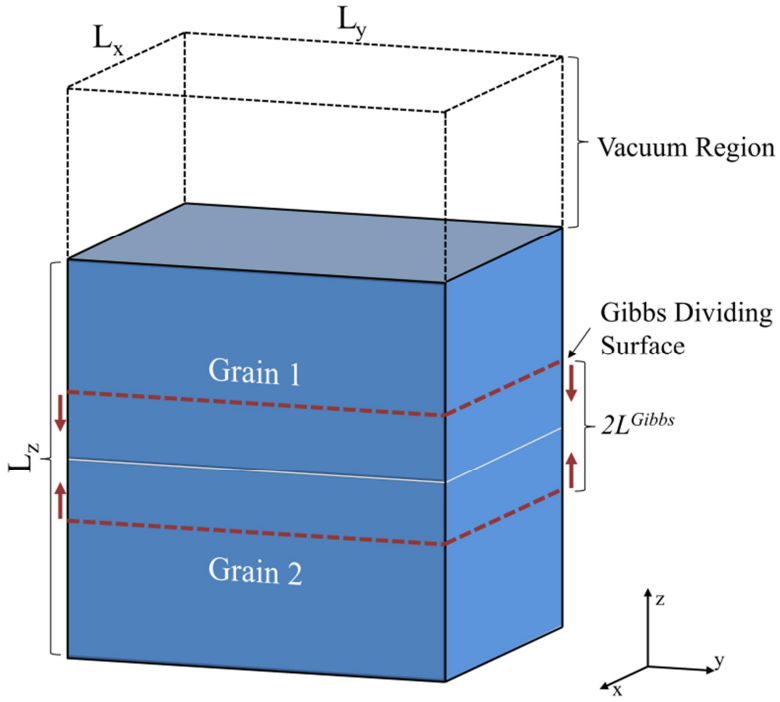

Figure 8.2: Schematic of the bicrystal (slab) model used to study alumina interfaces. Note, the vacuum region is imposed only when asymmetric lattice terminations prevent the formation of identical interface structures.

bicrystal slabs, as shown schematically in Figure 8.2. For most homophase interfaces, fully periodic bicrystal models are constructed with dimensions normal to the boundary chosen such that two identical interface structures are created with a minimum 40 Å separation, without the vacuum region. For other interfaces, asymmetric lattice terminations prohibit the modeling of two identical interface structures; therefore, these select interfaces are studied using bicrystal slab models created by the adjoining lattice regions and separated by a minimum 100 Å vacuum region. For all models, the dimensions parallel to the interface plane are chosen to minimize the strain experienced by both lattices due to the application of periodic boundary conditions. When possible, the adjoining planes of each opposing lattice region are terminated with Al and O ions, respectively, in order to satisfy the electrostatic interactions within the interface structure. For all models, the minimum energy interface structure is found through an iterative process that (i)

systematically translates one of the orientated crystal regions and (ii) performs a non-linear conjugate gradient energy minimization at each translation.

The minimum interface energy found through translations and energy minimizations is associated with a selected interface orientation relationship. When constructing heterophase interface models that are described solely by boundary planes, one must also consider the relative rotation in the interface plane between the lattice regions to find an optimal orientation relationship. In this work, the orientation relationship between lattice regions is chosen with the aid of virtual diffraction. First, three-dimensional diffraction intensities are computed for each lattice region using the methods described by Coleman et al. [42]. Next, the diffraction intensity data for each lattice are superimposed using the VisIt visualization software [88]. An optimal orientation relationship between the lattice regions is chosen by virtually rotating the diffraction data for one lattice until a maximum overlap of the diffraction intensities is achieved. This method proved successful in identifying the ideal minimum energy orientation relationship for the α-Al_2O_3 (0001) // γ-Al_2O_3 (111) interface [43] and is uniquely enabled by the virtual diffraction method [42].

Interface energies are calculated using two methods. For fully periodic bicrystals containing two identical interface structures, an averaged interface energy, E_{Int}^{ave}, for the entire model is computed via,

$$E_{Int}^{ave} = \frac{E_{12}^{Tot} - nE_1^{Unit} - mE_2^{Unit}}{2A} \quad . \tag{8.1}$$

Here, E_{12}^{Tot} is the total potential energy of the fully periodic bicrystal model, n and E_1^{Unit} are the number of unit cells and minimized potential energy for the bulk alumina phase in Grain 1, m and E_2^{Unit} are the number of unit cells and minimized potential energy for the bulk alumina phase

in Grain 2, and A is the area of the interface. Interface energies are also computed for all models using a method employing Gibbs dividing surfaces [89] to isolate a stoichiometric region containing the interface. Interface energies computed using Gibbs dividing surfaces, E_{Int}^{Gibbs}, are computed via,

$$E_{Int}^{Gibbs} = \frac{E_{12}^{Gibbs} - hE_1^{Unit} - kE_2^{Unit}}{A} \quad . \tag{8.2}$$

Here, E_{12}^{Gibbs} is the total potential energy of the atoms within the Gibbs region containing the interface, h is the number of unit cells associated with Grain 1 in the Gibbs region, and k is number of unit cells associated with Grain 2 in the Gibbs region. The Gibbs dividing surfaces are placed through an iterative process that takes equal steps in both directions normal to the interface while careful consideration is taken to maintain stoichiometry of the enclosed region and for each lattice. For complex orientations and phases, planar slices normal to the interfaces are not sufficient to enclose a stoichiometric region. In these cases, the necessary number of Al or O ions nearest to the Gibbs dividing surfaces are added to the Gibbs region in order to achieve stoichiometry. Because ReaxFF implements a variable charge equilibration scheme [90], the charge neutrality of the selected Gibbs region is not guaranteed at every placement of the dividing surfaces. Interface energies computed using Gibbs dividing surfaces are reported for Gibbs dividing surfaces located the smallest distance from the interface structure, L^{Gibbs}, where the averaged charge of the ions within the Gibbs region is below 0.005 q/atom.

Additionally, the work of adhesion for select bicrystal slab models is defined as the force needed to separate the adjoined lattice regions at the interface, creating two additional surfaces. Work of adhesion, W_{ad}, is computed via,

$$W_{ad} = \frac{\left(E_1^{Tot} + E_2^{Tot} - E_{12}^{Tot}\right)}{A} \quad . \tag{8.3}$$

Here, E_{i}^{Tot} (i = 1,2) is the total potential energy computed for slab models of each lattice region and E_{12}^{Tot} is the total energy of the bicrystal slab containing the interface. When computing work of adhesion, slab models for each region maintain the same terminating structure as found in the interface model, but are relaxed via a non-linear conjugate gradient method before computing E_{i}^{Tot}.

8.4 Results and Discussion

8.4.1 *α-Al_2O_3 homophase interfaces*

In order to validate the methods for computing interface energies, this work first reexamines five previously studied [44–61] twins formed by α-Al_2O_3 using both fully periodic bicrystal and bicrystal slab models. Table 8.4 lists the computed interface energies and work of adhesion for each of the α-Al_2O_3 interfaces. The averaged interface energy for each fully periodic bicrystal model is in good agreement with the interface energy computed using Gibbs dividing surfaces. However, computed work of adhesion do not show a clear correlation with the interface energies. ReaxFF predicts the ordering of E_{Int}^{ave} and E_{Int}^{Gibbs} as B < C < D < A < E indicating the prismatic twin (B) is the most energetically stable α-Al_2O_3 interface, whereas the ordering for W_{ad} follows A > B > D > C > E indicating the basal interface (A) requires the largest force for separation. The lack of correlation between the work of adhesion and interface energies stems from the creation of non-minimum energy alumina surfaces upon the separation of select bicrystal slab models. For example, the opposing lattice regions forming the minimum energy basal interface (A) are terminated by Al and O ions, respectively, which upon separation form high-energy surfaces (2.87 J/m^2) as compared to the stable α-Al_2O_3 (0001) surface (0.75 J/m^2) [41]. In Eq.

(8.3), the creation of two additional high-energy surfaces increases the values for E_{i}^{Tot} as compared to E_{12}^{Tot} resulting in a larger W_{ad} for the basal interface. Because the work of adhesion are found to be dependent on the surface structures created upon separation, energetic data for the remainder of this work is restricted to the interface energies computed using Gibbs dividing surfaces.

Table 8.4: Computed α-Al_2O_3 interface energies and work of adhesion using ReaxFF.

ID	E_{Int}^{ave} (J/m^2)	E_{Int}^{Gibbs} (J/m^2)	$2L^{Gibbs}$ (Å)	W_{ad}(J/m^2)
A	0.81	0.81	31.34	4.95
B	0.33	0.35	9.43	2.17
C	0.54	0.60	34.19	1.20
D	0.65	0.66	15.44	1.82
E	1.46	1.41	11.73	1.12

With a few exceptions, the magnitude and relative order of the α-Al_2O_3 interface energies predicted by ReaxFF are consistent with those predicted by Elsässer et al. [44–51] who used DFT-LDA computational methods. Both methods predict the prismatic twin (B) to be the most energetically stable α-Al_2O_3 boundary with interface energies of 0.35 and 0.30 J/m^2 predicted by ReaxFF and DFT-LDA [51], respectively. ReaxFF and DFT-LDA also predict the next energetically stable α-Al_2O_3 boundary as the rhombohedral twin (C) with interface energies of 0.60 and 0.63 J/m^2 [45]. Different from the results predicted by Elsässer et al. [45–51], ReaxFF predicts the pyramidal twin (D) to be more energetically stable than the basal twin (A). The interface energies for the pyramidal twin and basal twin modeled in this study by ReaxFF are 0.66 and 0.81 J/m^2, respectively, versus 1.88 and 0.73 J/m^2, respectively, predicted using DFT-LDA [44,46].

The differences between the current work and that predicted using DFT-LDA stems partly

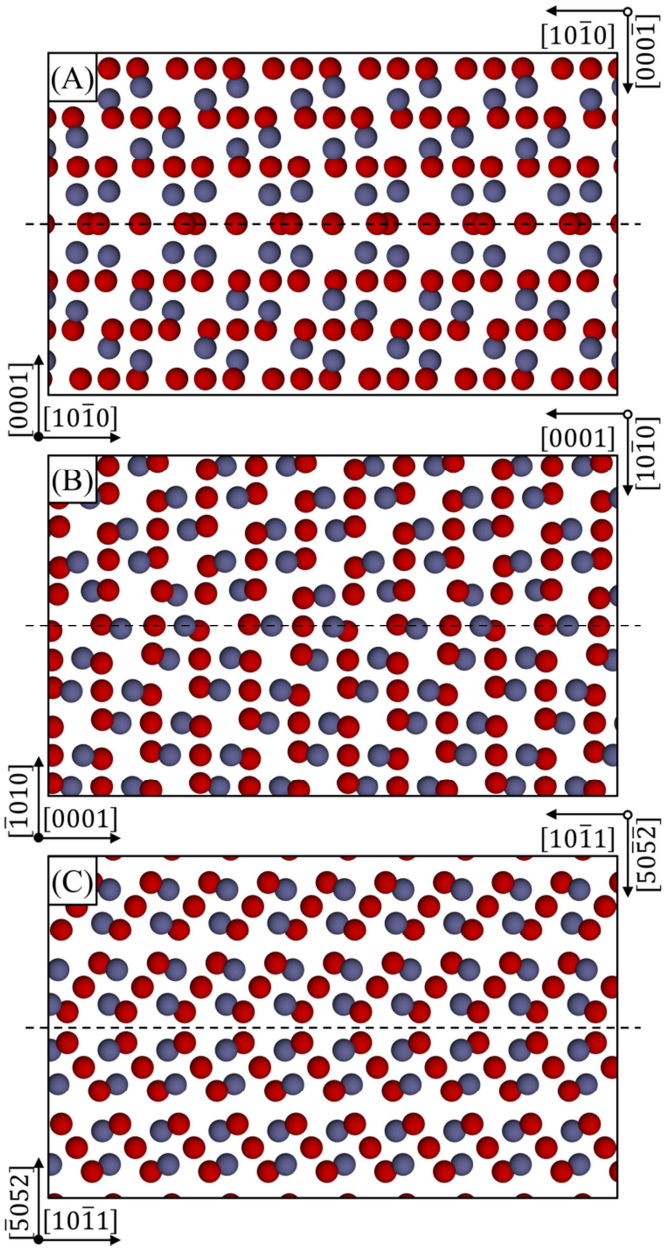

Figure 8.3: Minimum energy structures viewed along the $<1\bar{2}10>$ directions of special low Σ α-Al_2O_3 interfaces: (A) the basal twin (B) the prismatic twin, and (C) rhombohedral twin.

from the different approximations within the computational methods as well as deviations between the energy minimized structures. Figure 3 shows the structures of special low Σ α-Al_2O_3 twin interfaces, which are identified by their corresponding IDs in Table 1. Similar to prior studies [44,61], ReaxFF predicts the minimum energy basal interface structure (A) to be

centered about a mirror-symmetric O plane. Relaxations of the atomic structure normal to the basal interface are minimal; however, ReaxFF does predict more substantial relaxation within the central O plane than previously reported [44,61]. The minimum energy interface structures found using ReaxFF for the α-Al_2O_3 prismatic twin (B) and rhombohedral twin (C) boundaries are consistent with those found in the prior DFT-LDA work. Figure 4 shows the minimum energy structures predicted for the higher Σ α-Al_2O_3 interfaces studied. ReaxFF predicts an Al ion terminated α-Al_2O_3 pyramidal twin (D) structure, which is consistent with the prior DFT-LDA results [46].

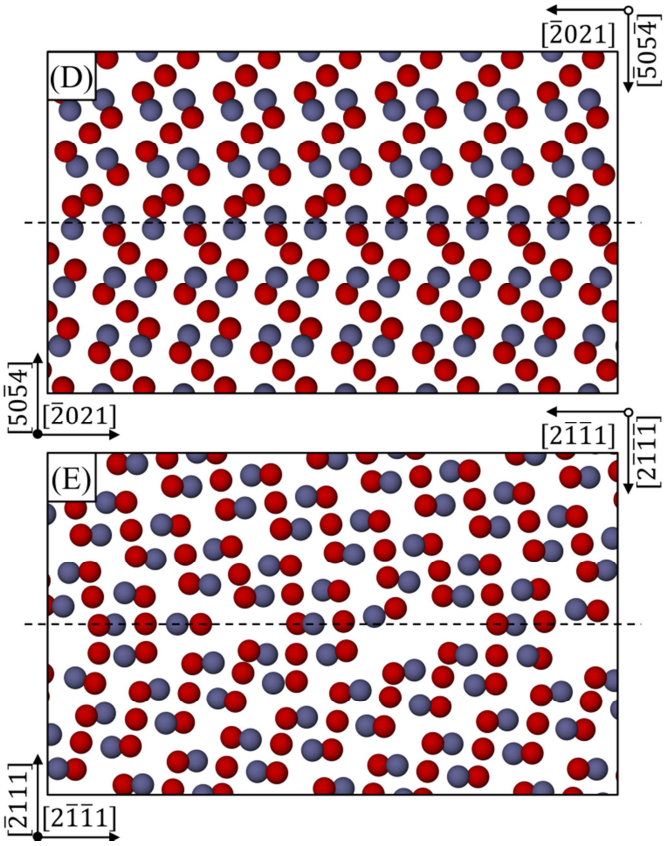

Figure 8.4: Minimum energy structures viewed along the $<1\bar{2}10>$ directions of higher Σ α-Al_2O_3 interfaces: (D) Σ13 pyramidal twin and (E) Σ11 $(10\bar{1}1)$ // $(10\bar{1}\bar{1})$ twin.

In Figure 8.4, the minimum energy α-Al_2O_3 $\Sigma 11$ $(10\bar{1}1)$ // $(10\bar{1}\bar{1})$ interface (E) was not explored by Elsässer et al. [45–51], but contains local structures similar to those predicted by Milas et al. [56] and Kenway [61] using DFT-GGA and MS computational methods, respectively. Due to computational limitations, the simulation cells used in the prior works were much smaller than those used in the current study, with interface plane dimensions of approximately 4.8 x 15.5 $Å^2$ versus 24.46 x 75.05 $Å^2$ used currently. The larger simulation cell used in this work allows a proper 79.1° rotation about the $[12\bar{1}0]$ axis of O ions oriented within the basal plane versus the ~73° rotation used previously to aid the construction of a smaller simulation cell. In addition, the larger simulation cell enables a more complete representation of the structures found within the interface plane. ReaxFF predicts large voids at local regions near the interface of the adjoining lattice regions which are similar to those found in low-energy interfaces predicted by both Milas et al. [56] and Kenway [61]. In addition, ReaxFF also predicts local regions of ions having more uniform spacing across the interface which was observed as the global minimum energy structure created by Milas et al. [56].

8.4.2 *Metastable Al_2O_3 homophase interfaces*

Three metastable homophase Al_2O_3 interface structures are studied in this work: a γ-Al_2O_3 {111} twin (F), a κ-Al_2O_3 {001} 120° twin (G), and a θ-Al_2O_3 {200} twin (H) boundary. Figure 8.5 shows snapshots of the energy minimized interface structures as well as describes the specific lattice orientations used in the study. The initial structures for each oriented lattice are derived from bulk κ-, γ-, and θ-Al_2O_3 structures determined by Yourdshahyan et al. [91], Paglia et al. [92] and Zhou et al. [93], respectively. As shown, the minimum energy γ-Al_2O_3 {111} twin interface (F) contains a central plane of O ions that relax to optimize the Al-O interactions.

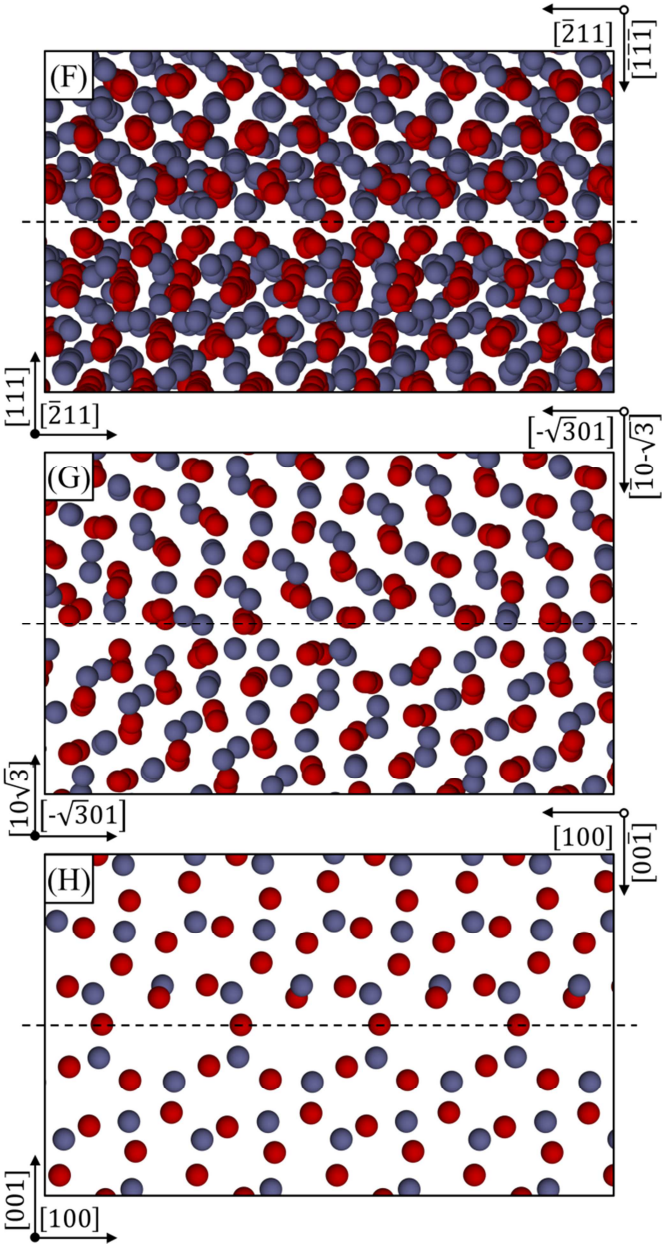

Figure 8.5: Minimum energy structures viewed along the misorientation axis of homophase interfaces constructed from metastable alumina: (F) γ-Al_2O_3 {111} twin, (G) κ-Al_2O_3 {001} 120° twin, and (H) θ-Al_2O_3 {200} twin.

Note, determination of the atomic relaxation within each region is difficult due to the complex structure of γ-Al_2O_3, which appears slightly non-crystalline even in bulk models due the distribution Al ions in O interstitial sites [92]. In Figure 8.5, the κ-Al_2O_3 {001} 120° twin (G) structure is formed with Al and O ion terminations at the interface. Similar to the α-Al_2O_3 Σ11

$(10\bar{1}1)$ // $(10\bar{1}\bar{1})$ interface (E), local regions of the κ-Al_2O_3 {001} 120° twin contain voids near the interface of the adjoining lattices while other local regions are filled with more uniformly spaced ions across the interface. Lastly, ReaxFF predicts that the θ-Al_2O_3 {200} twin (H) is centered about an O plane. The minimum energy θ-Al_2O_3 {200} twin shows asymmetric relaxations of the ions on either side of the central O plane. Specifically, small relaxations of the Al and O ions occur in the first layer of the upper θ-Al_2O_3 {200} lattice, whereas no relaxations are evident in the bottom region.

Table 8.5: Computed metastable Al_2O_3 interface energies modeled with ReaxFF.

ID	E_{Int}^{Gibbs} (J/m^2)	$2L^{Gibbs}$ (Å)
F	0.29	34.4
G	1.17	10.31
H	0.37	35.15

Table 8.5 lists the computed interface energies for each of the metastable homophase Al_2O_3 interface structures. ReaxFF predicts that both the γ-Al_2O_3 {111} twin (F) and the θ-Al_2O_3 {200} twin (H) have energies on the same order as that found for the lowest energy α-Al_2O_3 prismatic twin boundary (0.29 and 0.37 J/m^2, respectively). Differently, the computed interface energy for the κ-Al_2O_3 {001} 120° twin (G) is 1.17 J/m^2, which is on the order of the highest energy α-Al_2O_3 Σ11 $(10\bar{1}1)$ // $(10\bar{1}\bar{1})$ interface. It is interesting to note that the atomic charge distribution within the higher energy κ-Al_2O_3 {001} 120° twin requires a smaller L^{Gibbs} to achieve an effective neutral averaged charge within the Gibbs region than the other homophase interfaces constructed from metastable alumina phases.

8.4.3 *Heterophase Al_2O_3 interfaces*

The heterophase Al_2O_3 interfaces studied in this work include the (J-M) boundaries listed

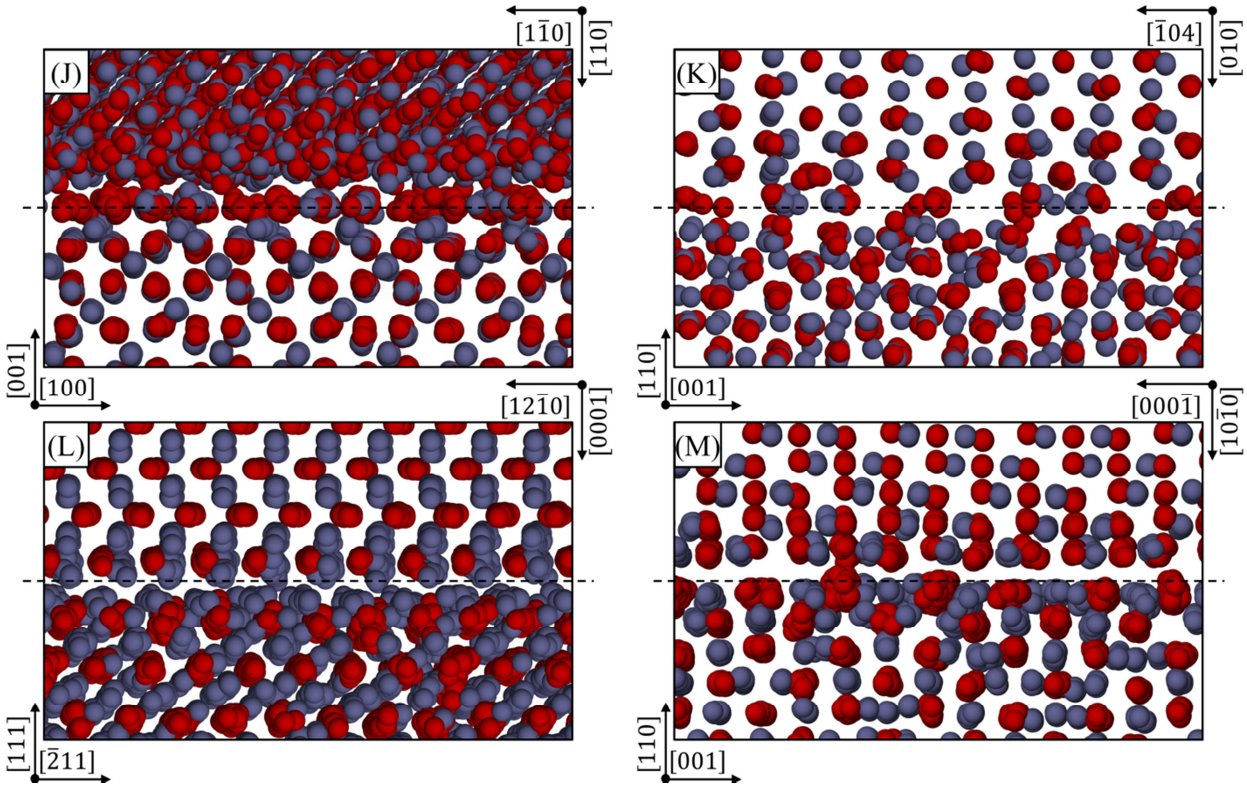

Figure 8.6: Minimum energy structures viewed along the misorientation axis of heterophase interfaces constructed from multiple alumina phases: (J) $(110)_\theta$ // $(100)_\gamma$ interface, (K) $(010)_\theta$ // $(0\bar{1}1)_\gamma$ interface, (L) $(0001)_\alpha$ // $(111)_\gamma$ interface, and (M) $(10\bar{1}0)_\alpha$ // $(110)_\gamma$ interface.

in Table 8.3. Figure 8.6 shows snapshots of each energy minimized heterophase interface, oriented such that γ-Al_2O_3 occupies the lower lattice region. In the $(110)_\theta$ // $(100)_\gamma$ interface (J), both lattices are terminated with a mixture of Al and O ions that relax into the interfacial region. The magnitude of the relaxations experienced by the Al and O ions located in the lower $(100)_\gamma$ lattice is greater than that found in the upper $(110)_\theta$ lattice and continues further into the bulk, upwards of 10 Å. Differently, in the $(010)_\theta$ // $(0\bar{1}1)_\gamma$ interface (K), the magnitude of the relaxations in the lower $(0\bar{1}1)_\gamma$ lattice is less than the relaxations in the upper $(010)_\theta$ lattice. These findings suggest that interface relaxations could be correlated to the <100> direction for both lattices in θ-Al_2O_3 // γ-Al_2O_3 interfaces.

In Figure 8.6, the $(0001)_\alpha$ // $(111)_\gamma$ interface (L) is constructed with an upper $(0001)_\alpha$ lattice region terminated by a plane of Al ions and a lower $(111)_\gamma$ lattice region terminated by a mixture of Al and O ions. Both Al and O ions in the $(0001)_\alpha$ lattice relax away from the interface towards the bulk whereas Al and O ions in the $(111)_\gamma$ lattice relax asymmetrically toward both the interface and bulk. The $(10\bar{1}0)_\alpha$ // $(110)_\gamma$ interface (M) appears at a nearly cleaved plane with isolated O ion clusters extending across the interface. In the $(10\bar{1}0)_\alpha$ // $(110)_\gamma$ interface, the behavior of relaxation is similar to the $(0001)_\alpha$ // $(111)_\gamma$ interface. However, the magnitude of the relaxations found in both α-Al_2O_3 // γ-Al_2O_3 interfaces examined is much less than that found in the θ-Al_2O_3 // γ-Al_2O_3 interfaces discussed previously.

Table 8.6 provides a list of the computed interface energies for the heterophase Al_2O_3 boundaries. Of all boundaries studied in this work, the heterophase $(0001)_\alpha$ // $(111)_\gamma$ interface (L) has the lowest interface energy, computed at 0.25 J/m^2; while, the heterophase $(010)_\theta$ // $(0\bar{1}1)_\gamma$ interface has the highest interface energy, computed at 2.61 J/m^2. Both the $(110)_\theta$ // $(100)_\gamma$ and the $(10\bar{1}0)_\alpha$ // $(110)_\gamma$ interfaces, have similar energies computed at 1.35 and 1.47 J/m^2, respectively, which are on the order of the highest interface energies calculated for the homophase boundaries.

Table 8.6: Computed heterophase alumina interface energies modeled with ReaxFF

ID	E_{Int}^{Gibbs} (J/m^2)	$2L^{Gibbs}$ (Å)
J	1.35	19.3
K	2.61	25.2
L	0.25	14.0
M	1.47	18.5

8.4.4 *Virtual diffraction of select Al_2O_3 interfaces*

To provide further validation of the interface structures sampled in this work, virtual SAED

is used to make direct comparisons of select interface models with available experimental

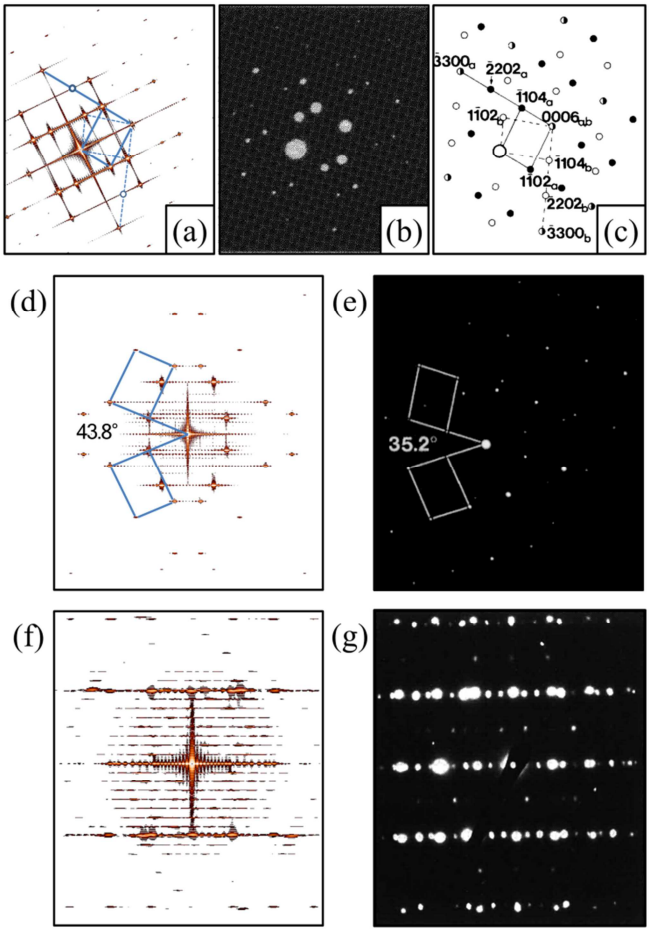

Figure 8.7: Comparison between virtual and experimental SAED patterns produced by (a-c) simulated and experimentally observed α-Al_2O_3 basal twin [63], (d-e) simulated α-Al_2O_3 Σ11 $(10\bar{1}1)$ // $(10\bar{1}\bar{1})$ interface and experimentally observed α-Al_2O_3 near Σ11 $(0\bar{1}11)$ // $(01\bar{1}1)$ interface [67], and (f-g) simulated and experimental $(0001)_\alpha$ // $(111)_\gamma$ interface [81].

patterns. Virtual SAED patterns are created for select interfaces using the methods described by Coleman et al. [42,43], which only require the wavelength of radiation λ, atomic positions, and atom types; no *a priori* knowledge of the crystal structure is assumed. The virtual diffraction algorithm generates an ultrahigh resolution, three-dimensional reciprocal lattice mesh using a 0.001 $Å^{-1}$ spacing in each direction. At each reciprocal lattice point, the algorithm computes the

diffraction intensities using the structure factor equation derived from kinematic diffraction theory (cf. [94,95]). Virtual SAED patterns are constructed by viewing a spherical slice of the diffraction intensity data parallel to the incident radiation, which represents the intersection of an appropriate Ewald sphere for the chosen radiation wavelength.

Figure 8.7(a-c) show virtual and experimental [63] SAED patterns for the α-Al_2O_3 basal twin interface (A) produced along to the $[1\bar{2}10]$ direction using 125 keV (λ=0.03275 Å) electron radiation. In Figure 8.7(a), the virtual SAED pattern has been rotated to match that of the experimental orientation. Similar to previous works [42,43], vertical and horizontal relrods emerge from the diffraction peaks in the virtual SAED pattern due to the finite volume of the simulation. The virtual SAED pattern computed for the α-Al_2O_3 basal twin interface closely matches the experimental pattern; however, it misses a single set of $\{\bar{2}202\}$ peaks as evident from the schematic of the diffraction pattern [63] in Figure 8.7(c). Analysis of the three-dimensional diffraction data shows that the $\{\bar{2}202\}$ peaks lie slightly off the Ewald sphere used to construct the virtual SAED pattern and would be visible through small tilts of the electron beam (or sample).

Figure 8.7(d-e) show a virtual SAED patterns for the α-Al_2O_3 $\Sigma 11$ $(10\bar{1}1)$ // $(10\bar{1}\bar{1})$ interface (E) alongside an experimental SAED pattern taken for a near $\Sigma 11$ $(0\bar{1}11)$ // $(01\bar{1}1)$ boundary created by diffusion bonding [67]. Both patterns are aligned parallel to their respective $<1\bar{2}10>$ tilt axis and use 400 keV (λ=0.016439 Å) electron radiation. The SAED patterns clearly identifies the differences between the two interfaces, showing that the modeled α-Al_2O_3 $\Sigma 11$ $(10\bar{1}1)$ // $(10\bar{1}\bar{1})$ interface has a $<1\bar{2}10>$ tilt misorientation of 43.8° while the near $\Sigma 11$ $(0\bar{1}11)$ // $(01\bar{1}1)$ experimental sample contains a 35.2° misorientation. However, the SAED patterns does show similar symmetry of the diffraction peaks within the virtual and experimental SAED

patterns. Note, the modeled interface structure with the larger misorientation angle predicts a 0.29 J/m^2 lower interface energy from that reported in [67].

Figure 8.7(f-g) show virtual and experimental [81] SAED patterns for the $(0001)_\alpha$ // $(111)_\gamma$ interface (L) taken along to the $[10\bar{1}0]_\alpha$ and $[0\bar{1}1]_\gamma$ directions using 1200 keV (λ=0.00736 Å) electron radiation. The major diffraction peaks found in the virtual SAED pattern closely match those found in the experimental pattern. However, additional peaks appear in the experimental patterns due to the presence of a second γ-Al_2O_3 orientation contained within the experimental sample [81] but not represented in the simulation.

8.5 Conclusions

In this work, alumina interfaces are modeled using the ReaxFF interatomic potential in order to characterize their atomic structure and to extract interface energy data. This study includes a selection of homophase α-Al_2O_3, γ-Al_2O_3, θ-Al_2O_3, and κ-Al_2O_3 interfaces as well as heterophase α-Al_2O_3 // γ-Al_2O_3 and θ-Al_2O_3 // γ-Al_2O_3 interfaces. The computational methods are validated using five α-Al_2O_3 homophase interfaces, which have been studied in depth by prior atomistic simulations. The current computational methods are then applied to study homophase interfaces constructed with metastable alumina lattices and heterophase alumina interfaces constructed from multiple alumina phases, which have never before been modeled. Virtual SAED patterns are constructed for select alumina interfaces in order to obtain direct experimental validation of the simulation results.

Interface energies computed using ReaxFF for α-Al_2O_3 homophase boundaries show good agreement with those found in prior atomistic studies. However, the minimum energy structures found for the Al_2O_3 basal interface structure and the α-Al_2O_3 $\Sigma 11$ $(10\bar{1}1)$ // $(10\bar{1}\bar{1})$ interface models deviate slightly from prior results. ReaxFF predicts the homophase γ-Al_2O_3 {111} twin and the

θ-Al_2O_3 twin to have energies on the same order as that found for the lowest energy α-Al_2O_3 prismatic twin boundary, whereas the predicted interface energy for the κ-Al_2O_3 {001} 120° twin is on the order of the highest energy α-Al_2O_3 $\Sigma 11$ $(10\bar{1}1)$ // $(10\bar{1}\bar{1})$ interface.

The lowest energy boundary modeled in this study is the $(0001)_\alpha$ // $(111)_\gamma$ interface. As mentioned, virtual diffraction is used to help optimize the orientation relationship of the $(0001)_\alpha$ // $(111)_\gamma$ interface and other heterophase interfaces defined solely by their interface planes. While results for the $(0001)_\alpha$ // $(111)_\gamma$ interface show that greater overlap of three-dimensional diffraction intensities from each lattice region correlate with lower energy interfaces, further studies should be performed to prove if this correlation holds true for more general interfaces and other material systems.

The interface energies tabulated in this work cover the greatest number and widest span of alumina boundaries explored using a consistent computational model, ReaxFF. These data add to recent alumina bulk and surface energies computed using ReaxFF [41] such that future predicted mesoscale models polymorphic alumina may be performed.

Acknowledgements

The authors acknowledge support of the National Science Foundation under grant #0954505. Additional support is provided by the 21st Century Professorship in Mechanical Engineering at the University of Arkansas. This work utilized the Extreme Science and Engineering Discovery Environment (XSEDE), which is supported by National Science Foundation grant #OCI-1053575. The authors thank Prof. Adri van Duin for useful discussions concerning ReaxFF and equilibration procedures as well as Prof. Christopher Weinberger for useful discussions regarding heterophase interfaces.

References

[1] Gitzen WH, editor. (1970) Alumina as a Ceramic Material. Westerville, Ohio: Wiley-American Ceramic Society.

[2] Knözinger H and Ratnasamy P. (1978) Catalytic aluminas: Surface models and characterization of surface sites, Catalysis Reviews: Science and Engineering, **17**, 32–70.

[3] Selinder TI, Fietzke F, and Klostermann H. (2004) PVD-Al2O3-coated cemented carbide cutting tools, Surface and Coatings Technology, **189**, 186–192.

[4] Costescu RM, Cahill DG, Fabreguette FH, Sechrist ZA, and George SM. (2004) Ultra-low thermal conductivity in W/Al2O3 nanolaminates., Science, **303**, 989–90.

[5] Aryasomayajula A, Randall NX, Gordon MH, and Bhat DG. (2008) Tribological and mechanical properties of physical vapor deposited alpha alumina thin film coating, Thin Solid Films, **517**, 819–823.

[6] Mellali M, Fauchais P, and Grimaud A. (1996) Influence of substrate roughness and temperature on the adhesion / cohesion of alumina coatings, Surface and Coatings Technology, **81**, 275–286.

[7] Cremer R, Witthaut M, Neuschu D, Erkens G, Leyendecker T, and Feldhege M. (1999) Comparative characterization of alumina coatings deposited by RF, DC and pulsed reactive magnetron sputtering, Surface and Coatings Technology, **121**, 213–218.

[8] Belkind A, Freilich A, Song G, Zhao Z, Scholl R, and Bixon E. (2003) Mid-frequency reactive sputtering of dielectrics : Al2O3, Surface and Coatings Technology, **175**, 88–93.

[9] Halvarsson M, Nordén H, and Vuorinen S. (1993) Microstructural investigation of CVD α-Al2O3/κ-Al2O3 multilayer coatings, Surface and Coatings Technology, **61**, 177–181.

[10] Vuorinen S and Karlsson L. (1992) Phase transformation in chemically vapour-depositeed κ-alumina, Thin Solid Films, **214**, 132–143.

[11] Skogsmo J, Halvarsson M, and Vuorinen S. (1992) Microstructural study of the κ-Al2O3 to α-Al2O3 transformation in CVD κ-Al2O3, Surface and Coatings Technology, **54-55**, 186–192.

[12] Halvarsson M and Vuorinen S. (1996) Microstructure and performance of CVD κ-Al2O3 multilayers, Materials Science and Engineering: A, **209**, 337–344.

[13] Schneider JM, Sproul WD, and Matthews A. (1997) Phase formation and mechanical properties of alumina coatings prepared at substrate temperatures less than 500°C by ionized and conventional sputtering, Surface and Coatings Technology, **95**, 179–183.

[14] Borosy AP, Silvi B, Allavena M, and Nortier P. (1994) Structure and bonding of bulk and surface θ-Alumina from periodic Hartree-Fock calculations, The Journal of Physical Chemistry, **98**, 13189–13194.

[15] Digne M, Sautet P, Raybaud P, Euzen P, and Toulhoat H. (2004) Use of DFT to achieve a rational understanding of acid-basic properties of γ-alumina surfaces, Journal of Catalysis, **226**, 54–68.

[16] Jamting A, Ring M, Ruppi S, and Swain M V. (1995) Mechanical characterization of kappa and alpha alumina films on hard metals using indentation methods, Journal of Hard Materials, **6**, 67–87.

[17] Kathrein M, Schintlmeister W, Wallgram W, and Schleinkofer U. (2003) Doped CVD Al2O3 coatings for high performance cutting tools, Surface and Coatings Technology, **163-164**, 181–188.

[18] Trinh DH, Back K, Pozina G, Blomqvist H, Selinder TI, Collin M, Reineck I, Hultman L, and Högberg H. (2009) Phase transformation in κ- and γ-Al2O3 coatings on cutting tool inserts, Surface and Coatings Technology, **203**, 1682–1688.

[19] Zywitzki O, Hoetzsch G, Fietzke F, and Goedicke K. (1996) Effect of the substrate temperature on the structure and properties of Al2O3 layers reactively deposited by pulsed magnetron sputtering, Surface and Coatings Technology, **82**, 169–175.

[20] Osada A, Nakamura E, Homma H, Hayahi T, and Oshika T. (2006) Wear mechanism of thermally transformed CVD Al2O3 layer, International Journal of Refractory Metals and Hard Materials, **24**, 387–391.

[21] Eklund P, Sridharan M, Singh G, and Bøttiger J. (2009) Thermal Stability and Phase Transformations of γ-/Amorphous-Al2O3 Thin Films, Plasma Processes and Polymers, **6**, S907–S911.

[22] Doremus RH. (2006) Diffusion in alumina, Journal of Applied Physics, **100**, 101301.

[23] Priester L and Lartigue S. (1991) Description and Role in High-Temperature Deformation of Grain Boundaries in α-Alumina Ceramics, Journal of the European Ceramic Society, **8**, 47–57.

[24] Watanabe T. (1983) Grain boundary sliding and stress concentration during creep, Metallurgical and Materials Transactions A, **14**, 531–545.

[25] Cook RF and Schrott AG. (1988) Calcium segregation to grain boundaries in alumina, Journal of the Australian Ceramic Society, **71**, 50–58.

[26] Blanchard CR and Page RA. (1992) Grain boundary sliding microdisplacement measurements during the crep of alumina, Journal of the American Ceramic Society, **75**,

1612–1620.

[27] Phillips DS and Shiue YR. (1984) Grain-Boundary Microstructures in Alumina Ceramics, Advances in Ceramics, 357–367.

[28] Farrer JK, Ravishankar N, Michael JR, and Carter CB. (2001) Grain boundary migration in alumina, MRS Symposia Proceedings, **652**, Y1.2.1–Y1.2.6.

[29] Harding JH. (2003) Experiment and theory of diffusion in alumina, Journal of the American Ceramic Society, **86**, 554–559.

[30] Nettleship I, McAfee RJ, and Slaughter WS. (2002) Evolution of the Grain Size Distribution during the Sintering of Alumina at 1350°C, Journal of the American Ceramic Society, **85**, 1954–1960.

[31] Dillon SJ, Harmer MP, and Rohrer GS. (2010) Influence of interface energies on solute partitioning mechanisms in doped aluminas, Acta Materialia, **58**, 5097–5108.

[32] Dillon SJ, Miller H, Harmer MP, and Rohrer GS. (2010) Grain boundary plane distributions in aluminas evolving by normal and abnormal grain growth and displaying different complexions, International Journal of Materials Research, **101**, 50–56.

[33] Dillon SJ and Harmer MP. (2007) Multiple grain boundary transitions in ceramics : A case study of alumina, Acta Materialia, **55**, 5247–5254.

[34] Dillon SJ and Harmer MP. (2006) Intrinsic grain boundary mobility in alumina, Journal of the American Ceramic Society, **89**, 3885–3887.

[35] Larsson A, Halvarsson M, and Vuorinen S. (1998) Microstructural investiagation of heat-treated CVD κ-Al2O3 multilayer coatings, International Journal of Refractory Metals and Hard Materials, **16**, 369–376.

[36] Ruppi S. (2005) Deposition , microstructure and properties of texture-controlled CVD a-Al2O3 coatings, International Journal of Refractory Metals and Hard Materials, 1–11.

[37] Ofori-Opoku N and Provatas N. (2010) A quantitative multi-phase field model of polycrystalline alloy solidification, Acta Materialia, **58**, 2155–2164.

[38] Tiaden J. (1999) Phase field simulations of the peritectic solidification of Fe–C, Journal of Crystal Growth, **198-199**, 1275–1280.

[39] Nestler B, Garcke H, and Stinner B. (2005) Multicomponent alloy solidification: Phase-field modeling and simulations, Physical Review E, **71**, 041609.

[40] Van Duin ACT, Dasgupta S, Lorant F, and Goddard WA. (2001) ReaxFF: A Reactive Force Field for Hydrocarbons, The Journal of Physical Chemistry A, **105**, 9396–9409.

[41] Coleman SP and Spearot DE. (2014) Atomistic simulation and virtual diffraction characterization of stable and metastable alumina surfaces, Acta Materialia, Submitted.

[42] Coleman SP, Spearot DE, and Capolungo L. (2013) Virtual diffraction analysis of Ni [0 1 0] symmetric tilt grain boundaries, Modelling and Simulation in Materials Science and Engineering, **21**, 055020.

[43] Coleman SP, Sichani MM, and Spearot DE. (2014) A computational algorithm to produce virtual x-ray and electron diffraction patterns of interfaces from atomistic simulations, JOM, **66**, 408–416.

[44] Marinopoulos AG, Nufer S, and Elsässer C. (2001) Interfacial structures and energetics of basal twins in α-Al2O3: First-principles density-functional and emperical calculaitons, Physical Review B, **63**, 165112.

[45] Marinopoulos AG and Elsässer C. (2000) Microscopic structure and bonding at the rhombohedral twin interface in α-Al2O3, Acta Materialia, **48**, 4375–4386.

[46] Fabris S and Elsässer C. (2001) Σ13 ($10\bar{1}4$) twin in α-Al2O3: A model for a general grain boundary, Physical Review B, **64**, 245117.

[47] Marinopoulos AG and Elsässer C. (2001) Density-functional and shell-model calculations of the energetics of basal-plane stacking faults in sapphire, Philosophical Magazine Letters, **81**, 329–338.

[48] Elsässer C and Marinopoulos AG. (2001) Substitutional cation impurities in α-Al2O3: ab-initio case study of segragation to the rhombohedral twin boundary, Acta Materialia, **49**, 2951–2959.

[49] Fabris S and Elsässer C. (2002) Ab-initio theory of grain boudnary segregation in α-Alumina: Energetics, atomistic and electronic structures, MRS Symposia Proceedings, **7551**, 1–6.

[50] Fabris S and Elsässer C. (2003) First-principles analysis of cation segregation at grain boundaries in α-Al2O3, Acta Materialia, **51**, 71–86.

[51] Fabris S, Nufer S, Elsässer C, and Gemming T. (2002) Prismatic Σ3 ($10\bar{1}0$) twin boundary in α-Al2O3 investigated by density functional theory and transmission electron microscopy, Physical Review B, **66**, 155415.

[52] Suzuki H, Matsubara H, Kishino J, and Kondoh T. (1998) Simulation of surface and grain boundary properties of alumina by molecular dynamics method, Journal of the Ceramic Society of Japan, **106**, 1215–1222.

[53] Ogawa T, Kuwabara A, Fisher CAJ, Moriwake H, Matsunaga K, Tsuruta K, and Kitaoka S. (2014) A density functional study of vacancy formation in grain boundaries of undoped

α-alumina, Acta Materialia, **69**, 365–371.

[54] Galmarini S, Aschauer U, Tewari A, Aman Y, Van Gestel C, and Bowen P. (2011) Atomistic modeling of dopant segregation in α-alumina ceramics: Coverage dependent energy of segregation and nominal dopant solubility, Journal of the European Ceramic Society, **31**, 2839–2852.

[55] Nakamura K, Mizoguchi T, Shibata N, Matsunaga K, Yamamoto T, and Ikuhara Y. (2010) First-principles sliding simulation of Al-terminated Σ13 pyramidal twin grain boundary in α -Al2O3, Philosophical Magazine Letters, **90**, 159–172.

[56] Milas I, Hinnemann B, and Carter E a. (2008) Structure of and ion segregation to an alumina grain boundary: Implications for growth and creep, Journal of Materials Research, **23**, 1494–1508.

[57] Nakamura K, Mizoguchi T, Shibata N, Matsunaga K, Yamamoto T, and Ikuhara Y. (2007) First-principles study of grain boundary sliding in α-Al2O3, Physical Review B, **75**, 184109.

[58] Chen J, Xu Y-N, Rulis P, Ouyang L, and Ching W-YY. (2005) Ab initio theoretical tensile test on Y-doped Σ=3 grain boundary in α-Al2O3, Acta Materialia, **53**, 403–410.

[59] Nishimura H, Matsunaga K, Saito T, Yamamoto T, and Ikuhara Y. (2003) Atomic structures and energies of Σ7 Symmetric tilt grain boundaries in alumina bicrystals, Journal of the American Ceramic Society, **86**, 574–580.

[60] Exner M and Finnis MW. (1996) Atomistic simulation of grain boundaries in alumina, Materials Science Forum, **207-209**, 225–228.

[61] Kenway PR. (1994) Calculated structures and energies of grain boundaries in α-Al2O3, Journal of the American Ceramic Society, **77**, 349–355.

[62] Wilson M, Exner M, Huang Y-M, and Finnis MW. (1996) Transferable model for the atomistic simulation of Al2O3, Physical Review B, **54**, 15683–15689.

[63] Morrissey KJ and Carter CB. (1984) Faceted grain boundaries in Al2O3, Journal of the American Ceramic Society, **67**, 292–301.

[64] Carter CB and Morrissey KJ. (1983) Grain-boundary structure in Al2O3, Advances in Ceramics, **6**, 303–323.

[65] Morrissey KJ and Carter CB. (1983) Dislocations in twin boundaris in Al2O3, Advances in Ceramics, **6**, 85–95.

[66] Höche T, Kenway PR, Kleebe H-J, Finnis MW, and Rühle M. (1994) The structure of special grain boundaries in α-Al2O3, Journal of Physics and Chemistry of Solids, **55**,

1067–1082.

[67] Höche T, Kenway PR, Kleebe H-J, and Rühle M. (1994) High-resolution transmission electron microscopy studies of a near Σ11 grain boundary in α-alumina, Journal of the American Ceramic Society, **77**, 339–348.

[68] Gemming T, Nufer S, Kurtz W, and Rühle M. (2003) Structure and chemistry of symmetiric tilt grain boundaries in α-Al2O3: I, Bicrystals with “Clean” Interface", Journal of the American Ceramic Society, **86**, 581–589.

[69] Höche T and Rühle M. (1996) Structure and composition of a special twin boundary in α-Al2O3, Materials Science Forum, **207-209**, 97–100.

[70] Watanabe T, Yoshida H, Yamamoto T, Ikuhara Y, and Sakuma T. (1999) Grain boundary energy and atomic structure in alumina bicrystals, Materials Science Forum, **304-306**, 601–606.

[71] Ikuhara Y, Watanabe T, Yamamoto T, Saito T, Yoshida H, and Sakuma T. (1999) Grain boundary structure and sliding of alumina bicrystals, MRS Symposia Proceedings, **601**, 125–132.

[72] Grimmer H, Bonnet R, Lartigue S, and Priester L. (1990) Theoretical and experimental descriptions of grain boundaries in rhombohedral α-Al2O3, Philosophical Magazine A, **61**, 493–509.

[73] Swiatnicki W, Lartigue-Korinek S, and Laval JY. (1995) Grain boundary structure and intergranular segregation in Al2O3, Acta Metallurgica et Materialia, **43**, 795–805.

[74] Shin W, Seo W-S, and Koumoto K. (1998) Grain-boundary grooves and surface diffusion in polycrystalline alumina measured by atomic force microscope, Journal of the European Ceramic Society, **18**, 595–600.

[75] Levin I and Brandon DG. (1998) Metastable alumina polymorphs: Crystal structures and transition sequences, Journal of the American Ceramic Society, **81**, 1995–2012.

[76] Larsson A and Ruppi S. (2001) Microstructure and properties of CVD γ-Al2O3 coatings, International Journal of Refractory Metals and Hard Materials, **19**, 515–522.

[77] Ollivier B, Retoux R, Lacorre P, Massiot D, and Férey G. (1997) Crystal structure of κ-alumina: an X-ray powder diffraction, TEM and NMR study, Journal of Material Chemistry, **7**, 1049–1056.

[78] Morrissey KJ, Czanderna KK, Merrill RP, and Carter CB. (1985) Transition alumina structures studied using HREM, Ultramicroscopy, **18**, 379–386.

[79] Yamaguchi G, Yasui I, and Chu W-C. (1970) A new method of preparing θ-alumina and

the interpretation of its x-ray-powder diffration pattern and electron diffraction pattern, Bulletin of the Chemical Society of Japan, **43**, 2487–2491.

[80] Akatsu T, Scheu C, Wagner T, Gemming T, Hosoda N, Suga T, and Rühle M. (2000) Morphology and microstructure of the Ar+ -ion sputtered (0001) α-Al2O3 surface, Surface Science, **165**, 159–165.

[81] Gemming T, Clarke DR, and Rühle M. (1999) Polymorphic Phase Transformations in Al2O3, in: Koiwa M, Otsuka K, Miyazaki T (Eds.). Proc. from Int. Conf. Solid-Solid Phase Transform. Kyoto, Japan: .

[82] Cai S-H, Rashkeev S, Pantelides ST, and Sohlberg K. (2003) Phase transformation mechanism between γ- and θ-alumina, Physical Review B, **67**, 1–10.

[83] Lindulf N, Halvarsson M, Nordén H, and Vuorinen S. (1994) Microstructural investigation of the κ-Al2O3 → α-Al2O3 transformation in multilayer coatings of chemically vapour deposited κ-Al2O3, Thin Solid Films, **253**, 311–317.

[84] Cai S-H, Rashkeev S, Pantelides ST, and Sohlberg K. (2002) Atomic Scale Mechanism of the Transformation of γ-Alumina to θ-Alumina, Physical Review Letters, **89**, 1–4.

[85] Plimpton SJ. (1995) Fast parallel algorithms for short-range molecular dynamics, Journal of Computational Physics, **117**, 1–19.

[86] Zhang Q, Çağın T, van Duin ACT, Goddard WA, Qi Y, and Hector LG. (2004) Adhesion and nonwetting-wetting transition in the Al/α-Al2O3 interface, Physical Review B, **69**, 045423.

[87] Sen FG, Qi Y, van Duin ACT, and Alpas AT. (2013) Oxidation induced softening in Al nanowires, Applied Physics Letters, **102**, 051912.

[88] VisIt. (2014) Https://wci.llnl.gov/codes/visit/.

[89] Wolf DE and Nozières P. (1988) Interfacial properties of elastically strained materials, Zeitschrift für Physik B Condensed Matter, **70**, 507–513.

[90] Rappe AK and Goddard WA. (1991) Charge equilibration for molecular dynamics simulations, The Journal of Physical Chemistry, **95**, 3358–3363.

[91] Yourdshahyan Y, Ruberto C, Bengtsson L, and Lundqvist BI. (1997) First-principles calculations on the atomic and electronic structure of κ-Al2O3, Physical Review B, **56**, 8553–8558.

[92] Paglia G, Rohl AL, Buckley CE, and Gale JD. (2005) Determination of the structure of γ-alumina from interatomic potential and first-principles calculations: The requirement of significant numbers of nonspinel positions to achieve an accurate structural model,

Physical Review B, **71**, 1–16.

[93] Zhou RS and Snyder RL. (1991) Structures and transformation mechanisms of the η, γ and θ transition aluminas, Acta Crystallographica Section B, **47**, 617–630.

[94] Warren BE. (1990) X-Ray Diffraction, first ed. New York: Dover Publications.

[95] Williams DB and Carter CB. (2009) Diffraction of Small Volumes, in: Transm. Electron Microsc. Part 2 Diffr., second ed. New York: Springer.

Appendix 8.1

College of Engineering
Department of Mechanical Engineering
(479) 575-3153
(479) 575-6982 (FAX)

UNIVERSITY OF ARKANSAS

Mechanical Engineering Building
Fayetteville, Arkansas 72701

Coleman, S.P., Spearot, D.E. (2014) Atomistic simulation and virtual diffraction characterization of homophase and heterophase alumina interfaces, Acta Materialia, submitted.

I certify that Mr. Shawn Coleman is the first author of the paper and completed greater than 51% of the work in this publication.

Sincerely,

Douglas E. Spearot, Ph.D.
Dissertation Director
Associate Professor and 21st Century Professorship
Department of Mechanical Engineering
University of Arkansas
Fayetteville, AR 72701
Office: 479-575-3040
E-mail: dspearot@uark.edu

Appendix 8.2

Author Rights

Elsevier supports the need for authors to share, disseminate and maximize the impact of their research. We take our responsibility as stewards of the online record seriously, and work to ensure our policies and procedures help to protect the integrity of scholarly works.

Author's rights to reuse and post their own articles published by Elsevier are defined by Elsevier's copyright policy. For our proprietary titles, the type of copyright agreement used depends on the author's choice of publication:

For subscription articles: These rights are determined by a copyright transfer, where authors retain scholarly rights to post and use their articles.

For open access articles: These rights are determined by an exclusive license agreement, which applies to all our open access content.

In both cases, the fundamental rights needed to publish and distribute an article remain the same and Elsevier authors will be able to use their articles for a wide range of scholarly purposes.

Details on how authors can reuse and post their own articles are provided below.

Help and support

For reuse and posting not detailed below, please see our posting policy, or for authors who would like to:

- Include material from other sources in your work being published by Elsevier, please visit: Permission seeking guidelines for Elsevier authors.
- Obtain permission to re-use material from Elsevier books, journals, databases, or other products, please visit: Obtaining permission to reuse Elsevier material
- Or if you are an Elsevier author and are contacted by a requestor who wishes to re-use all or part of your article or chapter, please also refer them to our Obtaining Permission to Re-Use Elsevier Material page.
- See our FAQ on posting and copyright queries.
- Contact us directly, please email our Permissions Help Desk.

How authors can use their own journal articles

Authors can use their articles for a wide range of scholarly, non-commercial purposes as outlined below. These rights apply for all Elsevier authors who publish their article as either a subscription article or an open access article.

We require that all Elsevier authors always include a full acknowledgement and, if appropriate, a link to the final published version hosted on Science Direct.

For open access articles these rights are separate from how readers can reuse your article as defined by the author's choice of Creative Commons user license options.

Authors can use either their accepted author manuscript or final published article for:	
✓	Use at a conference, meeting or for teaching purposes
✓	Internal training by their company
✓	Sharing individual articles with colleagues for their research use* (also known as 'scholarly sharing')
✓	Use in a subsequent compilation of the author's works
✓	Inclusion in a thesis or dissertation
✓	Reuse of portions or extracts from the article in other works
✓	Preparation of derivative works (other than for commercial purposes)

*Please note this excludes any systematic or organized distribution of published articles.

http://www.elsevier.com/journal-authors/author-rights-and-responsibilities

Chapter 9: Conclusions

9.1 Summary of Major Findings

Recall, the three main objectives of this work are (1) to develop and implement a virtual diffraction algorithm that generates x-ray and electron diffraction patterns directly form atomistic simulation data without *a priori* knowledge of the simulated crystal structure, (2) to utilize molecular statistics and molecular dynamics simulations to evaluate the energetic stability of different bulk alumina models as well as characterize metastable and stable alumina surfaces, and (3) to utilize molecular statistics and virtual diffraction to characterize homophase and heterophase alumina interfaces. The major findings of this work towards meeting these objectives are highlighted below.

- In preparation for the development and implementation of an advanced virtual diffraction algorithm, traditional methods of characterizing atomistic simulations are explored in a study that identifies the mechanisms of motion associated with a large-angle Ni grain boundary induced by synthetic, crystal-orientation-dependent driving forces [1]. The face-centered cubic Ni structure enables both a slip-vector analysis [2] and exploration of continuum metrics for microrotation and strain [3] in the Ni $\sum$37 (570) [001] symmetric tilt grain boundary. The study focuses on the motion of this large-angle Ni grain boundary below the interface roughening temperature, where there is greater concern that the non-physical nature of the driving force could promote non-physical results [4,5]. Comparison between synthetically driven and shear driven simulations using traditional atomistic simulation characterization methods reveals that the synthetic-driving forces do not alter the mechanism of grain boundary motion. In addition, nudged elastic band

calculations show that the transition path and energy barriers for motion are not appreciably altered by the application of the synthetic driving force. It is important to emphasize that although great insights are gained from the use of a slip-vector analysis and the exploration of continuum metrics of microrotation and strain within this work, the same characterization techniques are not possible in the alumina material system due to the complexity of their crystal structures.

- The traditional methods of characterizing atomistic simulations are unable to uniquely identify each alumina phase considered; therefore, an novel virtual diffraction algorithm is developed and implemented [6–8]. Virtual diffraction methods are analogous to their experimental counterparts and model the scattering of electromagnetic radiation from individual atoms in order to identify the structure of a material system. The new virtual diffraction algorithm, implemented into LAMMPS [9], creates an ultra-high resolution three-dimensional mesh of reciprocal space. Diffraction intensities are computed at each reciprocal space mesh point using the structure factor equation [10], which is evaluated via the summation of inverse Fourier transform functions incorporating each atomic position. Unlike prior virtual diffraction algorithms [11–18], the current method does not require *a priori* knowledge of the crystal system and does not map the atomic positions onto a regular grid in order to utilize fast Fourier transforms. Instead, the algorithm requires only knowledge of the atom type and position as well as the wavelength of the incident radiation. Additionally, the new virtual diffraction method uses the same mesh algorithm to create both x-ray diffraction (XRD) line profiles and selected area diffraction (SAED) patterns, which are then constructed by a unique analysis and

visualization routine.

- The virtual diffraction algorithm is validated by studying low-angle and large-angle Ni [010] symmetric tilt boundaries, such that direct comparisons can be made to prior experimental and atomistic results [6,7]. Virtual SAED patterns viewed along the tilt axis clearly reveal the misorientation angle created by each bicrystal model. Similar to prior experimental work, subsidiary peaks appear near the {002} reflections in low-angle grain boundaries, which correspond to the dislocation spacing found in the grain boundary structure. Vertical and horizontal relrods aligned with the simulation domains also appear from the main diffraction peaks due to the finite volume explored [19]. A relrod analysis for varying sized simulations show that the predicted intensity profiles match well to the analytical expression derived from fundamental diffraction theory [19]. Relrods from the finite volume simulations are also shown to influence the predicted XRD line profiles. The predicted XRD line profiles for each grain boundary simulation show diffraction peaks at the expected Bragg angles; however, secondary peaks emerge near the {002} reflection due to relrods. At other Bragg angles, the predicted XRD line profiles show broadening due the local strain associated with the grain boundary structure.

- The computational costs to perform virtual diffraction in its initial implementation could have limited the scope of this study. Therefore, the initial implementation of the virtual diffraction algorithm within LAMMPS is upgraded to take advantage of multilevel parallelism and heterogeneous computing [8]. In addition, the virtual diffraction

algorithm is also incorporated into an automated workflow to allow high throughput studies of alumina bulk, surfaces, and interfaces [8]. By incorporating OpenMP parallelization and enabling offloading to many integrated core (MIC) hardware, the virtual diffraction algorithm gains a 4.6x speed up over the original MPI based implementation. The improved algorithm is then linked to the SEAGrid science gateway [20,21] to automate the molecular dynamics simulation, virtual diffraction characterization, and visualization desired for this study through the submission of a single input deck.

- Molecular dynamics and molecular statics simulations of bulk α-, γ-, θ-, and κ-Al_2O_3 at 0, 300, 500, and 700 K show that ReaxFF [22] correctly predicts α-Al_2O_3 as the lowest energy crystalline phase [23]. Virtual SAED patterns and XRD line profiles taken of each phase are unique, which enables a distinct method for identification of each phase. Additionally, XRD line profiles of 0 K energy minimized bulk alumina are in good agreement with their experimental diffraction patterns [24–27]. Despite these successes, however, bulk simulations using ReaxFF predict a lower energy amorphous alumina phase. Virtual SAED patterns are used to characterize the amorphous Al_2O_3 systems and confirm that similar amorphous structures arise from the same thermal treatment imposed on each alumina phase.

- Atomistic simulations of 11 α-, γ-, θ-, and κ-Al_2O_3 surface structures are performed at 0, 300, 500, and 700 K using the ReaxFF potential [22] in order to extract surface energies and characterize the surface structures [23]. At 0 K, the predicted minimum energy

surface structures and energies are in good agreement with previous atomistic studies [28–30]. However, ReaxFF predicts significant surface reconstructions within select structures at temperatures below what is to be expected from experiments [31–33]. It is believed that these reconstructions are driven by the unnatural bias for amorphization within ReaxFF potential, which are promoted by the extra degrees of freedom associated with the free surface and the thermal energy available at temperatures. Analysis of several reconstructed surfaces reveal negative surface energies resulting from the creation of lower energy structures as compared to the bulk phases.

- Virtual SAED patterns are used to help identify the orientation and structures of each surface model as well as to gain experimental validation through direct comparisons of select results to prior work [23]. At 0 K, virtual SAED patterns show mostly discrete reflection peaks at the expected orientations; however, virtual SAED patterns taken at temperature reveal peak smearing within select patterns due to surface relaxations and reconstructions. Because the diffraction peaks associated with the reconstructed surfaces remain intact, complete amorphization of these surface structures is not reached due to the constraints imposed by the internal structure. Virtual XRD line profiles of select negative energy θ-Al_2O_3 surfaces are also performed and reveal a distinct pattern that is different from bulk θ-Al_2O_3 indicating the transformation of the system into a lower energy crystalline phase.

- Molecular statics simulations of 12 homophase and heterophase alumina interfaces are performed at 0 K using the ReaxFF potential [22] in order to characterize the interface

structure and extract interface energies [34]. The structures and interface energies of five α-Al_2O_3 twin interfaces show good agreement with prior atomistic studies [35–41] providing validation for the current analysis methods. Homophase interfaces constructed from adjoining regions of a single metastable alumina phase as well as heterophase interfaces constructed from multiple alumina phases are investigated for the first time through atomistic simulations. For heterophase interfaces defined solely by the interface planes, virtual diffraction is used to help achieve the optimal orientation relationship of the adjoining lattice regions. In addition, virtual SAED patterns computed for select interfaces show good agreement to prior experimental results [42–44], which provide further validation for the atomistic simulations.

In summary, virtual diffraction methods are developed, implemented, and improved throughout this work in order to be used as an advanced characterization tool for atomistic simulations. ReaxFF [22] is used to model alumina bulk, surface, and interface structures and to extract pertinent energetic data. Combined, the tabulated data provides the widest scope ever performed on the alumina material system using a consistent computational model. The consistent computational model will allow quantitative comparisons to be made in future phase-field simulations (cf. [45–47]) of polymorphic alumina vapor deposition, as is discussed in Section 9.2. Because this work identifies an incorrect bias within the ReaxFF potential for constructing lower energy amorphous structures, a detailed study of the effects of ion bombardment could not be performed. However, preliminary results from ion bombardment simulations as well as new techniques of using virtual diffraction as an advance analysis tool are discussed in Section 9.2.2.

9.2 Recommendations for Future Works

The data and insights gained from the atomistic simulations performed on the alumina system as well as the virtual diffraction methods developed for this study lay foundations for a multitude of future works. Atomistic simulations performed in the current study highlight the structures and energetics of bulk, surface, and interface alumina systems that influence the microstructure evolution and properties of polymorphic alumina under different processing conditions. However, these data alone cannot predict the necessary processing conditions to achieve tailored alumina properties because of their limited spatiotemporal resolution. Instead, future mesoscale simulations, such as phase-field methods, are needed to extend the materials simulations into a larger spatiotemporal regime such that accurate predictions of the developing microstructure can be made varying processing conditions. The energetic data collected throughout this study will be key inputs into these predictive mesoscale models of polymorphic and polycrystalline alumina physical vapor deposition. Specifically, these energies can aid in the development of an accurate free-energy functional to evolve the solid-state alumina transformations explored by phase-field simulations.

The virtual diffraction algorithm developed for this work shows tremendous promise in advancing future materials simulations by providing additional insights and characterization capabilities, especially in connection with similar experimental studies. In its current state, the virtual diffraction algorithm can be easily applied to any atomistic simulation with corresponding experimental comparison to provide both validation of the modeled system and offer greater understanding to the experimentally observed phenomena. For example, virtual diffraction methods implemented into combined atomistic simulation and experimental studies can provide

insights into the evolution of materials properties in systems at extreme conditions, such as shock or severe plastic deformation. In these cases, virtual SAED patterns and XRD line profiles would be useful to help provide connections between the underlying microstructure evolution, such as grain growth and rotation, to the effects on the material properties.

Future works can also take advantage of the extensive three-dimensional intensity data computed by the virtual diffraction algorithm to help construct more accurate simulations and provide insights to damage and deformation processes. For example, advance analysis of diffraction data using visualization software may help optimize the necessary interface orientation relationships to achieve low-energy boundaries as discussed in [34] and in a further preliminary study detailed in Section 9.2.1. Similarly, visualization software can be used to provide greater insights to damage and deformation by tracking the deviation of diffraction intensities throughout a simulation. Examples of this analysis technique are shown in the preliminary results for ion bombardment simulations that are detailed in Section 9.2.2.

Lastly, the current virtual diffraction algorithm can be augmented to model other experimental characterization techniques based on diffraction, such as electron backscatter diffraction (EBSD). For example, preliminary work conducted in collaboration with Professor Eric Homer at Brigham Young University shows that new analysis techniques applied to the three-dimensional diffraction intensity data can simulate EBSD and produce Kikuchi patterns from atomistic simulations [48]. The analysis techniques implemented for virtual EBSD integrates different regions of the three-dimensional diffraction intensity data, which could help increase the resolution capabilities of the resulting patterns.

9.2.1 *Optimization of Interface Orientation Relationships*

Advanced analysis techniques using virtual diffraction data suggest a promising method for

optimizing interface orientation relationships in complex systems. Preliminary work conducted on heterogeneous alumina interfaces [34] and for the Al (111) / α-Al_2O_3 (0001) interface, has led to a method of optimizing the relative rotation of grains by using virtual SAED patterns. Figure 9.1 shows a depiction of the method whereby computed diffraction patterns created by the individual lattice regions are superimposed to create a prediction for the diffraction pattern created by the interface. In Figure 9.1, the crystal regions are rotated to achieve a maximum overlap of the virtual diffraction pattern peaks, which corresponds to higher coincidence of atoms at the interface.

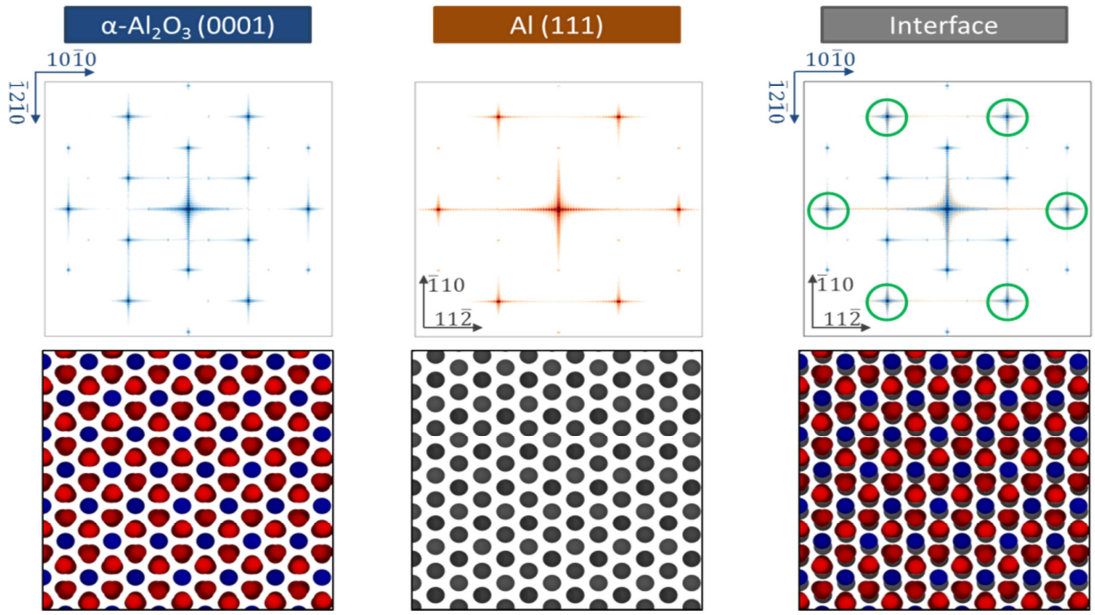

Figure 9.1: Schematic showing the method used to obtain an optimal orientation relationship for the Al (111) / α-Al_2O_3 (0001) interface by superimposing diffraction peaks from the adjoining lattice regions.

The work of adhesion, W_{ad} , is computed for both the optimized misorientation and an initial misorientation constructed with the α-Al_2O_3 region rotated 90° counterclockwise from optimal. Work of adhesion represents the force needed to separate the two regions at the interface and is computed using the equation,

$$W_{ad} = \left(E_1^{Tot} + E_2^{Tot} - E_{12}^{Tot}\right)/ A \ , \qquad (9.1)$$

where E_i^{Tot} (i = 1, 2) is the total energy of the slab model for each region, E_{12}^{Tot} is the total energy of the interface slab, and A is the area of the grain boundary. The work of adhesion of the optimal misorientation is higher than the initial model (0.8 J/m^2 versus 0.4 J/m^2). Because the same terminating planes are used in both models, the higher work of adhesion indicates the presence of a more energetically stable interface. A selected area diffraction pattern oriented along the grain boundary plane for the stable interface is shown in Figure 9.2 and compared to a pattern obtained by Medlin et al. in their experimental study [49]. The virtual diffraction pattern matches well to the experimental pattern and provides further validation of the optimal orientation relationship created by the analysis of virtual diffraction patterns.

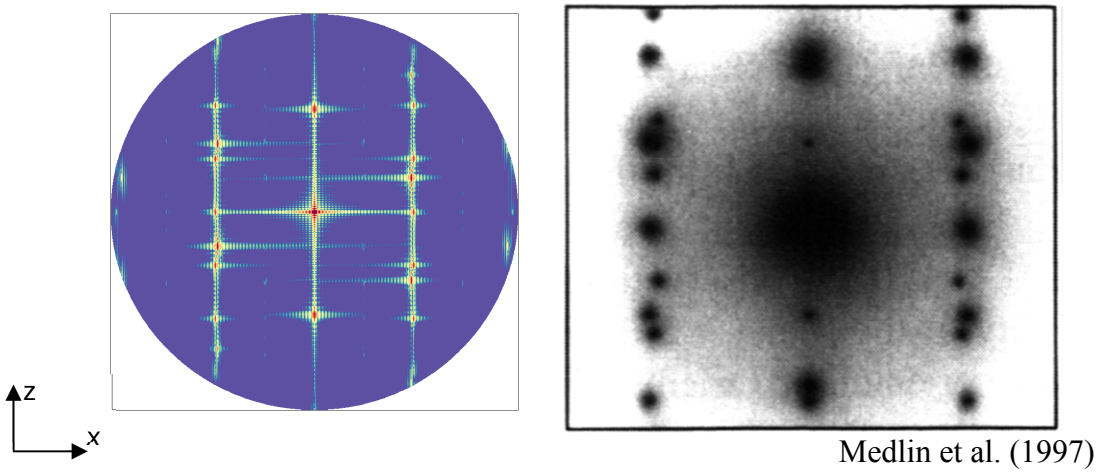

Figure 9.2: Comparison of virtual electron diffraction pattern of Al (111) / α-Al2O3 (0001), to the experimental pattern by Medlin et al. [49].

Future work is needed to investigate the relationship between the overlapping diffraction intensities of opposing lattice regions and their corresponding interface energies in order to prove if this correlation holds true for more general interface and other material systems. Ideally, this

work will be conducted initially on a simpler FCC metal such that greater analysis can be conducted in order to connect the diffraction patterns directly to previously studied interface relationships.

9.2.2 *Ion Bombardment*

Preliminary simulations of a single aluminum ion bombarding onto alumina surfaces using the ReaxFF potential [22] have incorporated advanced virtual diffraction analysis techniques to measure the deviations in SAED patterns throughout the simulation. In this study, slab models of the α-Al_2O_3 (0001) and γ-Al_2O_3 (111) surfaces as well as a slab model containing a γ-Al_2O_3 (111) // α-Al_2O_3 (0001) interface are constructed approximately 5 nm thick and equilibrated to

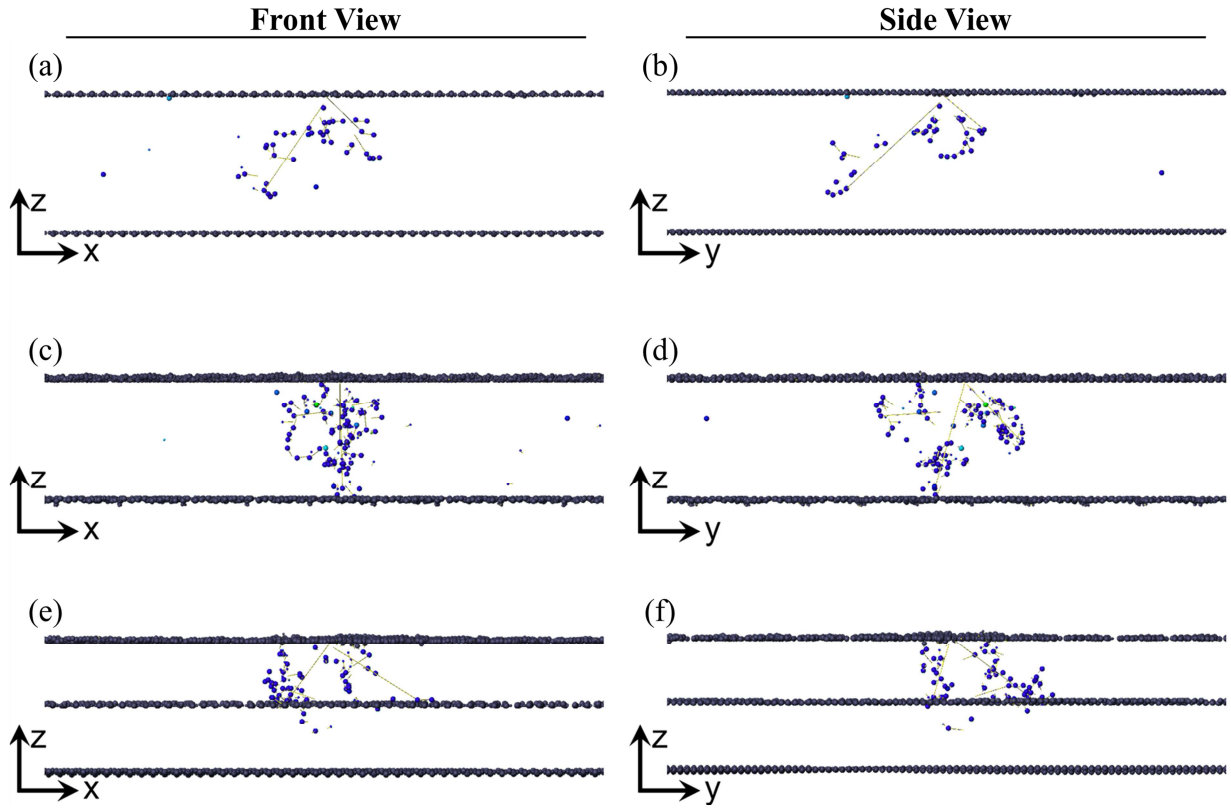

Figure 9.3: Simulated 1 keVAl ion bombardment captured at 2.000 ps impacting (a-b) α-Al_2O_3 (0001), (c-d) γ-Al_2O_3 (111), and (e-f) γ-Al_2O_3 (111) // α-Al_2O_3 (0001) slab models. Atoms are filtered for displacements greater than 1.5 Å or having 0.5 eV/atom kinetic energy. Colored here by kinetic energy 0.5-1.0 eV.

300 K. Note, the interface slab model is oriented such that the α-Al_2O_3 (0001) lattice is located on the top region. After equilibration, the centermost Al ion on the upper regions of each slab model is provided an additional 1 keV velocity normal to the surface in order to simulate ion bombardment while keeping the correct stoichiometry of the system. Snapshots of the ion bombardment simulations at 2.0 ps show no appreciable phase transformation as shown in Figure 9.3. However, measurements of the deviation of between the current and equilibrated SAED patterns, shown at 2.0 ps in Figure 9.4, are able to identify damage correlated to small changes in the crystal structure.

In Figure 9.4, the deviation between the SAED patterns taken at equilibration and after 2.0 ps from the initial ion bombardment reveal emerging peaks (red) and decaying peaks (blue) at different locations for each slab model. Here, emerging peaks closer to the origin of the SAED patterns indicate an expansion of the corresponding lattice direction while peaks emerging further from the origin indicate a contraction in the lattice direction. Figure 9.4 shows that expansion and compression of the lattice are isolated to specific directions within the each model, which provides insight into possible mechanisms for the initiation of phase transformations. However, because ReaxFF has been shown to unnaturally bias amorphization of the alumina structure [23], the accuracy of these ion bombardment simulation is questionable. To further characterize the nanoscale mechanisms leading to nucleation and phase transformation during physical vapor deposition using ion bombardment future work is needed that incorporates a more appropriate interatomic potential.

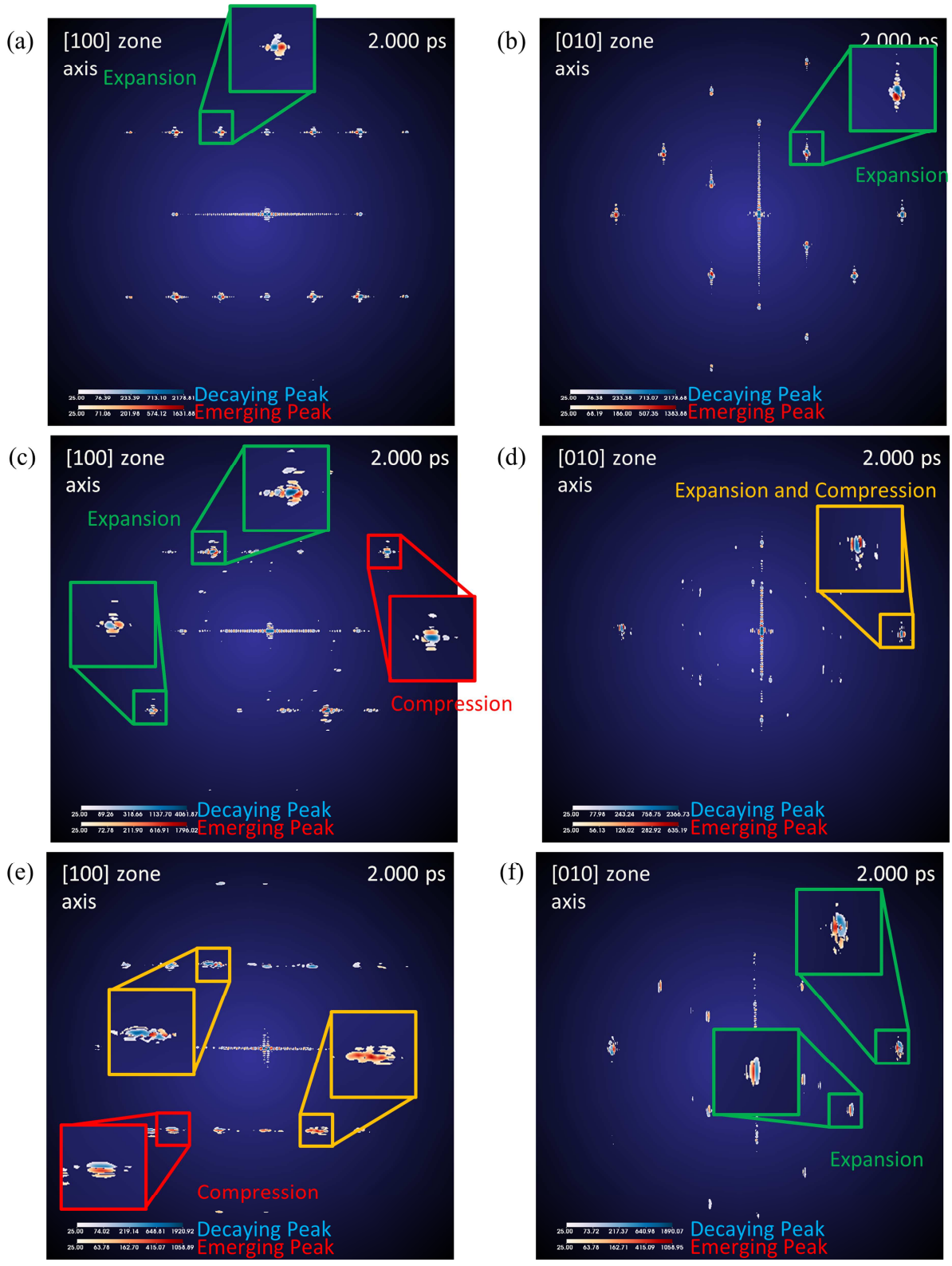

Figure 9.4: Deviation in the computed SAED patterns 2.0 ps after 1 keVAl ion bombardment captured at 2.000 ps impacting (a-b) α-Al_2O_3 (0001), (c-d) γ-Al_2O_3 (111), and (e-f) γ-Al_2O_3 (111) // α-Al_2O_3 (0001) slab models.

References

[1] Coleman SP, Spearot DE, and Foiles SM. (2014) The effect of synthetic driving force on the atomic mechanisms associated with grain boundary motion below the interface roughening temperature, Computational Materials Science, **86**, 38–42.

[2] Zimmerman JA, Kelchner CL, Klein PA, Hamilton JC, and Foiles SM. (2001) Surface Step Effects on Nanoindentation, Physical Review Letters, **87**, 165507.

[3] Tucker GJ, Zimmerman JA, and McDowell DL. (2010) Shear deformation kinematics of bicrystalline grain boundaries in atomistic simulations, Modelling and Simulation in Materials Science and Engineering, **18**, 015002.

[4] Olmsted DL, Holm EA, and Foiles SM. (2009) Survey of computed grain boundary properties in face-centered cubic metals—II: Grain boundary mobility, Acta Materialia, **57**, 3704–3713.

[5] Janssens KGF, Olmsted DL, Holm EA, Foiles SM, Plimpton SJ, and Derlet PM. (2006) Computing the mobility of grain boundaries, Nature Materials, **5**, 124–7.

[6] Coleman SP, Spearot DE, and Capolungo L. (2013) Virtual diffraction analysis of Ni [0 1 0] symmetric tilt grain boundaries, Modelling and Simulation in Materials Science and Engineering, **21**, 055020.

[7] Coleman SP, Sichani MM, and Spearot DE. (2014) A computational algorithm to produce virtual x-ray and electron diffraction patterns of interfaces from atomistic simulations, JOM, **66**, 408–416.

[8] Coleman SP, Pamidighantam S, Van Moer M, Wang Y, Koesterke L, and Spearot DE. (2014) Performance improvement and workflow development of virtual diffraction calculations, XSEDE14, In Press.

[9] Plimpton SJ. (1995) Fast parallel algorithms for short-range molecular dynamics, Journal of Computational Physics, **117**, 1–19.

[10] Warren BE. (1990) X-Ray Diffraction, first ed. New York: Dover Publications.

[11] Bristowe PD and Sass SL. (1980) The atomic structure of a large angle [001] twist boundary in gold determined by a joint computer modelling and X-ray diffraction study, Acta Metallurgica, **28**, 575–588.

[12] Budai J, Bristowe PD, and Sass SL. (1983) The projected atomic structure of a large angle [001] Σ= 5 (θ=36. 9°) twist boundary in gold: Diffraction analysis and theoretical predictions, Acta Metallurgica, **31**, 699–712.

[13] Oh Y and Vitek V. (1986) Structural multiplicity of Σ=5(001) twist boundaries and interprtation of x-ray diffraction from these boundaries, Acta Metallurgica, **34**, 1941–1953.

[14] Fitzsimmons MR, Vaudin MD, and Sass SL. (1988) Structural multiplicity and the interpretation of X-ray diffraction observations from grain boundaries, Scripta Metallurgica, **22**, 105–110.

[15] Brandstetter S, Derlet PM, Van Petegem S, and Van Swygenhoven H. (2008) Williamson–Hall anisotropy in nanocrystalline metals: X-ray diffraction experiments and atomistic simulations, Acta Materialia, **56**, 165–176.

[16] Stukowski A, Markmann J, Weissmüller J, and Albe K. (2009) Atomistic origin of microstrain broadening in diffraction data of nanocrystalline solids, Acta Materialia, **57**, 1648–1654.

[17] Markmann J, Bachurin D, Shao L, Gumbsch P, and Weissmüller J. (2010) Microstrain in nanocrystalline solids under load by virtual diffraction, EPL (Europhysics Letters), **89**, 66002.

[18] Kimminau G, Nagler B, Higginbotham A, Murphy WJ, Park N, Hawreliak JA, Kadau K, Germann TC, Bringa EM, Kalantar DH, Lorenzana HE, Remington BA, and Wark JS. (2008) Simulating picosecond x-ray diffraction from shocked crystals using post-processing molecular dynamics calculations, Journal of Physics: Condensed Matter, **20**, 505203.

[19] Williams DB and Carter CB. (2009) Diffraction of Small Volumes, in: Transm. Electron Microsc. Part 2 Diffr., second ed. New York: Springer.

[20] Dooley R, Milfeld K, Guiang C, Pamidighantam S, and Allen G. (2006) From Proposal to Production: Lessons Learned Developing the Computational Chemistry Grid Cyberinfrastructure, Journal of Grid Computing, **4**, 195–208.

[21] Shen N, Y. F, and Pamidighantam S. (2014) E-science infrastructures for molecular modeling and parameterization, Journal of Computer Science, In Press.

[22] Sen FG, Qi Y, van Duin ACT, and Alpas AT. (2013) Oxidation induced softening in Al nanowires, Applied Physics Letters, **102**, 051912.

[23] Coleman SP and Spearot DE. (2014) Atomistic simulation and virtual diffraction characterization of stable and metastable alumina surfaces, Acta Materialia, Submitted.

[24] Ishizawa N, Miyata T, Minato I, Marumo F, and Iwai S. (1979) A structural investigation of α-Al203 at 2170K, Acta Crystallographica Section B, **36**, 228–230.

[25] Verwey EJW. (1935) The structure of the electrolytic oxide layer on aluminium,

Zeitschrift für Kristallographie, **91**, 317–320.

[26] Husson E and Repelin Y. (1996) Structural studies of transition aluminas: Theta alumina, European Journal of Solid State and Inorganic Chemistry, **33**, 1223–1231.

[27] Ollivier B, Retoux R, Lacorre P, Massiot D, and Férey G. (1997) Crystal structure of κ-alumina: an X-ray powder diffraction, TEM and NMR study, Journal of Material Chemistry, **7**, 1049–1056.

[28] Marmier A and Parker SC. (2004) Ab initio morphology and surface thermodynamics of α-Al2O3, Physical Review B, **69**, 115409.

[29] Sun J, Stirner T, and Matthews A. (2006) Structure and surface energy of low-index surfaces of stoichiometric α-Al2O3 and α-Cr2O3, Surface and Coatings Technology, **201**, 4205–4208.

[30] Blonski S and Garofalini SH. (1993) Molecular dynamics simulations of α-alumina and γ-alumina surfaces, Surface Science, **295**, 263–274.

[31] French TM and Somorjai GA. (1970) Composition and surface structure of the (0001) face of α-alumina by low-energy electron diffraction, The Journal of Physical Chemistry, **74**, 2489–2495.

[32] Barth C and Reichling M. (2001) Imaging the atomic arrangements on the high-temperature reconstructed α-Al2O3 (0001) surface, Nature, **414**, 54–57.

[33] Sohlberg K, Pantelides ST, and Pennycook SJ. (2001) Surface reconstruction and the difference in surface acidity between gamma- and eta-alumina., Journal of the American Chemical Society, **123**, 26–9.

[34] Coleman SP and Spearot DE. (2014) Atomistic simulation and virtual diffraction characterization of homophase and heterophase alumina interfaces, Acta Materialia, Submitted.

[35] Marinopoulos AG and Elsässer C. (2000) Microscopic structure and bonding at the rhombohedral twin interface in α-Al2O3, Acta Materialia, **48**, 4375–4386.

[36] Fabris S and Elsässer C. (2001) Σ13 ($10\bar{1}4$) twin in α-Al2O3: A model for a general grain boundary, Physical Review B, **64**, 245117.

[37] Marinopoulos AG and Elsässer C. (2001) Density-functional and shell-model calculations of the energetics of basal-plane stacking faults in sapphire, Philosophical Magazine Letters, **81**, 329–338.

[38] Elsässer C and Marinopoulos AG. (2001) Substitutional cation impurities in α-Al2O3: ab-initio case study of segregation to the rhombohedral twin boundary, Acta Materialia, **49**,

2951–2959.

[39] Fabris S and Elsässer C. (2002) Ab-initio theory of grain boudnary segregation in α-Alumina: Energetics, atomistic and electronic structures, MRS Symposia Proceedings, **7551**, 1–6.

[40] Fabris S and Elsässer C. (2003) First-principles analysis of cation segregation at grain boundaries in α-Al2O3, Acta Materialia, **51**, 71–86.

[41] Fabris S, Nufer S, Elsässer C, and Gemming T. (2002) Prismatic Σ3 ($10\bar{1}0$) twin boundary in α-Al2O3 investigated by density functional theory and transmission electron microscopy, Physical Review B, **66**, 155415.

[42] Morrissey KJ and Carter CB. (1984) Faceted grain boundaries in Al2O3, Journal of the American Ceramic Society, **67**, 292–301.

[43] Höche T, Kenway PR, Kleebe H-J, and Rühle M. (1994) High-resolution transmission electron microscopy studies of a near Σ11 grain boundary in α-alumina, Journal of the American Ceramic Society, **77**, 339–348.

[44] Gemming T, Clarke DR, and Rühle M. (1999) Polymorphic Phase Transformations in Al2O3, in: Koiwa M, Otsuka K, Miyazaki T (Eds.). Proc. from Int. Conf. Solid-Solid Phase Transform. Kyoto, Japan: .

[45] Ofori-Opoku N and Provatas N. (2010) A quantitative multi-phase field model of polycrystalline alloy solidification, Acta Materialia, **58**, 2155–2164.

[46] Tiaden J. (1999) Phase field simulations of the peritectic solidification of Fe–C, Journal of Crystal Growth, **198-199**, 1275–1280.

[47] Nestler B, Garcke H, and Stinner B. (2005) Multicomponent alloy solidification: Phase-field modeling and simulations, Physical Review E, **71**, 041609.

[48] Thomas J, Homer ER, Coleman SP, and Spearot DE. (2014) Simulated Kikuchi diffraction patterns for structures containing defects, Modelling and Simulation in Materials Science and Engineering, In Preparation.

[49] Medlin DL, McCarty KF, Hwang RQ, Guthrie SE, and Baskes MI. (1997) Orientation relationships in the heteroepitaxial aluminum films on sapphire, Thin Solid Films, **299**, 110–114.